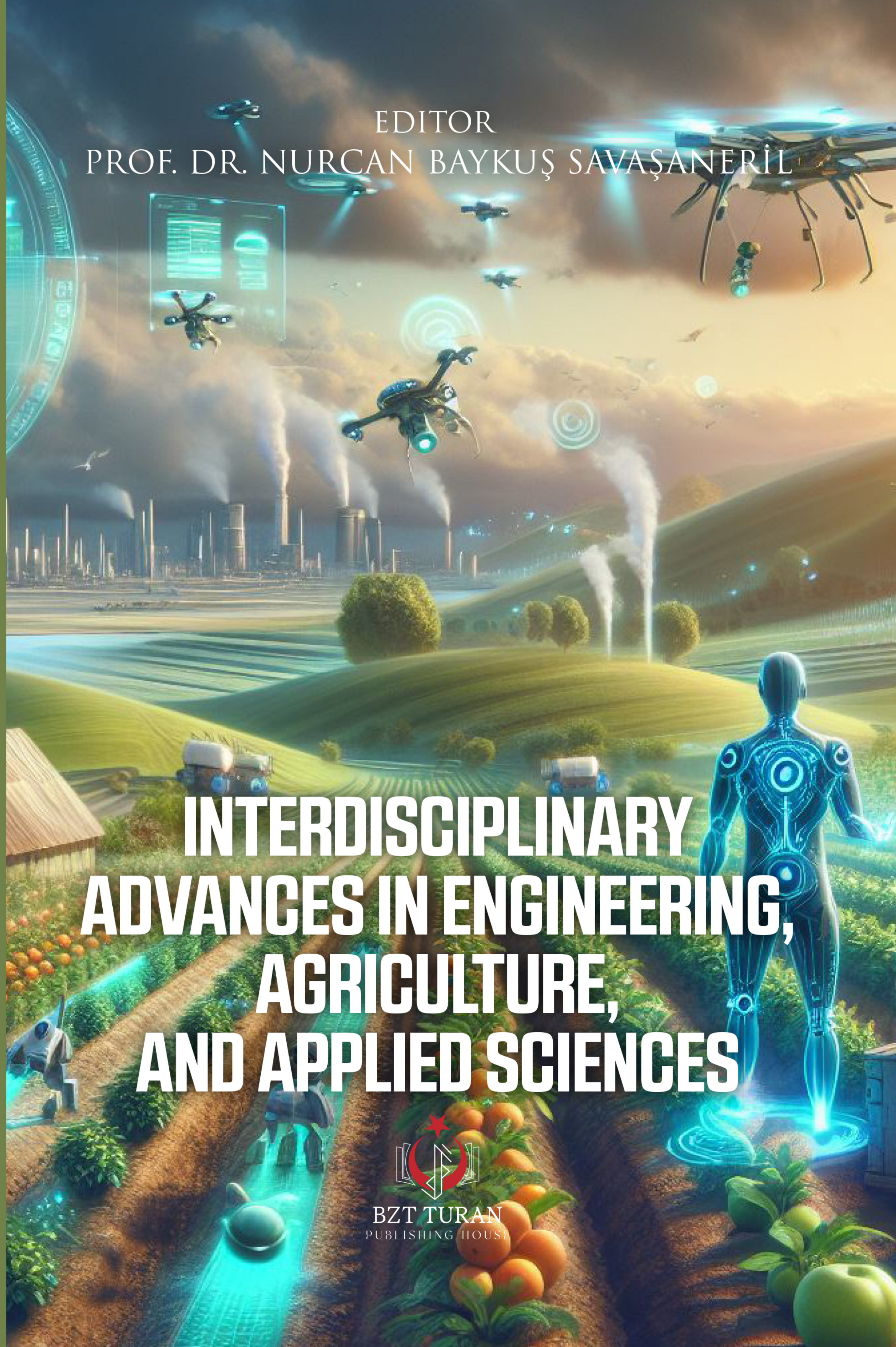

EDITOR

PROF. DR. NURCAN BAYKUŞ SAVAŞANERİL

INTERDISCIPLINARY ADVANCES IN ENGINEERING, AGRICULTURE, AND APPLIED SCIENCES

BZT TURAN
PUBLISHING HOUSE

INTERDISCIPLINARY ADVANCES IN ENGINEERING, AGRICULTURE, AND APPLIED SCIENCES

EDITOR:
PROF. DR. NURCAN BAYKUŞ SAVAŞANERİL

Nurcan BAYKUŞ SAVAŞANERİL was born on April 1, 1970, in İzmir, Turkey. She received her bachelor's degree from the Mathematics Department of Ege University in 1991 and completed her master's degree at the Graduate School of Natural and Applied Sciences of Dokuz Eylul University in 1995. In July 2003, she obtained her Ph.D. from the same university, focusing on parabolic partial differential equations. She began her career as a teaching assistant at Dokuz Eylul University in 1992, and in October 2010, she became an Assistant Professor, followed by her promotion to Associate Professor in March 2011, when she was appointed to an associate professorship. In 2012, she was assigned to the Mathematics Department of Selçuk University for a four-year term, and in 2016, she was appointed as a Professor in the Machine and Drawing Construction Program at Dokuz Eylul University. Between 2018 and 2019, she served as the director of Dokuz Eylul University Bergama Vocational School, and she currently holds the position of Head of the Department of Machine and Metal Technologies at Dokuz Eylul University İzmir Vocational School. Prof. Dr. Nurcan Baykuş Savaşaneril has published 34 international articles, presented full-text papers at 53 international symposiums, and authored several books, including "General Mathematics I," "General Mathematics II," "Mathematics I for Vocational Schools," "Mathematics II for Vocational Schools," "Calculus I," and "Calculus II." With her expertise in mathematics, she has made significant contributions to education and academic research, actively participating in various journals and symposiums.

9 789952 854107

www.bztturanpublishinghouse.com
/bztturanpublishinghouse

INTERDISCIPLINARY ADVANCES IN ENGINEERING, AGRICULTURE, AND APPLIED SCIENCES

Editor

Nurcan BAYKUŞ SAVAŞANERİL

Published by
BZT TURAN PUBLISHINGHOUSE
Certificate Number: 202401
Delaware, United States
and Baku, Azerbaijan

www.bztturanpublishinghouse.com
info@bztturanpublishinghouse.com

INTERDISCIPLINARY ADVANCES IN ENGINEERING, AGRICULTURE, AND APPLIED SCIENCES

Nurcan BAYKUŞ SAVAŞANERİL

Language: English
Publication Date: December 2024
Cover designed by Kağan SARGI
Print and digital versions typeset by BZT TURAN Media Co. Ltd.

E-ISBN: 978-9952-8541-0-7
DOI: https://doi.org/10.30546/19023.978-9952-8541-8-3.2024.203.

OPEN ACCESS

Suggested Citation:

Savaşaneril, N. (2024). INTERDICIPLINARY ADVANCES IN ENGINEERING, AGRICULTURE , AND APPLIED SCIENCES. BZT TURAN PUBLISHING HOUSE.

DOI: https://doi.org/10.30546/19023.978-9952-8541-8-3.2024.203.

BZT TURAN
PUBLISHING HOUSE

Editor

Nurcan BAYKUŞ SAVAŞANERİL was born on April 1, 1970, in İzmir, Türkiye. She received her bachelor's degree from the Mathematics Department of Ege University in 1991 and completed her master's degree at the Graduate School of Natural and Applied Sciences of Dokuz Eylül University in 1995. In July 2003, she obtained her Ph.D. from the same university, focusing on parabolic partial differential equations. She began her career as a teaching assistant at Dokuz Eylül University in 1992, and in October 2010, she became an Assistant Professor, followed by her promotion to Associate Professor in March 2011, when she was appointed to an associate professorship. In 2012, she was assigned to the Mathematics Department of Selçuk University for a four-year term, and in 2016, she was appointed as a Professor in the Machine and Drawing Construction Program at Dokuz Eylül University. Between 2018 and 2019, she served as the director of Dokuz Eylül University Bergama Vocational School, and she currently holds the position of Head of the Department of Machine and Metal Technologies at Dokuz Eylül University İzmir Vocational School. Prof. Dr. Nurcan Baykuş Savaşaneril has published 34 international articles, presented full-text papers at 53 international symposiums, and authored several books, including "General Mathematics I," "General Mathematics II," "Mathematics I for Vocational Schools," "Mathematics II for Vocational Schools," "Calculus I," and "Calculus II." With her expertise in mathematics, she has made significant contributions to education and academic research, actively participating in various journals and symposiums.

PREFACE

The purpose of this book is to present comprehensive and innovative approaches to solving challenging problems in the fields of engineering and applied mathematics. It focuses in particular on the two-dimensional heat equation and delves deeply into how this equation can be solved across different geometric domains (square, rectangular, elliptical, and triangular). The solution methods for these geometric regions have been developed based on Green's functions and elliptic functions, and these novel approaches are compared to classical methods. The book also details how the results of these methods compare to those obtained through traditional discretization techniques, Discrete Fourier Transforms, Separation of Variables Method, and the Finite Element Method. The findings demonstrate that these new approaches provide more accurate and reliable results. The book emphasizes how these methods can be practically applied to complex geometries commonly encountered in disciplines such as engineering and physics, offering a valuable resource for researchers at all levels.

The book also includes experimental studies on the geomechanical behavior of alabastrine-type gypsum. In this context, a detailed analysis of uniaxial and triaxial tests carried out on gypsum samples obtained from the Sivas region is presented, focusing on the long-term stability of these samples. The deformation properties and creep behavior of alabastrine-type gypsum over time are examined, revealing important results for underground storage systems. The book offers new insights into the behavior of gypsum in underground openings such as natural gas storage and provides a comprehensive understanding of how these structures change over time. The data presented in this section serve as an essential guide for researchers working in the fields of underground engineering and geotechnics.

Other sections of the book focus on modern technologies used in agriculture and engineering, as well as their applications. In particular, the analyses of agricultural machinery and automation systems shed light on the future of modern agriculture. The evolution of agricultural machinery, combined with artificial intelligence and IoT-based technologies, is shown to make agriculture more sustainable and efficient. This section details how robots, sensors, and data-based management systems are shaping the future of agricultural practices. Additionally, the evaluation of how these technologies align with the United Nations' Sustainable Development Goals highlights how agriculture is transforming on a global scale.

Furthermore, the use of composite materials in the maritime and energy industries is another key topic in this book. It examines in detail how the mechanical properties of composite materials change in marine environments and the impact these changes have on material performance. Additionally, the analysis of connection systems used in natural gas and oil extraction, and how they behave under varying loads and depths, is presented. The solutions in this section are obtained using ANSYS software, and important design parameters are identified. These types of technical analyses offer practical solutions, particularly for engineers working in the fields of marine engineering and energy systems design.

The book also addresses the role of plastics in modern life. As the significance of plastics continues to grow, the environmental and health impacts of these materials become increasingly important. Evaluations of plastic materials produced using high-quality raw materials and modern technologies are provided, with a focus on optimizing production processes and minimizing environmental impacts.

This book brings together modern solutions and innovative approaches to a wide range of scientific topics, serving as an indispensable reference for researchers working in the fields of engineering and applied mathematics. It provides in-depth information on solutions to complex problems and technical analyses, while also shedding light on practical applications.

Prof. Dr. Nurcan BAYKUŞ SAVAŞANERİL Editor Interdisciplinary Advances in Engineering, Agriculture, and Applied Sciences,2024

CONTENTS

Chapter 1 1
Functional Three-Axis Mobile Solar-Powered Agriculture In Future Agricultural Technology Automation
BAHATTİN AGADAY

Chapter 2 19
An Overview of Composite Materials for Marine Applications
GÜRCAN ATAKÖK, DUDU MERTGENÇ YOLDAŞ

Chapter 3 42
Investigation of Teeth in Connection Used in Marine Oil Extraction
DUDU MERTGENÇ YOLDAŞ

Chapter 4 66
Experimental Investigations and Comparison of Machining Parameters on Cast Polyamide and Steel ASTM A1040 at CNC Milling Machines
GÜRCAN ATAKÖK

Chapter 5 108
Rayleigh Investigation of Kerf Ratios in Abrasive Water Jet Cutting: Dimension Analysis and Rayleigh Method
İBRAHİM AY

Chapter 6 134
Innovations in Agricultural Machinery: Artificial Intelligence, Robotics, and Sustainability
MEHMET ÇEVİK

Chapter 7 165
Environmentally Friendly Friction Materials
MUSTAFA ÖNCÜL

Chapter 8 185
The Effect of Infill Density on the Mechanical Properties of PLA Materials Produced by FDM Method
NECMETTİN YİĞİTTÜRK

Chapter 9 210
Analysis of Solution of the Two-Dimensional Heat Equation in Terms of Elliptic Functions
Nurcan BAYKUŞ SAVAŞANERİL

Chapter 10 248
Creep Behaviours of the Alabastrine Type Gypsums Under Uniaxial and Triaxial Loading Conditions
AHMET TURAN ARSLAN

FUNCTIONAL THREE-AXIS MOBILE SOLAR- POWERED AGRICULTURE IN FUTURE AGRICULTURAL TECHNOLOGY AUTOMATION

Bahattin AGADAY

Chapter 1

Functional Three-Axis Mobile Solar-Powered Agriculture In Future Agricultural Technology Automation

BAHATTİN AGADAY[1]

1- Introduction

In recent years, the agriculture sector has witnessed a significant transformation driven by advancements in automation and robotics, referred to as Agriculture 4.0. This shift is critical for enhancing productivity, sustainability, and efficiency in farming practices. (Biswas and Aslekar 2022) emphasize the role of automation and robotics in improving agricultural productivity, highlighting innovative technologies that optimize resource usage and increase crop yields.

The integration of digital tools and the Internet of Things (IoT) has further revolutionized agricultural management. (Dayıoğlu and Turker, 2021) provide a comprehensive review of how digital transformation is paving the way for a sustainable future in agriculture, while (Villa-Henriksen et al., 2020) explore the implementation challenges and potential of IoT in agricultural settings. These digital innovations enable real-time monitoring and data-driven decision-making, making precision agriculture techniques increasingly viable (Shafi et al., 2019).

Moreover, historical advancements in agricultural technologies have laid the groundwork for today's innovations. A review of various patents reveals a continuous evolution of tools aimed at improving agricultural efficiency, from early irrigation systems (US1017578A, 1912) to contemporary robotic platforms designed for multifaceted

---

[1] Lecturer, Dokuz Eylül University, Türkiye, https://orcid.org/ 0000-0002-9059-7423

agricultural functions (WO2013181069A1, 2013). As these technologies continue to evolve, the collaboration between traditional farming practices and modern technological solutions becomes essential for addressing global challenges such as climate change and food security.

This paper aims to examine the current landscape of automation and robotics in agriculture, focusing on their contributions to productivity and sustainability, while also addressing the challenges associated with their implementation.

In today's conditions, halting the deterioration in the agricultural sector will only be possible through technological innovation. The increased use of technology in agriculture will reduce human error, bring more uncultivated land into production, and enhance efficiency through controlled applications and the effective use of resources. As a result, many challenges in the agricultural field will be addressed, improving social welfare.

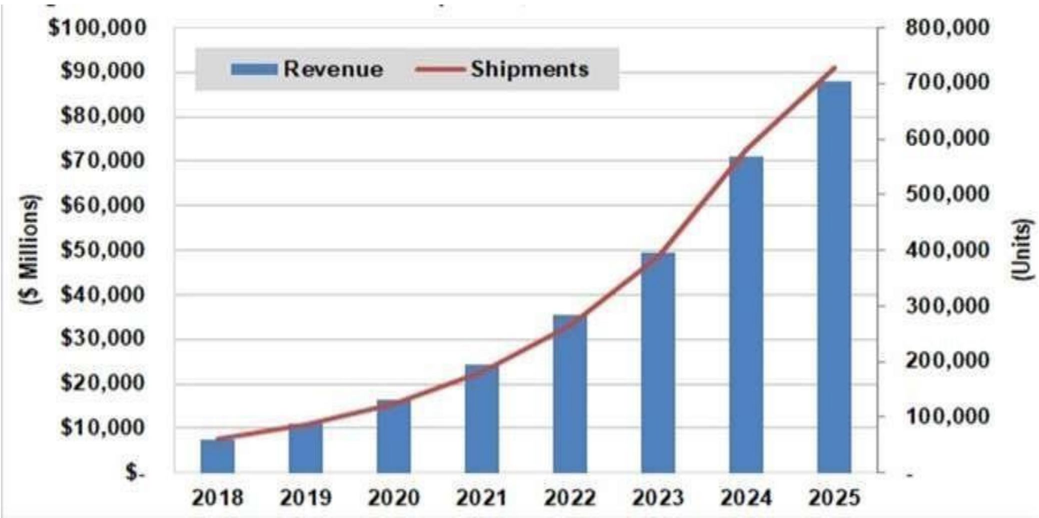

Figure 1 Agricultural robot market (Market Analysis / June 3, 2019 https://www.edge-ai-vision.com/2019/06/agricultural-robot- shipments-to-reach-727000-units-annually-by-2025/)

Current agricultural technologies include autonomous tractors and harvesting machines, automated irrigation systems, monitoring sensors and cameras, drone applications (for monitoring and spraying), operational robots, and integrated systems. This study will explore "three-axis mobile solar-powered agricultural automation" as a future agricultural technology, examining the innovations it will bring, its functional structure, and its adaptability to different agricultural applications.

1.1 System Structure

The invention consists of parallel steel or carbon fiber ropes stretched across poles erected at the four corners of the agricultural land, mounted on movable pulleys. These pulleys function similarly to a cable car system. The taut wires running along both sides of the field are moved by the motorized pulley system. Fixed to these wires are bridge heads that transfer resources like water, energy, data, and air to the bridge and facilitate the movement of the bridge ropes. The linear movement of the bridge along the wires provides "Y" axis movement. Motors at the bridge heads provide "X" axis movement of the moving platform body along the bridge, which also acts as a moving platform with idler wheels.

The movement of the transfer line is facilitated in this system. DC energy transfer can also be applied through these ropes. The head, which allows for "Z" directional movement, is connected to vertically moving shafts that are fixed to the carriage on the bridge and serves as a connection platform. Depending on the type of application, this head provides connections for robot arms, irrigation sprinklers, and energy transfer. A hybrid mechanism is used here, combining a rope system for horizontal movement across large areas and a vertical bearing system to reduce shaking and increase precision. The flexible structure of the system can be adapted according to different applications. It is also possible to use double carriages on the same bridge or to operate two tractors from the same head, with double carriages functioning on the bridge. The rotating head, connected to the shaft, automatically locks onto the apparatus in use (robot arm, tractor data and energy connection, irrigation, spraying apparatus, etc.), forming the interface.

The system's installation size can be up to 100x400m, but in special cases, the range of operation can be extended for kilometers with automatic locking water connections from supply lines laid on the ground every four hundred meters. Similarly, the size of the operational area can be expanded by applying similar modules.

The system derives its energy from solar power, with photovoltaic energy platforms integrated into the storage, energy, and pump roofs. The supporting poles are also utilized for this purpose. The system can run directly on clean energy or by storing it. Grid sharing is possible depending on energy availability. The water pump system lines in some agricultural lands can also be adapted for this purpose. The integration of the three-axis system, even for electric tractor applications, will significantly reduce energy costs, carbon footprint, mechanical issues, and eliminate the need for rechargeable batteries.

Additionally, artificial intelligence (AI)-supported software manages the system either locally or remotely (fed by sensor data) according to energy levels and the prioritization of agricultural tasks. This enhances operational efficiency.

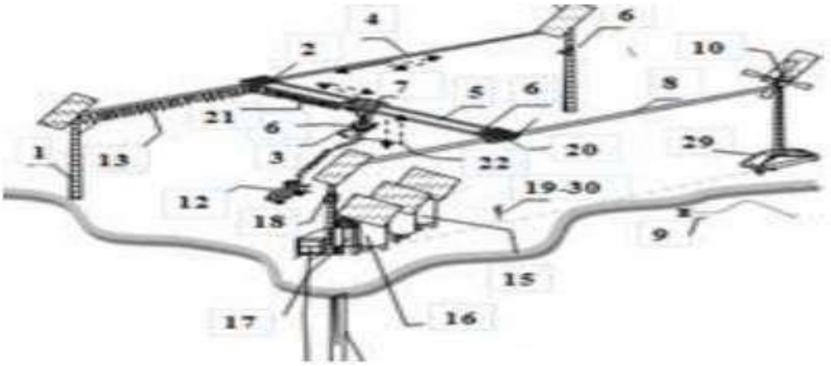

Figure 2 Schematic three-axis agricultural automation (patent image)
(b.agaday Patent inventor "Solar powered three-axis mobile agricultural automation"
https://patents.google.com/patent/WO2015199629A1/ar)

2. Advantages of the Invention Over Similar Systems

2.1 Energy

Energy usage in agriculture is critical for soil cultivation, sowing, irrigation, spraying, and harvesting. These operations are typically performed with machinery adapted to tractors. Energy costs vary depending on the type of agricultural activity. Today, many agricultural activities have led to increased mechanization and rising emission values, especially as countries develop. Additionally, grain prices surged by 87% in 2022 due to regional conflicts.

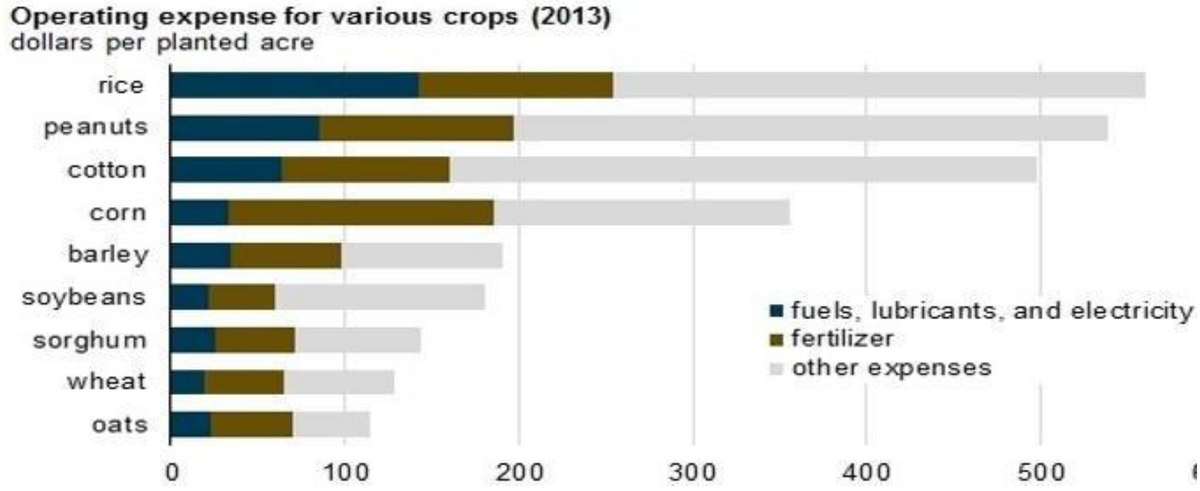

Figure 3 Table Costs by product type (2013 Agricultural)

One significant disadvantage of energy use in agriculture is its carbon footprint. At the COP26 Climate Summit, it was reported that global greenhouse gas emissions from agriculture and food production have increased by 17% over the last 30 years. In 2019, the global agriculture and food system emitted 17 billion tonnes of carbon dioxide, accounting for 31% of total global emissions. This issue will likely worsen as agricultural mechanization increases in developing countries. The high power demand of current agricultural practices has limited the use of clean energy in this sector.

Electric tractors, unlike electric cars, are not yet widely developed. Robots powered by photovoltaic (PV) panels have been developed, but they are primarily designed for observation purposes. The current efficiency of PV panels makes it impractical to achieve the 100-150 kW required for vehicle applications due to the large surface area needed. Some examples of these limitations are provided below.

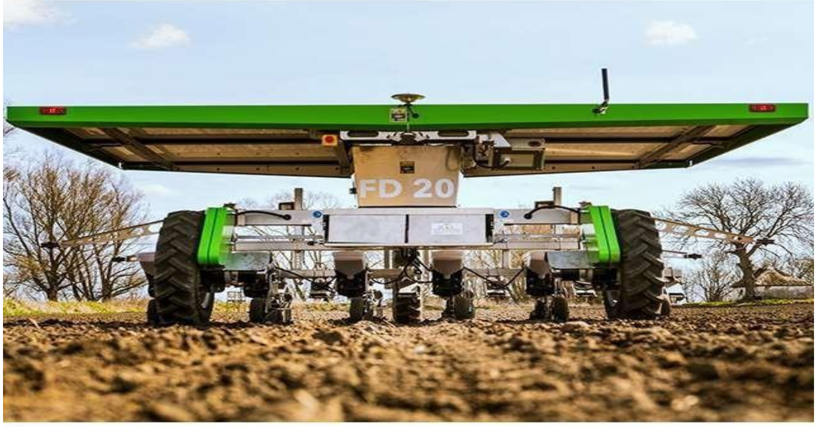

Figure 3 Fully automatic PV Driven agricultural robot Source: (FarmDroid) (https://www.dtnpf.com/agriculture/web/ag/news/article/2022/01/01/solar-powered-robot)

What sets the developed FD20 apart from other systems is its ability to perform tasks such as seed planting and weed collection using higher-powered solar panels. FD20 is a fully automated, solar-powered field robot that precisely sows seeds and performs mechanical weed control.

The robots shown in the images below are examples of observation robots, designed for tasks that do not require high energy, such as plant monitoring and soil sampling.

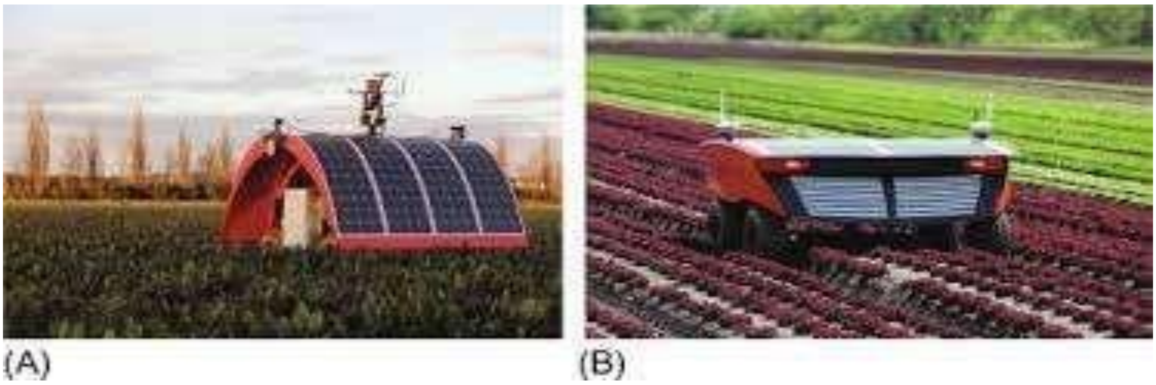

Figure 4 PV Implemented agricultural robots

(Chapter 7 - Applications of solar PV systems in agricultural automation and robotics https://www.sciencedirect.com/science/article/abs/pii/B9780128196106000077)

The developed system stands out from others by using clean energy sources at high power levels. Large solar panels installed on the warehouse and poles provide the necessary power, either directly or through DC storage. As a result, engine and maintenance costs are reduced, and the overall system cost is quite affordable. There are no additional costs, such as those associated with battery-powered tractors, and the system can operate autonomously anywhere on the farm without time limitations. A robotic arm tractor can work in sync with the system. Unlike cable-connected systems, which can cause product damage, this system avoids such issues. It is even possible to operate two tractors on a single bridge.

The system also allows AI-supported autonomous agricultural activities to be performed and monitored remotely. The bridge cup (trolley) is equipped with cameras, lighting, and communication systems. Tractor or irrigation connections are autonomously made via the arm on the vertical rotating head. The system can be adapted to both field and tree-based farming.

This system reduces emissions, lowers input costs, and optimizes monitoring, development, and harvesting practices.

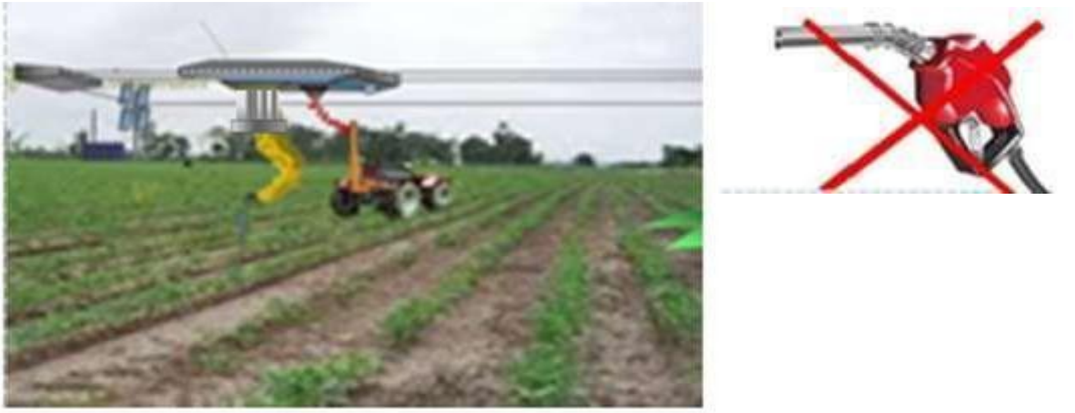

Figure 5 Schematic, Three axis solar powered tractor application

2.2 Irrigation Spraying

The irrigation system automation involves water pumping, storage, electro-ionized trace metal supplementation, and pressurized transfer to the nozzles. In small, flat fields, water is pumped from a pump at the bridgehead through narrow and deep water channels running along the rope line. In larger fields, it is done by moving carriers that are locked with a robot arm to a chimney located every 400 meters from the pipes laid on the ground along the rope line.

2.2.1 Runoff Irrigation

This method, also known as "wild irrigation," is an old technique. Excessive and uncontrolled use of water results in significant water loss and causes damage to both the soil and the plants.

2.2.2 Drip Irrigation

Drip irrigation plays an important role in modern irrigation practices. However, in large agricultural lands, it faces challenges such as ground covering, limitations in the use of agricultural vehicles, and blockages at the flow ends. In the developed system, funnel-shaped drippers are periodically refilled. Liquid fertilizer is also applied directly to the roots through this method. The system provides the benefit of hose-free usage for trees like plum and peach orchards.

2.2.3 Sprinkler Irrigation

Sprinkler irrigation is the most common method in field agriculture. Pivot irrigation, a wheeled column application, is widely used. However, its major disadvantage is that it can damage crops by crushing the plants in cultivated fields, leading to losses. Similar issues are observed with sprinkler irrigation performed using tractors.

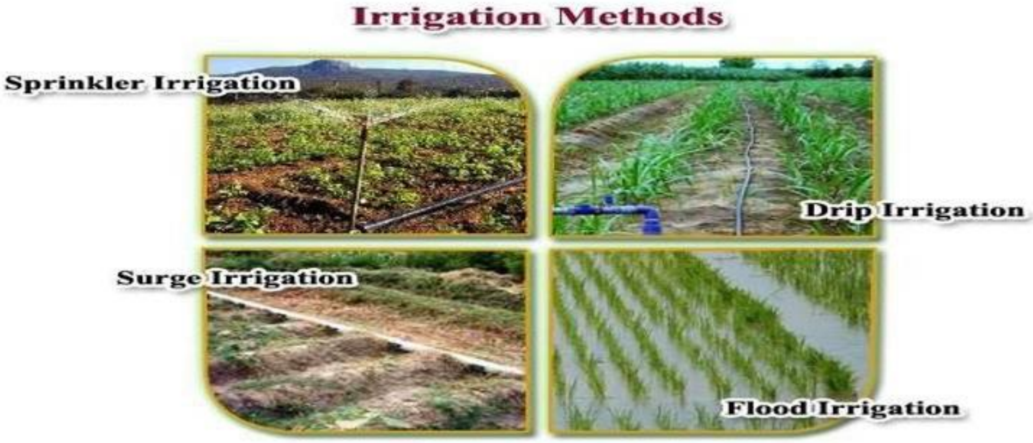

Figure 6 irrigation types

https://agritech.tnau.ac.in/agriculture/agri_irrigationmgt.html

In the developed system, water is utilized as a fountain along the bridge or through apparatus connected to the head. It can be applied at any time, independent of external conditions. The irrigation effectiveness is evaluated using thermal cameras, leaf sensors, and subsoil sensors, allowing for real-time control of the irrigation amount. There is no loss due to crushing in the cultivated area, and there are no limitations imposed by hose movement or sprinkler pipes.

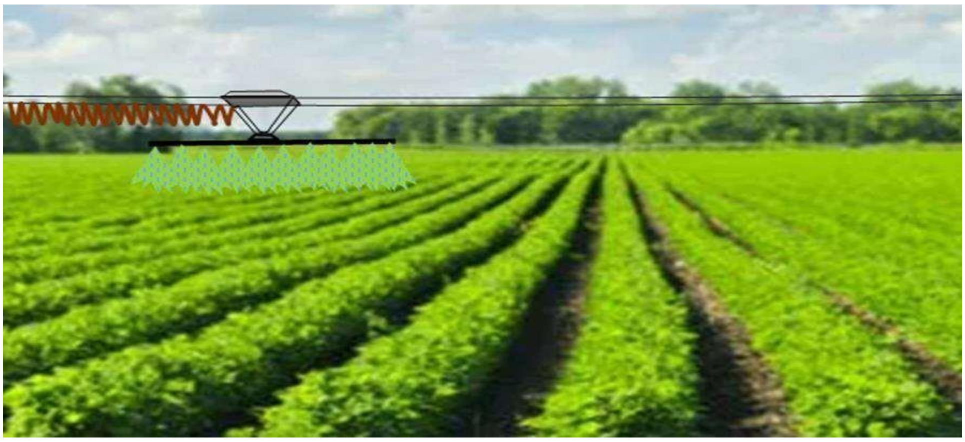

Figure 7 Schematic rainwatering

Using clean energy, the most appropriate energy levels, irrigation times, and amounts are selected with the support of artificial intelligence. The same system is also utilized for liquid fertilizer application and spraying. This system enables efficient execution of irrigation spraying, a feature not commonly found in other robotic systems.

2.2.3 Spraying

Liquid fertilization and protective spraying are performed using sprinkler systems. In these activities, significant losses occur due to wheel contact with the vehicles.

Figure 8 Agricultural spraying (US Environmental Protection Agency)

Spraying and liquid fertilization are sometimes applied at the base of the plants and other times directly on the leaves. Particularly, spraying can pose a risk to workers. In recent years, drone applications have gained popularity due to their reduced ground contact. However, the small size of the drone's reservoir can be a disadvantage in terms of uniform application and charging. The system developed for control, spraying, and fertilization efficiency offers robotic applications that are advantageous in terms of non-contact operation and control.

2.3 Land Structure

The three-axis agricultural application is largely unaffected by the soil structure in most agricultural operations. It can function effectively in challenging conditions such as mud and rocky terrain. Particularly on sloping land, such as during tea harvesting, operations are performed by selecting the appropriate apparatus. Most operations do not require field contact, including irrigation, spraying, and development control

.Figure 9 Tea cultivation slope 70%

A-Source:Sondakika Ekonomi. B- https://bayburt.tarimorman.gov.tr/

Another important factor contributing to the loss of agricultural products is the damage inflicted on the ground by agricultural tools. In recent years, the increasing power demand has led to a significant rise in vehicle weights. For example, the weight of a combine harvester has increased from four tonnes to 36 tonnes. This crushing effect is also experienced during spraying, irrigation, weed harvesting, and fertilization. However, the developed system's lack of ground contact eliminates this issue, resulting in minimal harvest loss. Additionally, reducing frictional contact helps decrease energy loss.

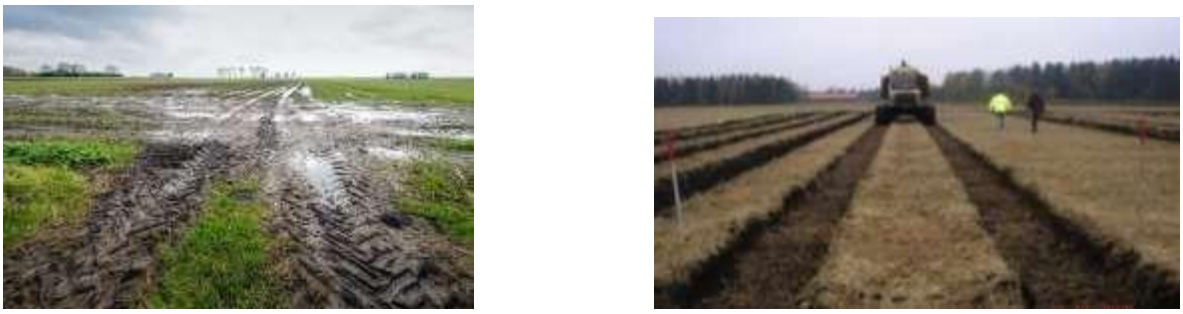

Figure 10 Wheel destruction of agricultural land (continental-tires)

2.4. Sensor and Imaging

In today's agricultural technologies, imaging systems are becoming increasingly prevalent. In addition to fixed applications in the field, drone applications are also on the rise, particularly for imaging and thermal camera usage. While drone applications are effective in close areas, they are less effective in remote regions.

Figure 11Smart agriculture technology (www.orbcomm.com)

Figure 12 Remote sensing applications (eTreena . https://spudsmart.com/remote-sensing-technology-current-use-future-outlook/)

An important feature of the developed system is its ability to precisely control every point of the field, whether in close proximity or at remote locations. The system optimizes irrigation based on data from subsoil moisture sensors, as well as leaf and ground thermal images. Thermal cameras mounted on the bridge, along with macro imagers, ultrasonic repellents, and motion sensors, feed data to the central data center. The thermal camera converts images of leaves, regional humidity, and live animals into actionable data, while the macro viewer monitors comparative plant development and assesses leaf and crop damage. Movement sensors control intrusion, security, and agricultural pest monitoring, while ultrasonic systems are especially effective in deterring bird flocks during attacks.

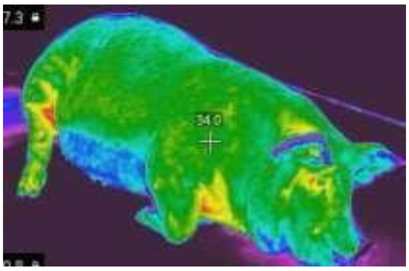

Figure 13 Thermal temperature control

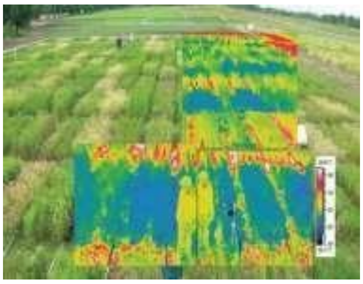

Figure 14 Wildlife thermalimaging

Figure 15 Macro disease imaging

(https://www.gst-ir.net/news-events/infrared-knowledge/395.html,
https://www.blackview.hk/blog/guides/applications-of-heat-imaging-in-agriculture,
https://www.nature.com/articles/s41598-022-21498-5)

Imaging cameras provide the advantage of live control and monitoring, making them essential for remote management. They facilitate the observation of various situations and are particularly advantageous for security purposes. For instance, ultrasonic systems, along with sound and water cannon applications, can be automatically activated in response to a detected herd of pigs by motion sensors and cameras. The high mobility of the system along the ropes allows for the easy implementation of these applications.

2.5. Robot Arm Tractor Synchronization

One of the main components of automation is the robot arm application. In addition to magnetic locking for water line connections and solar energy tractor connections, it facilitates the connection of various devices and apparatus, adapting to the specific characteristics of agricultural activities. For example, while positioning the tree-shaking apparatus attached to the arm to the appropriate branch, it can also be utilized to control tea-cutting scissors or to collect ripe fruit.

The three-axis moving system is employed in agriculture, as well as in fruit tree cultivation. Collecting dates from tall date palms is particularly challenging and labor-intensive. However, because the system can operate at any height, these tasks can be efficiently performed using the robot arm.

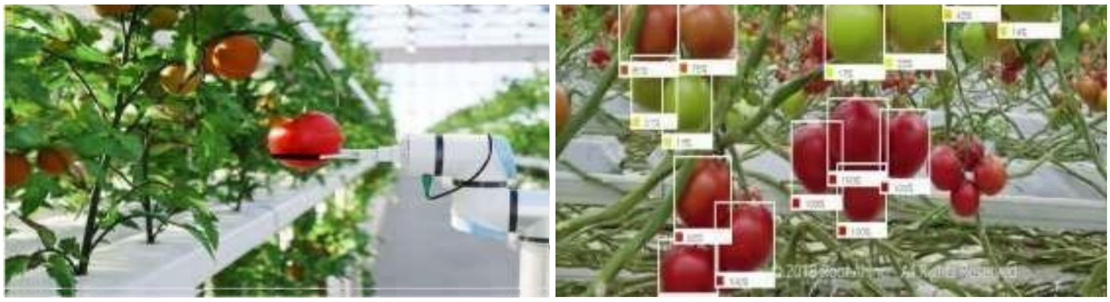

Figure 16 Fruit picking with a robotic armSource : Piranka/E+ via Getty Images

2.6. Storage

The storage area is located at the beginning of the land and includes water pumps, water mineral enrichment systems, automatic pesticide tanks, liquid fertilizer tanks, a water tank, agricultural vehicles, and cold storage facilities. The liquid fertilizer and spraying tanks are equipped with filling ports at the entrance. Incoming products undergo a security check before being admitted inside. Once the products are received in the acceptance area and weighed, the outer door is closed, and transport within the warehouse is carried out by carrier robots.

The same procedure is followed for products placed in cold storage. These operations can be performed both remotely and on-site. The warehouse area can be controlled by the robotic arm on the bridge, which also serves as a garage for the tractor.

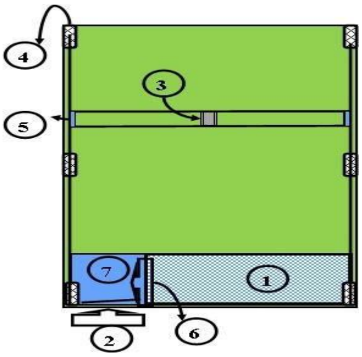

Figure 17 Schematic general layout structure

1- Warehouse (PV panel area)

2- automatic entrance door

3- Bridge trophy(car)

4- Rope poles

5- Bridgeheads

6- Intermediate passage gate

7- Reception area

3. Conclusion

The developed system, "Solar-Powered Three-Axis Mobile Agricultural Automation," is poised to play a significant role in the agricultural technologies of the future, utilizing clean energy and solar-powered tractors. This system caters to a wide range of agricultural products with its applications, AI-supported software, and capabilities for both on-site and remote control.

It enables fast and accessible agricultural operations via overhead lines while ensuring minimal ground disturbance. The system enhances efficiency by optimizing the use of water, pesticides, and fertilizers through its integrated sensors. Additionally, it provides security and a synchronized structure that further boosts its operational effectiveness.

The installation of this system can be conducted on-site, and it is anticipated that similar applications developed from this study will offer solutions to challenging agricultural tasks in the future.

References

Biswas, N. & Aslekar, A. (2022). Improving Agricultural Productivity: Use of Automation and Robotics. *2022 International Conference on Decision Aid Sciences and Applications (DASA),* Chiangrai, Thailand, pp. 1098-1104. doi: 10.1109/DASA54658.2022.9765207.

Burt, E. C., Wood, R. K., & Bailey, A. C. (1992). Some comparison of average to peak soil-tire contact pressures. *Trans. ASAE,* 35, 401-404.

Dayıoğlu, M.A. & Turker, U. (2021). Digital Transformation for Sustainable Future - Agriculture 4.0: A Review. *Journal of Agricultural Sciences,* 27(4), 373-399. https://doi.org/10.15832/ankutbd.986431.

Eurostat data. apri_pi15_ina and apri_pi15_outa. Retrieved from https://ec.europa.eu/eurostat/web/products-eurostat-news/w/DDN-20230112-1.

Hassan, Q.F. (2018). *Internet of Things A to Z: Technologies and Applications.* John Wiley & Sons: Hoboken, NJ, USA.

Navulur, S. & Prasad, M.G. (2017). Agricultural management through wireless sensors and internet of things. *Int. J. Electr. Comput. Eng.*, 7, 3492. [Google Scholar] [CrossRef] [Green Version].

Shafi, U., Mumtaz, R., García-Nieto, J., Hassan, S.A., Zaidi, S.A., & Iqbal, N. (2019). Precision agriculture techniques and practices: From ideas to applications. *Sensors,* 19, 3796. [Google Scholar] [CrossRef] [PubMed] [Green Version].

United Nations Climate Change Conference (COP26). Retrieved from https://unfccc.int/climate-action/gca-events/global-climate-action-at-cop-26?gad_source=1&gclid=CjwKCAjw5qC2BhB8EiwAvqa41mEJJJ3X5NdCca8JqE63Z5rsDsR78iMHoCAzt7UAWVgWGbXqMRScDQBoCMOMQAvD_BwE.

Villa-Henriksen, A., Edwards, G.T., Pesonen, L.A., Green, O., & Sørensen, C.A.G. (2020). Internet of Things in agricultural farming: Implementation, applications, challenges and potential. *Biol. Eng.*, 191, 60-84. [Google Scholar] [CrossRef].

Patent Citations

US1017578A (1912-02-13). Irrigating apparatus. William Perry Mcmillan.

US1502997A (1924-07-29). Aerial transporter. Marrian Harry Herber Blakemore.

US2024374A (1935-12-17). Overhead irrigation system. Moody E. Langebrake.

FR2518869A1 (1983-07-01). Installation pour traiter des plantes cultivées en rangées, notamment des vignes et des arbres fruitiers.

US4612996A (1986-09-23). Robotic agricultural system with tractor supported on tracks. Kimberly Hills, Ltd.

US20030145759A1 (2003-08-07). Travelling highline system. Rodnunsky James Lewis.

S20050024005A1 (2005-02-03). System and method for facilitating fluid three-dimensional movement of an object via directional force. Jim Rodnunsky.

US20050105970A1 (2005-05-19). Hillside farming module and system. Faris Sadeg M.

US20110106451A1 (2011-05-05). Multiple sensor system and method for mapping soil in three dimensions. Colin Christy.

US20110127229A1 (2011-06-02). Actuation system configured for moving a payload. Gm Global Technology Operations, Inc.

EP2622955A1 (2013-08-07). Landwirtschaftliche Maschine mit einem System zur selbsttätigen Einstellung eines Bearbeitungsparameters und zugehöriges Verfahren. Deere & Company.

WO2013181069A1 (2013-12-05). Robotic platform method for performing multiple functions in agricultural systems. Rowbot Systems LLC.

US20130345876A1 (2013-12-26). Suspended robot systems and methods for using same. Irobot Corporation.

AN OVERVIEW OF COMPOSITE MATERIALS FOR MARINE APPLICATIONS

Gürcan ATAKÖK, Dudu Mertgenç YOLDAŞ

Chapter 2

An Overview of Composite Materials for Marine Applications

GÜRCAN ATAKÖK[1], DUDU MERTGENÇ YOLDAŞ[2]

1. Introduction

Composites consist of a reinforcement embedded in a matrix. The reinforcement helps the matrix to take the desired shape and improve its overall mechanical properties (Bhardwaj, et. al.,2015). The composite material consists of two or more phases, physically or chemically different, appropriately distributed, with an interface separating them. It has properties that cannot be described alone Chawla (2019). Composite materials provide advantages such as higher specific strength and stiffness than conventional materials Deutsch (1978). Composites have higher strength-to-weight and modulus-to-weight ratios than metal materials Mallick (2007).

The properties of composites are determined by the fibres laid or laminated into the matrix (Alam, et. al.,2010). To improve the mechanical properties of composites, the reinforcement consists of the shape of the fibres. This allows it to be both strong and flexible Chawla (2016). The specific stiffness and strength of reinforcing fibres have been continuously improved. Compared to metals, glass, kevlar, boron and carbon fibres are more durable and stiffer (Shenoi and Wellicome,

---

[1] Marmara University /TURKEY, gatakok@marmara.edu.tr https://orcid.org/0000-0002-5275-2429)

[2] Lecturer , Dokuz Eylül University, Türkiye, dudu.yoldas@deu.edu.tr https://orcid.org/0000-0002- 1700-4310)

1993). There are three key properties for fibres to be used as high performance materials Dresher (1969).

Firstly, the smaller grain size relative to the microstructure unit allows both higher strength and lower defects to be achieved (De Lamotte and Perry, 1970). Secondly, the high aspect ratio allows the load applied through the matrix to be transferred to the strong and stiff fibre. Thirdly, due to its versatility, it can be used in a large number of different ways. The most common type of high-performance composite materials is fibre-reinforced plastic. To create a fibre- reinforced composite, high-strength and low-density fibres are placed in a plastic matrix. This increases durability. The matrix maintains the alignment of the fibres by distributing the load around the fibres Figueiredo, J. L., Bernardo, C. A., Baker, R. T. K., & Hüttinger, K. J. (2013). The matrix is also protected from environmental risks due to moisture and temperature Gon, Das, Paul, and Maity and (2012). In the application of fibre reinforced composites, the combination of the fibre and matrix layer in various layers and reaching the desired thickness is known as laminate. The physical and mechanical properties depend on the fibre orientation of each layer Li, H., Wei, Y., & Wang, L. (2021).

Composite materials reduce their weight while increasing strength and stiffness . Anisotropic properties create different mechanical properties of composites in all directions. Therefore, they are not symmetrical with respect to all their axes or planes (David, et. al., 2020).

Figure 1 shows the most common composite structures. Figure 1a shows unidirectional, Figure 1b bidirectional and Figure 1c multidirectional laminates. Unidirectional fibre is used in one direction, bidirectional in both directions and multidirectional achieves high strength by combining various fibre orientations (Liu, D., Tang, Y., & Cong, W. L.,2012. Xu, et. al., 2016).

Since the early 1960s, there has been an increasing demand for materials with high strength but lighter weight in a wide variety of fields such as aerospace, marine and construction industry. The research and development effort on composite materials started in 1965 Schier, J. F., & Juergens, R. J. (1983).

The properties of fibre reinforced polymer (FRP) composite materials such as high strength-to-weight ratio, corrosion resistance, formability, good fatigue life are the advantages of FRPs compared to conventional materials (Qureshi, et. al.,2020).

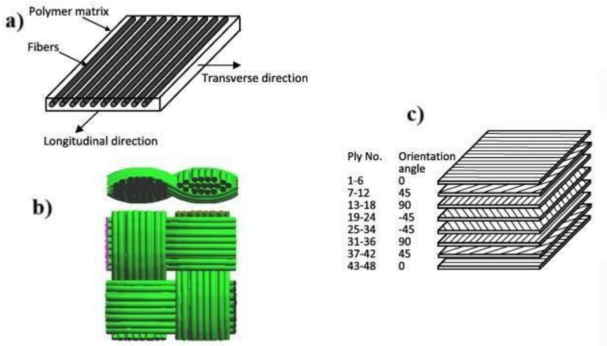

Figure 1. Composite structures a) FRP Unidirectional b) FRP Bidirectional and c) FRP Unidirectional semi-isotropic insertion array(Lee, Jeong Park, Kim, Cho 2008)

Initially FRP was used for lifeboats and pleasure boats. This has changed over the years, ranging from small components such as radar domes, masts and pipes to larger applications such as ship hulls, ship superstructures, submarines and offshore structures . The length, orientation and shape of the fibre broaden the application range of FRP composites to suit the mechanical needs. The most commonly used fibres are glass, carbon, boron, aramid, nylon and polyester fibres (Prashanth ,et. al.,2017).

2. Marine Composites

Carbon fibre reinforced polymers (CFRP) are strong and durable. However, glass fibre reinforced polymers (GFRP) are lighter and stiffer. In marine, these composite materials are widely used.

2.1. Glass Fibre Reinforced Plastics (GFRP)

GFRP properties are considered inexpensive, operable and stress resistant. GFRP is melted and heated to 1300°C. It is made through mixtures that are then powdered.E-glass and S-glass are among the most widely used camera reinforcements. E-glass is composed of calcareous aluminium borosilicate and S-glass of aluminium and magnesium oxides. E-glass is preferred because it is more water resistant than S-glass Dominic and Nandakumar 2016).

Composites are available in thermoset or thermoplastic content. The use of FRP materials provides benefits such as lightness, fuel consumption and cost reduction in marine vehicles. Marine vessels are lighter, use less fuel and are cheaper thanks to FRP composite materials. GFRP is widely used because it is compatible with various resins. Although CFRP has higher strength, GFRP is cheaper (Delzendehrooy, et. al., 2020).

Since the moduli of GFRP composites are not high, high modulus materials such as alumina, silicon carbide, carbon and boron have emerged in later years . Materials made of GFRP are lighter than steel and have higher stiffness than aluminium (Ramzan and Ehsan ,2009).

When welding is applied to prevent corrosion of the hulls of marine vessels, stress concentration in the area accelerates corrosion, which shortens the fatigue life (Gururaja and Rao, 2012).

GFRP materials are used in the marine field due to their high strength, corrosion resistance and high elasticity (Sathishkumar , et. al., 2014).

2.2. Carbon Fibre Reinforced Plastics (CFRP)

To produce carbon and graphite fibres, PAN or pitch is exposed to extremely high temperatures. These processes change the strength and chemical properties of the resin, improving its processability and compatibility. PAN-based contains polyacrylonitrile while pitch contains coal tar or pure petroleum. Since pitch-based fibres are harder and more brittle, PAN-based fibres are more commonly used Anon (1970).

High modulus (HM) and high strength (HS) carbon fibre types are produced in the industry, which do not experience deformation under high loads and can operate at high temperatures Jacob (2000). Degradation of the interfacial bond can change the properties of FRP composites. This affects the strength of the composite.

Matrices (Resins)

The reinforcing material and the matrix form a whole body with a certain shape as a result of physical, chemical and physicochemical processes when forming composite materials. Matrix qualities affect the properties of composite materials. The matrix binds the reinforcing material as a whole and distributes the load between the fibres. The intended use of the composite material affects the choice of matrix. The matrix affects the transverse tensile, compressive, shear, heat resistance and resistance to environmental conditions properties of composite materials. The superior mechanical properties of the matrices are demonstrated by the high dimensional cross-linking points. The brittleness of the high dimensional cross-linking points is their biggest disadvantage. This feature reduces the load carrying ability of the materials (Chen, et. al., 2002).

The matrices of composites can consist of various polymers. Thermosets and thermoplastics are two sections in which polymers can be analysed. Depending on the temperature, polymers are divided into two categories: thermoplastic and thermoset. The most commonly used resins in these matrices are thermosets, which are produced by an irreversible reaction (Baley, et. al., 2004).

However, thermoplastics are a type that can be softened and hardened by increasing and decreasing their temperature.The GFRP matrix consists of thermosetting polymers and the CFRP composite consists of thermoplastic polymers. According to researches, decreases in flexural strength, modulus and fracture toughness of composites exposed to seawater for a long time have been observed (Gellert and Turley,1999).

Thermosetting resins are excellent adhesives, resistant to high temperatures, flexible and have good chemical resistance. The most important component of the thermoset polymer family is epoxy. Epoxy is the most common matrix material due to its high T_g , high strength and modulus Johnson (2013).

2.3. Environmental Parameters

Composites in marine applications are affected by a number of environmental factors. These include temperature and humidity, ultraviolet radiation (UV) and solution. Composite materials are most commonly used in superstructures, recreational and commercial marine vessels.

2.3.1 Temperature and Humidity

Composite materials, which have advantages over traditional structured materials such as metals, are sensitive to heat and moisture in harsh and changing environmental conditions (Vaddadi et. al., 2003).

When composite materials are exposed to moisture, free water penetrates the hydrophilic groups of the fibre and forms intermolecular hydrogen bonds. This reduces the interface adhesion between fibre and matrix. In the degradation process, swelling of the fibres causes the growth of interface zones (Melo et. al., 2018).

Absorption of moisture from composite materials reduces the stiffness and durability of structures. Composite materials are frequently exposed to humid environment in marine environments. This has an impact on the physical and mechanical properties. The transport of water molecules through microcracks affects the mechanical performance of the matrix material (Kootsookos and Mouritz, 2004).

In composites, due to moisture absorption;

- Plasticisation, delamination and delamination of the fibre-matrix interconnection occur. These cause a decrease in mechanical properties (Idrisi and Mourad, 2021).
- The thermophysical, mechanical and chemical properties of the epoxy matrix are also altered due to moisture absorption Weitsman (1991).
- Moisture elastic modulus and glass transition temperature (Tg) reduce the mechanical properties of composite materials (Delasi and Whiteside,1978).
- Continuous exposure of composite materials to moisture degrades the

fibre-matrix bond, resulting in reduced microstructural integrity and interfacial bond strength. It also reduces the fatigue resistance, interlayer shear strength and impact tolerance properties of the matrix (Soutis and Turkmen,1997. Shen and Springer 1976).

Fick's law of diffusion describes how moisture is absorbed. The basis of existing moisture diffusion models is Fick's law, which has a constant diffusion coefficient Fick (1855). This law states that the mass of moisture absorption mass increases linearly with time and decreases after reaching saturation (Saidane et. al., 2016). Since the absorption of moisture in the fibre and matrix is different, the strain and stress regions are separate. The chemical structure of the matrix depends on temperature and environmental conditions (Bonniau and Bunsell,1981. Ellyin and Rohrbacher 2000). Moisture absorption at high water temperature causes a decrease in interfacial adhesion and tensile strength Ray (2006).

2.3.2 Ultraviolet Radiation

Solar radiation includes visible radiation, ultraviolet radiation and infrared radiation (Smoleń et. al., 2024). UV exposure is an important problem in the environmental durability of FRPs (Shokrieh and Bayat, 2007).

Photooxidative ageing, which causes the breakdown of polymer chains, the formation of free radicals and the reduction of the molecular weight of polymers, is carried out by ultraviolet radiation. As a consequence, discolouration and deterioration of material properties occur (Lu et. al., 2018). UV radiation reduces the molecular weight of polymers, which is known as photooxidative ageing (Liao et. al., 1998).

Prolonged exposure of the composite material to UV radiation accelerates the degradation process of the material and reduces its strength (Afshar et. al., 2024).

2.3.3 Solution

Seawater can degrade composite materials through hydrolysis reaction of the fibre or matrix interphase. Salt poses environmental problems for composites in the marine environment. Composite materials in the marine environment inhibit the absorption of components found in salt. The basis of this situation is the Fickian law. That is, the moisture uptake is highest for the first case, then the moisture uptake starts to decrease gradually due to the inhibition of salt and other components (Mourad et. al., 2010).

2.4 Adhesive Jointed Connections

The bonding process involves the use of a polymeric adhesive that bonds composite parts to other parts after curing (Martínez et. al., 2019). In other words, adhesive bonding is a material joining process in which an adhesive placed between the bonded surfaces solidifies to form an adhesive bond (Stamenović et. al., 2010).

In composite structures, there are three types of joining/bonding techniques: adhesive bonding, mechanical bonding and hybrid bonding. The use of bolts or rivets in fasteners affects the weight of the structure Katsiropoulos et. al., 2012). Adhesive bonded connections provide many advantages over mechanical fasteners such as lighter weight, more uniform stress distribution, flexibility in design and low cost Morris (1993).

Table 1. Comparison of bonding and mechanical joining of composites by adhesive bonding (Jadee and Othman, 2011)

Bonding with Gluing	**Mechanical Joining**
Low stress concentrations	High stress concentrations
High strength connection	Low strength connection
Difficult to dismantle	Easy to disassemble
Poorly recyclable joining material	Easy to recycle joining material
Lightweight joining	Heavy joining due to fasteners
External surfaces are not affected	Fasteners protrude to the outer surface
Excellent fatigue and corrosion performance	Prone to fatigue and corrosion
Difficult to inspect and requires a high level of quality control	Easy to inspect and requires a lower level of quality control
Surface preparation does not damage the bonded part	Drilling and bearing damage the part

The adhesive bonding process is influenced by the factors of surface preparation, adhesive type, filling, fixing, curing, manufacturing and working environment conditions. A comparison of these conditions between the stress distribution of a mechanically joined and adhesive bonded joint is shown in Figure 2 (Jadee and Othman, 2011).

Tensile tests, shear tests, compression and peel tests are performed to determine the adhesion properties. The most commonly used bonded connection is the tensile test as a single overlap connection test.

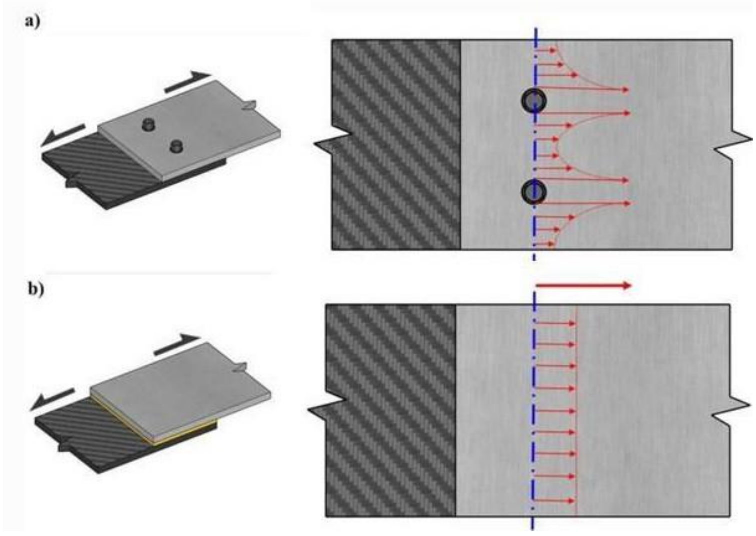

Figure 2. Stress distribution of two different types of a) mechanical b) bonded joints (Jadee and Othman, 2011)

Adhesive bonding has applications in marine, aerospace, dentistry, and other engineering fields (Silva et. al., 2018).

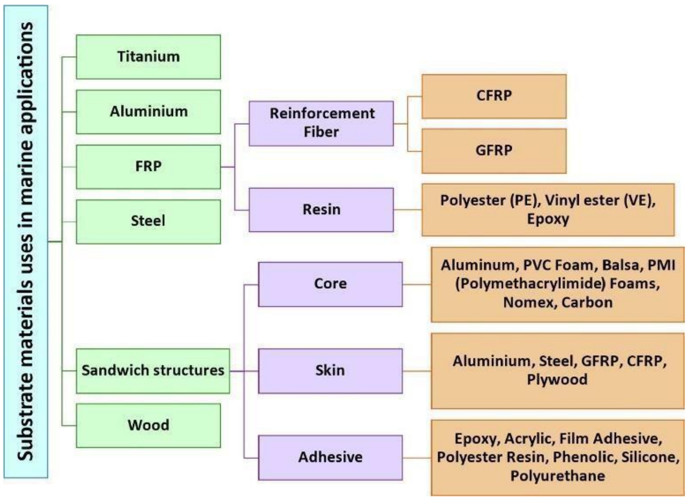
Substrate materials uses in marine applications
Titanium
Aluminium
FRP
Steel
Sandwich structures
Wood
Reinforcement Fiber
Resin
Core
Skin
Adhesive
CFRP
GFRP
Polyester (PE), Vinyl ester (VE), Epoxy
Aluminum, PVC Foam, Balsa, PMI (Polymethacrylimide) Foams, Nomex, Carbon
Aluminium, Steel, GFRP, CFRP, Plywood
Epoxy, Acrylic, Film Adhesive, Polyester Resin, Phenolic, Silicone, Polyurethane

Figure 3. Adhesive materials used in marine applications (Delzendehrooy et. al., 2022)

The performance of adhesively bonded joints depends on composite joining methods, surface preparation, parameters of adhesive and adherend properties, geometrical parameters such as adhesive thickness, lap length, orientation sequence, ply angle, filler (Budhe et. al., 2017).

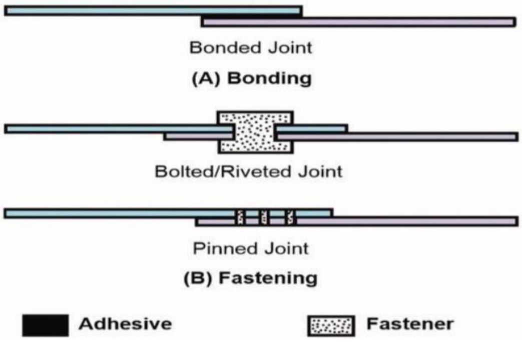

Figure 4. Methods of joining techniques (Jeevi et. al., 2019)

Various types of connections can be used to join the composite structure as shown, such as single lap joint, double lap joint, oblique butt joint, double-stage lap joint (Banea and Silve, 2009).

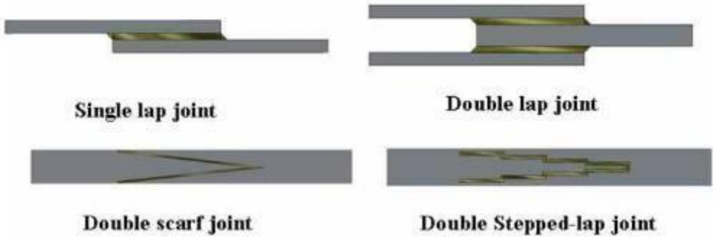

Figure 5. Adhesive connection shapes (Banea and Silva, 2009)

The aim of joint design is to achieve the maximum strength for a given joint area. Factors affecting joint design are the mechanical properties of the adhesive and substrate, stresses due to adhesive curing and joint geometry. In the connection to be joined with adhesive, the area to be glued must first be cleaned in order to apply the adhesive correctly. In this type of connection, the tensile strength is lower than the shear strength. In addition, stresses perpendicular to the adhesive connection based on tensile strength (peeling stresses) should be prevented. While the adhesive layer is thinner than one millimetre, in some applications it is thicker. For these thicker adhesive layers, a filler is usually added to the adhesive. The extreme stresses at the edges of the adhesive joint are caused by rigid transitions. By adapting the fibre orientation of the plies to be joined, the stresses can be minimised. The flexible adhesive can quickly dissipate high stresses Nijssen (2015).

Conclusion

This study comprehensively examined the mechanical properties of composite materials utilized in marine applications, emphasizing the effects of environmental factors such as moisture absorption, temperature fluctuations, and UV radiation. The experimental findings yielded several critical insights:

- **Mechanical Properties Degradation**: A notable decrease in tensile, flexural, and interlayer shear strength of composite materials was observed with increasing aging temperature and immersion time, while the weight fraction of these materials increased under similar conditions.
- **Matrix Degradation**: The investigation revealed significant matrix degradation in carbon/vinyl ester, glass/vinyl ester, carbon/epoxy, and glass/epoxy composites at various temperatures relevant to marine environments, with a particular emphasis on the severe effects of hygrothermal aging in glass/epoxy composites.
- **Impact of Water Diffusion**: Hydrothermal aging facilitated water infiltration into composite materials, leading to the separation of the fibre/matrix interface and crack propagation, which adversely affected essential mechanical properties, including elastic modulus, shear modulus, and Poisson's ratio.
- **Integrity Loss from Environmental Factors**: Environmental influences such as moisture absorption, reduced fracture toughness at the fibre-matrix interface, and UV-induced microcracks compromised the integrity of composite materials, subsequently deteriorating the load transfer efficiency between the matrix and fibres.
- **High-Temperature Fiber Degradation**: Fiber degradation was identified in glass/epoxy and glass/polyurethane composites subjected to high temperatures, although the overall modulus remained stable throughout the analysis.
- **Influence of Layer Count on Toughness**: The experimental results indicated that increasing the number of layers enhanced the toughness of both glass and carbon fibres, suggesting a direct correlation between layer count

and mechanical strength.

- **Effects of Moisture Ingress**: Moisture ingress in composite materials resulted in diminished interlaminar shear strength (ILSS) due to instability induced by matrix swelling, microcracks, microvoids, delamination, and separation of the fibre-matrix interface.
- **Performance Factors of Bonded Joints**: The effectiveness of bonded joints was influenced by various factors, including humidity, temperature, surface treatments, lap length, joint type, and adhesive thickness.
- **Adhesive Suitability**: The choice of adhesive was found to significantly impact the performance of composite joints, with effectiveness contingent upon the type of composite material and the specific environmental bonding conditions.
- **Bonding Method Impact**: The fracture process and strength of single-lap bonded composite joints were closely tied to the bonding method used, underscoring the importance of selecting appropriate bonding techniques for optimal joint performance.

These findings highlight the intricate relationship between environmental conditions and the mechanical performance of composite materials in marine applications. They provide vital insights that can inform the selection of materials and bonding methods to optimize performance and durability in challenging marine environments.

References

Afshar, A., Alkhader, M., Korach, C. S., & Chiang, F. P. (2015). Effect of long-term exposure to marine environments on the flexural properties of carbon fibre vinylester composites. *Composite Structures*, *126*, 72-77. https://doi.org/10.1016/j.compstruct.2015.02.008

Alam, S., Habib, F., Irfan, M., Iqbal, W., & Khalid, K. (2010). Effect of orientation of glass fibre on mechanical properties of GRP composites.*Journal of the Chemical Society of Pakistan*, *32*(3), 265-269.

Anon., 1970. New developments from Dowty Rotol. Eng. Mater. Des. 13 (11), 1343. https://doi.org/10.1016/B978-1-78242-250-1.00002-8

Bonniau, P. A., & Bunsell, A. R. (1981). A comparative study of water absorption theories applied to glass epoxy composites. *Journal of Composite Materials*, *15*(3), 272-293. https://doi.org/10.1177/002199838101500303

Baley, C., Davies, P., Grohens, Y., & Dolto, G. (2004). Application of interlaminar tests to marine composites. A literature review. *Applied composite materials*, *11*, 99-126.

Banea, M. D., & da Silva, L. F. (2009). Adhesively bonded joints in composite materials: an overview. *Proceedings of the Institution of Mechanical Engineers, Part L: Journal of Materials: Design and Applications*, *223*(1), 1-18. https://doi.org/10.1243/14644207JMDA219

Bhardwaj, A. R., Vaidya, A. M., Rawlani, M. V., & Bambhori, S. C. (2015). "Investigation of Machining Behaviour of Metal Matrix Composite: A Review. *International Journal on Recent Technologies in Mechanical and Electrical Engineering (IJRMEE)*, *2*(8), 68-70.

Budhe, S., Banea, M. D., De Barros, S., & Da Silva, L. F. M. (2017). An updated review of adhesively bonded joints in composite materials. International Journal of Adhesion and Adhesives, 72, 30-42. https://doi.org/10.1016/j.ijadhadh.2016.10.010

Chawla, K. K. (2012). *Composite materials: science and engineering*. Springer Science & Business Media.

Chawla, K. (2016). *Fibrous materials*. Cambridge university press.

Chen, X., Dam, M. A., Ono, K., Mal, A., Shen, H., Nutt, S. R., ... & Wudl, F. (2002). A thermally re-mendable cross-linked polymeric material. Science, 295(5560), 1698-1702. https://doi.org/10.1126/science.1065879

David Müzel, S., Bonhin, E. P., Guimarães, N. M., & Guidi, E. S. (2020). Application of the finite element method in the analysis of composite materials: A review. *Polymers*, *12*(4), 818. https://doi.org/10.3390/polym12040818

De Lamotte, E., & Perry, A. J. (1970). Diameter and strain-rate dependence of the ultimate tensile strength and Young's modulus of carbon fibres. *Fibre Science and Technology*, *3*(2), 157-166. https://doi.org/10.1016/0015-0568(70)90021-7

Delzendehrooy, F., Akhavan-Safar, A., Barbosa, A. Q., Beygi, R., Cardoso, D., Carbas, R. J. C., ... & da Silva, L. F. M. (2022). A comprehensive review on structural joining techniques in the marine industry. *Composite Structures*, *289*, 115490. https://doi.org/10.1016/j.compstruct.2022.115490

Deutsch, S. (1978). 23rd National SAMPE Symposium. *Society for the Advancement of Material and Process Engineering. California. USA*.

Delzendehrooy, F., Akhavan-Safar, A., Barbosa, A. Q., Beygi, R., Cardoso, D., Carbas, R. J. C., ... & da Silva, L. F. M. (2021). https://doi.org/10.1016/j.compstruct.2022.115490

Dresher, W. H. (1969). The age of fibres. *JOM*, *21*(4), 17-26.

Dominic, M., & Nandakumar, C. G. (2016). *'Investigations on Strength and Sustainability of Nonmetallic Laminated Composite Ship Structure*

(Doctoral dissertation, Cochin University of Science and Technology).

Ellyin, F., & Rohrbacher, C. (2000). Effect of aqueous environment and temperature on glass-fibre epoxy resin composites. *Journal of reinforced plastics and composites*, *19*(17), 1405-1427. https://doi.org/10.1177/073168400772678

Fick, A. (1855). Ueber diffusion. *Annalen der Physik*, *170*(1), 59-86. https://doi.org/10.1002/andp.18551700105

Figueiredo, J. L., Bernardo, C. A., Baker, R. T. K., & Hüttinger, K. J. (Eds.). (2013). Carbon fibres filaments and composites (Vol. 177). Springer Science & Business Media.

Gellert, E. P., & Turley, D. M. (1999). Seawater immersion ageing of glass-fibre reinforced polymer laminates for marine applications. *Composites Part A: Applied Science and Manufacturing*, *30*(11), 1259-1265. https://doi.org/10.1016/S1359-835X(99)00037-8

Gon, D., Das, K., Paul, P., & Maity, S. (2012). Jute composites as wood substitute. *International Journal of Textile Science*, *1*(6), 84-93 https://doi.org/10.5923/j.textile.20120106.05

Gururaja, M. N., & Rao, A. H. (2012). A review on recent applications and future prospectus of hybrid composites. *International Journal of Soft Computing and Engineering*, *1*(6), 352-355.

Idrisi, A. H., & Mourad, A. H. I. (2021). Fibre reinforced polymer composites sustainability under prolonged exposure to hot seawater: Experimental and prediction study. *Materials Letters*, *304*, 130689. https://doi.org/10.1016/j.matlet.2021.130689

Jacob, A. (2000). Racing catamaran relies on carbon fibre. *Reinforced Plastics*, *44*(3), 36-42.

Jadee, K. J., & Othman, A. R. (2011). Fibre reinforced composite structure with bolted joint-a review. *Key Engineering Materials*, *471*, 939-944. https://doi.org/10.4028/www.scientific.net/KEM.471-472.939

Jeevi, G., Nayak, S. K., & Abdul Kader, M. (2019). Review on adhesive joints and their application in hybrid composite structures. *Journal of Adhesion Science and Technology*, *33*(14), 1497-1520.

https://doi.org/10.1080/01694243.2018.1543528

Johnson, T. (2013). Thermoplastic vs. Thermoset Resins. *About. com Composites/Plastics. Np, nd Web*, *25*.

Katsiropoulos, C. V., Chamos, A. N., Tserpes, K. I., & Pantelakis, S. G. (2012). Fracture toughness and shear behaviour of composite bonded joints based on a novel aerospace adhesive. Composites Part B: Engineering, 43(2), 240-248. https://doi.org/10.1016/j.compositesb.2011.07.010

Kootsookos, A., & Mouritz, A. P. (2004). Seawater durability of glass- and carbon-polymer composites. *Composites science and technology*, *64*(10-11), 1503-1511. https://doi.org/10.1016/j.compscitech.2003.10.019

Lee, S. C., Jeong, S. T., Park, J. N., Kim, S. J., & Cho, G. J. (2008). Study on drilling characteristics and mechanical properties of CFRP composites. *Acta Mechanica Solida Sinica*, *21*(4), 364-368. https://doi.org/10.1007/s10338-008-0844-z

Li, H., Wei, Y., & Wang, L. (2021, December). A general model for predicting the off-axis performance of fibre reinforced composite materials. In *Structures* (Vol. 34, pp. 2087-2097). Elsevier. https://doi.org/10.1016/j.istruc.2021.08.118

Liu, D., Tang, Y., & Cong, W. L. (2012). A review of mechanical drilling for composite laminates. *Composite structures*, *94*(4), 1265-1279. https://doi.org/10.1016/j.compstruct.2011.11.024

Liao, K., Schultesiz, C. R., Hunston, D. L., & Brinson, L. C. (1998).

Long-term durability of fibre-reinforced polymer-matrix composite materials for infrastructure applications: a review.

Lu, T., Solis-Ramos, E., Yi, Y., & Kumosa, M. (2018). UV degradation model for polymers and polymer matrix composites. *Polymer degradation and stability*, *154*, 203-210. https://doi.org/10.1016/j.polymdegradstab.2018.06.004

Mallick, P. K. (2007). *Fibre-reinforced composites: materials, manufacturing, and design*. CRC press. https://doi.org/10.1201/9781420005981

Martínez-Landeros, V. H., Vargas-Islas, S. Y., Cruz-González, C. E., Barrera, S., Mourtazov, K., & Ramírez-Bon, R. (2019). Studies on the influence of surface treatment type, in the effectiveness of structural adhesive bonding, for carbon fibre reinforced composites. Journal of Manufacturing Processes, 39, 160-166. https://doi.org/10.1016/j.jmapro.2019.02.014

Melo, R. Q. C., Santos, W. R. G., Barbosa de Lima, A. G., Lima, W. M. P. B., Silva, J. V., & Farias, R. P. (2018). Water absorption process in polymer composites: Theory analysis and applications. *Transport Phenomena in Multiphase Systems*, 219-249.

Mourad, A. H. I., Abdel-Magid, B. M., El-Maaddawy, T., & Grami, M. E. (2010). Effect of seawater and warm environment on glass/epoxy and glass/polyurethane composites. *Applied Composite Materials*, *17*, 557-573. https://doi.org/10.1007/s10443-010-9143-1

Morris, C. E. (1993). Strong, durable adhesive bonding: some aspects of surface preparation, joint design and adhesive selection. Materials Research Labs Ascot Vale (Australia).

Nijssen, R. P. L. (2015). *Composite materials: an introduction*. Netherlands: Inholland University of Applied Sciences.

Prashanth, S., Subbaya, K. M., Nithin, K., & Sachhidananda, S. (2017). Fibre reinforced composites-a review. *J. Mater. Sci. Eng*, *6*(03), 2-6. https://doi.org/10.4172/2169-0022.1000341

Qureshi, J., Nadir, Y., & John, S. K. (2020). Bolted and bonded FRP beam-column joints with semi-rigid end conditions. *Composite Structures*, *247*, 112500. https://doi.org/10.1016/j.compstruct.2020.112500

Ramzan, E., & Ehsan, E. (2009). Effect of various forms of glass fibre reinforcements on tensile properties of polyester matrix composite. *Fac. Eng. Technol*, *16*, 33-39.

Ray, B. C. (2006). Temperature effect during humid ageing on interfaces of glass and carbon fibres reinforced epoxy composites. *Journal of colloid and interface science*, *298*(1), 111-117. https://doi.org/10.1016/j.jcis.2005.12.023

Saidane, E. H., Scida, D., Assarar, M., & Ayad, R. (2016). Assessment of 3D moisture diffusion parameters on flax/epoxy composites. https://doi.org/10.1016/j.compositesa.2015.10.008

Sathishkumar, T. P., Satheeshkumar, S., & Naveen, J. (2014). Glass fibre-reinforced polymer composites-a review. *Journal of reinforced plastics and composites*, *33*(13), 1258-1275. https://doi.org/10.1177/0731684414530

Silva, L. F. M., Öschner, A., & Adams, R. D. (2018). Handbook of Adhesion Technology (2 volumes), Springer. Heidelberg, Germany.

Schier, J. F., & Juergens, R. J. (1983). They force a fresh look at the design process. *Astronaut. Aeronaut.*, *21*(9), 44-49.

Soutis, C., & Turkmen, D. (1997). Moisture and temperature effects of the compressive failure of CFRP unidirectional laminates. *Journal of Composite Materials*, *31*(8), 832-849. https://doi.org/10.1177/0021998397031008

Shenoi, R. A., & Wellicome, J. F. (Eds.). (1993). *Composite Materials in Maritime Structures: Volume 1, Fundamental Aspects* (Vol. 1). Cambridge University Press.

Schier, J. F., & Juergens, R. J. (1983). They force a fresh look at the design process. *Astronaut. Aeronaut.*, *21*(9), 44-49.

Shen, C. H., & Springer, G. S. (1976). Moisture absorption and desorption of composite materials. *Journal of composite materials*, *10*(1), 2-20. https://doi.org/10.1177/002199837601000

Shokrieh, M. M., & Bayat, A. (2007). Effects of ultraviolet radiation on mechanical properties of glass/polyester composites. *Journal of Composite materials*, *41*(20), 2443-2455. https://doi.org/10.1177/0021998307075

Silva, L. F. M., Öschner, A., & Adams, R. D. (2018). Handbook of Adhesion Technology (2 volumes), Springer. Heidelberg, Germany.

Smoleń, J., Olesik, P., Nowacki, B., Godzierz, M., Kurtyka, K., Chaber, P., ... & Kozioł, M. (2024). The influence of UV radiation on the properties of GFRP laminates in underwater conditions. *Scientific Reports*, *14*(1), 7446. https://doi.org/10.1038/s41598-024-57999-8

Stamenović, M., Putić, S., Rakin, M., Medjo, B., & Čikara, D. (2011). Effect of alkaline and acidic solutions on the tensile properties of glass-polyester pipes. *Materials & Design*, *32*(4), 2456-2461. https://doi.org/10.1016/j.matdes.2010.11.023

Vaddadi, P., Nakamura, T., & Singh, R. P. (2003). Inverse analysis for transient moisture diffusion through fibre-reinforced composites. *Acta materialia*, *51*(1), 177-193. https://doi.org/10.1016/S1359-6454(02)00390-7

Weitsman, Y. J. (1991). Fatigue of composite materials. *New York: Elsevier*. AND Jones, F. R. (1999). Durability of reinforced plastics.

Xu, J., Mkaddem, A., & El Mansori, M. (2016). Recent advances in drilling hybrid FRP/Ti composite: A state-of-the-art review. *Composite Structures*, *135*, 316-338. https://doi.org/10.1016/j.compstruct.2015.09.028

INVESTIGATION OF TEETH IN CONNECTION USED IN MARINE OIL EXTRACTION

Dudu MERTGENÇ YOLDAŞ

Chapter 3

Investigation of Teeth in Connection Used in Marine Oil Extraction

DUDU MERTGENÇ YOLDAŞ[1]

1. Introduction

Oil and petroleum products are of vital importance today. In oil extraction systems, drill bits are used, operated by carpenters. The extraction process involves drilling and opening oil wells using bits that resemble standard drill bits. At this stage, the drill bit is inserted into the end of the drill pipe and positioned using a tall structure known as a drilling rig. The drill pipe is rotated by a turntable at the base of the tower, which is typically powered by a diesel engine. The threads in these systems are subjected to high stress during intensive operations. Managing and reducing this stress is crucial to extending the working life of the equipment. It is particularly interesting from a materials science perspective, as it involves reducing stress to optimize performance. Computer programs can be used to produce realistic simulations, offering significant advantages for designers and engineers. For accurate results, the correct model, values, and analysis methods must be selected (Altunsoy et al., 2004).

Joints used in oil extraction systems are essential components in both onshore and offshore operations. These joints connect pipelines in transmission systems and segments in the stress legs of offshore platforms. To prevent corrosion in oil extraction systems, automation must be implemented to ensure the effective functioning of cathodic protection systems, which are critical for maintaining system integrity (Bally, 1975).

The axes of the screw and coupling pair are aligned parallel to one another and pressed together under load. The stress values generated by this pressure can be both static and dynamic. The pipes used to extract crude oil from wells are connected by threaded joints. If the torque applied to these joints is insufficient, crude oil can leak through the threads. Conversely, excessive torque can create high pressure

---

[1] Lecturer, Dokuz Eylül University, Türkiye, dudu.yoldas@deu.edu.tr https://orcid.org/0000-0002- 1700-4310)

between the screw threads, leading to damage at welded points and gaps on contact surfaces (Carper et al., 1992). The connection system consists of a coupling and a screw. The threads of the screw engage with those in the coupling, rolling between them. These threads must remain continuously engaged. A peripheral gear connected to the coupling is rotated at a low speed. There are two main types of connections: standardized types defined by organizations such as the American Petroleum Industry (API) and the International Standards Organization (ISO), and proprietary designs developed by companies. To analyze these connections, it is necessary to evaluate the stress relations and coordinate systems using elasticity theory, where stresses such as σx\sigma_xσx, σy\sigma_yσy, τyx\tau_{yx}τyx, and τxy\tau_{xy}τxy are independent of the z-axis and are functions of x and y (Ucun, 2004).

The finite element method (FEM) was initially developed by mathematicians and later adopted by engineers. It was first used in stress analysis, and has since been applied to various fields such as fluid dynamics and heat transfer, where different fields such as stream functions, displacement fields, and temperature fields are analyzed (Joseph and Liao, 1994). FEM provides approximate solutions by breaking down complex problems into simpler substructures and solving each independently. The method has three key elements: first, the geometrically complex solution domain; second, the use of algebraic polynomials for each element; and third, obtaining nodal point values continuously from definition equations to derive desired outcomes (Tin, 2006).

In the finite element method, values at the nodal points are unknown and must be calculated. The variational principle is employed to form equations for the magnitude fields at the nodal points (Xu, 2003). The use of FEM and the introduction of computers into industrial applications have made it possible to analyze machine components that were previously studied only through costly experimental methods. ANSYS, a widely used finite element analysis software, has greatly enhanced the design and correction processes (Topçu and Taşgetiren, 1998).

In this thesis, the geometry of the connection system used in offshore oil extraction is analyzed using the finite element method. Solutions for different pressure variations were obtained using contact elements within the model. For each pressure value, contact states, frictional stresses, pressure variations, and shear stress variations were analyzed.

1.1. Geometric Modelling of the Connection

Screw threads are commonly used for connections in the natural gas and marine industries. These connections are subjected to various loading conditions, which generate stress along the surfaces where the tong and screw come into contact. In this study, factors such as the angles of the screw and tong surfaces, the material properties, and overloads can cause significant stresses. Before creating the finite element model for analysis, a geometric model of the connection was drawn in ANSYS software to establish the dimensional criteria. The dimensions and geometric model of the connection are presented in Figure 1.

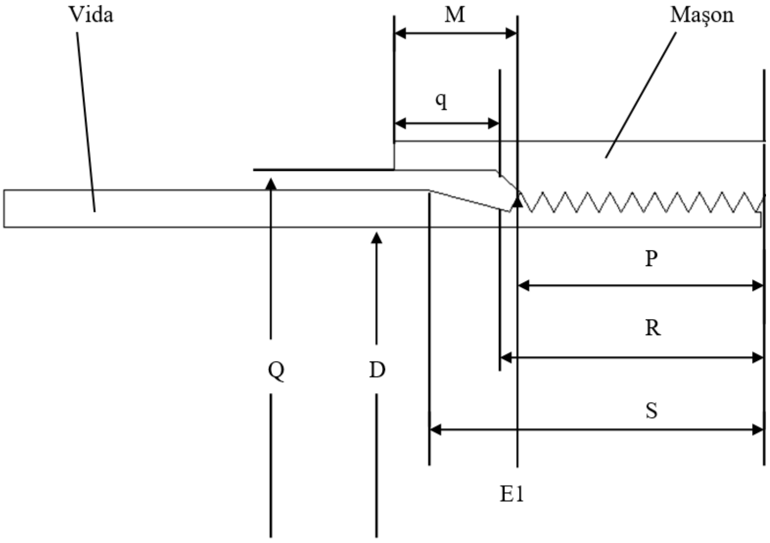

Figure 1. Dimensions and geometrical model of API pipe connection

The fixation on the right side of the link is shown in Figure 1, where it rotates around the y-axis and slides over itself. Fixation at a single point is necessary to prevent breaks between the links during movement. The dimensions of the screw threads used in this study are shown in Figure 2.

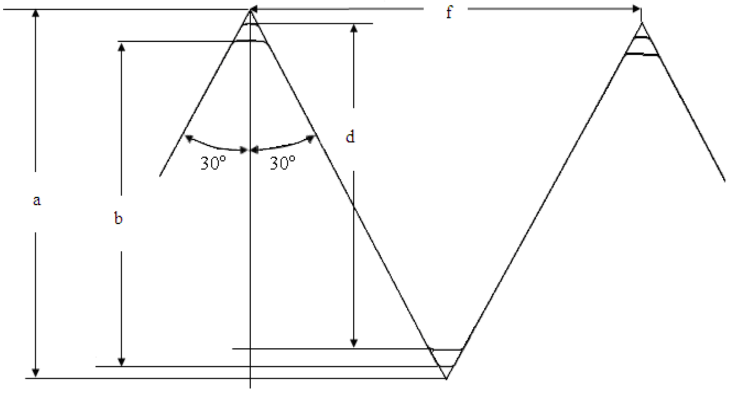

Figure 2. Dimensions of the screw threads used in the connection

Before moving to the three-dimensional stage of the connection, a two-dimensional drawing was first created using the dimensions in Table 1. These dimensions were determined based on API standards.

Table 2. Dimensions of pipework and threads in the system (Units mm).

Q	D	P	R	S	E1
141.3	143.69	23.80	35.72	46.74	138.41
M	q	a	b	d	f
16.56	12.82	2.74	1.04	2.41	3.17

Two different thread shapes have been proposed for API pipelines (Figure 3.). These threads, round and V-shaped, make the connection tighter and provide better distribution of loads.

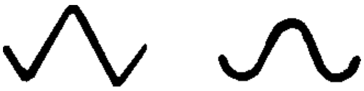

Figure 3. Different tooth shapes

A screw and a V-shaped thread were used for the connection. This thread shape was chosen because the sliding state and load distribution should be equal when connected.

1.2. Defining Material Properties

It is the stage of entering the material properties of the connection to be analysed and the coefficients to be used in the solution formulation into the programme. Poisson's ratio, modulus of elasticity, density, coefficient of friction and atmospheric pressure constitute these coefficients. Table 3. shows the mechanical properties of the material used in the analysis of the connection.

Table 3. Mechanical properties of screw and coupling material (AISI 4340)

Coefficient of friction	0,16
Atmospheric pressure (P_0) (N/m^2)	101300
Acceleration of gravity (g) (N/kg)	9,81
Poisson's ratio (v)	0,3
Modulus of Elasticity (E) (GPa)	200
Density (ρ) (kg/m^3)	1027

1.3. Calculation of Pressure Values to the Connection

When the slope of the connection is very low, it has been calculated as intense load at the points where the coupling and screw lie flat and the incoming loads act. The connection can deform under load, so its slope is considered to be non- zero. The height of the connection load is the sum of its density, gravitational acceleration and atmospheric pressure (1).

$$P \cdot h.\cdot.g \cdot P_0 \qquad (1)$$

P is the fluid pressure, h is the height, · is the density, g is the acceleration of gravity and P_0 is the atmospheric pressure. The fluid pressure calculations depend on the depth of the connection in the sea. The load at point B is the total load on the connection divided by the number of nodes (Figure 4.).

Figure 4. Pressure conditions at the connection

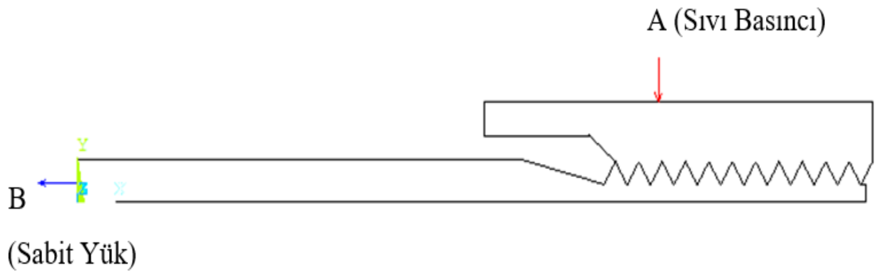

Although the load at point A varies with depth, the load at point B remains constant. Calculating the resulting pressure separately for each load and summing the results has the ability to modify the load.

1.4. Creating the Connection Model

Modelling, analysis and evaluation of the solution results of a problem are carried out in three different modules using the finite element method;

- In the analysis, the processes until the boundary conditions are applied to the model are performed in the preprocessor module of the programme.
- Analysing the problem in the solver module
- Additional calculations and numerical or visual evaluation of the results are performed in the post-processor module (Fetvacı and İmrak, 2004).

Since the geometry of the connection does not change in the length direction, the problem is considered as a two-dimensional stress problem and planar symmetry is considered in the loading conditions and geometry. Thus, the model is symmetric with respect to x and y planes in terms of both geometry and boundary condition. As a result, it is modelled in a way that shows the whole problem. As shown in Figure 5., in order to create the finite element model of the connection in the Ansys package programme, the front surface area was first created.

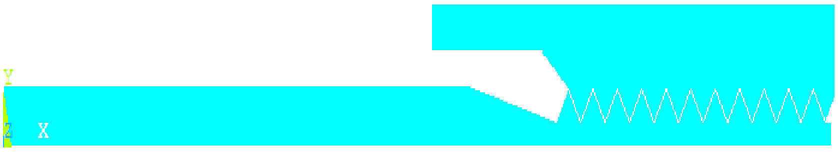

Figure 5. Front surface area of the connection

Then, the two-dimensional surface was rotated 90 degrees around the Y-axis to make it three-dimensional (Figure 6.). The resulting model consists of eight isoparametric nodes. The model contains 9376 elements and 8570 nodes. Each element is connected to each other through nodes.

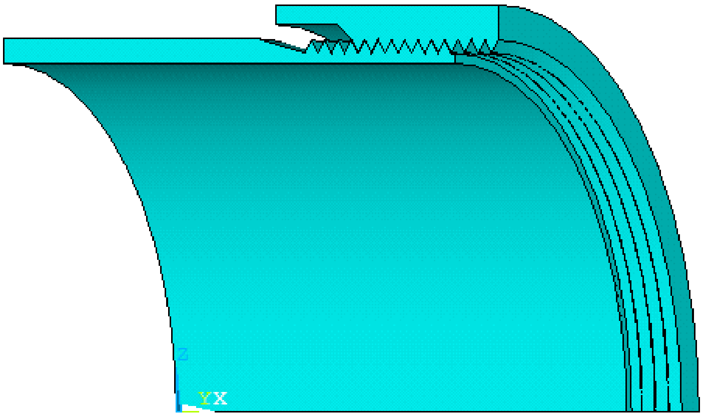

Figure 6. Creation of the 3D model of the connection by rotating it by 90°

Since too many nodes in the analysis of the three-dimensional system will make the solution very difficult, a model rotated by 22.5 degrees can also be used for the analyses obtained (Figure 7).

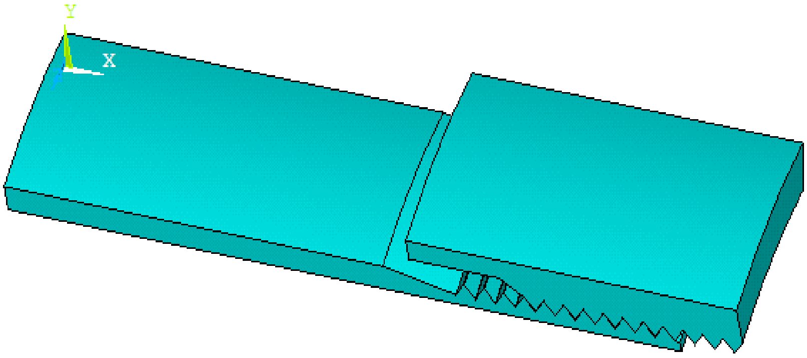

Figure 7. 3D modelling of the connection by rotating 22.5°

1.6. Mesh Modelling of the Connection

In an analysis using the finite element method, mesh generation is very important to perform numerical analysis in the basic fields of engineering such as thermal, structural, mechanical, fluid and electromagnetic. In the meshing process, the coordinates of both elements and nodes are determined (Huebner, et. al., 2001).

A mesh was created to convert the front surface area of this connection into a finite element model. The model was tested with three different mesh density sizes. Three different mesh densities were used to demonstrate the effect of the mesh size generated (Figure 8).

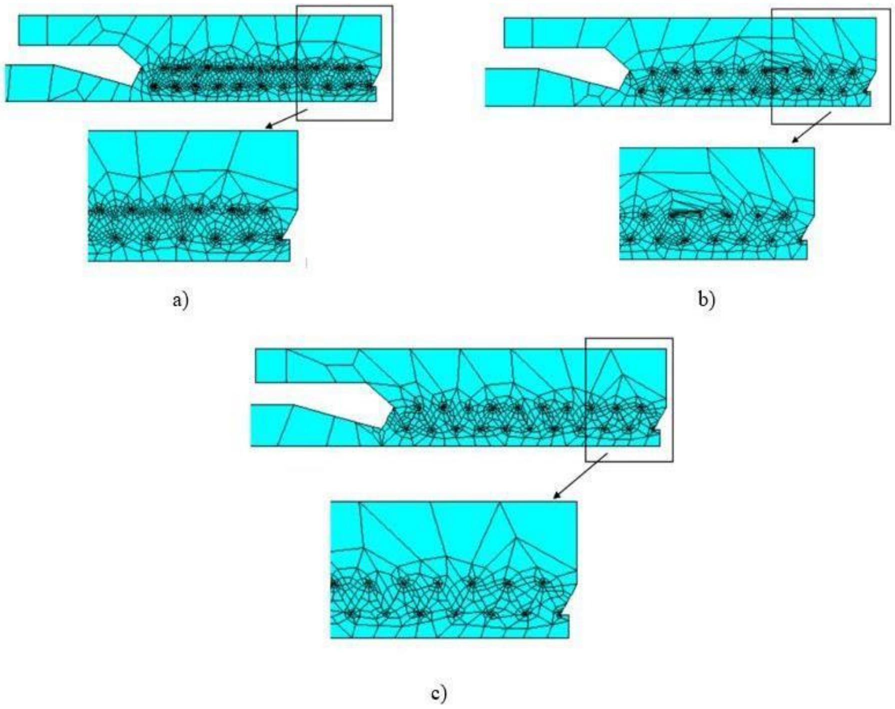

a) b) c)

Figure 8. Element size for mesh density (a) 8, (b) 9, (c) 10

1.6.1 Boundary Conditions of the Connection

The screw and coupling are applied to the nodal points on the x and y axis to fulfil the boundary condition of the connection (Figure 9). The system equations are set up and solved according to the boundary conditions of the programme. The solution involves calculating the displacements at all nodes. The displacements and stresses at any point in the element are calculated using the values at the nodal points and interpolation functions.

When fixed from the right side, the load will vary continuously depending on the sea depth. As shown in Figure 9., a constant force of 200 MPa was applied parallel to the screw.

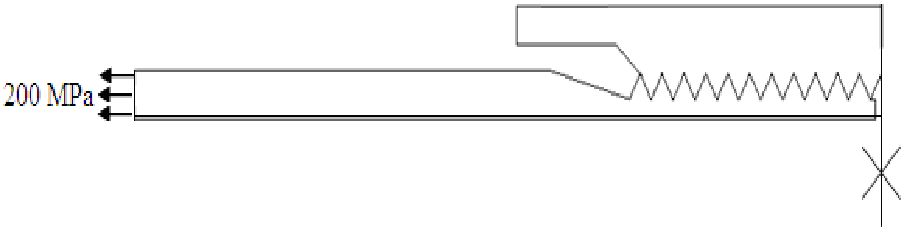

Figure 9. Load and boundary conditions of the connection

An 8-node isoparametric quadrilateral element (PLANE82) was used for modelling. PLANE82 has eight connection points as shown in Figure 10., and each connection point has two degrees of freedom. This element can change shape and displacement in the x and y directions. The plasticity of the element has the ability to flex and deform a lot Jones (2009).

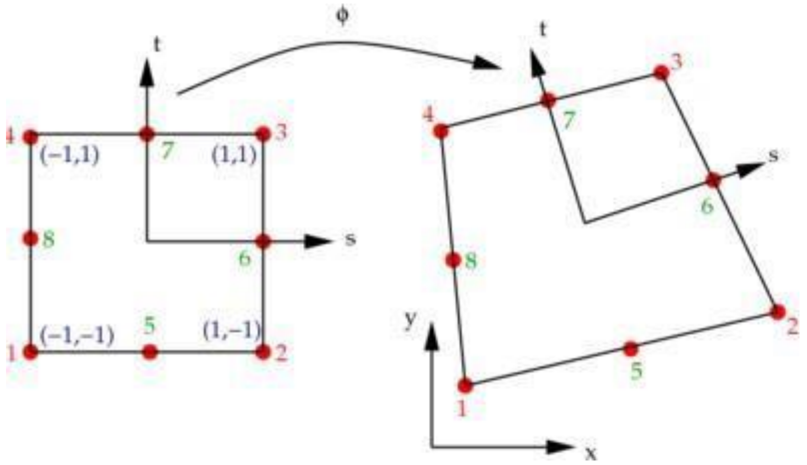

Figure 10. PLANE82 Isoparametric Quadrilateral Element with 8 Nodes

While creating the model in Ansys software, the analyses required for the calculation can be made. After the connection meshing process is completed, it is possible to determine the fasteners in the connection. In order to define a contact element, it is very important to select the coupling and screw area. Firstly, select the tong with which the connection is to be made from the field menu (Figure 11).

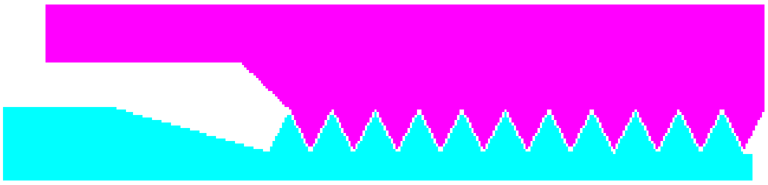

Figure 11. Mashon field selection

This is used to identify the points where contact between the surfaces is desired. Since it is not possible to make a connection between all the lines on the tongs, it is sufficient to select only the lines to be connected (Figure 12).

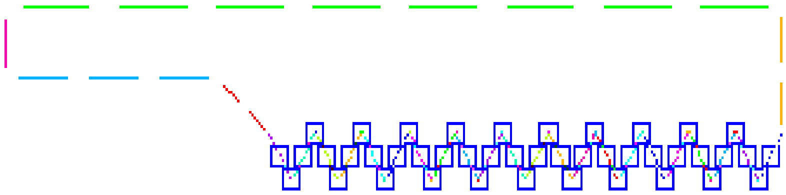

Figure 12. Lines to be on the contact in the mashon

After the lines defined for the connection on the tong are connected with nodes, the fasteners for the tong and screw are defined (Figure 13).

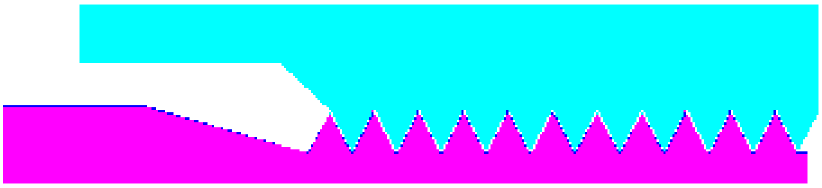

Figure 13. Screw area selection

The menus in the selection of the screw connect the fields to each other. Therefore, all lines related to the fields on the screw are selected and a connection is established between all lines (Figure 14).

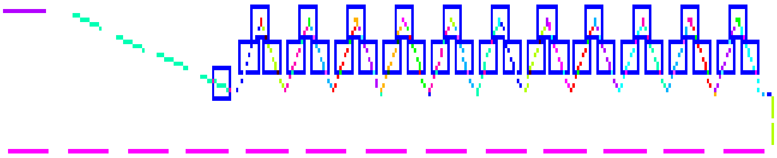

Figure 14. Lines to be in contact at the screw

ANSYS, a finite element software library, allows three different types of contact analyses with two and three dimensional elements. Node-node, surface-surface and node-node contact analyses and various algorithms are effectively used to model the interaction of elements with each other (Alyavuz and Anıl,2007).

In the analyses, since the dimensions of the finite elements forming the screw and the coupling are different, the surface-surface contact model is used for the screw and the coupling. The surface-surface contact model provides a solution if the nodes do not overlap. The screw was selected as the target surface and the tongs were selected as the contact surface. A contact pair was created at the interface of these two elements (Figure 15).

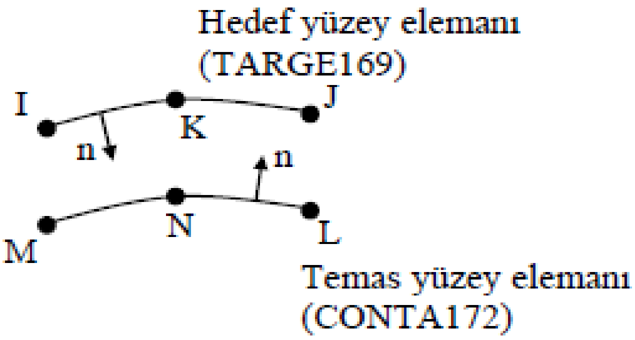

Figure 15. Contact elements

The TARGE169 and CONTA172 elements have three nodes that overlap with the nodes on the surface of the PLANE82 element. The node ordering of these components is critical for contact analysis. The typical contact surfaces must be modelled so that they face each other (Figure 16).

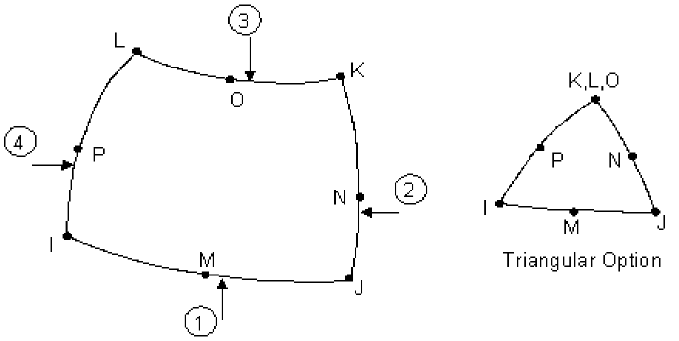

Figure 16. Plane82 structure

2. Analysis Results

In this study, stress analysis was investigated using finite element method. The screw and tongs were connected at different sea depths, equivalent (Von Mises) and AISI 4340 steel were used as stress criteria. As shown in Figure 17., the equivalent stress distribution occurring in the connection of the screw and tongs was analysed at points 1 and 2.

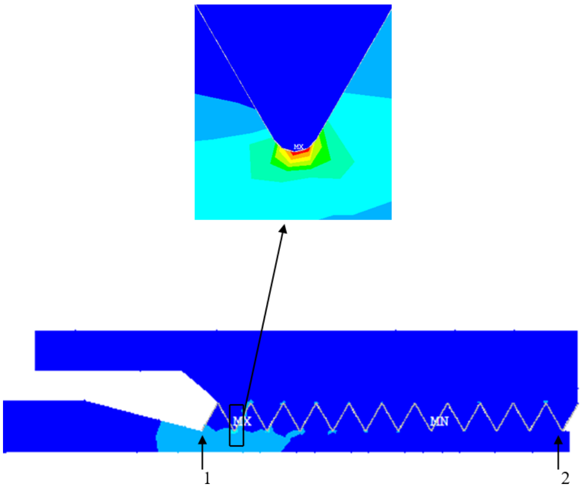

Figure 17. Points for stress analysis

The first teeth show maximum stresses as shown in Figure 17. These regions are considered as critical regions and the first withdrawal process is performed in these regions. It can be seen that there is a decreasing stress change starting from around the screw located at one point of the connection towards the two points of the connection. Despite the applied fluid pressure, no strain occurred in a significant part of the connection. Near point 2, the stress is low. The stress distribution effective on the screw is lower on the surface of the coupling.

Figure 18. shows the variation of the stress at points 1 and 2 due to different depths in the connection. Stress distributions are summed with depth, height, density, gravitational acceleration and atmospheric pressure. As shown in Figure 18., there is not much change from 0 to 0.5 at 500 metres. At 1000 and 2500 metres, the stress increased significantly. From 5 to 10, the stress decreased at 0 and 2500 metres, but the stress decreased very little at 5000 metres. At 100 and 500 metres the stress reductions started to converge. From 15 to 20 metres, the stresses from 100 to 2500 metres are close to each other, but the situation changes at 5000 metres. Up to 20 to 30 metres, the stresses ranging from 0 to 500 metres converged. These changes at different depths are due to the influence of height and pressure values on the connection over time.

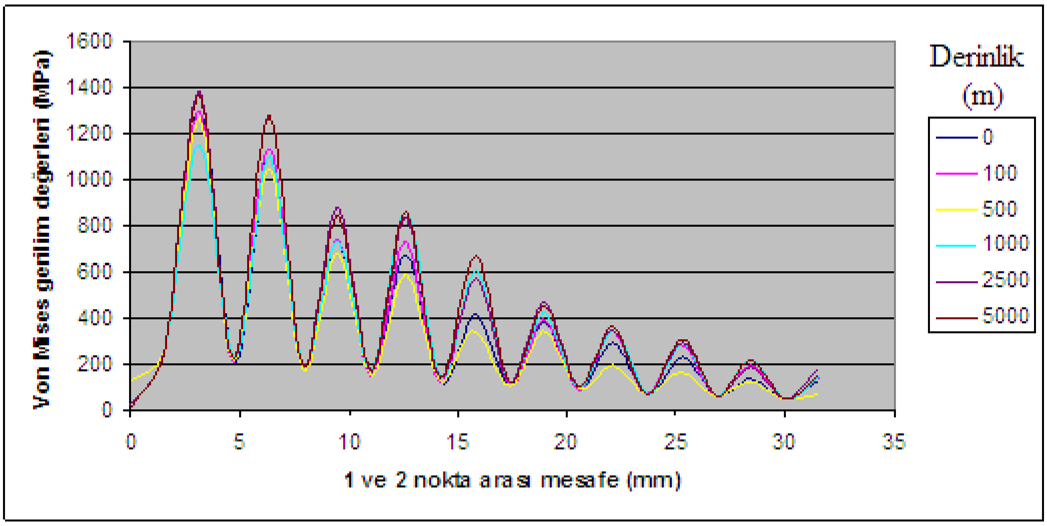

Figure 18. Equivalent stress variation at different depths

The incoming equivalent stress distribution at different depths in the screw and coupling connection is shown in Figure 19. The regions where the first threads are located show the highest stress level of the connection. The stresses on the surface of the tong changed very little at different depths. The highest stress value was observed where the first threads of the screw and the tong were in contact with each other. The screw and tong, together with the pull-outs, have a greater tensile effect at 5000 metres than at 0 metres, which is a remarkable factor at different depths. The sudden decrease and increase of the stress towards the sea depth started to produce the deformation of the first threads, which occurred at several different points.

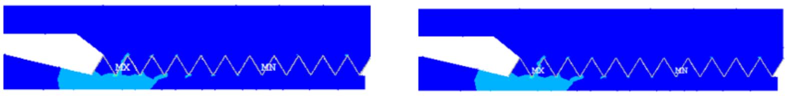

(a) 0 metre (b) 100 metre

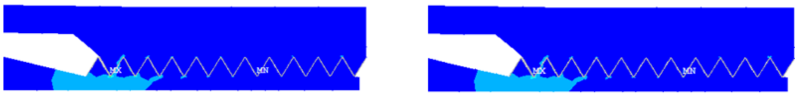

(c) 500 metre (d) 1000 metre

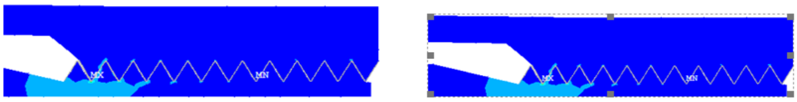

(e) 2500 metre (f) 5000 metre

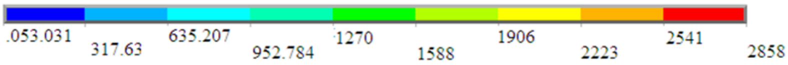

Figure 19. Von Mises stress distributions at different depths (MPa)

The analysis results obtained for the contact state of the connection show the contact state in the region where the first teeth are in contact (Figure 20).

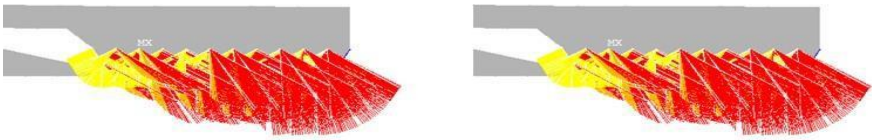

(a) 0 metre (b) 100 metre

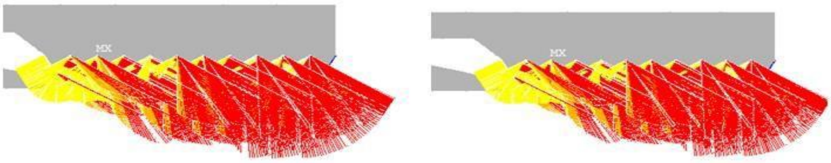

(c) 500 metre (d) 1000 metre

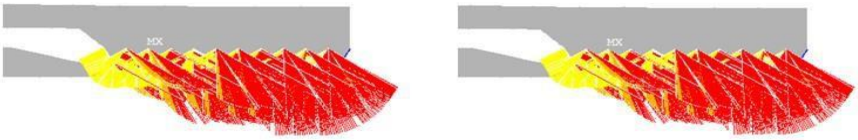

(e) 2500 metre (f) 5000 metre

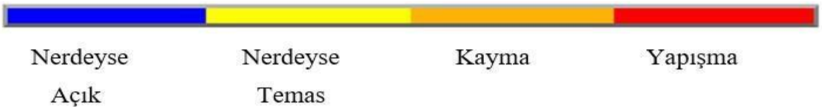

Figure 20. Interaction at different depths

In the case of interaction in the threads in Figure 20., it can be seen that a contact state is formed in the initial regions of the connection. The state of the connection at different depths changes with time and in some places adhesion, sliding, contact and openings are seen. Since elastic deformation occurred between the teeth and the teeth did not form the same contact state, the contact state of each region was different.

As shown in Figure 21., the frictional stresses occurring in the screw and coupling were analysed by determining various depths. The blue regions show the maximum frictional stresses. The frictional stresses are continuously decreasing in the green regions in the connection, while the yellow regions in the connection show the contact state. the threads in the first regions are open, while the threads in the last regions are slipped and stuck. However, as the depth and load increased, sliding was replaced by sticking.

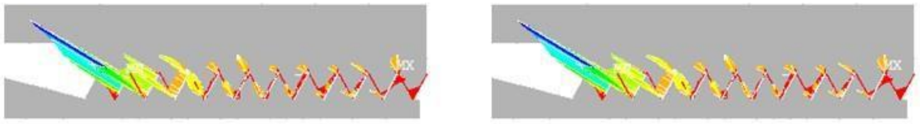

(a) 0 metre

(b) 100 metre

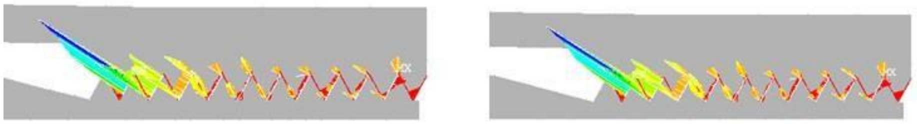

(c) 500 metre

(d) 1000 metre

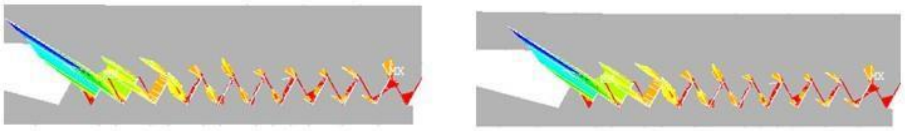

(e) 2500 metre

(f) 5000 metre

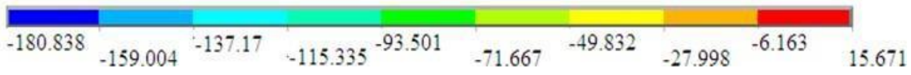

Figure 21. Friction stresses at different depths (MPa)

In the case of friction in the teeth in Figure 21., frictional stresses occur in the first teeth where the connection begins to pull out. Frictional stresses are caused by slippage between the teeth in contact. This is caused by the fluid pressure and depth reaching a maximum over time. The graph in Figure 22 was obtained despite taking different frictional stresses at the distance between the first tooth in the connection. Figure 4.8 shows that the frictional stress varies from 0.5 to 2, always in the same places. Between 1.5 and 2, it reached the same stress limit towards 0 as the stress increased. The fact that the friction stresses consistently reach the same limit indicates that the depth and load will not damage the joint.

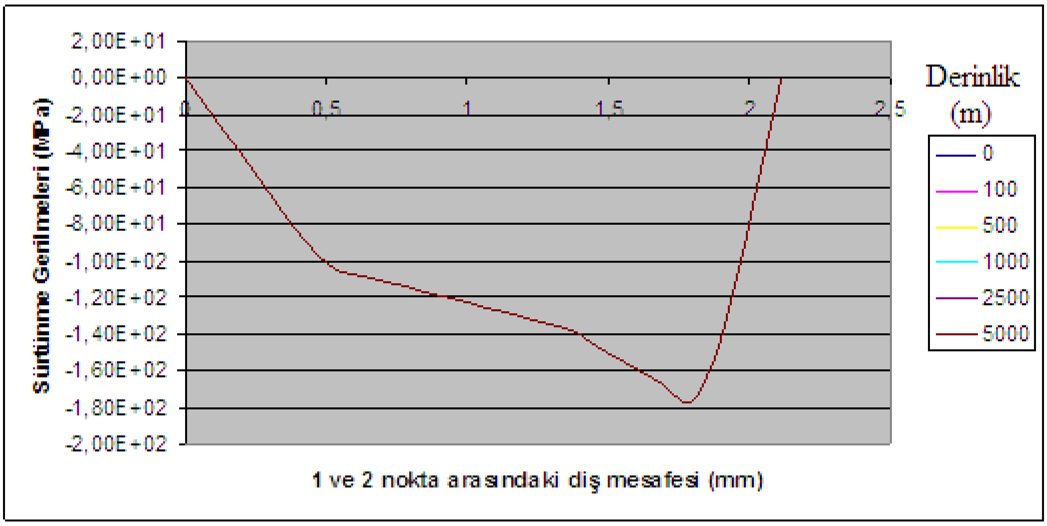

Figure 22. Variation of frictional stresses at different depths

In addition, since there is no change in frictional stresses in the case, the load on the connection is distributed at the same rate in the screw and the coupling, and the length of the screw length shows that the load distribution is equal. When the points are analysed in Figure 23 for the same depth and different threads in the screw and coupling;

At point A, there was an opening between the screw and the tong when slipping started, at point B, adhesion and contact in some parts of the thread, at point C, adhesion and slipping, and at point D, slipping and adhesion displacement of the threads over time.

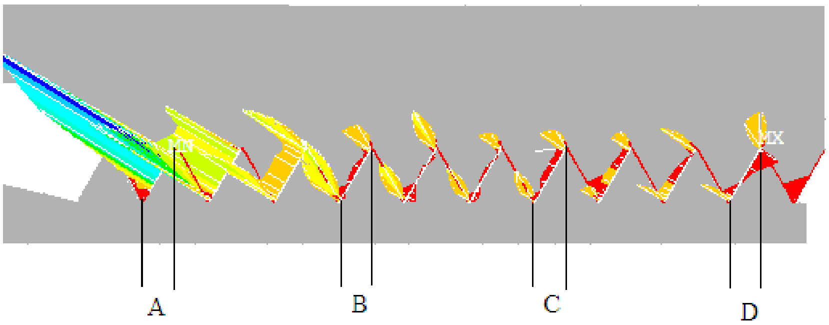

Figure 23. Frictional stress in different teeth at the same depth

From points A, B, C and D in Figure 1.23, the frictional stress graph in Figure 24 was obtained for different teeth at the same depth.

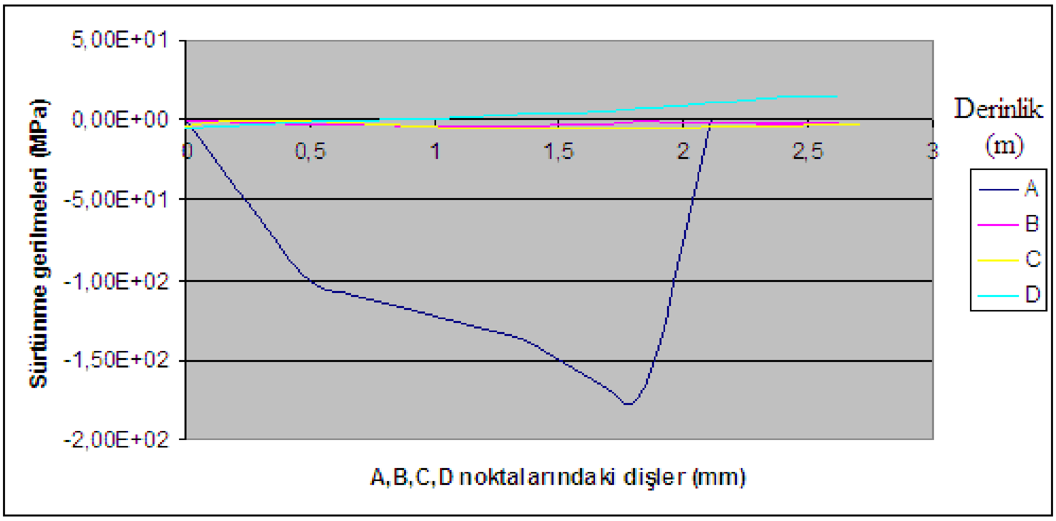

Figure 24. Variation of friction stresses in different teeth at the same depth

Friction stress in the teeth at points A,B,C and D in Figure 24;

- From 0 to 0.5 mm, a continuous frictional stress was formed at point A and did not change at point B.
- From 0.5 to 1.5 mm, a very small frictional stress increase at point B, C and D is almost identical,
- Between 1.5 and 2 mm, more frictional stress was observed at point A.
- From 1.5 to 2.5, there was no change at point B, an increase up to C, and a greater increase at point D than at the other points B and C,
- Between 2 and 2.5, it was observed that it increased significantly at point D compared to other points.
- At 5000 metres, the effect of pressure and depth on the slippage in the teeth was observed to be no difference at points B, C and D.

As shown in Figure 25., the pressure changes occurring in the screw and coupling were analysed by determining various depths.

The variation of the bonding pressure at different depth and load is lowest in the first teeth and the interdental gap is open due to slippage. In the dark blue regions, the adhesions between the teeth firstly shifted towards the contact state and then towards the contact state. At 5000 metres depth, the pressure changes from the first teeth to the last teeth.

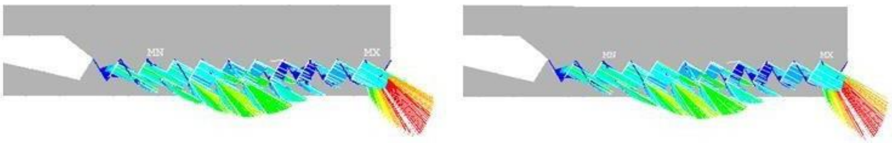

(a) 0 metre (b) 100 metre

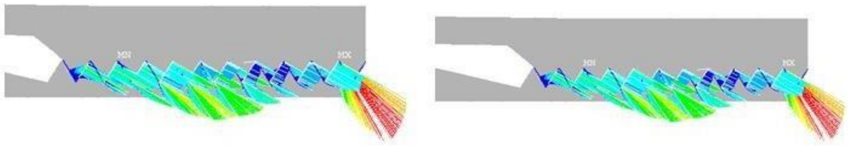

(c) 500 metre (d) 1000 metre

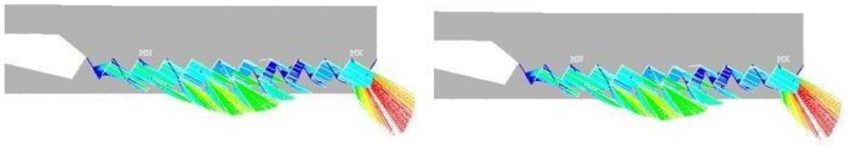

(e) 2500 metre (f) 5000 metre

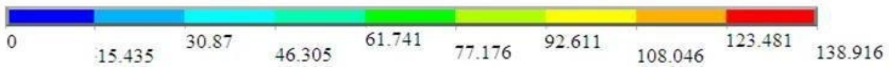

Figure 25. Compressive stresses at different depths (MPa)

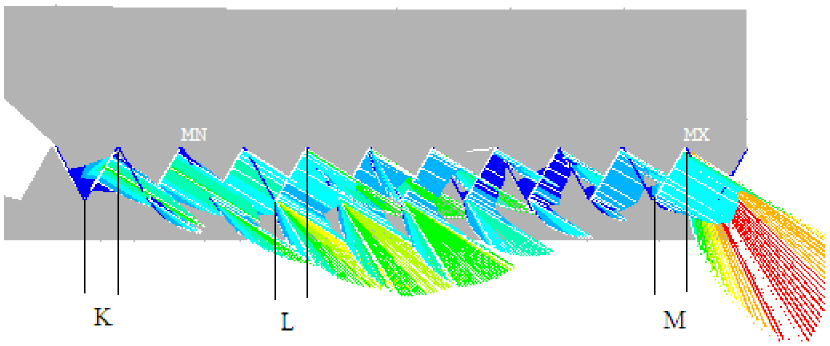

Figure 26. Pressure variation at the same depth in different threads

In Figure 26., it is observed that the opening in the teeth at point K widens towards the centre, slipping and contact between the teeth continues at points K, L and M, and adhesion is observed at point M.

From points A, B, C and D in Figure 26., the graph of pressure changes in different teeth at the same depth in Figure 27. was obtained

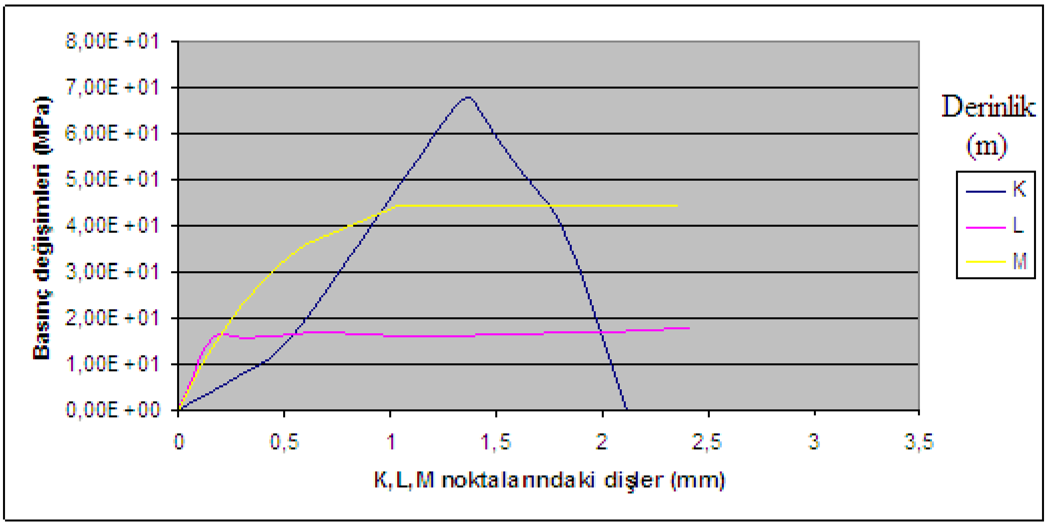

Figure 27. Pressure change graph at 100 meters depth in different threads

In Figure 27., pressure variation in the teeth at K, L and M points;

- From 0 to 0.5 mm, it did not change at point K and increased at point L.
- Increased at point M between 0 and 1.
- Between 1 and 1.5, it is highest at point K. However, a decrease is observed from 1.5 to 2.
- Between 0.5 and 2.5, it did not change at point L.
- 1 to 2.5 M has remained constant at the point
- Figure 28. shows the shear stresses occurring in the screw and coupling in the XY direction. These stresses were measured at various depths.

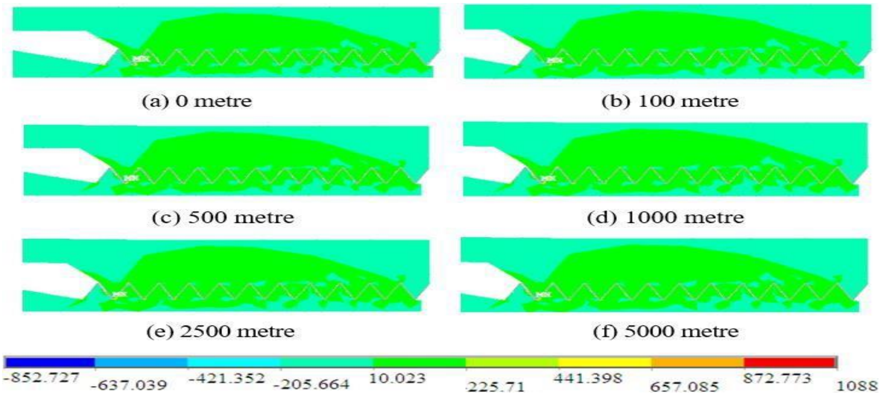

(a) 0 metre

(b) 100 metre

(c) 500 metre

(d) 1000 metre

(e) 2500 metre

(f) 5000 metre

Figure 28. Distribution of shear stresses at different depths (MPa)

Shear stresses appear to be concentrated in the central regions at all depths. However, a sudden pressure change increased the shear stress to a very high level. The shear stresses did not change significantly with the amount of load applied. The shear stress is higher in the areas close to the screw, but lower at the Mashon. It was also observed that more adhesion contact conditions occurred around the thread where the mashon was located.

The shear stresses in the XY direction were analysed by selecting the K and L points occurring in the screw and coupling (Figure 29).

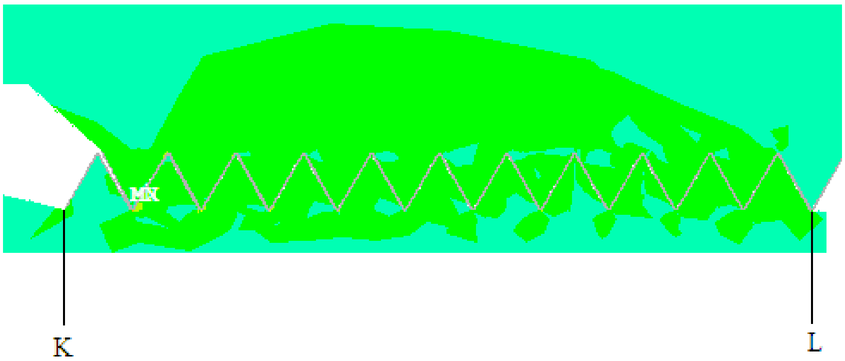

Figure 29. Shear stresses in XY direction at points K and L

In Figure 29., shear stresses are found in the regions where the first teeth are located and the highest shear stresses are found near the K point. At the determined depths, the shear stress increases in the regions close to point K and decreases in the regions towards point L. From the points K and L in Figure 29., the shear stress graph in XY direction at different depths is obtained in Figure 30.

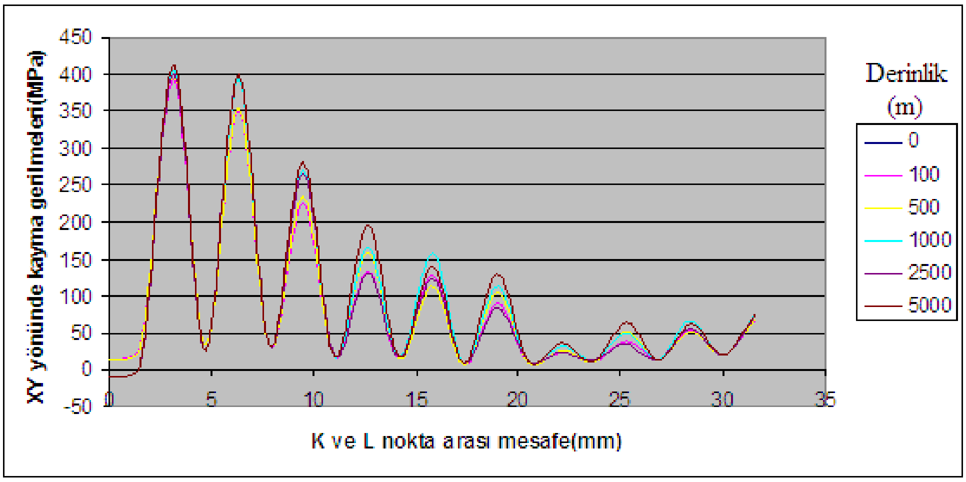

Figure 30. Shear stress graph in XY direction at different depths

Shear stress in XY direction at different depths in the teeth at points K and L in Figure 30.;

- 0 at 0 to 0.5 mm at 0 and highest at 5000 metres,
- Lowest at 5 to 10 mm and 0 to 2500 metres,
- 10 to 15 mm, 500 to 1000 mm, 15 to 20 mm and 0 to 2500 mm.
- . from 15 to 20 mm and from 0 to 2500 mm.

- It is highest at 5000 mm.
- Between 20 and 25 mm and a sudden decrease from 25 mm to 30 mm.

Conclusion

This study analyzed the equivalent (von-Mises) stress criteria, contact conditions, frictional stress effects, pressure variations, and shear stresses in connections formed using the finite element method. The following conclusions can be drawn from the findings:

- **Stress Concentration**: In the von-Mises analyses, the highest stresses were observed in the first teeth in contact. The sudden change in diameter of the shear stresses at the teeth caused discontinuities; however, this phenomenon was not present in other areas of the screw and tong. The geometry of the screw and tong contributes to these stress concentrations, even in the absence of depth and pressure.
- **Leakage Prevention**: When equal stresses are applied from a point, certain threads on the screw prevent the system from rupturing and ensure that no leakage occurs. The absence of a connection cover did not exert additional pressure on the surface of the tongs.
- **Pressure Maintenance**: Maintaining pressure at a desired point indicates that the teeth do not close and there is no leakage. The tensile pressure limit value can be estimated based on the pressure and deformation observed between the teeth. Shear stress predominantly occurs between the teeth and at their ends.
- **Thread Integrity**: If the mounting distance between the coupling and the screw is non-zero, it increases the risk of thread failure. Inadequate alignment of loads applied in both directions of the tongs can damage the connection.
-

- **Three-Dimensional Modelling**: By rotating the screw and coupling around a given Y-axis, a three-dimensional model of the connection can be created for further analysis. Changes in normal pressure distribution between the contact surfaces of the screw and coupling can lead to shear stress discrepancies between predicted and actual load values.
- **Dynamic Wear**: The highest stress values were found at the threads. The dynamic rotation of the tong and screw contributes to thread wear, ultimately reducing the overall strength of the connection.
- **Deformation and Cracking**: Over time, deformations and cracks may develop at the stress initiation points on the teeth. To mitigate this damage, it is essential to equip the system with a protective cover.
- **Thread Slippage**: Some threads on the screw experience slippage under stress, allowing for the connection to fail while maintaining a certain pressure level.

These findings underscore the critical importance of design considerations in the development of connections in marine applications, particularly regarding stress management and the prevention of structural failure.

References

Altunsoy, M., Ozcelik, O., & Erik, N.Y. (2004). Organic geochemical characteristics of the bituminous Eocene units in the Çorum - Suluova Basin, Central Anatolia. *Petroleum Geoscience*, 10, 163-171. https://doi.org/10.1144/1354-079302-564

Alyavuz, B., & Anıl, Ö. (2007). Analysis of Loading Transferred from Columns to Slotted Foundations by Nonlinear Finite Element Method. *Gazi University Engineering Architecture Faculty Journal*, 22(3).

Bally, A.W. (1975). A geodynamic Scenario for Hydrocarbon Occurrences. *World Petroleum Congress*, 2, 33-34.

Carper, H.J., Ertas, A., Issia, J., & C¸ uvalcı, O. (1992). Effects of Some Material Manufacturing and Operating Variables on the Friction Coefficient in OCTG Connections. *ASME Journal of Tribology*, 114, 698-705. https://doi.org/10.1115/1.2920938

Fetvacı, C., & İmrak, C. (2004). Finite Element Modelling of Spur Gear Wheels for Analysis of Tooth Bottom Stresses. Istanbul Technical University, Faculty of Mechanical Engineering, Istanbul.

Huebner, K. H., Dewhirst, D. L., Smith, D. E., & Byrom, T. G. (2001). *The Finite Element Method for Engineers*. John Wiley & Sons.

Joseph, D. D., & Liao, T. Y. (1994). Potential flows of viscous and viscoelastic fluids. *Journal of Fluid Mechanics*, 265, 1-23. https://doi.org/10.1017/S0022112094000741

Jones, R. M. (2009). *Deformation Theory of Plasticity*. Bull Ridge Corporation.

Topçu, M. & Taşgetiren, S. (1998). *Finite Element Method for Engineers*. Faculty of Engineering Matbaası, Denizli.

Tin, S. (2006). Design and Analysis of Single Overlap Bonding Connections. Master's Thesis, A. Kocatepe University, Institute of Science and Technology, Afyonkarahisar.

Ucun, İ. (2004). Stress and Vibration Analysis of Marble Cutting Discs with Finite Elements Method. Master's Thesis, A. Kocatepe University, Institute of Science and Technology, Afyonkarahisar.

Xu, W. (2003). Finite Element Method. *Pipeline Structural Analysis*, 1-6.

EXPERIMENTAL INVESTIGATIONS AND COMPARASION OF MACHINING PARAMETERS ON CAST POLYAMIDE AND STEEL ASTM A1040 AT CNC MILLING MACHINES

Gürcan ATAKÖK

Chapter 4

Experimental Investigations and Comparasion of Machining Parameters on Cast Polyamide and Steel ASTM A1040 at CNC Milling Machines

GÜRCAN ATAKÖK[1]

1. Introduction

Modern technology directs design engineers to use engineering plastics made from plastic raw materials with higher resistance to wear and corrosion. In laboratories, experiments, controls, and tests of all kinds of materials are conducted. The determination and testing of material properties from raw materials to finished products, and the control of material and product tests, constitute a separate sector. For any product to be made with technical plastics and composites, technology transfer and know-how are also provided by this sector. Preparing feasibility studies, solving production technical problems, product flow diagrams, cost and operational analyses, machine and equipment selection, facility installation and commissioning, and ensuring that the produced product meets the prescribed standards, product improvements, new technology and automation, and the adaptation of production lines are issues that need to be meticulously addressed.

Engineering plastics, which play a critical role in areas where advanced technology is used, have also become actively utilized in our daily lives in sports, recreation and entertainment areas, flooring, furniture, building and building equipment, the automotive sector, electronic goods, and household items that require high durability and temperature resistance. In the future, it is expected that they will become more prevalent in human life and will be among indispensable products. The rapid development of engineering

---

[1] Dr., Marmara University, TURKEY

https://orcid.org/0000-0002-5275-2429

plastics in a short period is primarily due to the material properties such as flexibility, elasticity, and strength that are expected from them. Those referred to as composite materials are particularly used in the aerospace, aviation, automotive, and construction sectors. The reasons for their production include not only the low weight and high strength of the material but also the cheap, simple, and standard quality of the production processes.

Engineering plastics, which have such an extensive family, have also made many contributions to the literature.

It is examined the modeling properties of HDPE/PA6 blends and found that blends with PA 6 content experienced problems when subjected to 45% bending as a result of extrusion molding. To reveal these problems, they used the artificial neural network model approach and compared this model with experimental data (Huang and Liao, 2002). Tests compared the material properties of EPDM/Polyamide TPV with chlorinated polyethylene and found that polyethylene provided better performance as a result of the experiments (Liu et al., 2002). It is examined the effects of drying on recycled glass fiber-reinforced Polyamide 6. This study highlighted the sensitivity of PA 6 to moisture, emphasizing the necessary precautions (Pedroso et al.,2001). Another study investigated the effect of thickness on the mechanical properties of injection-molded PA 6 and PA 6 nanocomposites. They conducted DMA and stress analyses, concluding that PA 6 nanocomposites exhibited better rigidity (Arochaa et al.,2003). Also it is studied for the interfacial tensions and temperature effects on polyamide/polyethylene and polycarbonate/polypropylene blends, finding that stresses decreased with temperature (Rheea et al., 2002). PA6 materials assessed the machinability of hardened AISI H13 and D2 molds through drilling and milling processes, investigating the impact on tool life (Chapleau et al., 2000). Another study examined the mechanical properties of recycled PET/HDPE composites, demonstrating their suitability for engineering applications and daily use through processes conducted on NC and CNC machines (Coldwell et al.,

2003. It is found that the effect of viscoelastic deformation on the machinability of polymers is related to surface quality, temperature, and high-speed cutting, and they investigated the impact of shear stress and surface roughness (Avila, Duarte, M , 2003). Researched the machinability of composite materials (Xiao, Zhang, 2002) demonstrated that the tensile strength of nylon-bonded Nd–Fe–B permanent magnet powders is affected by temperature and morphology (Lanza et al., (2002), King, Tansey (2002), Garrella et al., (2003)). Also it is investigated the mechanical properties and osmotic characteristics of polymerized polyamide thin films using the PDMA technique, comparing their tensile strength (Kima et al, 2002). Some researches examined the crystalline structure, structural information, and mechanical properties of biaxially oriented polyamide 6 films. They found that the material, when aged under room conditions, exhibited various crystallinity functions (Rheea,S, (2002)). It is researched polyamides and their modifications, conducting experiments related to the use of polyamide in the chemical industry (Demirer, (1992)). Also it is experimentally investigated the effect of temperature on the friction and wear characteristics of polyamide materials. For this purpose, a pin-on-disk test setup was developed, and wear tests were conducted at different sliding speeds and surface pressures within the selected p.v limit. It was noted that the wear characteristics did not change significantly for different sliding speeds and surface pressures within the same p.v limit (Parlar, (2002)). Another research experimentally examined the mechanical and tribological properties of blends of Polyamide 6 (PA6) and high-density polyethylene (HDPE) with and without regulatory additives. It was confirmed that wear is related to the ability to form a transfer film, and it was observed that the wear rate decreased when a good transfer film was formed (Palabıyık ,(2000)) and investigated the mechanical, physical, and morphological properties of polymer alloys of low-density polyethylene with polyamide-6 and polystyrene with high-density polyethylene (Taşdemir , (2002)). Suarez, at al's research looks at how BAAM technology is used to produce reinforced polyamide parts and then machine them, highlighting the benefits and encouraging outcomes that are seen. This work adds to the continuous progress in manufacturing, especially with reinforced polyamide materials, by merging additive manufacturing and subtractive machining. The results discussed in this article highlight the manufacturing sector's ability to integrate additive and subtractive processes, opening the door to more effective and superior production techniques (Suarez, (2024)). The features of the single point incremental sheet forming method are flexible enough to accommodate a broad spectrum of requirements and applications. The quality may result from improperly configured process parameters in incremental shaping. The single point incremental forming of polyamide 6 was carried out using the simulation program ABAQUS (Kharche, Barv, 2023). Another study demonstrates an appropriate geometry for turning and facing operations using high-speed steel cutting tools. In order to accomplish a clean machining with the least amount of roughness feasible, many angles were taken into consideration, including the tip, free, attack, and nose radius angles in the Polyamide PA-6 material (Quitiaquez et al., (2022)). The diverse and varied properties of polyamide as a material, which has become an integral part of our daily lives and industry, have led to an increase and diversification in experimental studies (Bertolini, (2020)).

The machinability of polyamide 6 was assessed with respect to chip shape and surface integrity (roughness, flaws, hardness, and crystallinity percentage). According to the results, cutting polyamide 6 within a particular temperature range—between -20°C and 20°C—is necessary to provide the best surface finish, or the lowest possible level of surface roughness and fault density. Furthermore, it is demonstrated that cryogenic cooling results in tougher surfaces than flood conditions while maintaining the same level of polymer crystallinity.

2. Engineering Plastics and Polyamide

Engineering plastics and composites are among the fastest-growing product types in today’s world. With new discoveries, their performance is increasing, their areas of application are expanding, and many issues are being addressed with new solutions. Knowing and applying these advancements create significant market opportunities for many companies (Yıldırım, (2002)).

Today, the role of petroleum-derived plastic in human life is becoming increasingly important. Particularly, the rapid developments in engineering plastics have significantly increased the use of plastic materials in all areas. The importance of plastic materials produced using high-quality raw materials and advanced technologies for the environment and human health is also very high. Therefore, manufacturing companies need to process high-quality raw materials with advanced technology and continuously integrate technology into production. In addition to following modern technologies, it is essential to recognize that the most important factor is "People First." Thus, besides quality production, the primary consideration should be to provide maximum benefit to users and ensure affordability. Additionally, throughout all stages from product design to customer delivery, zero defects, maximum production and delivery speed, and customer satisfaction should be prioritized. It is necessary to produce not only according to local standards but also to global standards (Mark, Geylord,(1998)).

Engineering plastics, which play a critical role in areas where advanced technology is used, have also become actively utilized in our daily lives in sports, recreation and entertainment areas, flooring, furniture, building and building equipment, the automotive sector, electronic goods, and household items that require high durability and temperature resistance. In the future, it is expected that they will become more prevalent in human life and will be among indispensable products (Kohan, (1995)).

In the rapid development of engineering plastics in a short time, the features expected from the material properties such as flexibility, elasticity and strength are at the forefront. The so-called composite materials are used especially in the space, aviation, automobile and construction sectors, and among the reasons for production is that the material is low weight and high strength, as well as the production processes are cheap, simple and of standard quality (Yıldırım, (2002)).

The design, analysis and testing of materials is a major engineering field. The combination of analytical methods with powerful computational tools, resulting in detailed visualization and simulation, was a revolution in materials research. We can see the results of the rapid approach that engineers developed, instead of the experimental method, in our daily lives.

The inside of a jet engine is where exhaust gases rotate the turbine blades thousands of times per minute and temperatures reach 3600 °C. The material in the blades must be resistant to the force and stress of heat and gases, light enough to achieve maximum efficiency, and long-lasting.

Copper is a highly conductive material, but it is soft. Mixing it with a very small amount of silver allows it to conduct electricity without loss. Inappropriate materials or mixing in an inappropriate amount of silver can cause problems such as power outages or telephone connections not being established in many regions. Engineers try to solve such requirements in the most appropriate way. Because there are materials that give better results than others in different situations due to their different properties. Computers using plastic photonic circuits direct data faster than electronic devices; photons move faster, plastic parts are lighter than metals, can store information more holistically and there is no magnetic interference. Ceramic materials allow engines to run hotter and fuel to be used more efficiently compared to metals.

Alloys produced by adjusting the carbon and other elements in steel allow steel to be used in many areas from shipbuilding to watchmaking. Bronze, which is formed by mixing tin with copper, can be used in industrial areas where strength is important, such as gears and bearings. Additives make some materials usable in different ways. For example, PVC plastic used in gutters, pipes and panels can be transformed into clothing or a tube that provides circulation between the heart and lungs with additives. Many products in the world are made of composite materials that combine different types of strength and flexibility. These include amorphous metals and shape memory alloys (smart materials) that behave according to environmental changes and remember their shapes. These materials are used in many products, such as devices that keep arteries open.

In the space age, many new materials were produced, while old materials were used in new areas. Fiberglass and reinforced plastics were cast to be used in the construction of car bodies and the keels of small ships. Carbon fiber had extraordinary properties that could be used as an alternative to metals in high-temperature turbine blades. As a result of ceramic research, materials resistant to high temperatures and suitable for heat shields were produced for use in space vehicles. With new analytical techniques, molecular and atomic imaging, atomic and molecular quantum calculations, material selection and production methods can now be determined as optimum.

Today, materials development is closer to engineering science than ever before. Engineers' ability to translate science into practice is reaching the atomic and molecular design stage. New analytical and computational techniques are taking engineers' work on material properties to new levels and offer extraordinary potential for the future (Karaküçük, 2000)).

Polyamide is a thermoplastic with high strength, hardness, good electrical and chemical properties, light weight and many types. Polyamide (trade name nylon), which was synthesized in 1928 and was the first engineering plastic, has varieties such as polyamide 6, polyamide 7, polyamide 6/6, polyamide 6/8, polyamide 6/10, polyamide 6/12, polyamide 11 and cast polyamide. Aliphatic polyamides are a class of polymers with high molecular weight and linear structure. High intermolecular forces in polyamides explain the high melting temperatures of polyamides, generally above 200 °C. If the length of the aliphatic part in the molecular chain increases, the melting temperatures decrease as can be seen in Table 1 (Yıldırım et al., (2002)).

Table 1. Melting Temperatures of Polyamides (Kohan, (1995))

Polyamide Type	**Melting Temperature T_m [° C]**
Polyamide 6/6	265
Polyamide 6/8	240
Polyamide 6/10	225
Polyamide 6/12	212
Polyamide 6	230
Polyamide 7	223
Polyamide 11	188
Polyamide 12	180

The most important disadvantage of polyamide, which can be easily shaped in injection and extrusion, is its high water absorption property. Polyamides absorb water due to the presence of amide groups. Water acts as a plasticizer. If polyamide contains more than 0.2% moisture, the mechanical properties of the product decrease, as well as defects and dimensional changes on its surface. Special applications are required when dimensional stability is required. Manufacturers usually provide data on the dimensional changes of products with relative humidity.

Polyamides are very resistant to solvents due to their high cohesive energy density and crystalline structure. Polyamides have extremely good abrasion resistance. Polyamide, a crystalline plastic, can be manufactured by molding, extrusion, solution, coating and casting. Polyamide granules can be improved in terms of mechanical properties with fiber reinforcements and various fillers. In general, these materials have very good fatigue strength, good creep strength, low coefficient of friction and very good impact strength, good chemical resistance and electrical properties. The properties of polyamides depend largely on the degree of crystallinity and the size of their morphological structure. Generally; production conditions affect this phenomenon. In the molding of polyamide 6, while a degree of crystallinity of 50-60% can be achieved with slow cooling and subsequent annealing, this value can be reduced to 10% with rapid cooling.

Having good mechanical and tribological properties, polyamide is used in the production of elements such as gears, cams, sliding bearings (up to steel rolling bearings), roller trough cages, slides. These parts do not need to be lubricated. It is also used as a coating on the slides of machine tools against wear. Polyamide is also used in the automotive industry in the production of many parts including carburetors, valves, gas and steam seals, propellers, high-strength field cables and various electrical materials, kitchen appliances, and solvent-resistant containers.

Polyamides, developed by DuPont and traded as nylon, were the first engineering plastics. The most widely used ones are given in Table 2. The table also shows several new polyamides developed since the first PA 66 and PA 6. The number of polyamide types developed by manufacturers is around 1500. All polyamide types can be improved in terms of mechanical properties with fibers and reinforcement materials. Polyamide, a crystalline polymer, can be manufactured by molding, extrusion, solution, coating and casting. The chemical formula of polyamides obtained by the reaction of an amine and an acid is given below (Kohan, (1995)).

$$nH_2N\text{-}(CH_2)_x\text{-}NH_2+nHOOC\text{-}(CH_2)_{y\text{-}2}\text{-}COOH=H\text{-}[HN\text{-}(CH_2)_x\text{–}NHCO\text{-}(CH_2)_{y\text{-}2}\text{-}CO]_n\text{–}OH+(2n-1)H_2O$$

$$_{n\,2}HN - (CH_2)_{x-1} - COOH = H - [HN - (CH_2)_{x-1} - CO]_n + (n-1)\,H_2O$$

Table 2. Commercial Polyamides (Karaküçük (2000))

My name is broad	**PA**
Poly(teirametilen adipamid)	4/6
Poly(hexametilen adipamid)	66
Poly(hexametilen azelamide)	69
Poly(hexametilen sebakamid)	610
Poly(hexametilen dodekanoamid)	612
Poly(dodesamethylene dodecanoamide)	1212
Poly(m-xylylene adipamide)	MXD6
Policoprolactam or polycaproamide	6
Poly(11-aminoandesanoamide)	11
Polidodecanolactam or polydodecanoamide	12

Polyamide, which was synthesized in 1928, was not used for more than 12 years before its importance was realized, but the USA, which could not make parachutes due to the fact that Japan had silk resources during the Second World War, revived the studies and put an alternative product to silk into the service of the industry (Yaşar, (2001)).

Polyamide, a thermoplastic product, defines a class with hardness, high strength, good electrical and chemical properties, light weight and many types.

Today, Nylon is a common class of plastic used in a variety of machine parts, electrical products, weapon and ammunition parts, sporting goods and many other places where its properties fit it.

Polyamide (ASTM) standards define 7 types and over 20 material grades. The US military specification MIL-M-20693 also shows 6 types. In the industry and market, there are also designations such as Nylon 6, Nylon 6.6, Nylon 6.10, Nylon 8. These are also based on the number of carbons in the diacids and diamines used during the production of polyamide. Table 3 shows the equivalences of polyamides expressed in this way in MIL-M-20693 (Karaküçük, (2000)).

Table 3. Commercial and Military Specification Equivalents of Polyamide

Commercial	**Types in MIL-M-20693**
Nylon 6	Type II, Type IV, Type V
Nylon 6.6	Type I, Type II, Type III
Nylon 6.10	Type III, Type IV
Nylon 8	Type IV

Copolymers of polyamide are also extremely valuable (such as PA/PI).

An important type of polyamide is castable polyamide. Most polymers cannot form a liquid with sufficient fluidity to fill the casting mold under the influence of heat and atmospheric pressure. Therefore, they must be forced into the mold cavity with high pressure. Extrusion or injection methods, which combine heat and high pressure, are applied to these polymers. However, some polymers, including polyamide, can be found in a liquid consistency that can be cast at atmospheric pressure. Castable polyamide is obtained from polyamide monomers. Complex-shaped parts weighing hundreds of kilograms can be cast from these monomers.

2.1. Synthesis of Polyamides

Polyamides are generally the reaction products of high carbon diamines and diacids. They constitute a class of polymers with a linear chain structure and a molar mass of 11000-40000. The reaction example is the production of Nylon 6.6 from hexamethylene diamine and adipine acid (Yaşar, (2001)).

2.2. Properties of Polyamides

Polyamides are a class of polymers with a high molecular weight and linear structure. They are solid, opaque, and sometimes transparent thermoplastic materials with a relative density ranging from 1.07 to 1.18. Transparent types transmit light at a rate of 85-90% .

Polyamide left in open air conditions shrinks slightly and loses some of its mechanical properties.

It has good resistance to petroleum oils, aliphatic and aromatic hydrocarbons, ketones and esters. Phenol, cresol and formic acid dissolve the polymer at room temperature. This is also used to determine the molar mass. The polymer, which is resistant to alkalis, is affected by strong acids and oxidizing agents.

Fillers such as pigments and glass fibers can be added to polyamide granules to give them the desired properties.

Polyamides, which have very good abrasion, fatigue and tensile strengths, are hygroscopic and therefore dried at 85-90°C for 3 hours before being fed to the forming device. The stiffness range varies widely in the polyamide family. Tensile strength is the same. Unfilled polyamide has a tensile strength of 500-800 kgf/ ^{cm2} .

Polyamide, which can be easily shaped by injection and extrusion, contains more than 0.2% moisture, the mechanical properties of the product decrease and defects are also seen on its surface. The parts coming out of the device are put into hot water and kept for a while in order to relieve the stresses. For example, a 25 mm thick PA part should be kept in water at 70°C for 15 minutes. Stress relief can also be done by keeping it in a suitable oven at 140°C for 15 minutes. However, the hot water system is preferred in terms of adjusting the internal humidity.

Sometimes hot potassium acetate solution is used as a more effective stress reliever and moisturizer. For this, 125 k of potassium acetate is mixed with 100 k of water and heated to 120 ° C. The process time varies between 15 minutes and 1 hour depending on the wall thickness of the molded part.

Some types, such as PA 6.6, absorb a lot of moisture. When this value reaches 8.5%, the mechanical properties of the material are lost. PA 6.10, 11 and 12, on the other hand, have high technical and commercial values because they absorb little moisture.

Conditioning in an atmosphere of 50% relative humidity takes a long time compared to water or aqueous solution.

In any case, care should be taken to ensure that the optimum value for humidity conditioning does not exceed 2.5% .

Polyamide is also good at impermeability to water vapor, air and oxygen. It does not harbor bacteria and fungi.

Polyamide items can be sterilized because of their high softening temperature.

It maintains its mechanical properties even at 100°C, even 150°C for PA 6.6.

The table below shows the moisture and mechanical property relationships of some PA types.

Table 4. Change in Mechanical Properties with Humidity (Intrinsic Humidity Ratio) in Some PA Types (Yaşar, (2001)).

		Humidity		Yield Strength		Modulus of Elasticity	
PA	Meltin	50%	Saturat	Dry	50% NN	Dry	50% NN
				N/ mm2	N/ mm2	N/mm ^{2} x10	N/mm ^{2} x10
6/	255	2.5	8.5	82.6	58.5	282	120
6	218	2.7	9.5	81.2	44.1	272	96
6/	210	1.6	5.0	58.5	50.9	199	107
6/	215	1.5	3.5	58.5	49	192	110
6/	212	1.3	3.0	60.6	51	203	124
11	185	0.8	1.9	58.5	53.7	131	100
12	174	0.7	1.4	55.0	52.3	134	103

(*) RH: Relative humidity

Polyamides can increase in size by nearly 1% due to their moisture absorption properties, so this feature should not be ignored in mold design and production (Yaşar, (2001)).

2.3. Friction and Wear

Polyamide has excellent friction and wear characteristics and is used in many applications without lubrication. The range of application can be extended by impregnation with oil, fibre or filler reinforcement. In general, friction and wear data are not published in the commercial literature, probably because of the poor reproducibility of friction measurements. These measurements depend on many variables including equipment, temperature, roughness and hardness of the counter surface, pressure and speed (Kohan, (1995)).

The p v value obtained by multiplying the surface pressure and the ambient speed ·is an important parameter for polymers to be used as a sliding bearing material. The p ·v (Pressure x Speed) limit is given as the determination of the maximum pressure that can be applied to the bearing material according to a given speed. The maximum pressure that can be applied is limited by the strength of the material, and the maximum speed is limited by the temperature increase. In determining the limit values, μthe loss of 25 m of material from the surface in 100 hours due to abrasion is taken as the basis.

2. 4. Moisture Absorption Feature

Moisture absorption is defined as the percentage of weight gain due to water absorption by the polymer. Standard test techniques such as keeping it in water for 24 hours are described in the relevant standards. Tests can be applied at different temperatures for different periods of time. There is no obligation to use water as the liquid. Moisture absorption is a very important quantity as it can affect the dimensions of the polymer as well as its mechanical and electrical properties. Polymers with very low moisture absorption rates are superior to others in terms of dimensional stability (Kohan, (1995)).

Water uptake by polyamides is reversible. The amount of water absorbed depends on:

- Relative humidity and ambient temperature,
- The duration of exposure to moisture,
- Polyamide type, crystallinity and reinforcements or fillers. The rate of moisture absorption depends on the type of polyamide, temperature, crystallinity of the polyamide and thickness of the polyamide section.

The result of the decrease in moisture uptake for any given percentage of relative humidity is less property change and greater dimensional stability. The equilibrium moisture content is insensitive to temperature except for the high methyl/amide polyamides PA 11 and PA 12. For example, PA 11 contains 1.9% moisture at 23°C and 3.0% at 100°C. To a first approximation, the time to reach equilibrium is directly proportional to the square of the thickness and decreases with increasing relative humidity. This is explained by the amide acting as a barrier near the surface, preventing water movement into the interior. It is difficult to remove the last traces of moisture by desorption. In this case, drying of the amide groups near the surface allows the last traces of moisture to spread to the surface.

2. 5. Dimensional Stability

When exposed to different environmental conditions (such as humidity, temperature, etc.), a change in the dimensions of the part occurs due to moisture, solvent absorption, stress reduction (due to moisture removal or temperature) and thermal expansion. The amount of dimensional change depends on the polyamide, humidity and temperature.

2. 6. Effect of Polyamide Type

The absorbed moisture can be assumed to be distributed uniformly throughout the part. As expected, polyamides with a higher methylene/amide ratio take up less moisture and undergo less dimensional change at any given relative humidity. Polyamides containing hydrophobic materials such as mineral fillers, fiber reinforcement, hydrocarbon elastomers as reinforcement, and flame retardants show less water uptake and therefore less dimensional change. The behavior of resins with added plasticizers varies depending on the solubility of the plasticizer in water and whether the water to which it is exposed is vapor or liquid. Fiber orientation is also a factor. Dimensional change in the direction of orientation as a result of moisture uptake is less than in the perpendicular direction. These differences are the same for 33% glass fiber reinforced PA 66.

2. 7. Effects of Humidity and Temperature

During the molding process of the part, the absorption of moisture in the polyamide causes a change in size as a result of the reduction in stress and the expansion due to the absorption of moisture. The change in size depends on the part thickness and the molding conditions. These two opposing effects cause a single change in size. This change is quite small. For example, the change in size of a 3.2 mm thick PA 66 part produced by injection at 50% RH for one year is less than 0.1%. This example explains why polyamide is successfully used in critical dimension requirements such as gears and coils. Depending on the change in humidity, there is also a change in the absorption or release of moisture. However, the moisture absorption/extraction rate is quite low and as a result the change in size is small. For example, when an injection-produced PA 66 part reaches equilibrium at 50% RH (± 10% RH change), its dimensions change by less than 0.4%.

In polyamides exposed to high temperatures, there is a decrease in stress and shrinkage as a result of heat treatment. The amount of change depends on the thickness of the part and the injection temperature. In heat-treated parts, there is a change in size due to moisture absorption. At first glance, it can be seen that the linear change in dimensions as a result of moisture absorption in an unstressed part is approximately 1/3 of the change in the part that has been moistened. The change in size in polyamide parts is a result of thermal expansion.

The linear thermal expansion coefficients give rise to the following results:

- The coefficient of linear thermal expansion depends on the temperature. The humidity in the test sample affects the coefficient of thermal expansion of polyamide. For example, the coefficient of expansion of PA 66 is 8.1x10 $^{-5}$ /K, while this value is 11.71x10 $^{-5}$ /K for saturated PA 66.

- The coefficient of linear thermal expansion of glass fiber reinforced polyamides is anisotropic. For example, the coefficient of linear thermal expansion of 30% to 33% glass fiber reinforced PA 66 in the direction of orientation is approximately 1/3 of the coefficient in the perpendicular direction.

3. Polyamide Fibers

3.1. Polyamide 66 (PA 66)

It is a polyamide formed by the polymerization of hexamethylenediamine and adipic acid. It is the oldest engineering plastic and was created in America in 1930. Therefore, its original widespread use is in the American and British markets. Compared to PA6, it is harder, unyielding, unbreakable, durable and also brittle. The insistence on using PA66 instead of PA6 is preferred for situations where very high hardness is required and the ability to recover quickly from damage is required. It is a material that can be easily processed in machines. It is available in the markets in sizes prepared by automatic machines according to ISO 9002 standards (Özpideciler , (2003)).

It is a good material in terms of abrasion resistance depending on environmental factors. Thanks to its self-lubricating feature, the friction coefficient is low, and the material generally does not need to be lubricated additionally in sliding areas of use. It has very high tensile strength and compression strength. It is a more durable material compared to polyamide 6. It is a material suitable for machining applications due to its high durability. It also has aging resistance and features suitable for all types of weather. It is available in natural colors.

Its weak points are that it absorbs moisture from the air. Even though it is in smaller amounts compared to PA 6, it absorbs moisture and can change the mechanical properties and the properties of the final form of the material.

It is preferred in mechanical areas because it is much harder than PA6 mechanically. Areas of use of Polyamide 66: It is preferred in parts such as gear sets, pulleys, pulleys, friction preventive guides, mechanical parts, wheels due to its mechanical properties that are more important than shock resistance. It is very easy to use in automatic tools and machines. It is suitable for contact with food. It should be avoided in this area because its electrical properties change in humid environments. It is a material resistant to alkali, inorganic components and solvents.

PA 66, known as the most durable of all commercially available polyamide polymers, has the highest melting point. PA 66 melts at 264 °C and has a continuous use temperature of 120 °C. Because of its partially crystalline structure, some parts of parts made of PA 66 exhibit a crystalline structure while others exhibit an amorphous structure. The amount of crystallinity can be increased or decreased by changing the manufacturing conditions, thus changing the mechanical properties. The properties can be further improved by adding PTFE, MoS2 and graphite to polyamide 66. Due to its water absorption properties, care must be taken during production; however, if the finished parts are allowed to take in water later, it is seen that their compressive strength will increase. The part can obtain water from the humidity of the air; however, this is a very slow process and the process can usually be accelerated by immersion in hot water at 60 °C.

PA 66 has very high bending and tensile strength, high impact strength, low coefficient of friction and is one of the most suitable materials for working under load. Resistant to alkalis and many organic solvents, PA 66 is not resistant to strong acids, especially at high temperatures. PA 66 is sometimes used to prevent gas passage because it has very low permeability to many gases, except for water vapor.

All polyamides become brittle over time in an oxygen environment at 80 ° C. UV rays can also cause the same effect. To overcome this problem, glass fiber or UV stabilized types are used.

The performance of a PA 66 part exposed to heat depends on the resin quality of the PA 66, the part geometry, the nature of the heat source and the mechanical loading. Consequently, the resistance to thermal deformation of the part cannot be predicted from standardized comparative tests. For example, PA 66 around the cartridge case of a heavy weapon can be exposed to firing temperatures of over 1000°C. However, since the exposure time is short, it will not deform at all. Pure PA 66 is widely used in electrical applications and can withstand short-term temperature changes caused by overload or electric arcing.

When the properties of temperature and chemical resistance, strength and workability are combined, PA 66 is a very good material for the automotive sector. The tendency to use less costly and lighter systems containing polymer instead of metal parts is rapidly increasing. In recent years, glass fiber reinforced PA 66 has started to be used instead of brass used in most radiator tanks. Graphite reinforced PA 66 is used in intake manifolds and fuel lines. It is also widely used in throttle cable guidance, guidance in gear change systems, and transmission systems in odometers. These are the parts that are particularly exposed to wear and tear, and therefore are of interest to the study.

Especially in applications in the automotive sector, the temperature of PA 66 parts can rise up to 70 ° C. This was considered as an important parameter in determining the temperature limits of the study.

MoS_2 or PTFE reinforced PA 66 and glass fibre reinforced PA 66 are widely used in gear wheels, pulleys and idler pulleys, bearing bushes where low creep resistance, resistance to bending fatigue and dimensional stability are required. Pure PA 66 is used in nuts, bolts, pins, railway insulator pads and spray nozzles where low friction and corrosion are not desired. Reinforced products are increasingly used in bucket elevator buckets where toughness, rigidity and abrasion resistance are required. Reinforced PA 66 is also widely used in chain and conveyor belt connections, fan blades, pump impellers, irrigation sprinklers, pump housings, pipe connections, window frame insulation and manometer housings.

3.2. Polyamide 6 (PA 6)

Polyamide polymer group is a polymer whose usage is rapidly increasing among high-specification engineering plastics. It is used intensively in the automotive sector, electronics and household goods, in areas requiring high strength and temperature.

It is a very long-lasting polyamide semi-crystalline thermoplastic material formed as a result of caprolactominning polymerization. It is a widely used material in the machine industry. Polyamide 6, one of the rational solutions in industrial plastics, is a hard plastic. With its superior technical features, it finds wide use in construction, ship, transportation, engineering sectors; packaging, agriculture and food, textile, paper, leather, iron-steel and chemical industries.

Lightproof. It is a product processed by machining or injection molding as rod, sheet, pipe and profile. PA 6 is a semi-crystalline, high strength thermoplastic engineering material for various applications.

Its basic characteristics are very durable, good sliding properties, resistant to abrasion; electrical insulation , easy to shape. It can be easily welded and bonded. It is hard, rigid and slippery. It is a material that is resistant to diesels, many oils and machine oils with cleaning agent, has good mechanical strength and has water collecting properties. It increases the resistance of the part against vibration and sudden impacts.

Generally used as gear wheel, shaft bearing, piston guide, rollers, strike plate, friction shaft bearing.

Polyamide 6 provides more perfect compatibility and economy according to the place of use with its alloys that can be made with glass, paint, oil, etc. materials. It works without oil or with very little oil, and its mechanical strength is high. Therefore, it is the ideal material to be used in gears. It is not as hard and wear-resistant as cast polyamide, nor as haypon as POM. The material has the feature of collecting water in its body. It increases the resistance of the part against vibration and sudden impacts. Thus, it allows the dynamic stresses that will occur during the use of the part to be eliminated in the body. Tolerance should be given to the material, because it is affected by even the humidity in the air and changes in size.

It is generally natural in color, but manufacturers can give it color. Polyamide 6 has many advantages that are not found in other plastics due to its chemical structure and crystal structure. Some of these features are:

- High mechanical strength, greater wear resistance.
- Can be used in wide temperature range (-50° C / + 60° C),
- Resistance to humidity, gasoline and solvents,
- Very easy mechanical processing,
- High impact resistance,
- High electrical insulation properties,
- Hard but flexible,
- Wide usage temperature,
- It is a self-lubricating substance.

PA 6 is very resistant to some solvents. It does not dissolve in any solvent under 70°C. It is aromatic and aliphatic. It is not affected by hydrocarbons, vegetable and mineral oils. It is resistant to weak acids and bases. It can be processed very easily on universal machines such as lathe, drill, milling machine, planer, saw that work on metal. It can be drilled. It is easier to work with PA 6 than many brass and aluminum works. During processing, there is generally no need for lubrication and cooling materials. The best result is obtained with high speed feed or highspeed slow feed. P6 has superior mechanical, thermal, electrical and its chemical properties, combined with its easy machinability on universal machines, are used in the production of components such as gears, bearings, bushings, pulleys in various industrial applications. It is superior to metals and other plastics in terms of both performance and economy. It is flexible. It does not break under shock loads, works silently, and is much lighter than metals. It is not suitable for contact with food. It has high UV stabilization. It can be used in electrical appliances depending on the humidity rate. It is resistant to inorganic components and solvents.

Most commonly used areas: Pulleys, wheels, cogs, rings, pressure cylinders, flanges, filter plates, concrete casting plates, soybean press plates, conveyor rollers, worm screws, joint parts, belt bearings, belt pulleys, valves, valve parts, rail connections, cable car and overhead line pulleys, elevator pulleys, housings and bearings, cylindrical gear wheels, gear shafts, gear segments.

PA 6 is a synthetic thermoplastic with a high crystallinity, low moisture activity, molecular weight ranging from 8,000 to 100,000 g/mol, which can also be manufactured by casting, and is the best among nylon types in terms of mechanical and physical properties.

PA 6 has high impact resistance due to its molecular weight and structure, and is preferred in applications where abrasion and impact resistance must be very high and moisture activity must be low. The friction and wear properties of the system depend on many parameters such as the material pair, roughness of the surfaces, contact geometry, whether there is a lubricant at the interface, load, speed and temperature. The main factors affecting the friction coefficient and wear rate of PA 6 are the surface roughness and hardness of the material pair, the applied pressure, the length of the contact path, the temperature of the rubbing surfaces and the lubrication status. Accordingly, PA 6 products are suitable for the production of parts such as bearings, gears, wear plates, joint parts, cylinders etc. and are preferred instead of brass, bronze, steel and stainless steel when necessary.

At low and normal sliding speeds, in abrasive environments with dust, sand and the like, the working life of this polymer is 2-10 times longer than that of cast iron, iron, bronze and steel. PA 6 is resistant to weak acidic and basic chemicals and organic solvents (Kohan, (1995)).

Polyamides are materials with very good to medium transparency, high strength, medium hardness depending on the crystal percentage, and are relatively impermeable to gases, oils and aromas. Due to their hydrophilic structure, they only form a mediocre barrier against water vapor. Their melting points are 175-255°C depending on the product; resistance to low temperatures varies between (-50)-(-70)°C.

Due to the difficulty of processing, the application areas of monofilms are very limited. Films made of PA 12 or co-extrusion of PA 12 and PA 6 are used in sausage packaging. The main areas of use of polyamides are laminates, and especially their combinations with polyolefins are preferred because they complement the water barrier and welding properties of polyamide. Non-oriented PA combinations are used in thermoformable tray type packaging materials (especially in the packaging of meat products, fish and cheese) with the use of additional barriers (Savaşçı et al., (2002)).

Due to their high mechanical properties, polyamides are successfully used in the production of cams, gears and sliding bearings (up to steel rolling bearings), and these parts do not require additional lubrication (Karaküçük, 2000)).

In the automotive industry, polyamide is used in the production of many parts including carburetors, valves, gas and steam seals, propellers, high-strength field cables and various electrical materials, kitchen appliances, and solvent-resistant containers.

PA 6.10 is preferred in production due to its good properties such as dimensional stability and low moisture absorption and is used in the production of fibers for many civil and military purposes and for the textile industry.

Flowmeters are produced from transparent polyamide type as required by the feature. This product is also used in the electrical and electronics industry (Karaküçük, (2000)).

PA 6 can be supplied as a semi-finished product, in the form of sheets and logs. It can be easily processed on normal wood and metal benches. It is possible to obtain a clean and smooth surface by using high speed (minimum 150 m/min.) when processing on a lathe. The blades must be sharp and suitable for the process. It can be easily drilled using sharp spiral tips. It is recommended to use drill bits with a tip angle of 115° and a helix angle of 10-20°. Standard milling cutters used for soft metals are sufficient to process PA 6. It is possible to obtain clean surfaces with special cutters. Care must be taken to ensure that all blades are very sharp.

Polyamide is used in the production of the following parts in the machinery sector: Pulleys and silent gear mechanisms; seals; all kinds of ring seals; shock absorber equipment; tap and valve seals; ball and needle valve and cover bearings; bearings and bearing housings; slide bushings; sliding surfaces; wormgears; belt pulleys; rolling bearings, shafts, shafts; impact blocks and drill bushes, especially in large machines; valve thimbles; seals and adapters for hydraulic sealing; gil pallets; vibration blocks; pump elements; bearings and wear parts for lathe chucks and rotary tables; all kinds of couplings.

Automotive sector: Bushings, bearings, sliding plates, scissor blocks, work machines rotating system bearings, pulleys, guide rollers, transport vehicles rail guides, rack and pinion systems and screw transmission bearings. In ships and transportation; ship propellers, propeller shafts, bearings, chain sliding guides, bearings, instead of brass surfaces, ship crane machinery parts, portholes, ram horns, ventilation covers.

Textile industry: Printing rollers, ironing, finishing, dyeing, purging roller coatings, gauges, all kinds of bearing systems, all kinds of gears, slide rails, shuttles, spindle arms, spindle plates, reels, reel supports, textile helices, yarn travellers, wadding reels.

Food industry: Transfer screws, star gear transmitters and all kinds of mechanical parts, worm screws and segments in bottling and filling plants (Kohan, (1995)).

PA 6 serves many industries due to its hard and durable nature. These include machine construction, manual and mechanical handling, construction machinery, packaging and filling units, textile machinery, shipbuilding, automotive industry, mining, food industry, and medical devices (Özpideciler, (2003)).

In these industries, they are used as various cylinders, rope tensioners, rope grooves, guide and bush sliding bearings, bearing segments, drive bearings, sliding blocks and plates, wear strips, protection strips, shaft elbows, bevel and spur gears, worm screws, valve bearings, cutting and pressing plates, ceramic and concrete molds and many similar elements.

In the electrical industry, it is used in electrical plugs, on-off switches, coils and conductors. Toughness, wear and heat resistance are important factors in these areas. It can also be used as a fuel tank due to its very good gasoline resistance.

Polyamides constitute the most important group of engineering plastics. Within this group, Polyamide 6 is quite hard and has resistance to impact even at low temperatures. With its harmonious combination of properties, PA 6 finds wide use in various sectors, especially automotive and electrical & electronics.

PA 6 is frequently used in every field. The reason for this is that it is a unique material that can be used in many ways. For example, in the textile field, dresses, socks, underwear, swimsuits, tracksuits, daily clothes, umbrellas, suitcases, awnings, parachutes, tents, sleeping bags are examples of these. In addition to carpets, rugs and home textiles, technical fiber materials such as cables, ropes, nets, fishing rods, tarpaulins, safety belts, airbags, mechanical rubber materials are also made of polyamide (Guo et al., (2001)).

Polyamide 6 has many advantages over other materials. It also covers 60% of other polyamide types used in the world in terms of price.

If we examine the areas of use in the automotive sector separately: Using PA 6 in air intake manifolds reduces the weight and price of the vehicle, while increasing engine performance, compared to other metal materials.

In internal combustion engines, the air intake manifold takes air from the cylinders and returns it. The part where this process takes place has a complex corrugated structure that challenges manufacturers. In addition, the material to be used must be able to resist explosions caused by increased internal pressure, engine vibrations, high temperatures and residues formed by contact with gasoline and oil. Polyamide 6 can respond to all of these.

Compared to metals, synthetic resins provide advantages in performance and production in the intake manifold. It increases engine power and fuel efficiency. (Since the temperature of the incoming air decreases, its density will also increase.) The horsepower of the engine will increase due to the smoothness resulting from its structure. The weight of the manifold will decrease by 50% compared to aluminum and will be 25-50% cheaper.

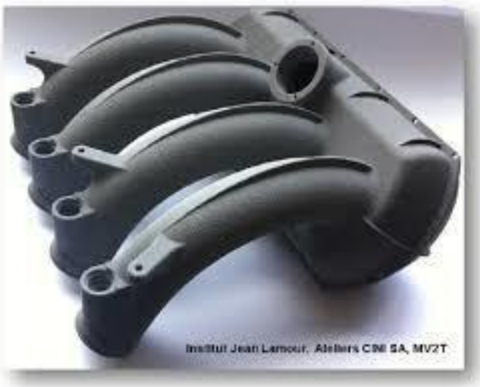

Figure 1. Example of Polyamide Usage in the Automotive Industry (Manifold)

Balancing feature of Polyamide 6, it contributes to the forces (instantaneous and general) and rigidity. It provides an advantage over PP (Polypropylene) in high temperatures and extreme resistance to fuel (Figure 1).

Compared to other types of polyamide, many processes can be applied to the material, increasing mold stability and decreasing product prices. It provides positive effects on heat resistance, surface appearance and smoothness in short and long-term use.

Polyamide 6 provides advantages in air ducts and pumps and many other complex automotive parts. For example, when considering the safety requirements of the protective part where airbags are placed, the use of Polyamide 6 allows for less weight and cost compared to metals. Thus, PA 6 provides strength, prevents material fatigue, and minimizes wear and friction (Figure 2).

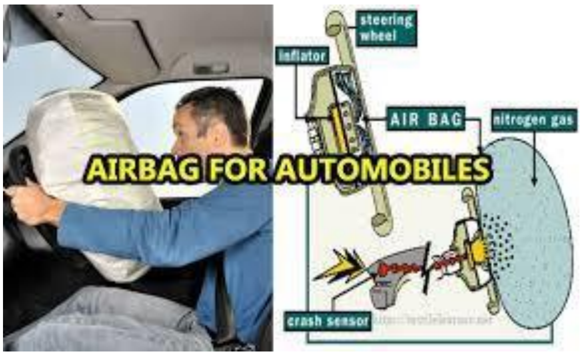

Figure 2. Protective Part Where Airbags Made of Polyamide Are Placed

In the textile sector, the use of PA 6 in carpets and rugs is both aesthetic and prevents discoloration and contamination as a result of use. Positive effects are achieved by using minimum energy during production. PA 6 is also used in scarves.

One of the most interesting examples in the medical sector is the dentist's chair. It is now more comfortable. There are even chairs that record the patient's sitting position and adjust accordingly on subsequent visits (Figure 3).

Figure 3. Example of Polyamide Use in the Medical Sector

An example of seats is those used in stadiums. They are produced in different colors and sizes, and are fireproof so that hooligans cannot cause damage (Figure 4).

Figure 4. Production of Stadium Seats from Polyamide

It does not produce poisonous gas, does not retain dirt and dust, and is at economical prices. The nets used by fishermen in the maritime sector are also made of PA 6. The reason for this is that the fishing lines must remain intact despite the stresses and the salinity of the sea. In the electrical and electronics sector, it is used as a protector in chips in the computer industry, in places where it will not compromise stability even at high temperatures.

The main properties of polyamides are excellent hardness/strength ratio, high mechanical strength, good electrical insulation, flame retardancy, high resistance to chemicals, high abrasion resistance and high moisture absorption.

PA 6 products find application in many sectors due to their excellent thermal and mechanical properties and superior price/performance ratio. Glass fiber reinforced PA 6 is used primarily in the automotive industry, mirror bodies, wheel covers, engine fans, exterior panels, engine covers, seat bodies and many other places. In addition, portable hand tools, office furniture bodies, white goods and transformers are among the main ones among their wide application areas. These products are also used in the electrical and electronics industry, and flame-retardant ones are generally preferred for this sector. Impact resistant PA 6 products are the most suitable materials to be preferred for sports and safety helmets, various handles, rifle butts and office chairs. Glass bead reinforced PA 6 is used in white goods body applications where strength is sought together with isotropy. Mineral filled ones are used in cable connectors, clothing buttons and ignition switch bodies. Flame retardants are widely used in various parts of electrical and electronics and automotive industries, such as plugs, buttons, connectors, air guides, water heater slugs, compressed air compressor bodies, electric heater body parts and other household appliances (Mann, (1999)).

3. 3. Polyamide 6.6 (PA 6.6)

Polyamides, which are included in the glass fiber filled and reinforced, flame retardant, impact resistant, stabilized and colored product group, constitute the most important group of engineering plastics. In this group, polyamide 6.6 has the highest hardness, abrasion resistance and deformation temperature under heat. The harmonious combination of the features it contains Polyamide 6.6 finds wide use in various sectors, especially in the automotive and electrical and electronics sectors.

Its main properties are as follows: excellent hardness/strength ratio, high mechanical durability, good electrical insulation, flame retardancy, high resistance to chemicals, superior abrasion resistance, high moisture absorption, preservation of fastnesses at high temperatures, ease of processing, excellent price/performance ratio (Mann, (1999)).

Polyamide 6.6 products find application in many sectors due to their excellent thermal and mechanical properties and superior price/performance ratio. Glass fiber reinforced PA 6.6 is used primarily in the automotive industry, in door handles, seat parts, radiator heater bodies, engine fans, gear lever parts and other bodies. Zippers and portable hand tools are also among the main ones in a wide range of applications. These products are also used in the electrical & electronics industry, and flame-retardant ones are generally preferred.

Impact resistant products, carrier car wheels, cable connectors and connector fastening screws are the most suitable materials to be preferred. Glass bead reinforced PA 6.6 is used in automotive distributor caps, fan motor housings and bearing rings, and some white goods applications where hardness is sought together with isotropy. Mineral filled PA 6.6 is used in ignition switch housings, insulation parts and side signal sockets. Flame retardant PA 6.6 is widely used in electrical and electronics and automotive industries, plugs, sockets, buttons, connectors, circuit breakers, relays, fuse boxes, high voltage cable holders and various parts of other household goods.

3. 4. Cast Polyamide 6

There is no size or quantity limit in production by manufacturing companies. It is possible to produce very large sizes and desired shapes of parts economically with special manufacturing techniques. Areas of use It is possible to make steel bush gears, pulleys, mixer propellers or steel shaft nylon cylinders by using the techniques specific to polyamide production and the mechanical strength of metals. These and similar steel reinforced cast polyamide 6 machine parts are widely used in the paper, textile, chemical, printing and food industries.

Due to its lightness, resistance to corrosion, impact, abrasion, and its ability to operate without oil and silently, it has replaced iron, steel, aluminum, bronze and many plastics in the production of rotating and sliding moving machine parts and equipment. The production technique is extremely economical in terms of the production of products such as bearings, gears, wear plates and pulleys in all sizes and quantities.

Cast polyamide 6 has a very wide range of applications due to its properties such as high modulus of elasticity, good abrasion resistance, good chemical resistance, good weather resistance, high melting temperature. In addition to its mechanical and chemical properties, the production technique can also be considered as the reason for choosing cast polyamide. The mechanical strength of cast PA 6 parts produced by the casting method is much superior to other polyamide parts produced by injection and extrusion (Mark, Geylord, 1998)).

The shape of the semi-finished parts is ready to be stocked. PA 6 and its copolymers can be processed with standard cutting tools and machining methods such as planing, turning, milling, and drilling. Lubrication should be applied to prevent excessive heat build-up that may occur during processing due to softening and surface roughness.

For many of the reasons mentioned above, such as lightness, good abrasion resistance, cavitation resistance, sound and vibration damping, cast PA 6 is widely used in transportation and industrial applications.

It is used in the wings and rudders of the thrust propellers of boats. It is used as a pulley in containers and mobile cranes. Cast PA 6 pulleys reduce dead weight, increase the stability of the crane and allow larger loads to be lifted. The diameters of the pulleys are between 250 mm and 1250 mm. The creep phenomenon should be taken into account when designing these pulleys. It is also used as a sealing element in pipe connections.

4. Material preparation and property measurement

The cast Polyamide 6 with the trade name Kestamid was provided by Polikim Ltd., Gebze, Turkey. The resin is produced by Bayer, Germany. It is cut into small pieces: 100x100, 100x150 and 150x150. A1040 steel which is appropriate with DIN 17200 is used for comparison with PA6. The material is analyzed by Yildiz Technical University and these rations of elements are obtained: Fe 96,45%; C 0,423%; Si 0,299%; Mn 0,815%; P 0,0184%; S 0,0154%; Cr 1,11%; Mo 0,204%; Ni

0,179%; Al 0,017%. Our university's CNC Laboratory's CNC Milling Machine Johnford VMC – Model 550 is used for machining. Technical properties of CNC Machine are: Fanuc controlled, three axes, linear and circular tool paths with using ISO programming system are designed. No coolant is used.

For cutting force measurement microprocessor-controlled, Kistler5019b 3-channel charge amplifier and Quartz three-component dynamometer system is used. All functions can also be adjusted and queried via an RS-232C interface. And after getting datas from ISA CIO-DAS1602 I/O board, DynoWare is used as a software. It is particularly suitable for force measurements with Kistler dynamometers and force sensors. An extensive database supports the main charge amplifiers. Measuring chain configurations are automatically tested for correctness. It is particularly suitable for multi-component force measurement such as: Cutting force measurements and general multi-component force measurement (Figure 5).

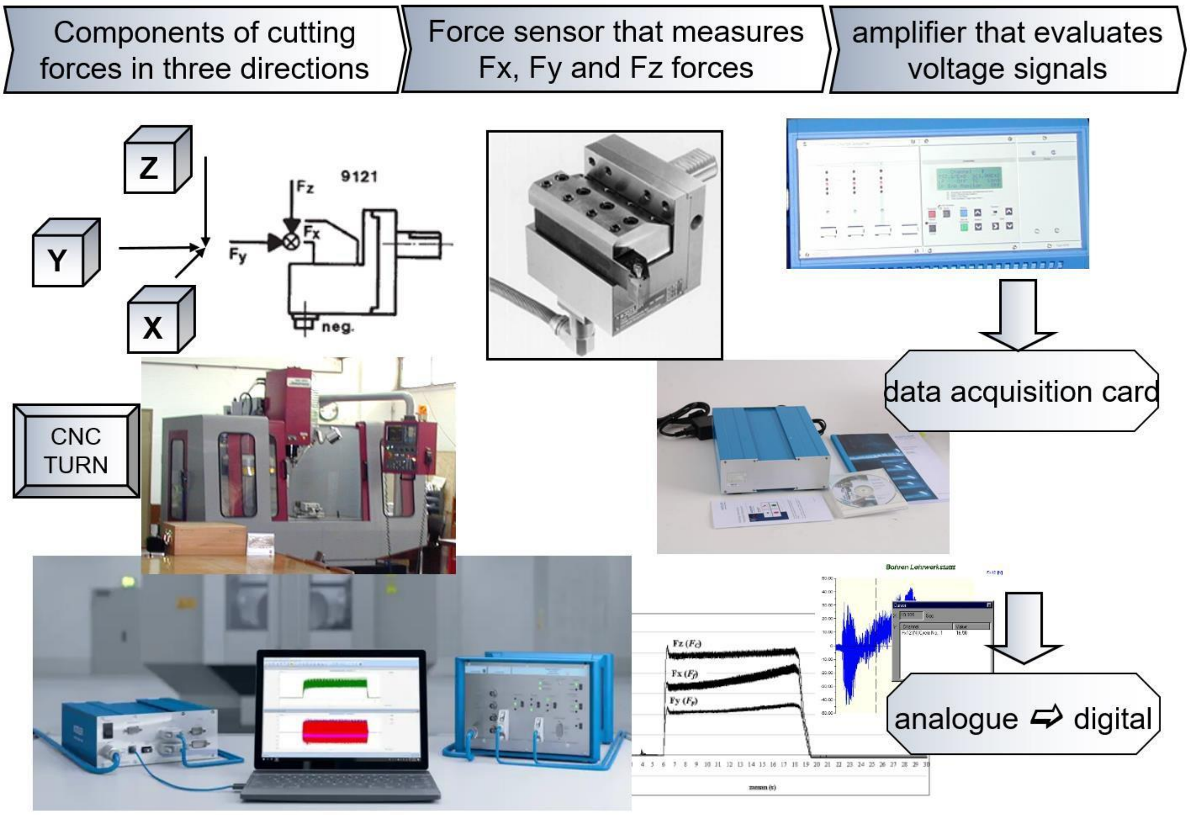
Components of cutting forces in three directions
Force sensor that measures Fx, Fy and Fz forces
amplifier that evaluates voltage signals
Z
Y
X
Fz
9121
Fx
Fy
neg.
CNC TURN
data acquisition card
analogue ⇨ digital
Fz (Fc)
Fx (Ff)
Fy (Fp)

Fig. 5. Dynamometer – amplifier – I/O board- computer program cycle

While machining of material is continuing, heating at intersection of the tool and PA6-steel is measured by OMEGASCOPE Handheld Infrared Thermometer OS532 Series with built-in dot/circle laser sighting. The infrared thermometers offer solutions for many noncontact temperature measurement applications. Emissivity adjustable in 0.01 increments, and the OS530 series provides versatility when measuring a variety of surfaces.

For measuring the vibration SCHENCK VIBROTEST 60 system is used. It is specifically conceived for the purpose of overall vibration, spectrum, process-value and time-based data measurements. VIBROTEST 60 is the realisation of a measuring instrument technically designed for evaluation of machine condition, accurate diagnosis of damage and faults and achievement of the most modern standard for "condition-based" maintenance strategy.

Before milling, both of the materials' surface roughness is measured by MarSurf Perthometer M1 Surface Texture Measuring Instrument to compare the results at the end of milling with linear and circular tool paths. This instrument serves for determining and documenting the most common parameters as per DIN EN ISO/AMSE/prEN 10049 (R_a, R_z, R_{max}, and RP_c). After carrying out a test measurement, periodic and aperiodic profiles can be identified and the cutoff set according to standards automatically Its measuring range is up to 150 µm The roughness profile and measuring record is printed.

The tool we select for machining at CNC machine is a DIN 844 Norm, HSS imperial four flute endmill sizes 10 mm diameter and all the milling operations are done by this tool (Figure 6).

Fig. 6. Endmill used for machining

5. Machining of Polyamide Materials

The most important issue in cutting tools, which are widely used in shaping plastic materials as well as metallic materials, is to perform the process at the lowest possible cost and in the most appropriate way to the required quality expectations. In order to achieve this, the cutting tool material must be selected correctly depending on the properties of the plastic material to be processed and the cutting speed. Cutting tool materials can be briefly divided into three main groups: Metal-based, carbide-based and ceramic-based materials. At the same time, this order also shows the historical development of cutting tool materials. Metal-based tools are used at lower costs but at lower temperatures and speeds. Carbide-based tools are characterized by their high red hardness and high cutting speeds. Ceramic materials, on the other hand, minimize the interaction between the workpiece and the tool material thanks to their mechanical and chemical stability at high temperatures, despite their toughness disadvantages and costs.

When choosing a tool, there are many factors that affect tool life:

1. Process accuracy
2. Choosing the right tool according to the material
3. Using the right amount of cooling water or oil (Water flow, pressure, Oil ratio, etc.)
4. Selection of CNC machine (Machine power, maximum speed and rigidity)
5. The fixture used in the CNC machine should clamp the part rigidly (correctly clamp)
6. The tool should be coated according to the material (coating type, coating thickness)
7. Cutting angles of the tool (The tool's ability to remove chips and also remove heat)
8. Speed and feed given to the tool, cutting speed
9. Holder used for the tool (Shrink and hydraulic holders give good results.)
10. Carelessness while taking measurements (Even taking measurements with a caliper on PCD tools can damage the tool.)

Since the speed did not exceed 1500 rpm in the study, a cylindrical shank right helix, right cutter, and a 10 mm diameter end mill in HSS quality in DIN 844 standard were used.

In this study, cast polyamide 6 and Steel A1040's machinability at CNC machines is compared and all the results are listed. Two toolpaths are selected: Linear and circular. Also feed rates with 100, 150 and 200 mm/min are used in turn in order. Spindle speed was 1000 rev/min and depth was 2 mm. This experiment is done for PA6 and A1040 (Figure 7).

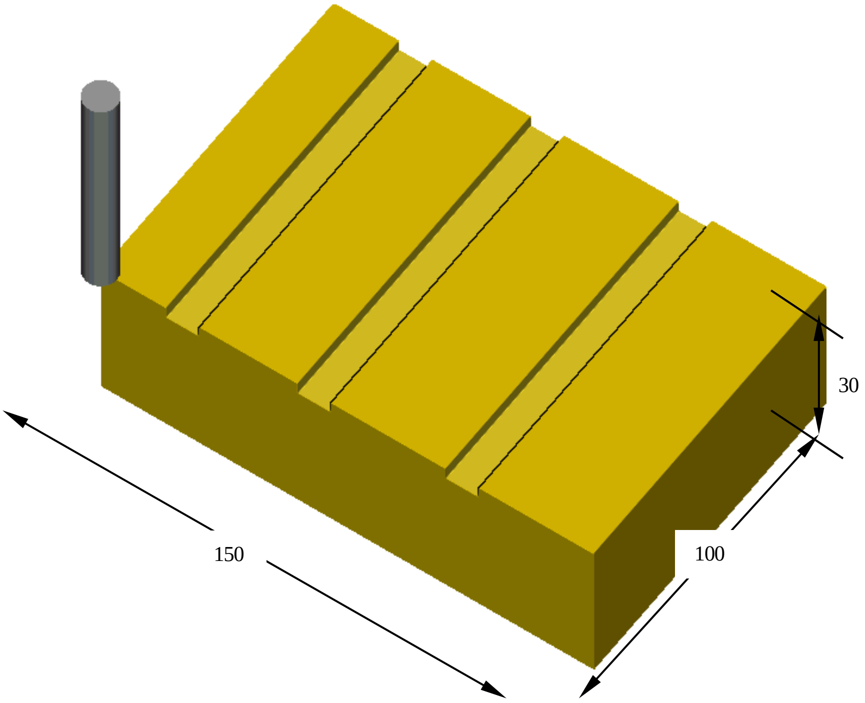

Fig. 7. Measurement of Polyamide and milling with linear toolpaths, feed rates with 100, 150 and 200 mm/min spindle speed: 1000 rev/min.

4. Results

In the first process, both polyamide and metal materials were cut lengthwise; with 100, 150 and 200 mm/min feed, 1000 rpm speed, 2 mm depth of cut, HSS diameter 10 mm end mill. In each of these processes; cutting forces (x, y and z axes), vibration values, temperature changes and obtained surface roughness values were determined graphically and numerically. Then, after milling in the vertical axis direction continued until the middle of the piece, radius (rounding) was made in the counterclockwise direction with a radius of 10 mm and the process was continued in the horizontal axis. Milling was performed with a HSS 10 mm end mill at 100, 150 and 200 mm/min feed, 1000 rpm speed and 2 mm depth of cut. The cutting forces (in x, y and z axes) acting on the workpiece during cutting, vibration values, temperature changes and the obtained surface roughness values were determined graphically and numerically (Figure 8).

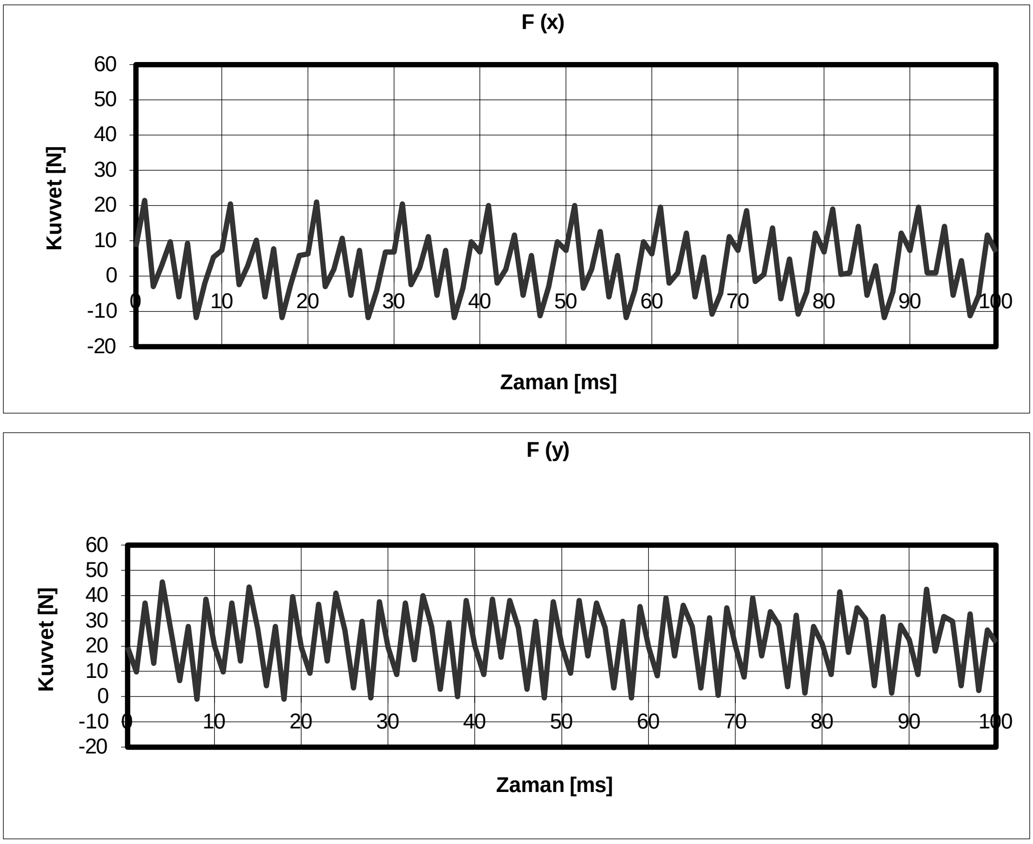

Figure 8. Force graph on X and Y axis of polyamide in linear tool path n: 1000 rev/min,f: 150 mm/min,d: 2 mm

While machining of Polyamide the main problem was wrapping of chips around tool. With low feed rates, chips stay front of the tool that causes temperature increasing, but higher feed rates we didn’t see this problem. Temperature was about 43-65 °C. When we compare PA6 with steel, we can see from diagrams of forces that there is not inappropriate changes. After machining of A1040 the diagrams became different. Temperatures went up to 79 °C and from the diagrams of forces, we consider that the difference between minimum and maximum points were too high. For Z axis because there is little force acting, little changes were recorded (Figure 9).

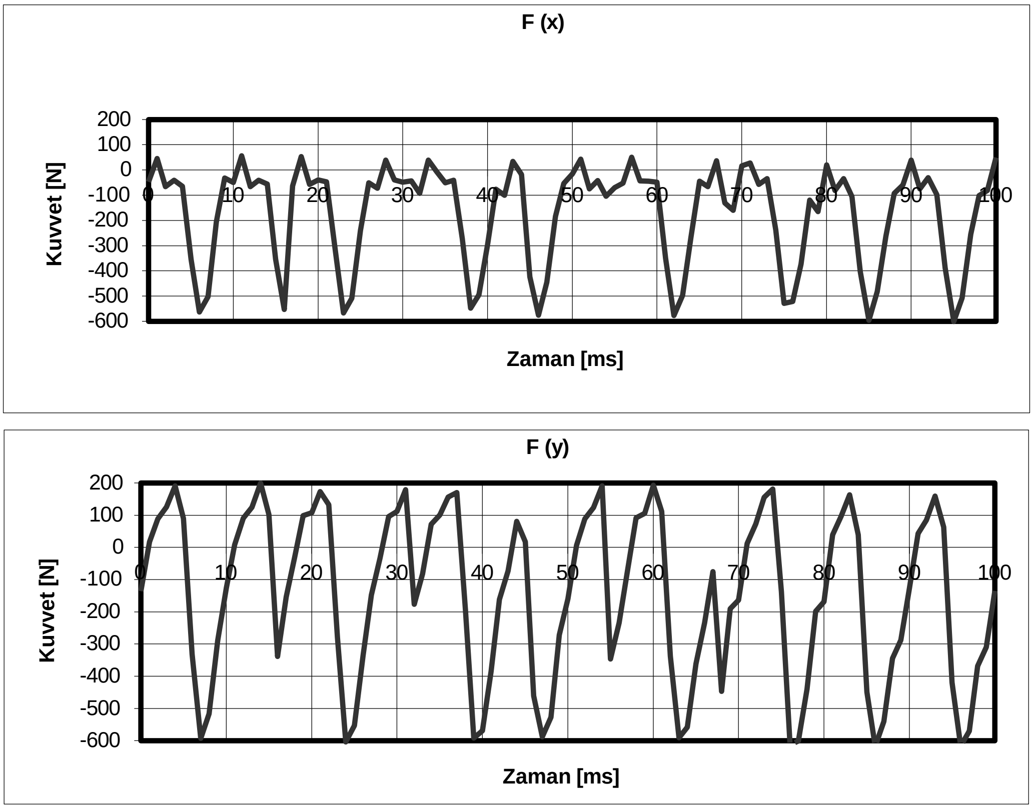

Figure 9. Force graph of A1040 Steel in linear tool path n: 1000 rev/min, f: 150 mm/min,d: 2 mm X and Y axis

The number of processing methods and variants that are available for thermoplastics is now so large that it is difficult to retain an overview of them all. Selecting the correct process has a major influence on the production costs and the attainable molded part quality. A large number of molded parts can be produced in comparable quality by different processes. Apart from the requirements placed on the quality and the design of the molded parts, the choice of process is also influenced by the proposed number of articles, the machines that are already available and the acceptable production costs. The specific advantages and drawbacks of the processes for the two applications in question are compared and discussed. The estimate of the production costs included in these examples reveals the impact of batch size on process selection.

5. Conclusions

Uncommon machining situations may involve adjustments that may have a rigidity defect that must be approached with care, and the programmed speeds and feeds should initially be set to the lowest level. It is always possible to increase these speeds later, with prior knowledge of scientific studies conducted with similar materials and tools, as well as experience gained on the machine where the machining actually takes place.

In addition to machinability, special attention should be paid to the requirements and tolerances given for the surface finish. In such operations, the aim is to obtain a good finish, but it must be remembered that reducing the amount of material removal in order to obtain an unnecessarily high surface quality, also considering the values in this study, would be a waste of time and money. The next point to remember is that a designer may specifically require a "rough" finish, which is the content of the information in the technical drawing and is actually the requirement of the job. The programmer must also ensure that the machine operator is sensible in order to fully appreciate what the machining operations require.

The surface finish is affected by the cutting tool conditions. The tool performance starts to decrease from the moment the tool is first used and eventually becomes ineffective in the final pass. However, there may be temporary results in dimensional characteristics, such as unacceptable vibration, deformation of the work and eventually complete failure of the tool. An inappropriate choice of cutting speeds and feed rates can accelerate this process, so much so that when making decisions in this regard, tool life should be well considered.

It is useful to know when a tool life is reached. For example, replacement will be made before total failure occurs. Very complex CNC machines or equipment that senses the tool conditions automatically, applied to chip removal systems, can give this answer. In the meantime, the part programmer can also consult the literature to decide which speeds and feeds to use to give an acceptable tool life in order to achieve the basic goal of chip removal in the least possible time.

In the machinability test, the issues related to the determination of the above feed rate were strictly followed, and the data can be expressed using two methods for the control of the machine spindle rotation numbers. Both of these have a numerical value, and one expresses a "constant cutting speed" and the other expresses the "machine spindle speed".

The cutting speed, together with factors such as tool life, surface smoothness and the need for chip removal power or machine power consumption, should also give values that are equally satisfactory and provide the highest material removal amounts under these conditions.

In the part cutting process, the height of the workpiece constantly decreases when processing metal materials and polyamide. For this reason, if the spindle rotation number is increased at a varying rate in parallel with this event, only in this case can the chip removal efficiency be maintained. This smoothly changing increase, which ensures that cutting remains very efficient in chip removal for a certain work material, is achieved automatically, that is, automatically, thanks to the ease of programming the constant surface cutting speed.

A suitable example to explain the value of the ease of programming the constant cutting speed is the part cutting process. However, a process where such a facility is used is not an absolutely critical process.

In the study conducted, the factors affecting the cutting speed, such as the type of material, the type of cutting tool, whether or not coolant is used, and the power of the machine, were taken into consideration, and force, vibration, and temperature measurements were made at values where both polyamide and A1040 steel could be processed.

In the study conducted, the cutting forces (in the x, y, and z axes), vibration values, temperature changes, and the obtained surface roughness values were determined graphically and numerically. Accordingly, it was observed that the forces were close to 0 in all three directions and the temperature was between 25-29 °C before starting the cutting process. When polyamide material was used and processing was done on the linear tool path, the jumps at approximately 100 and 500 Hz in the vibration graph indicate the vibration of the machine's servo motor, and since these values were desired to be seen in all graphs, no filtering process was applied

References

Arocha, P., Mehler, C., Puskas, E., & Altsta, V. (2003). Effect of sample thickness on the mechanical properties of injection-molded polyamide-6 and polyamide-6 clay nanocomposites. *Polymer, 44*(2241), 2241–2247.

Avila, F., & Duarte, M. (2003). A mechanical analysis on recycled PET/HDPE composites. *Polymer Degradation and Stability, 80*(373), 373–380.

Bertolini, R., et al. (2020). Machinability of polyamide 6 under cryogenic cooling conditions. *Procedia Manufacturing, 48*(419), 419–427.

Chapleau, N., Favis, B. D., & Carreau, P. J. (2000). Measuring the interfacial tension of polyamide/polyethylene and polycarbonate/polypropylene blends: Effect of temperature. *Polymer, 41*(6695), 6695–6699.

Coldwell, H., Woods, R., Paul, M., Koshy, P., Dewes, R., & Aspinwall, D. (2003). Rapid machining of hardened AISI H13 and D2 moulds, dies and press tools. *Journal of Materials Processing Technology, 135*(301), 301–312.

Demirer, H. O. (1992). *Polyamide modification* (Master’s thesis). ITU, Institute of Science, Istanbul, Türkiye.

Garrella, M., Shih, A., Mac, B., Curziod, E., & Scattergoode, R. (2003). Mechanical properties of nylon bonded Nd–Fe–B permanent magnets. *Journal of Magnetism and Magnetic Materials, 257*(32), 32–44.

Guo, T., Song, M., Hao, J., & Zhang, B. (2001). Compatibility and mechanical properties of polyamide-6/polystyrene/diblock poly(styrene-b-ethylene oxide) copolymer blends. *European Polymer Journal, 37*(241), 241–247.

Huang, H. X., & Liao, C. M. (2002). HDPE/PA6 blends: Parison formation behaviour in extrusion blow molding. *Polymer Testing, 20*(2), 2–6.

Karaküçük, N. (2000). Looking back (materials). *Engineer and Machinery, 34*(3), 3–5.

Kharche, A., & Barve, S. (2023). Experimental investigations of machining parameters on polyamide 6 using single point incremental forming. *Materials Today: Proceedings, 80*(993), 993–1001.

Kim, K., Kang, M., Kim, J., Jung, Y., & Kim, N. (2002). A study on the precision machinability of ball end milling by cutting speed optimization. *Journal of Materials Processing Technology, 130–131*(357), 357–362.

King, D., & Tansey, T. (2002). Alternative materials for rapid tooling. *Journal of Materials Processing Technology, 121*(313), 313–318.

Kohan, M. I. (1995). *Nylon plastics handbook* (pp. 5–45). Verlag, Munich.

Lanza, R., Melkote, S., & Kotnis, M. (2002). Machinability of rapid tooling composite board. *Journal of Materials Processing Technology, 127*(243), 243–247.

Liu, X., Huang, H., Xie, Z., Zhang, Y., Zhang, Y., Sun, K., & Min, L. (2002). EPDM/polyamide TPV compatibilized by chlorinated polyethylene. *Polymer Testing, 22*(9), 9–16.

Mann, D., Van den Bos, J. C., & Way, A. (1999). Chapter 3 - Plastics and reinforcements used in automobile construction. In *Automotive plastics and composites* (2nd ed., pp. 25–60). Elsevier Science.

Mark, H. F., & Geylord, N. G. (1988). Polymer science. In *Encyclopedia of polymer science and technology* (Vol. 2, pp. 332–357). U.S.A.

Palabıyık, İ. M. (2000). *Experimental investigation of mechanical and tribological properties of blends of polyamide 6 (PA6) and high density polyethylene (HDPE) with and without modifier additives* (Master’s thesis). ITU Mechanical Engineering.

Parlar, Z. (2002). *Experimental investigation of the effect of temperature on friction and wear characteristics of polyamide materials* (PhD thesis). ITU Institute of Science.

Pedroso, A. G., Mei, L. H. I., Agnelli, J. A. M., & Rosa, D. S. (2001). The influence of the drying process time on the final properties of recycled glass fiber reinforced polyamide 6. *Polymer Testing, 21*(229), 229–232.

Quitiaquez, P., Cocha, J., Quitiaquez, W., et al. (2022). Investigation of geometric parameters with HSS tools in machining polyamide 6 using Taguchi method. *Materials Today: Proceedings, 49*(181), 181–187.

Rhee, S., & White, J. (2002). Crystal structure, morphology, orientation, and mechanical properties of biaxially oriented polyamide 6 films. *Polymer, 43*(5903), 5903–5915.

Savaşçı, Ö., Uyanık, N., & Akovalı, G. (2002). Plastics and plastic technology in general. PAGEV Publications, Istanbul, Türkiye.

Suarez, A., et al. (2024). Analysis of the machining process of short carbon fiber-reinforced polyamide additive manufactured parts. *Journal of Materials Research and Technology, 30*(3406), 3406–3419.

Taşdemir, M. (2000). Comparison of mechanical properties of first and second hand low density polyethylene/polyamide 6/ethylene vinyl acetate polymer alloy with different ratios. In *Materials 2000 8th Denizli Materials Symposium*, Pamukkale, Turkey.

Xiao, K. Q., & Zhang, L. C. (2002). The role of viscous deformation in the machining of polymers. *International Journal of Mechanical Sciences, 44*.

Yaşar, H. (2001). *The world of plastics* (pp. 5–30). MMO Publications, Istanbul, Türkiye.

Yıldırım, K., Aydın, N., Çelikbilek, A., & Güçer, Ş. (2002). Kaliteli yaşam için teknik tekstiller ve kullanım alanları. *Kimya Teknolojileri, 17*(25), 25–35.

Özpideciler, G. (2003). *Engineering plastics*. Alhan-Çağrı Endüstri A.Ş.

RAYLEIGH INVESTIGATION OF KERF RATIOS IN ABRASIVE WATER JET CUTTING: DIMENSION ANALYSIS AND RAYLEIGH METHOD

İbrahim AY

Chapter 5

Rayleigh Investigation of Kerf Ratios in Abrasive Water Jet Cutting: Dimension Analysis and Rayleigh Method

İBRAHİM AY[1]

1. Introduction

In the Paleolithic Era, humanity developed a method of counting by making notches and scratches on cave or rock walls using wood and bone fragments. In the Neolithic Era, after acquiring the right to land ownership, people began to use weight-measurement units (Ören, 2008). Research by historians indicates that the first efforts to establish measurement standards took place in the Babylonian civilization and later in the Egyptian and Roman civilizations. For instance, the Babylonians used cylindrical sealed weights around 1900 BCE (Koçaş, 2009).

The Egyptians and Romans developed the concepts of dimension and measurement both for financial reasons and for the design and construction of their large structures. However, the ideas of that era were quite complex and ambiguous. During the Renaissance, thoughts on the nature of dimension and measurement evolved significantly with thinkers like Galileo (1564-1642) and Descartes (1596-1650), transforming scientific and philosophical perspectives. Leonardo da Vinci (1452-1519) was a pioneering figure in hydraulic engineering and recognized the importance of physical modeling in describing nature. Later, Newton (1642-1726), Leibniz (1642-1716), and Euler (1707-1783) began to consistently engage with dimensional problems, contributing to the development of physical and mathematical knowledge (Longo, 2021).

With the rapid advancement of scientific studies worldwide, the need for a common system of measurement arose among scientists. The use of

---

[1] Lecturer , Dokuz Eylül University, Türkiye,ibrahim.ay@deu.edu.tr, https://orcid.org/0000-0003-3006-6425

different units made it difficult to compare scientific data, hindering scientific progress. This also led to confusion, disputes, and economic losses in trade. As a result, the International Bureau of Weights and Measures (BIPM) was established with the signing of the Metre Convention by seventeen states in Paris on May 20, 1875. This convention was amended in 1921. By 1960, the International System of Units (SI) was established by a resolution of the 11th General Conference on Weights and Measures (CGPM). SI is used as the preferred unit system worldwide for science, technology, industry, and trade. Brochures published by the BIPM, intended to introduce and explain SI, list decisions related to the metric system that date back to the first CGPM meeting in 1889. There are also non-SI units used globally, which are still employed in certain fields (e.g., the oil barrel) or in some countries (such as inch, foot, yard). The CIPM sees no justification for continuing the use of these units in modern scientific and technical work (BIPM, 2019).

The process of internationally standardizing unit systems is still progressing slowly and causing significant problems. For example, the Mars Climate Orbiter spacecraft, sent to Mars, cost NASA $125 million in damages. This occurred because one of the software programs controlling the thrusters calculated the force in pounds, while another part of the software received the data in newtons. Due to this mismatch, the satellite, which was designed to study the atmosphere and climate of Mars, disintegrated in the planet’s atmosphere in 1999 when an attempt was made to place it into orbit (Longo, 2021; Sarı, 2021).

Today, we measure a physical quantity by comparing it with a known quantity of the same kind. Here, the quantity is expressed as a numerical value along with a unit. A unit is the standard reference value used for measuring a physical quantity, and every quantity has its own unique unit. It makes no sense to express a physical quantity merely as a numerical value, such as stating that the pressure is 180. It could be 180 Pa or 180 bar. 180 bar is 18 000 000 Pa, and the difference is significant.

According to SI, there are 7 fundamental quantities that can be measured directly and are independent of other quantities (BIPM, 2019). These are time, length, mass, electric current, thermodynamic temperature, amount of substance, and luminous intensity (Table 1)

Table 1. Fundamental Quantities, Units, and Dimensions Used in the SI System

Base quantity		Base unit		Symbol for dimension
Name	Typical symbol	Name	Symbol	
time	t	second	s	T
length	l, x, r, vb.	metre	m	L
mass	m	kilogram	kg	M
electric current	I, i	ampere	A	I
thermodynamic temperature	T	kelvin	K	Θ
amount of substance	n	mole	mol	N
luminous intensity	Iv	candela	cd	J

Universal references are used to define these fundamental units, ensuring that measurements taken in different places and at different times are consistent and easily comparable. For example, let’s consider the kilogram. In 1795, Article 5 of the Law on Weights and Measures in France defined units, describing a gram as the weight of a cubic centimeter of ice at its melting point (France, 1795). In 1889, a platinum-iridium mass preserved under specific conditions at the BIPM was defined as the mass of the international prototype of the kilogram, and sources written or published before 2020 describe the kilogram based on this definition. However, today , the kilogram is defined more universally by the Planck constant (BIPM, 2019).

Nonetheless, several non-SI units such as minute, degree, liter, and others, which are widely used and expected to remain in use for a long time, are also accepted by CIPM. Fundamental quantities are organized within the system of dimensions. Each fundamental quantity also represents a dimension, which expresses the physical nature of the quantity.

Other quantities such as area, volume, force, velocity, acceleration, and power are derived by combining fundamental quantities (Table 2).

Table 2. Some Derived Quantities

Derived quantity	Typical symbol of quantity	Derived unit expressed in terms of base units	Dimension Expression
ares	A	m^2	L^2
force (newton)	N	$kg\ m\ s^{-2}$	$M\ L\ T^{-2}$
pressure, stress (pascal)	Pa	$kg\ m^{-1}\ s^{-2}$	$M\ L^{-1}\ T^{-2}$
density	ρ	$kg\ m^{-3}$	$M\ L^{-3}$

The dimensions of these derived quantities are written as the products of the powers of the dimensions of the fundamental quantities. In general, the dimension of any quantity Q is expressed as a dimensional product. This representation helps us understand the more complex relationships of derived quantities.

$$\dim QQ = TT^{\alpha\alpha}LL^{\beta\beta}MM^{\gamma\gamma}II^{\delta\delta}\Theta^{\varepsilon\varepsilon}NN^{\zeta\zeta}JJ^{\eta\eta}$$

Here, α, β, γ, δ, ϵ, ζ, and η are called dimensional exponents, and they can be positive, negative, or zero (BIPM, 2019). For example, the unit of speed is m/s ($m\ s^{-1}$ or $m\cdot s^{-1}$), which dimensionally consists of length (L) and time (T). For speed, α = -1 and β = 1, while the exponents γ, δ, ϵ, ζ, and η are 0.

$$vv = LL\ TT^{-1}$$

Dimensional consistency requires that the exponents of the fundamental dimensions on both sides of an equation be equal. Such an equation is independent of the measurement system used. If two expressions with dimensional consistency are multiplied by or divided by one another, the new equation obtained will also maintain dimensional consistency. However, dimensional consistency may not always hold in the new equation resulting from addition or subtraction operations (Aydın et al., 2020).

To facilitate representation and comprehension, SI units can be multiplied by coefficients that are powers of 10 (BIPM, 2019). For example, instead of expressing 0.005 m, it is clearer to express it as 5 mm, which is 5 times 10^{-3} (milli). Or, instead of writing 60 000 000 Pa, it is more appropriate to express it as 60 MPa, which is 60 times 10^{6} (mega). Some multipliers, along with their names and symbols used in the SI system, are given Table 3.

Table 3. Some SI Prefixes

Name	Symbol	Faktor
giga	G	10^9
mega	M	10^6
kilo	k	10^3
hecto	h	10^2
deca	da	10^1
deci	d	10^{-1}
senti	c	10^{-2}
milli	m	10^{-3}
micro	μ	10^{-6}
nano	n	10^{-9}

2. Dimensional Analysis

Dimensional analysis is a mathematical technique used in the analysis of physical systems to understand how the units of physical quantities are converted and how relationships are determined. In dimensional analysis, homogeneity is an important concept and requires the exponents of the fundamental dimensions on both sides of the equation f(A)=f(B) to be equal.

Although the requirement for the homogeneity of physical formulas was known by Euler and Fourier, its use as a tool was developed in the third quarter of the 19th century through the works of Lord Rayleigh, Bertrand, and Carvallo (Debongnie, 2016; Longo, 2021). One of these works is the "Method of Dimensions" chapter in The Theory of Sound, published in 1877, by John William Strutt (better known as the 3rd Baron, Lord Rayleigh), an important figure in the historical development of dimensional analysis (Strutt, 1877)(Figure 1). Rayleigh was a prominent scientist with contributions and theories in many disciplines, including light, sound, and chemistry, and he was awarded the Nobel Prize in Physics in 1904 for his discovery of argon (Nobel, 1904). Another important work is Bertrand's study titled "On Homogeneity in Physical Formulas (Sur l'homogénéité dans les formules de la physique)," published in 1878 (Bertrand, 1878). Bertrand had also previously worked on the principle of similarity in mechanics (Bertrand, 1848).

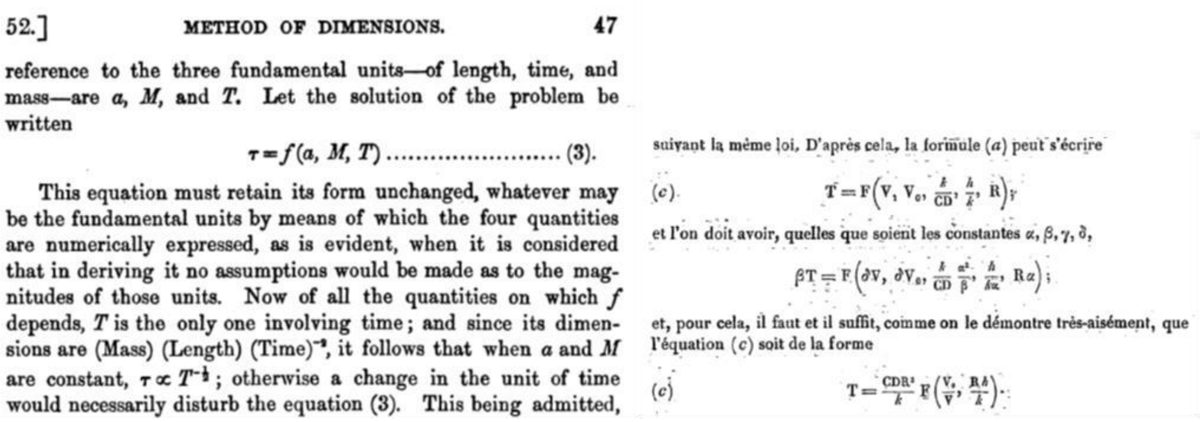

52.] METHOD OF DIMENSIONS. 47

reference to the three fundamental units—of length, time, and mass—are a, M, and T. Let the solution of the problem be written

$$\tau = f(a, M, T) \quad\ldots\ldots\ldots\ldots (3).$$

This equation must retain its form unchanged, whatever may be the fundamental units by means of which the four quantities are numerically expressed, as is evident, when it is considered that in deriving it no assumptions would be made as to the magnitudes of those units. Now of all the quantities on which f depends, T is the only one involving time; and since its dimensions are (Mass) (Length) $(\text{Time})^{-2}$, it follows that when a and M are constant, $\tau \propto T^{-\frac{1}{2}}$; otherwise a change in the unit of time would necessarily disturb the equation (3). This being admitted,

suivant la même loi. D'après cela, la formule (a) peut s'écrire

$$(c) \qquad \mathrm{T} = \mathrm{F}\left(\mathrm{V}, \mathrm{V}_0, \frac{k}{\mathrm{CD}}, \frac{h}{k}, \mathrm{R}\right);$$

et l'on doit avoir, quelles que soient les constantes $\alpha, \beta, \gamma, \delta$,

$$\beta\mathrm{T} = \mathrm{F}\left(\partial\mathrm{V}, \partial\mathrm{V}_0, \frac{k}{\mathrm{CD}}\frac{\alpha^2}{\beta}, \frac{h}{k\alpha}, \mathrm{R}\alpha\right);$$

et, pour cela, il faut et il suffit, comme on le démontre très-aisément, que l'équation (c) soit de la forme

$$(c) \qquad \mathrm{T} = \frac{\mathrm{CDR}^2}{k}\mathrm{F}\left(\frac{\mathrm{V}_0}{\mathrm{V}}, \frac{\mathrm{R}h}{k}\right).$$

Figure 1. Rayleigh on the left (Strutt, 1877) and on the right (Bertrand, 1878)

In 1892, Carvallo and Vaschy aimed to formulate a more general theorem about dimensions (Longo, 2021). Vaschy proposed that every relationship between physical quantities could be reduced to a relationship between dimensionless quantities. According to Vaschy, every meaningful physical equation containing n variables could be rewritten as an equation with n - p dimensionless parameters, where p is the number of fundamental dimensions used (Vaschy, 1892). In 1911, Riabouchinsky (1882–1962) formulated a theorem that yielded practically the same results (Riabouchinsky, 1911).

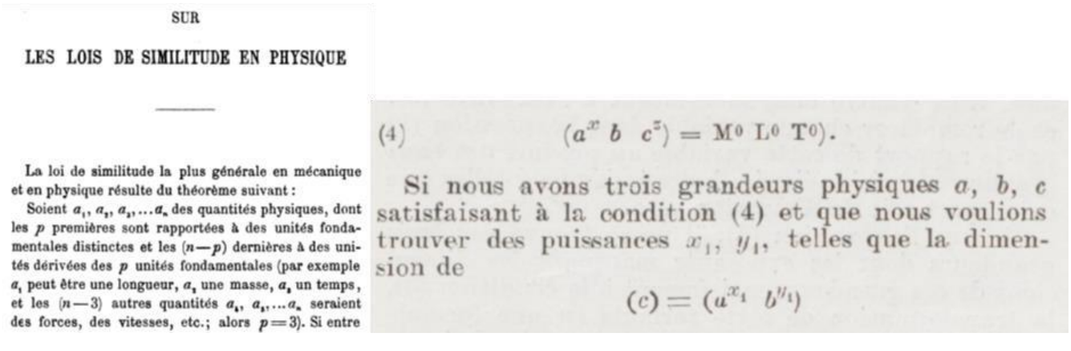

SUR

LES LOIS DE SIMILITUDE EN PHYSIQUE

La loi de similitude la plus générale en mécanique et en physique résulte du théorème suivant :

Soient $a_1, a_2, a_3, \ldots a_n$ des quantités physiques, dont les p premières sont rapportées à des unités fondamentales distinctes et les $(n-p)$ dernières à des unités dérivées des p unités fondamentales (par exemple a_1 peut être une longueur, a_2 une masse, a_3 un temps, et les $(n-3)$ autres quantités $a_4, a_5, \ldots a_n$ seraient des forces, des vitesses, etc.; alors $p = 3$). Si entre

$$(4) \qquad (a^{x}\ b\ \ c^{z}) = \mathrm{M}^0\ \mathrm{L}^0\ \mathrm{T}^0).$$

Si nous avons trois grandeurs physiques a, b, c satisfaisant à la condition (4) et que nous voulions trouver des puissances x_1, y_1, telles que la dimension de

$$(c) = (a^{x_1}\ \ b^{y_1})$$

Figure 2. Left (Vaschy, 1892) and Right (Riabouchinsky, 1911)

The work that popularized the method known today as the Π theorem was published by Buckingham in 1914 (Buckingham, 1914; Debongnie, 2016). In 1915, Rayleigh addressed Boussinesq's heat transfer problem in his article titled "Principle of Similarity" (Strutt, 1915). By calculating the exponents in the equation set $h = a^x \theta^y v^z c^u K^v$ Rayleigh derived the following equation.

$$h = KKKK\theta\,\left(\frac{KKaaaa}{KK}\right)^{zz}$$

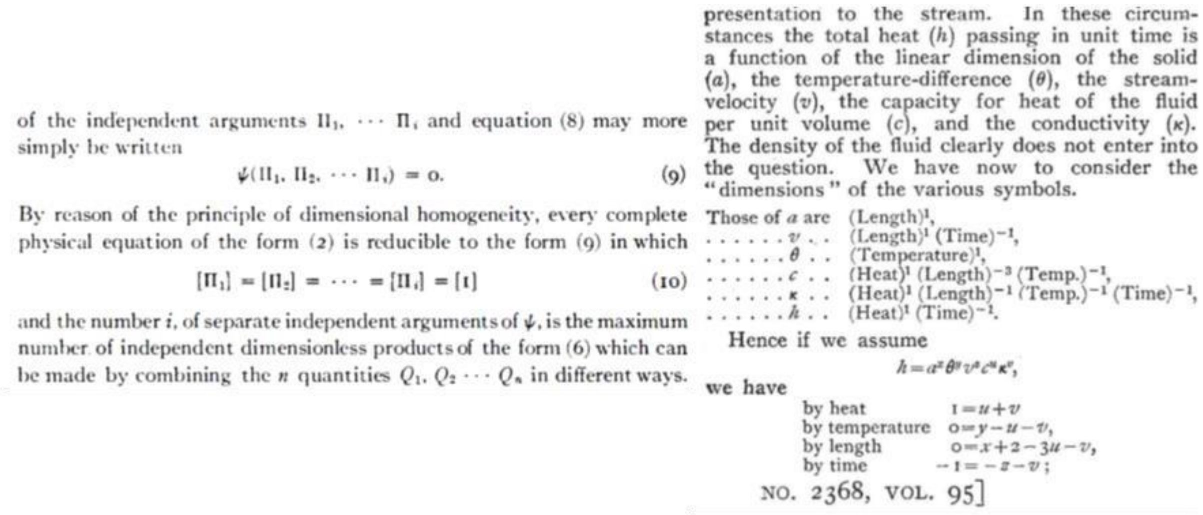

of the independent arguments $\Pi_1, \cdots \Pi_i$ and equation (8) may more simply be written

$$\psi(\Pi_1, \Pi_2, \cdots \Pi_i) = 0. \qquad (9)$$

By reason of the principle of dimensional homogeneity, every complete physical equation of the form (2) is reducible to the form (9) in which

$$[\Pi_1] = [\Pi_2] = \cdots = [\Pi_i] = [1] \qquad (10)$$

and the number i, of separate independent arguments of ψ, is the maximum number of independent dimensionless products of the form (6) which can be made by combining the n quantities $Q_1, Q_2 \cdots Q_n$ in different ways.

presentation to the stream. In these circumstances the total heat (h) passing in unit time is a function of the linear dimension of the solid (a), the temperature-difference (θ), the stream-velocity (v), the capacity for heat of the fluid per unit volume (c), and the conductivity (κ). The density of the fluid clearly does not enter into the question. We have now to consider the "dimensions" of the various symbols.

Those of a are (Length)^1,
. . . . v . . (Length)^1 (Time)$^{-1}$,
. . . . θ . . (Temperature)^1,
. . . . c . . (Heat)^1 (Length)$^{-3}$ (Temp.)$^{-1}$,
. . . . κ . . (Heat)^1 (Length)$^{-1}$ (Temp.)$^{-1}$ (Time)$^{-1}$,
. . . . h . . (Heat)^1 (Time)$^{-1}$.

Hence if we assume

$$h = a^x \theta^y v^z c^u \kappa^v,$$

we have

by heat $1 = u + v$
by temperature $0 = y - u - v$,
by length $0 = x + 2 - 3u - v$,
by time $-1 = -z - v$;

NO. 2368, VOL. 95]

Figure 3. On the left (Buckingham, 1914) and on the right Rayleigh (Strutt, 1915)

We have attempted to illustrate how Rayleigh arrived at the equation in Table 4. The necessary background information can be seen in Figure 3. We will later use this analysis as the Rayleigh Method. Note: In the journal, it appears that "z" has likely been mistakenly printed as "2" in the expression 0=x+z−3u−v for Length.

Table 4. Analytical calculation for Rayleigh's solution.

Heat	Temperature	Length	Time
1 = u + v	0 = y - u - v	0 = x + z - 3u - v	-1 = -z -v
u = 1-v	0 = y - (1-v) - v ile y=1		v = 1-z
u = 1-(1-z) ile u=z			
		0 = x + z - 3z - (1-z) 0 = x + z -3z - 1 + z 0 = x - 1 -z x = 1 + z	
$h = KK^{xx}\,\theta^{y}\,aa^{zz}\,aa^{uu}\,KK^{vv}$ $h = a^{1+z}\,\theta^1\,v^z\,c^z\,K^{1-z}$ $h = a^1 a^z\,\theta^1\,v^z c^z\,\frac{K}{K^z} = Ka\,\theta\,(\frac{avc}{K})^z$			

3. Abrasive Water Jet – AWJ

When high-pressure water is passed through a nozzle with a diameter of 0.1-1.0 mm and directed onto a material from a certain distance, the water hitting the surface removes material particles through the erosion force created, thus performing the cutting process (İ. Ay, 2010). Water jets were first used in the 1800s in the mining industry, primarily in coal washing processes in various countries, particularly Russia, and in gold mines in California between 1853-1856 (Summers, 1995), as well as in the cutting and excavation of relatively soft soils and rocks (Akçın, 1987). The first commercial system related to water jet machines was introduced in 1971 through the efforts of Franz, and was brought to life by McCartney Manufacturing Company, which is now part of the Ingersoll-Rand Corporation. This new water-jet cutting machine was first purchased by Alton Boxboard in 1972 to cut paper tubes in the furniture industry (Grygla, 2007).

In today's industry, abrasive water jets, in which abrasive particles are added to the water in a controlled manner, are most commonly used. Among these abrasives, garnet is the most widely used, although different abrasives such as silica sand and silicon carbide can also be used (Hashish, 1984). Abrasive water jet systems primarily consist of a high-pressure pump, an abrasive reservoir, a cutting head, a motion system, software, and other auxiliary parts. The general structure of the water jet can be seen in Figure 4.

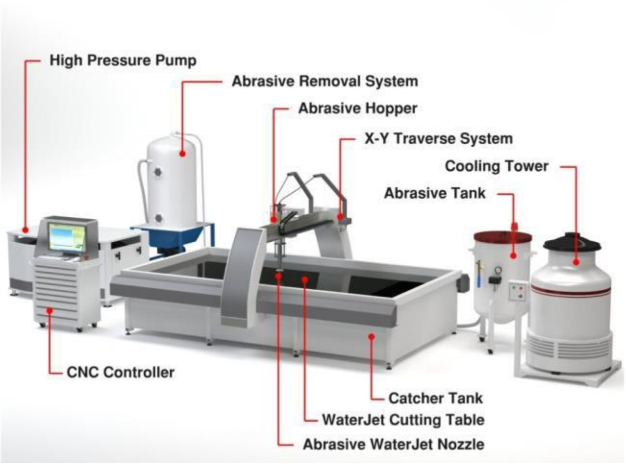

Figure 4. Abrasive Waterjet (Jacobs, 2023)

Since the waterjet process is non-thermal, it is preferred in the industry for cutting heat-sensitive materials (Schwieger et al., 2004) and in risky work areas such as nuclear power plants. For example, in 1999, abrasive waterjet was used for the first time for the dismantling of a nuclear power plant in Kahl, Germany (Louis et al., 2007).

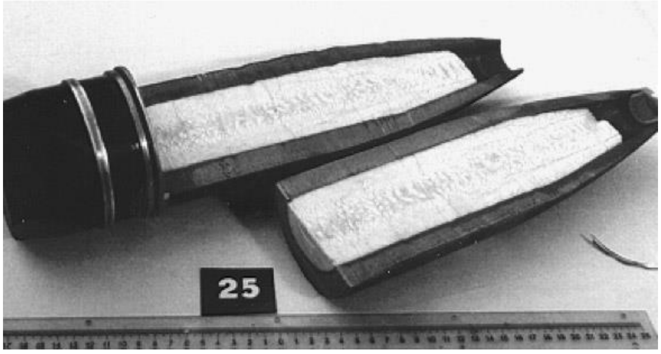

Figure 5. 100 mm TNT antipersonnel shell split in two by water jet (Louis et al., 2007)

Water jet technology can also be applied in other processes such as turning, milling, and drilling. The cutting surfaces of processed materials exhibit a surface roughness of 5-10 μm, with a cutting width of around 1-2 mm. As the cutting depth increases, noticeable waves are observed on the cut surfaces in the opposite direction of the cutting motion. While the upper part of the surface is quite smooth, the lower part becomes rough and wavy. This condition increases the surface roughness. Figure 6 shows the behavior of water during the cutting of PMMA (Polymethyl methacrylate) with a water jet. Here, the cutting speed is 6 mm/s, and the time interval between squares is 0.04 s (Orbanic & Junkar, 2008). Research indicates that the linear marks on the cut surface are directly related to the loss of energy in the jet stream (Akkurt et al., 2002). Improvements in surface quality can be achieved with cutting parameters (optimum parameters) that enhance cutting performance (Akkurt, 2006).

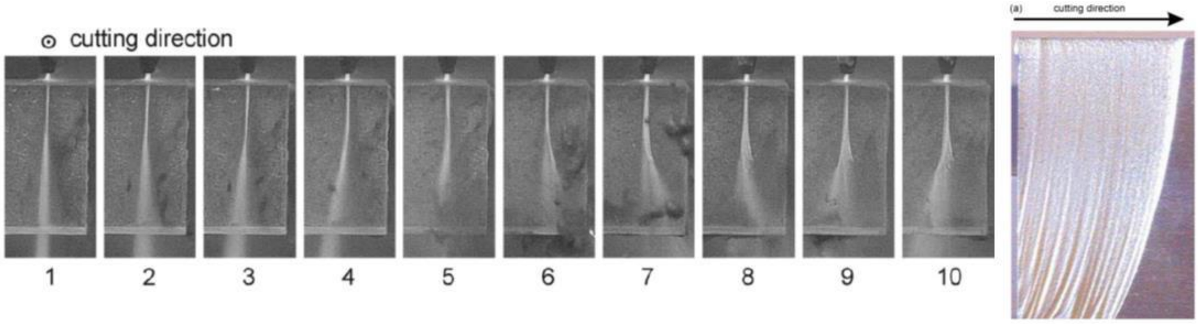

Figure 6. Parabolic behavior of water (Orbanic & Junkar, 2008)

Water at high speeds tends to increase in diameter as it moves away from the nozzle. Therefore, the distance between the workpiece and the nozzle is an important factor in the cut slope. The feed rate also significantly affects the width at which the jet enters and exits the workpiece (Figure 7).

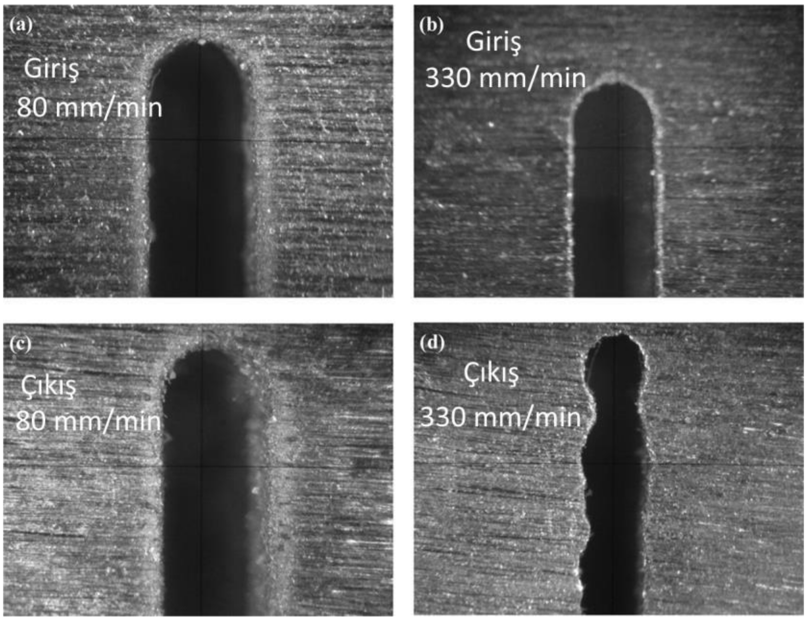

Figure 7. Effect of feed rate on cut width (M. Ay et al., 2010)

One method of evaluating this difference in entry and exit to the workpiece is to calculate the bevel of the cut. The bevel is the difference between the widths of the top cut and the bottom cut divided by twice the height (Figure 8).

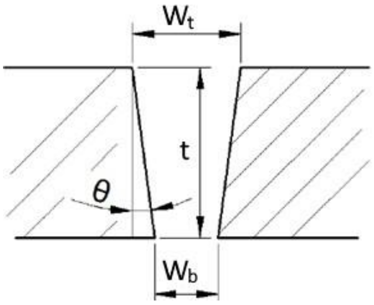

$$\theta = \tan^{-1}\frac{W_t - W_b}{2t}$$

Figure 8. Cut geometry

In abrasive water jet cutting, there are many variables such as water jet pressure, nozzle diameter, the size, shape, density, hardness of the abrasive used, the flow rate of the abrasive, the length of the mixing tube where the abrasive is mixed with water, and the inner diameter of the mixing pipe (Hashish, 2015). In addition to these, the physical, mechanical, and thermal properties of the material are also important variables that affect the process.

4. Regression Analysis

Regression analysis is a statistical method used to examine the relationships between two or more variables. This analysis seeks to understand how a dependent variable (outcome) is influenced by one or more independent variables (inputs). The expression of the relationship between the variables through a mathematical function forms the basis of regression analysis. The function or equation used to show the relationship between two variables is called the regression equation (Özmen et al., 2018). Although such models were developed in the pre-computer era of statistics, they still hold great importance today. This is because linear models, due to their simple structures, are easy to understand and effectively explain how inputs influence the output. This provides a significant advantage, especially when dealing with complex data (Hastie et al., 2009).

A simple linear regression equation can be expressed as follows.

$$YY = ff(XX) + ee$$

Y is the true value, f(x) represents the function to be used for estimation, and e represents the error. We can express a single factor equation with x as the independent variable as follows:

$ff(xx_{ii}) = aa + bbxx_{ii}$

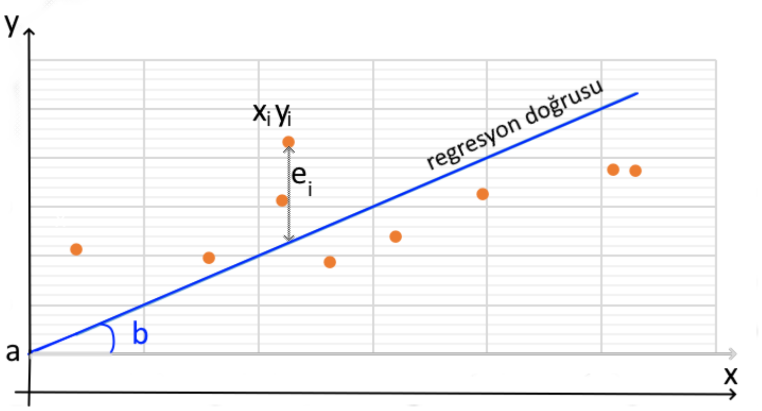

Figure 9. Regression line

The least squares method is generally used to give results close to the true value of Y_i for $f(x_i)$. In a single factor linear model, the coefficients a and b that will minimize the sum of the squared errors Σe_i^2 can be calculated as follows.

$$bb = \frac{\sum_{ii=1}^{nn} (xx_{ii} - x\bar{\bar{x}})(yy_{ii} - y\bar{\bar{y}})}{\sum_{ii=1}^{nn} (xx_{ii} - x\bar{\bar{x}})^2} \quad vvvvyyaa\ bb = \frac{nn \sum xx_{ii}yy_{ii} - \sum xx_{ii} \sum yy_{ii}}{nn \sum_{ii} xx^2 - (\sum xx_{ii})^2}$$

$$aa = y\bar{y} - bbx\bar{\bar{x}}$$

In real life, effects are often not linear. Despite its simplicity, the traditional linear model frequently fails in such cases (Hastie et al., 2009). In these situations, different models and solutions, such as nonlinear regression or logistic regression, are implemented.

Regression equations are generally not homogeneous, as most models include an intercept (constant term) between the dependent and independent variables. This intercept makes the equation non-homogeneous. However, some special cases that only include independent variables can be considered homogeneous.

5. An Attempt to Analyze Kerf Ratio with the Rayleigh Method

In abrasive water jet cutting, the literature mainly examines outcomes such as surface roughness, the widths of the upper and lower kerfs, taper resulting from kerf differences, and the amount of material removed. In these studies, various methods such as regression models, artificial neural network models, and dimensional analysis are used and examined statistically. In the investigation of processing with abrasive water jets, the difference between the entrance and exit kerf widths can be examined using the kerf ratio. That is, the ratio of the upper kerf width (Wt) to the lower kerf width (Wb) can be used (Abdullah et al., 2016; Ambardekar & Shaikh, 2013).

$$r = \frac{W_t}{W_b}$$

The ideal value of the ratio r is 1, which indicates that the cut is taper-free. In this section, the Rayleigh Method will be used to model the kerf ratio. The results of an experimental study will be utilized for modeling, and the model will also be tested on other studies independent of this one.

In the Rayleigh method, the relationship between the primary independent variables, which are considered to influence the studied phenomenon, is expressed as a dimensionally homogeneous exponential function. This expression includes a dimensionless constant term (c). By equalizing the exponents on both sides of the equation based on dimensional homogeneity, the structure of the equation is obtained. The unknown exponents in the equation are determined numerically based on experimental results (Aydın et al., 2020).

The variables we will use in our model are Wk (kinetic power), σ (yield strength of the material), SOD (stand-off distance between the nozzle and workpiece) and TS (traverse speed). σ, SOD and TS are information related to the material and the operation. The energy expended per unit time will be obtained from other known factors related to the operation and used as a variable.

$$r = f(W_k, \sigma, SOD, TS)$$

$$r = C\, W_k^{a}\, \sigma^{b} SOD^{c}\, TS^{d}$$

Table 5. Variables Shaping the Model

	Faktör	Symbol	Unit	Dimension
	Kinetic Power (Theoretical)	W_k	W	ML^2T^{-3}
AWJ properties (in W_k)	Pressure	P	Pa	$ML^{-1}T^{-2}$
	Velocity of water	v_w	$m\cdot s^{-1}$	LT^{-1}
	Velocity of abrasive	Theoretical $v_a \approx v_w$	$m\cdot s^{-1}$	LT^{-1}
	Water mass-flow rate	m_w	$kg\cdot s^{-1}$	MT^{-1}
	Diameter Of Orifice	d_o	m	L
	Density Of Water	ρ_w	$kg\cdot m^{-3}$	ML^{-3}
	Abrasive mass-flow rate	m_a	$kg\cdot s^{-1}$	MT^{-1}
AWJ properties	Traverse Speed	TS	$m\cdot s^{-1}$	LT^{-1}
	Stand off Distance	SOD	m	L
Material properties	Yield Strength	σ	MPa	$ML^{-1}T^{-2}$

Let us assume that the speed of the water is theoretically the same as the speed of the abrasives mixed with the water (Momber, 1998).

$$v_w = \sqrt{\frac{2 \times P}{\rho_w}} \approx v_a$$

The flow rate of the abrasives is known. The flow of water per unit time depends on its density, the diameter of the orifice, and its velocity.

$$\dot{m}_w = \frac{\pi}{4} \times d_o^2 \times \rho_w \times v_w$$

$$\dot{m}_w = \frac{\pi}{4} \times d_o^2 \times \rho_w \times \sqrt{\frac{2 \times P}{\rho_w}}$$

Both water and abrasives have kinetic energy due to their masses and velocities. The energy expended per unit time can be calculated by assuming their velocities are equal to the total mass:

$$W_k = \frac{1}{2} \times (\dot{m}_w + \dot{m}_a) \times v_w^2$$

By incorporating the flow rates and velocities into the equation, we can rearrange it accordingly

$$WW_{kk} = \frac{1}{2} \times \left(\left(\frac{\pi\pi}{4} \times dd_{oo}^{2} \times \rho\rho_{ww} \times \sqrt{\frac{2 \times PP}{\rho\rho_{ww}}}\right) + m\dot{m}_{aa}\right) \times \frac{2 \times PP}{\rho\rho_{ww}}$$

$$WW_{kk} = \left(\frac{\pi\pi}{4} \times dd_{oo}^{2} \times PP \times \sqrt{\frac{2 \times PP}{\rho\rho_{ww}}}\right) + \frac{PP \times m\dot{m}_{aa}}{\rho\rho_{ww}}$$

$$\rho\rho_{ww} \sim 1000\ kkkk\ mm^{-3}\ iiçiiii$$

$$WW_{kk} = \left(\frac{\pi\pi}{4} \times dd_{oo}^{2} \times \sqrt{\frac{PP^{3}}{500}}\right) + \frac{PP \times m\dot{m}_{aa}}{1000}$$

For calculation convenience, if pressure (P) is used in MPa, orifice diameter (do) in mm and flow rate (ma) in g/s, the energy consumed per unit time will be determined in kW.

$$WW_{kk} = \left(\frac{\pi\pi}{4} \times 10^{-6} \times dd_{oo}^{2} \times \sqrt{\frac{10^{18} \times PP^{3}}{500}}\right) + \frac{10^{6} \times PP \times 10^{-3} \times m\dot{m}_{aa}}{1000}$$

$$WW_{kk} = \left(\frac{\pi\pi}{4} \times 10^{-6} \times dd_{oo}^{2} \times 10^{9} \times \sqrt{\frac{PP^{3}}{500}}\right) + \frac{10^{3} \times PP \times m\dot{m}_{aa}}{1000}$$

$$WW_{kk} = 10^{3} \times \left(\left(\frac{\pi\pi}{4} \times dd_{oo}^{2} \times \sqrt{\frac{PP^{3}}{500}}\right) + \frac{PP \times m\dot{m}_{aa}}{1000}\right) \rightarrow 10^{3}\ kkiikkkk$$

To create the equation, variables are written in terms of dimensions.

$$rr = \frac{LL}{LL} = 1 = LL^{0}$$

$$WW_{kk} = MMLL^{2}TT^{-3} = MM^{aa}LL^{2aa}TT^{-3aa}$$

$$\sigma\sigma = MMLL^{-1}TT^{-2} = MM^{bb}LL^{-bb}TT^{-2bb}$$

$$SSSSSS = LL = LL^{cc}$$

$$TTSS = LLTT^{-1} = LL^{dd}TT^{-dd}$$

$$rr = CC\ WW_{kk}^{aa}\ \sigma\sigma^{bb}SSSSSS^{cc}\ TTSS^{dd}$$

$$MM^{0}LL^{0}TT^{0} = (MMLL^{2}TT^{-3})^{aa} \times (MMLL^{-1}TT^{-2})^{bb} \times LL^{cc} \times (LLTT^{-1})^{dd}$$

$$MMMMMMMM\ (MM)\ MM^{0} = MM^{aa}MM^{bb} \rightarrow MM + bb = 0$$

$$LLLLiikkLLh\ (LL)\ iiçiiii\ LL^{0} = LL^{2aa}LL^{-bb}LL^{cc}LL^{dd} \rightarrow 2MM - bb + cc + dd = 0$$

$$TTiimmLL\ (TT)\ iiçiiii\ TT^{0} = TT^{-3aa}TT^{-2bb}TT^{-dd} \rightarrow -3MM - 2bb - dd = 0$$

In a system of 3 equations with 4 unknowns, exponents are determined in a way that they can be expressed with a single exponent.

Table 6. Determining exponents

M	L	T
$aa + bb = 0$	$2aa - bb + cc + dd = 0$	$-3aa - 2bb - \mathrm{d} = 0$
$bb = -aa$		$bb = -aa$ $-3aa - 2(-aa) - dd = 0$ $-3aa + 2aa - dd = 0$ $-aa - dd = 0$ $dd = -aa$
	$dd = bb = -aa$ $2aa + aa + cc - aa = 0$ $2aa + cc = 0$ $cc = -2aa$	

The exponents are substituted into the equation and necessary adjustments are made.

$$rr = \mathrm{C} \times WW_{kk}^{aa} \times \sigma\sigma^{-aa} \times SSSSDD^{-2aa} \times TTSS^{-aa}$$

$$rr = CC \times WW_{kk}^{aa} \times \frac{1}{\sigma\sigma^{aa}} \times \frac{1}{SSSSDD^{-2aa}} \times \frac{1}{TTSS^{-aa}}$$

$$rr = CC \times \left(\frac{WW_{kk}}{\sigma\sigma \times SSSSDD^{2} \times TTSS}\right)^{aa}$$

Control:

$$MM^0LL^0TT^0 = \left(\frac{MMLL^2TT^{-3}}{\mathrm{ML^{-1}T^{-2}} \times LL^2 \times \mathrm{LT^{-1}}}\right)^{aa} = \left(\frac{MMLL^2TT^{-3}}{MMLL^2TT^{-3}}\right)^{aa} = (1)^{aa} = 1$$

Here, C is a dimensionless constant term, and a is the exponent. These two unknowns are determined in a way that fits the experimental results, denoted by r. The variables in the model consist of fundamental units. For calculation convenience, the unit of W_k can be expressed in W, and the unit of σ in GPa. Similarly, when the units of SOD and TS are written in mm, homogeneity is preserved. Giga 10^9, and milli is 10^{-3} (Table 3).

$$MM^0LL^0TT^0 = CC \times \left(\frac{WW_{kk}}{\sigma\sigma \times SSSSDD^2 \times TTSS}\right)^{aa} = \left(\frac{MMLL^2TT^{-3}}{10^9 \times \mathrm{ML^{-1}T^{-2}} \times 10^{-6} \times LL^2 \times 10^{-3} \times \mathrm{LT^{-1}}}\right)$$

$$MM^0LL^0TT^0 = \left(\frac{MMLL^2TT^{-3}}{MMLL^2TT^{-3}}\right)^{aa} = (1)^{aa}$$

The unknown values of C and a in the equation need to be determined as the best-fitting numbers for the experimental results. The dataset is organized as a Taguchi L9 design (

Table 7), and the constants were searched using Nonlinear Regression Analysis with IBM SPSS Statistics (v27) software. The material used in the experimental set to find the model constants is Inconel 718, with a yield strength of 1 100 MPa (1.1 GPa), an orifice diameter of 0.1 mm, and a nozzle diameter of 1.1 mm.

Using the Levenberg-Marquardt algorithm, with initial values of 0 for C and a, the values found were 1.664851 for C and -0.046495 for a.

$$rr = 1.664851 \times \left(\frac{WW_{kk}}{\sigma\sigma \times SSSSDD^{2} \times TTSS}\right)^{-0.046495} \quad SS00 \quad rr$$

$$= 1.664851 \times \left(\frac{\sigma\sigma \times SSSSDD^{2} \times TTSS}{WW_{kk}}\right)^{0.046495}$$

According to the model, as the distance between the nozzle and the workpiece, the material's yield strength, and the feed rate increase, the slope increases, whereas it decreases when the applied power increases. Looking at the power equation (W_k), increasing the pressure, orifice diameter, and abrasive flow rate reduces the slope. Experimental results also show that increases in feed rate and the distance between the workpiece and nozzle increased the slope, while an increase in abrasives reduced it (Figure 10).

Table 7. Experimental Results (İ. Ay, 2010; M. Ay & Ay, 2016)

Pressure	Transverse speed	Abrasive flow rate	Stand off Distance	Kerf top width	Kerf bottom width	Ratio wt/wb
MPa	mm/s	g/s	mm	mm	mm	mm/mm
P	**TS**	**ma**	**SOD**	**wt**	**wb**	**r**
300	1.0000	1.6670	2	1.266	0.988	1.2814
300	1.6667	2.9170	3	1.274	0.945	1.3481
300	2.5000	4.1670	4	1.316	1.042	1.2630
340	1.0000	2.9170	4	1.366	1.084	1.2601
340	1.6667	4.1670	2	1.248	1.016	1.2283
340	2.5000	1.6670	3	1.228	0.868	1.4147
380	1.0000	4.1670	3	1.307	1.117	1.1701
380	1.6667	1.6670	4	1.294	0.921	1.4050
380	2.5000	2.9170	2	1.209	0.923	1.3099

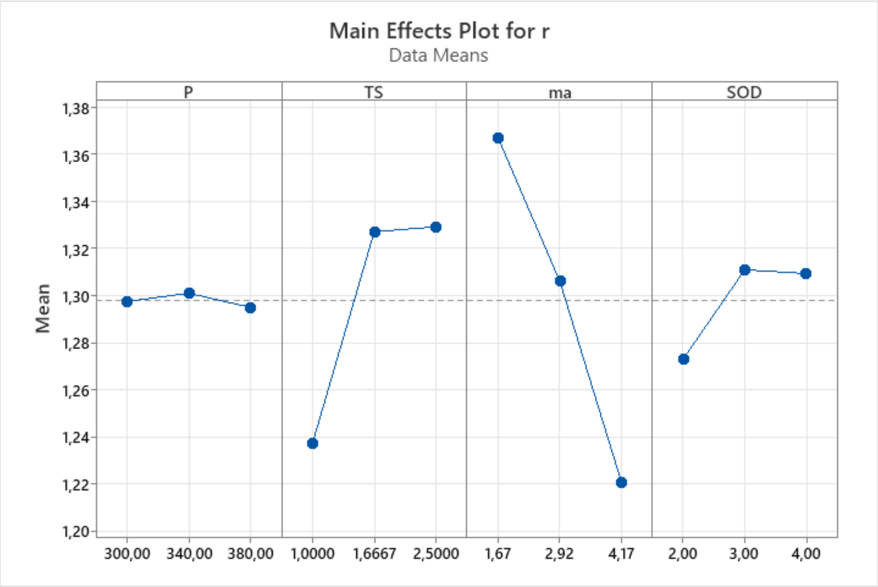

Figure 10. Main effect plot

The model's results will be validated against other datasets independent of the dataset used for analysis. For comparison, a linear regression analysis was performed with the variables used in the model and included in the validation checks. The regression equation obtained with SPSS is as follows:

$$rr = 1.387165 - (7.356 \times 10^{-5} \times WW_{kk}) + (0.016244 \times \mathrm{SOD}) + (0.056571 \times \mathrm{TS})$$

The software excluded the constant variable σ from the dataset.

When σ was added to the model and tested on other data, the results were highly unsatisfactory, so it was deemed appropriate to leave the model as it is.

The predictions and error rates made using the regression and dimensional analysis model are shown inTable 8. The error is calculated as a percentage, with X being the experimental result and Y the predicted value.

$$\%ee = 100 \times \frac{XX - YY}{XX}$$

Example 1. Calculating predictions for experiment:

$$rr = \frac{WW_{tt}}{WW_{bb}} = \frac{1.266\ \mathrm{mm}}{0.988\ \mathrm{mm}} = 1.28138$$

$$WW_{kk} = \left(\frac{\pi\pi}{4} \times 0.1^{2} \times \sqrt{\frac{300^{3}}{500}}\right) + \frac{300 \times 1.667}{1\,000} = 2.3252\ kkWW$$

$$rr_{dddddd} = 1.664851 \times \left(\frac{(1.1\ GGGGGG) \times (2\ mmmm)^{2} \times (1\ mmmm)}{2\,325\ \mathrm{W}}\right)^{0.046495} = 1.24386$$

$$rr_{rrrrrr} = 1.387165 - (7.356 \times 10^{-5} \times 2\,325) + (0.016244 \times 2) + (0.056571 \times 1)$$
$$= 1.305197$$

$$\mathit{DDDDmmDDDDDDDDDDDDDGGDD\ mmDDmmDDDD\ DDrrrrDDrr\ \%DD} = 100 \times \frac{1.28138 - 1.24386}{1.28138} = 2.92\ \%$$

$$\mathit{RRDDRRrrDDDDDDDDDDDD\ DDrrrrDDrr\ \%DD} = 100 \times \frac{1.28138 - 1.305197}{1.28138} = -1.8587\ \%$$

Table 8. . Estimates and absolute % errors

Run No.	Dimensional Model		Regression Model	
	mm/mm		mm/mm	
	r (predictions)	absolute error %e	r (predictions)	absolute error %e
1	1.2439	2.9 %	1.3052	1.9 %
2	1.3135	2.6 %	1.3316	1.2 %
3	1.3665	8.2 %	1.3674	8.3 %
4	1.3072	3.7 %	1.2738	1.1 %
5	1.2478	1.6 %	1.2477	1.6 %
6	1.3370	5.5 %	1.3736	2.9 %
7	1.2568	7.4 %	1.1846	1.2 %
8	1.3379	4.8 %	1.3085	6.9 %
9	1.2701	3.0 %	1.2882	1.7 %

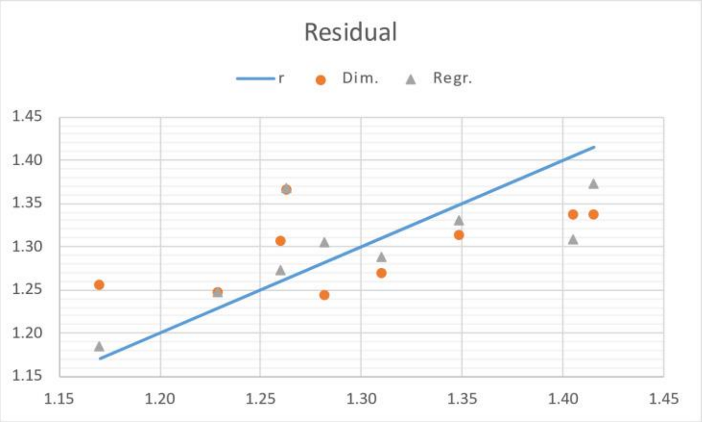

Figure 11. Distances of predictions from experimental results

The smallest error obtained with the dimensional analysis model was 1.6% and the largest error was 8.2%. The smallest error obtained with the regression equation was 1.1% and the largest error was 8.3%. The models were tested with other experiments and the results are given in Table 9.

Table 9. Control of the model with other studies

Studies	Number of experiments	Material	min errors		max errors	
			Dim.	Regr.	Dim.	Regr.
(Sisodia et al., 2024)	20	AISI 440C	19.74 %	22.03 %	60.62 %	60.78 %
(Kumar et al., 2023)	29	Inconel 718	3.04 %	0.17 %	39.72 %	43.03 %
(Rammohan et al., 2022)	27	RHA Steel	2.09 %	1.23 %	29.69 %	48.84 %
(Arun et al., 2021)	9	Dublex 2205 SS	34.02 %	32.69 %	84.31 %	84.59 %
(Shukla & Singh, 2017)	25	AA6351 T6	18.81 %	0.83 %	47.92 %	41.49 %
(M. Ay & Ay, 2016) *for models*	*9*	*Inconel 718*	*1.59 %*	*1.08 %*	*8.20 %*	*8.26 %*

In predictions of cut rates from studies independent of the model setup, the smallest error was 2% and the largest was 84%, while for the regression model, these values were 0.17% and 85%, respectively.

For AISI 440C (Sisodia et al., 2024), the percentage errors of the dimensional model (19.74% minimum, 60.62% maximum) are lower than those of the regression model (22.03% minimum, 60.78% maximum).

In the study on Inconel 718 (Kumar et al., 2023), the percentage error of the regression model (0.17% minimum, 43.03% maximum) gave better results than the dimensional model (3.04% minimum, 39.72% maximum).

For Duplex 2205 SS (Arun et al., 2021), both models show high error percentages. For this material, both the dimensional and regression models provided similar results, but the errors were quite high.

For RHA Steel (Rammohan et al., 2022), the dimensional model performed better (2.09% minimum, 29.69% maximum), while the regression model had a higher maximum error (48.84%).

For AA6351 T6 (Shukla & Singh, 2017), although the regression model had a very low minimum error percentage (0.83%), its maximum error percentage (41.49%) was not better than the maximum error of the dimensional model (47.92%).

6. Conclusion

When evaluating the results, it should not be overlooked that the models established are simple and not complex in structure. In some cases, the dimensional model performed better than the regression model, but for some materials, the regression model achieved lower error percentages. This indicates that the selection of either model should consider their performance across different materials. Additionally, the type and properties of the material are significant factors affecting the effectiveness of these models.

The impact of each factor used in the models on the process outcomes is important. Determining the optimal combination is critical in balancing machining quality, efficiency, and costs. Therefore, optimizing each model according to specific material and process conditions is necessary to achieve the best results.

References

Abdullah, R., Mahrous, A., & Barakat, A. (2016). Surface quality of marble machined by abrasive water jet. *Cogent Engineering*, *3*(1), 1178626. https://doi.org/10.1080/23311916.2016.1178626

Akçın, A. N. (1987). Yüksek Basınçlı Su Jetleri ile Yapılan Kesme ve Parçalama Çalışmaları. *Madencilik*, *26*(2), 27–35.

Akkurt, A. (2006). Aşındırıcılı Su Jeti Uygulamaları ve Üretimde Yoğun Kullanıma Sahip Malzemelerin Delinmesi. *Trakya Univ J Sci*, *7*(2), 161–169. http://fbe.trakya.edu.tr/

Akkurt, A., Şeker, U., & Ercan, F. (2002). Aşındırıcılı Su Jetleri (AWJ) ile İşlemede Enerji Kaybı Olayı: Deneysel Tahmin, Karakterizasyon ve Modellenmesi. *Politeknik*, *5*(2), 137–147.

Ambardekar, V. S., & Shaikh, A. A. (2013). An Investigation on Kerf Geometry for Abrasive Waterjet Cutting of Metal-Polymer-Metal Laminate. *International Journal of Innovative Technology & Adaptive Management (IJITAM)*, *1*(2), 2347–3622.

Arun, M., Sathishkumar, N., Arunkumar, N., Jose, J. J., Fathah, I. A., & Kumar, K. N. (2021). Process parameters optimization in machining of duplex 2205 stainless steel alloy using AWJM technique. *Materials Today: Proceedings*, *46*, 1390–1395. https://doi.org/10.1016/j.matpr.2021.02.491

Ay, İ. (2010). *Süper Alaşımların Aşındırıcılı Sujeti ile İşlenebilirliğinin Araştırılması* [Master, Fen Bilimleri Enstitüsü]. https://tez.yok.gov.tr/UlusalTezMerkezi/tezDetay.jsp?id=FPT0IGDPLrm2uBszwejwtA

Ay, M., & Ay, İ. (2016). The Prediction and Optimization of the Effects of Abrasive Waterjet Cutting Parameters On Kerf. *Acta Physica Polonica A*, *129*(4), 762–766. https://doi.org/10.12693/APhysPolA.129.762

Ay, M., Çaydaş, U., & Hasçalik, A. (2010). Effect of traverse speed on abrasive waterjet machining of age hardened inconel 718 nickel-based superalloy. *Materials and Manufacturing Processes*, *25*(10), 1160–1165. https://doi.org/10.1080/10426914.2010.502953

Aydın, A. F., Erdik, T., Güven, H., Fakıoğlu, M., Akça, M. S., Cengiz, A. İ., & Deneri, E. Z. (2020). *Mühendislikte Fiziksel Modelleme* (İ. Öztürk, H. Özgün, & M. E. Erşahin, Eds.; 1st ed.). Türkiye Su Enstitüsü (SUEN).

Bertrand, M. J. (1848). Note sur La Similitude en Mécanique. *Journal de l'École Polythechnique*, *19*, 189–197.

Bertrand, M. J. (1878). Sur l'homogénéité dans les formules de la physique. *Comptes Rendus*, *86*(15), 916–920.

BIPM. (2019). *The International System of Units (SI): Vol. (updated in 2024)* (9th ed.). Bureau international des poids et mesures. https://www.bipm.org/en/publications/si-brochure

Buckingham, E. (1914). On Physically Similar Systems; Illustrations of the use of Dimensional Equations. *Physical Review*, *4*(4), 345–376. https://doi.org/10.1103/PhysRev.4.345

Debongnie, J.-F. (2016). *Sur le Théorème de Vaschy-Buckingham*. http://hdl.handle.net/2268/197814

France. (1795). *Loi Relative aux poids et mesures. Du 18 germinal, an 3.e de la République française, une et indivisible*.

Grygla, S. M. (2007). *An Investigation of Methods to Homogeneously Entrain and Suspend Abrasive Particles in a Low Pressure Dental Water Jet* [Master, Brigham Young University]. https://scholarsarchive.byu.edu/etd/1303/

Hashish, M. (1984). A modeling study of metal cutting with abrasive-waterjets. *Transactions of the American Society of Mechanical Engineers - ASME*, *106*, 88–100.

Hashish, M. (2015). WaterJet Machining Process. In A. Y. C. Nee (Ed.), *Handbook of Manufacturing Engineering and Technology* (pp. 1651–1686). Springer London. https://doi.org/10.1007/978-1-4471-4670-4_75

Hastie, T., Tibshirani, R., & Friedman, J. (2009). *The Elements of Statistical Learning* (2nd ed.). Springer New York. https://doi.org/10.1007/b94608

Jacobs, P. (2023, November 21). *Waterjet Machine*. İmage. https://www.cncmasters.com/cnc-waterjet-buyers-guide/

Koçaş, İ. (2009). Ölçü Birimleri ve Metroloji. *Bilim ve Teknik*, 28–33.

Kumar, A., Kumar, P., & Kumar, R. (2023). A study of kerf quality of Inconel 718 using abrasive water jet cutting. *Materials Today: Proceedings*, *81*, 261–266. https://doi.org/10.1016/j.matpr.2021.03.185

Longo, S. G. (2021). *Principles and Applications of Dimensional Analysis and Similarity*. Springer International Publishing. https://doi.org/10.1007/978-3-030-79217-6

Louis, H., Pude, F., von Rad, Ch., & Versemann, R. (2007). Abrasive Water Suspension Jet Technology Fundamentals, Application and Developments. *Welding in the World*, *51*(9–10), 11–16. https://doi.org/10.1007/BF03266595

Momber, A. W. (1998). The kinetic energy of wear particles generated by abrasive–water-jet erosion. *Journal of Materials Processing Technology*, *83*(1–3), 121–126. https://doi.org/10.1016/S0924-0136(98)00050-8

Nobel. (1904). *The Nobel Prize in Physics 1904*. Nobel Prize Outreach AB. https://www.nobelprize.org/prizes/physics/1904/summary/

Orbanic, H., & Junkar, M. (2008). Analysis of striation formation mechanism in abrasive water jet cutting. *Wear*, *265*(5–6), 821–830. https://doi.org/10.1016/j.wear.2008.01.018

Ören, H. (2008). *Eski Yakındoğu'da Ölçü Birimleri*. Unpublished Master's Thesis, Sosyal Bilimler Enstitüsü, Pamukkale Üniversitesi, Pamukkale.

Özmen, A., Er, F., Atlas, M., Aslanargun, A., Peker, K. Ö., Şıklar, E., & Sönmez, H. (2018). *İstatistik* (A. Özmen & B. F. Şeniş, Eds.). Anadolu Üniversitesi.

Rammohan, S., Kumaran, S. T., Uthayakumar, M., Korniejenko, K., Nykiel, M., & Velayutham, A. (2022). Prediction of Abrasive Waterjet Machining Parameters of Military-Grade Armor Steel by Semi-Empirical and Regression Models. *Materials*, *15*(12). https://doi.org/10.3390/ma15124368

Riabouchinsky, D. (1911). Méthode des Variables de Dimension Zéro, et son Application en Aérodynamique. *L'Aérophile*, *1*, 407–408.

Sarı, H. (2021, December 14). *Fizikte Boyut ve Birimler*. Bilim ve Genç TÜBİTAK. https://bilimgenc.tubitak.gov.tr/makale/fizikte-boyut-ve-birimler

Schwieger, K., Carrero, V., Rentzsch, R., Becker, A., Bishop, N., Hille, E., Louis, H., Morlock, M., & Honl, M. (2004). Abrasive Water Jet Cutting as a New Procedure for Cutting Cancellous Bone - In Vitro Testing in Comparison with the Oscillating Saw. *Journal of Biomedical Materials Research Part B: Applied Biomaterials*, *71B*(2), 223–228. https://doi.org/10.1002/jbm.b.10078

Shukla, R., & Singh, D. (2017). Experimentation investigation of abrasive water jet machining parameters using Taguchi and Evolutionary optimization techniques. *Swarm and Evolutionary Computation*, *32*, 167–183. https://doi.org/10.1016/j.swevo.2016.07.002

Sisodia, V., Gupta, S. K., Salunkhe, S., Murali, A. P., & Kumar, S. (2024). An Experimental Investigation on Machining of Hardened AISI 440C Stainless Steel Using Abrasive Water Jet Machining Process. *Journal of Materials Engineering and Performance*, *33*(2), 961–977. https://doi.org/10.1007/s11665-023-08040-y

Strutt, J. W. B. R. (1877). *The Theory of Sound* (1st ed., Vol. 1). Macmillan and Co.

Strutt, J. W. B. R. (1915). The Principle of Similitude. *Nature*, *95*(2368), 66–68. https://doi.org/10.1038/095066c0

Summers, D. A. (1995). *Waterjetting Technology*. Taylor & Francis. https://doi.org/10.1201/9781482294828

Vaschy, A. (1892). Sur Les Lois De Similitude En Physique. *Annales Télégraphiques*, *19*, 25–28.

INNOVATIONS IN AGRICULTURAL MACHINERY: ARTIFICIAL INTELLIGENCE, ROBOTICS, AND SUSTAINABILITY

Mehmet ÇEVİK

Chapter 6

Innovations in Agricultural Machinery: Artificial Intelligence, Robotics, and Sustainability

MEHMET ÇEVİK[1]

1. Introduction

The evolution of agricultural machinery reflects the broader transformation of farming from manual labour to a highly mechanized industry. Initially, farming relied heavily on basic hand tools such as hoes, sickles, and plows. These tools, though labour-intensive, were essential in shaping early agriculture and were often powered by human or animal labour. The reliance on manual effort meant limited farm productivity and inefficiency, with small-scale operations and lower crop yields.

The 19th-century Industrial Revolution marked a significant turning point in agricultural machinery development. Steam-powered engines were introduced, enabling the creation of larger and more complex machines like steam tractors and threshing machines.

This period saw the beginning of mechanized plowing, planting, and harvesting, which significantly reduced the labour required and increased the speed and scale of farming operations.

The 20th century saw the rise of motorized equipment, with gasoline and diesel-powered tractors revolutionizing agriculture by enabling larger, more efficient farming operations. Tractors became multipurpose machines, capable of pulling various implements like plows, seeders, and cultivators. The advent of combine harvesters, which could simultaneously harvest and thresh crops, further boosted farm productivity. Innovations such as mechanized irrigation systems also allowed for more precise water management, contributing to higher yields.

Today, agricultural machinery incorporates advanced technologies such as GPS, sensors, and robotics.

---

[1] Prof. Dr., İzmir Kâtip Çelebi University, Türkiye, mehmet.cevik@ikcu.edu.tr

ORCID: 0000-0002-6366-5566

GPS-guided tractors and precision planters allow for precise seed placement, reducing waste and optimizing field use. Automated systems for harvesting, spraying, and even autonomous machinery are transforming farms into highly efficient, data-driven operations. The integration of artificial intelligence (AI) and machine learning (ML) has enabled predictive maintenance, further enhancing the reliability and lifespan of modern machinery.

The mechanization of agriculture has led to a massive increase in farm productivity. Where once farming required extensive human labour, machines now perform the bulk of the work, allowing for larger-scale operations and higher yields. Mechanization has also increased efficiency, reducing the time and resources needed to plant, tend, and harvest crops. As a result, food production has risen to meet the demands of growing populations, while technological advances have enabled sustainable and precision farming practices that conserve resources and reduce environmental impact.

This evolution of agricultural machinery continues to shape the future of farming, leading to smarter, more sustainable agricultural practices.

2. Precision Agriculture Tools

Precision agriculture has emerged as a game-changing approach to farming, leveraging advanced technology and data analytics to optimize farming operations at an unprecedented scale. Central to this innovation are specialized machinery like GPS-guided tractors, automated seeders, and planters, which have revolutionized how farmers manage their fields.

2.1. GPS-Guided Tractors

One of the most significant advancements in precision agriculture is the use of GPS-guided tractors. These machines are equipped with GPS systems that allow them to navigate fields with pinpoint accuracy, often within a few centimetres (Santana-Fernández et al., 2010). By following precise routes, these tractors minimize overlaps and gaps during planting, fertilizing, and harvesting. This reduces fuel consumption, labour costs, and wear and tear on equipment. Additionally, GPS-guided systems ensure even distribution of inputs like seeds, fertilizers, and pesticides, leading to more efficient use of resources (Cheema et al., 2023).

2.2. Automated Seeders and Planters

Automated seeders and planters are designed to optimize the planting process by controlling the depth and spacing of seeds with high precision. These machines can be programmed to adjust planting density based on soil conditions, moisture levels, and crop requirements. This precision ensures that each seed is placed at the ideal depth and spacing, reducing competition among plants and improving germination rates. By using automated systems, farmers can achieve uniform crop growth and optimize field use, leading to higher yields and more consistent crop quality.

Amer et al. (2020) developed an automated planting machine tailored for Palestinian agriculture, designed to enhance planting speed and precision by accurately transplanting seedlings according to local plant dimensions and spacing requirements. Simulation and experimental results confirmed the prototype's effectiveness in performing smooth and precise planting operations, from plowing to covering the soil. Mukherjee et al. (2021) developed the Agri-bot, a cloud-connected device with remote control capabilities. The bot was programmed to operate for specific periods to plant seeds and cover the field, while also monitoring and displaying soil moisture levels onboard.

2.3. Resource Optimization and Waste Reduction

One of the core benefits of precision agriculture machinery is the optimization of resource use. By integrating data from sensors, weather reports, and soil analyses, these machines can tailor their operations to the specific needs of different areas within a field. For example, variable-rate technology can adjust the amount of fertilizer or pesticide applied in real-time, ensuring that only the necessary amount is used. This reduces input costs, minimizes environmental impact, and prevents the over-application of chemicals, which can degrade soil health. Maraveas et al. (2022) reviewed recent literature on the role of Internet of Things (IoT) in Agriculture 4.0, focusing on challenges and future prospects for developing nations. The review emphasizes how IoT can aid in resource optimization and waste reduction, offering potential benefits for countries with limited resources for precision agriculture technologies.

2.4. Yield Improvement

The control enabled by GPS-guided tractors and automated machinery ensures consistent crop growth, leading to healthier plants and increased yields. By optimizing planting density, reducing input waste, and ensuring that crops receive the right amount of nutrients and protection, farmers can maximize the potential of their land. Furthermore, real-time monitoring and data collection allow for quick adjustments in response to changing conditions, preventing yield losses due to drought, pests, or nutrient deficiencies. Javaid et al. (2022) provided an overview of Agriculture 4.0, detailing key technologies and specific domains within smart farming. They highlighted how these technologies, including digitized equipment and cloud computing, streamline operations, improve yield, and coordinate machinery to assess processing conditions and input needs.

3. Drones and UAVs in Agriculture

There is a growing body of research on the use of drones and unmanned aerial vehicles (UAVs) in agriculture. These studies explore various applications, including crop monitoring, precision farming, and soil analysis. Drones are utilized for their ability to collect high-resolution images and data, which can be used to assess crop health, monitor irrigation, and optimize the use of fertilizers and pesticides. An example of drones used in agriculture is shown in Figure 1.

Maslekar et al. (2020) highlighted that modern agricultural practices leverage IoT, remote sensing, and UAVs for enhanced crop management, with UAVs providing high-resolution images to identify and control pests even in rugged terrains, surpassing the capabilities of traditional pest management tools. del Cerro et al. (2021) provided an overview of unmanned aerial vehicles (UAVs) in agriculture, including their historical development, classification, common applications, advantages, and relevant civil drone legislation affecting agricultural use. Velusamy et al. (2022) reviewed successful techniques for precision crop monitoring and pest management using UAVs, assessing various UAV types and their applications for early disease detection, and discussing the deployment of remote sensing technologies and their quality of service.

Figure 1. Drones in agriculture. Source: agtech.folio3.com

Abbas et al. (2023) discussed how drones, with their high spatial resolution and efficiency, are increasingly used for early detection and monitoring of plant diseases, offering significant advantages over traditional methods by providing rapid, high-resolution data and potentially reducing manual labour and costs in agriculture.

The following subsections highlight some of the significant research and findings in this field, demonstrating how UAVs are revolutionizing agricultural practices by enhancing efficiency and accuracy in farm management.

3.1. Crop Monitoring

Drones equipped with high-resolution cameras capture detailed images of crops, allowing farmers to monitor their health visually. These images can be used to detect issues such as pest infestations, disease outbreaks, or nutrient deficiencies. Early identification of these problems enables targeted interventions, reducing the need for broad-spectrum treatments (Namani & Gonen, 2020). These specialized cameras capture data beyond the visible spectrum, including near-infrared and red-edge wavelengths.

Multispectral cameras can assess plant health by analysing light reflectance patterns, which indicate chlorophyll content and other health indicators. Hyperspectral cameras provide even more detailed information, allowing for the identification of specific plant stress factors.

3.2. Crop Health Analysis

Drones frequently use vegetation indices like the Normalized Difference Vegetation Index (NDVI) to evaluate plant health. NDVI is derived from the ratio of near-infrared to visible light reflected by plants, with healthy vegetation reflecting more near-infrared light and less visible light. In contrast, stressed or unhealthy plants reflect less near-infrared light. This index is instrumental in creating detailed health maps of crops.

4K drones, which offer a resolution of 3840 x 2160 –four times that of 1080p– are employed for this purpose. These drones are equipped with dual high-resolution RGB cameras and a multispectral sensor that captures data across various wavelengths. This combination enables precise crop health analysis and monitoring. Farmers use these 4K drones to perform regular crop health surveys. For example, if certain areas are found to have lower NDVI values, targeted treatments such as additional fertilization or pest control can be applied where necessary, enhancing crop yield and reducing the need for blanket applications of inputs. Additionally, by capturing images at different growth stages, drones can track crop development over time. This temporal data offers insights into growth patterns and aids in predicting optimal harvest times.

3.3. Irrigation Management

Drones equipped with thermal sensors measure surface temperatures, which correlate with soil moisture levels. Areas of the field with higher temperatures often indicate lower moisture levels. By creating detailed moisture maps, drones help identify zones in need of irrigation or suffering from overwatering.

Some advanced systems integrate thermal imaging with GIS (Geographic Information Systems) to create real-time irrigation management maps. These maps guide precision irrigation systems to adjust water application rates based on specific field needs.

3.4. Irrigation System Inspection:

Drones can fly over irrigation infrastructure to inspect for leaks, blockages, or malfunctions. Visual and thermal imaging can reveal issues such as broken pipes or malfunctioning sprinkler heads, allowing for timely repairs and maintenance. By analysing the coverage patterns of sprinklers or drip irrigation systems, drones help ensure that water is distributed evenly. This analysis can identify areas with poor coverage or excessive runoff, enabling adjustments to improve efficiency.

3.5. Soil Health Assessment

Drones equipped with specialized sensors or imagery can help map soil composition across a field. This includes identifying variations in soil texture, organic matter content, and nutrient levels. These maps are essential for precision agriculture as they guide soil management practices such as targeted fertilization and amendment applications. Drones can capture images and data to assess soil erosion patterns and compaction issues. Erosion can be identified through changes in surface features, while compaction can be inferred from vegetation stress or growth anomalies. This information supports soil conservation efforts and helps in designing effective soil management strategies.

3.6. Field Variability Analysis

Drones create detailed topographic maps that show elevation changes within a field. This information is crucial for understanding water flow patterns, which can influence erosion, drainage, and irrigation planning. By analysing aerial data, drones help in selecting representative soil sampling locations. This ensures that soil tests are conducted in areas that accurately reflect field variability, leading to more precise recommendations for soil treatments.

3.7. Advantages of Drones in Agriculture

- **Rapid Data Collection:** Drones can cover large areas quickly, providing comprehensive data with minimal manual effort. This reduces the time and labour involved in traditional field surveys.

- **Reduced Costs:** By optimizing resource use based on detailed data, drones help reduce costs associated with fertilizers, pesticides, and water. This not only lowers input costs but also minimizes environmental impact.
- **Immediate Feedback:** Drones provide real-time data, allowing farmers to make prompt decisions. For instance, if a pest infestation is detected, corrective measures can be taken before the problem spreads.
- **Enhanced Decision-Making:** The detailed, high-resolution data collected by drones supports more informed decision-making, leading to better management practices and improved crop outcomes.

4. Robotics in Farming

The use of robots and autonomous equipment in agriculture represents a significant advancement in farming technology, offering solutions for tasks such as harvesting, weeding, and planting. These innovations have the potential to dramatically reduce labour costs, increase efficiency, and enhance overall productivity on farms (Ünal & Topakci, 2015). Yépez-Ponce et al. (2023) reviewed the use of mobile robotics in smart farming, highlighting their benefits in reducing costs, environmental impact, and optimizing harvests. The article discussed current technologies, algorithms, and results, while addressing challenges such as environmental conditions, costs, and technical requirements, and concluded with the potential for a fully autonomous, low-cost agricultural mobile robotic system.

4.1. Robotic Harvesters

Robotic harvesters are designed to autonomously pick fruits, vegetables, and other crops. An autonomous fruit-picking machine is a type of orchard robot, primarily used for apple harvesting, and is evaluated based on four criteria: speed, accuracy, intelligence, and durability. While current robots are slower than humans, they can operate 24/7, ultimately improving efficiency over time. Accuracy is constantly improving through advancements in visual processing and robotic technology. The most intelligent robots can adapt to changing environmental conditions, though human workers are still needed for problem solving. Durability is crucial, as machines must be robust and weather-resistant to be effective long-term.

Equipped with advanced sensors, cameras, and ML algorithms, these robots can identify ripe produce, determine the optimal picking technique, and handle the crops delicately to avoid damage. The Octinion Rubion (see Figure 2), for example, uses a soft robotic gripper to gently pick strawberries.

By automating the harvesting process, these robots reduce the need for manual labour, which is especially beneficial in regions facing labour shortages. They also operate around the clock, leading to faster harvesting times and reduced crop loss.

4.2. Weeding Robots

Weeding robots utilize a combination of cameras, sensors, and AI to differentiate between crops and weeds. They can either mechanically remove weeds or apply targeted herbicides, minimizing the impact on desirable plants.

Some commercial examples of weeding robots include the Oz robot (see Figure 3) by Naïo Technologies, which utilizes a combination of GPS and machine vision to navigate fields and remove weeds. Similarly, the EcoRobotix weeding robot (see Figure 4) uses precision spraying to target weeds, minimizing herbicide use and reducing environmental impact. Laser weeding robots have been developed and are now being actively utilized in agricultural fields. Zhu et al. (2022) designed a YOLOX-based weeding robot that uses a blue light laser for non-contact weed removal in cornfields, featuring a tracked mobile platform, weed identification system, and a five-degree-of-freedom robotic arm for precise laser targeting. The robot distinguishes weeds from corn seedlings using plant texture and shape, calculates weed coordinates via monocular ranging, and eliminates the weeds with the laser.

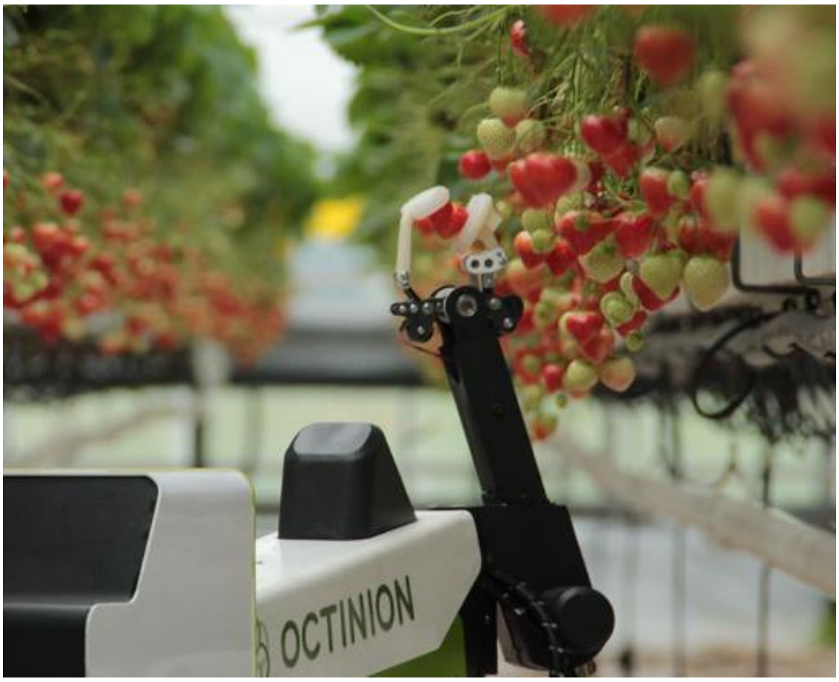

Figure 2. Octinion Rubion strawberry picking robot.
Source: octinion.com/strawberry-picker

These robots reduce the need for manual weeding, which can be labour-intensive and time-consuming. They also help in reducing the overall use of herbicides, leading to more sustainable farming practices.

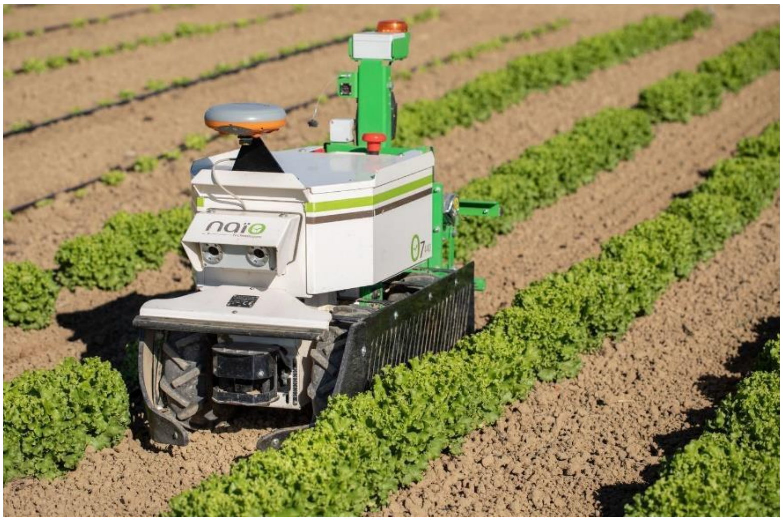

Figure 3. Naïo Technologies' Oz robot. Source: naio-technologies.com/en/oz/

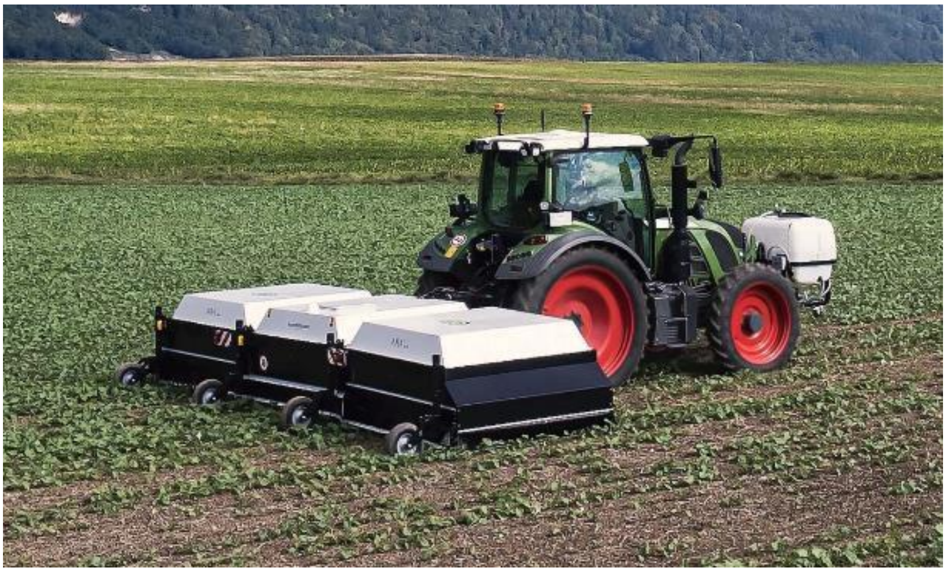

Figure 4. EcoRobotix weeding robot. Source: ecorobotix.com/en/ara/

4.3. Automated Planters

Automated planters are designed to plant seeds at precise depths and spacings. These machines can be equipped with GPS systems to ensure accurate placement and can adjust planting parameters based on soil conditions and crop type. Ünal and Topakci (2015) developed a remote-controlled, GPS-guided autonomous robot that can be controlled via 3G internet and used for image-processing applications, with real-time video transmission capabilities. Field tests showed the robot achieved linear target point precision of 10 to 12 cm and distributed target point precision of 15 to 17 cm.

The Ecorobotix and Farmdroid (see Figure 5) robots, for example, can plant seeds with high precision, and the Precision Planting system offers advanced control over seed placement and depth. By automating the planting process, these systems reduce labour costs and ensure uniform planting, which can lead to more consistent crop growth and higher yields.

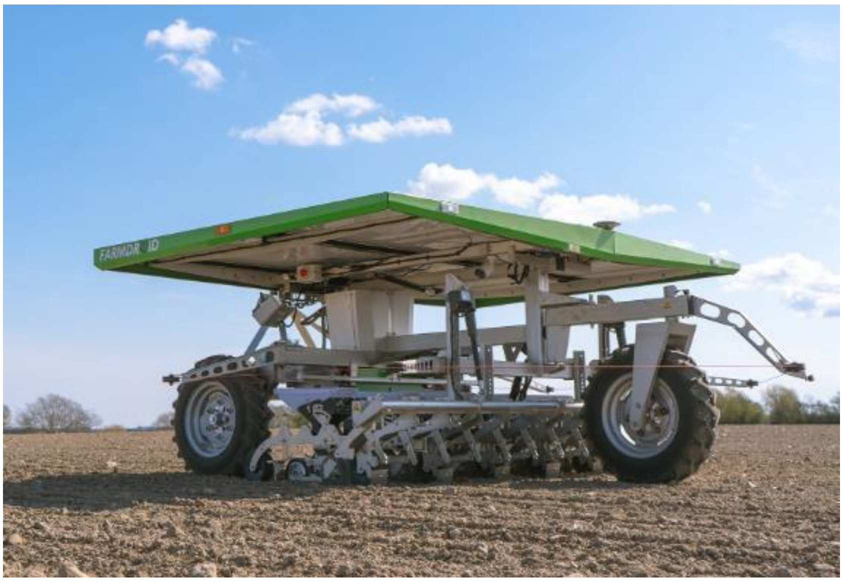

Figure 5. Farmdroid automatic seeding and weeding robot. Source: farmdroid.com

4.4. Potential to Reduce Labour Costs

The integration of robots and autonomous equipment in agriculture significantly reduces labour costs by:

- **Minimizing Manual Labour:** Automating repetitive and physically demanding tasks reduces the reliance on manual labour, which is often expensive and scarce.
- **Increasing Efficiency:** Robots and autonomous systems work continuously and with high precision, improving operational efficiency and reducing the time required for tasks.
-
- **Addressing Labour Shortages:** In regions facing labour shortages, these technologies provide a viable solution to maintain productivity levels without the need for additional human resources.

5. Artificial Intelligence and Machine Learning

AI and ML are transforming agriculture by enhancing machinery performance, optimizing planting schedules, and predicting equipment maintenance needs (Meshram et al., 2021). There has been a significant surge in research exploring the applications of AI and ML in agriculture, particularly in areas such as crop monitoring, yield prediction, and precision farming. These studies aim to optimize farming practices by improving efficiency, reducing resource consumption, and enhancing decision-making through data-driven insights.

Ahmad and Nabi (2021) conducted a comprehensive survey on agriculture, covering topics such as AI, IoT, ML, and other related technologies, providing insights into their applications and advancements in the agricultural sector. Liakos et al. (2018) presented a comprehensive review of ML applications in agricultural production systems, categorizing research into crop management, livestock management, water management, and soil management. They highlighted how ML is transforming farm management systems by leveraging sensor data to create AI-enabled programs that provide real-time recommendations and insights for improved decision-making in agriculture. Shaikh et al. (2022) emphasized the potential of information and communications technologies in agriculture, discussing challenges and detailing the roles of robotics, IoT devices, ML, AI, and sensors in modern farming practices.

5.1. Precision Control and Automation

AI-powered systems use adaptive algorithms to adjust machinery settings in real-time based on field conditions. For example, modern tractors equipped with AI can modify their speed, engine power, and implement settings to match soil conditions and crop type, ensuring optimal performance and reducing fuel consumption (Ahmad & Nabi, 2021). ML models analyse data from sensors and cameras on machinery to improve its operational efficiency. For instance, algorithms can forecast the best times for specific tasks, like planting or harvesting, based on historical data and current field conditions (Liakos et al., 2018).

5.2. Performance Monitoring

AI systems use predictive analytics to monitor machinery performance. Sensors collect data on factors such as engine temperature, fuel consumption, and wear patterns. ML algorithms analyse this data to provide insights into how machinery is performing and identify areas for improvement. AI can enable real-time adjustments to machinery settings based on live data, such as soil moisture levels or crop growth stages. This dynamic response helps maintain machinery efficiency and reduces the risk of operational issues.

5.3. Data-Driven Decision-Making

AI algorithms analyse historical weather data, soil conditions, and crop growth patterns to recommend optimal planting schedules. By integrating these factors, AI can predict the best planting times to maximize yields and minimize risks from adverse weather conditions. ML models use historical crop data and current field conditions to forecast growth stages and predict the best times for planting and harvesting. These models can adjust recommendations based on real-time weather updates and soil conditions (Ahmad & Nabi, 2021).

5.4. Variable Rate Technology

AI-driven precision planting systems use data from sensors and imagery to adjust seed planting rates and depths in real-time. This precision planting ensures that seeds are planted at the optimal density and depth for different soil conditions within the same field, leading to more uniform crop growth and better yields.

5.5. Predictive Maintenance

AI is also used for predicting equipment maintenance needs. These systems analyse data from sensors embedded in machinery to monitor its condition. For example, sensors track vibrations, temperature, and operational stresses, and ML algorithms identify patterns that signal potential issues (Shaikh et al., 2022). ML models use historical maintenance records and real-time sensor data to predict when components are likely to fail. This allows for proactive maintenance scheduling, reducing downtime and preventing costly breakdowns.

5.6. Maintenance Optimization

AI helps optimize maintenance resource allocation by predicting which parts are most likely to need attention and when. This ensures that maintenance teams are prepared and that spare parts are available, minimizing equipment downtime and operational disruptions. By identifying maintenance needs with precision, AI reduces unnecessary maintenance activities and associated costs, resulting in greater cost efficiency. It enables a shift from reactive maintenance (fixing issues as they arise) to a more cost-effective preventive approach.

5.7. Examples in Practice

5.7.1. Agricultural Operations Management System:

An advanced agricultural management system utilizes AI and ML to analyse data on machinery performance, field conditions, and planting schedules. The system aggregates information from various sources, including sensors on machinery and in the field, to generate actionable insights for farmers. This data-driven approach helps optimize field operations and improve overall efficiency. By providing detailed recommendations based on integrated data, this system enhances operational efficiency and supports more informed decision-making in daily farm management. It helps farmers streamline their operations, leading to better resource use and increased productivity.

5.7.2. Field Data Analysis System

This system employs ML algorithms to analyse comprehensive field data, including weather conditions, soil quality, and crop performance. By processing this data, the system forecasts optimal planting and harvesting times and recommends the best practices for input usage. Farmers benefit from personalized recommendations that help improve crop yields and manage resources more effectively. The system's insights enable more precise decision-making, contributing to better crop management and overall farm efficiency.

6. Internet of Things and Smart Farming:

IoT-enabled devices play a crucial role in modern agriculture by connecting machinery with real-time data systems. This connectivity enhances machinery operations and supports better decision-making through several key mechanisms (Shaikh et al., 2022; Ahmad & Nabi, 2021; Liakos et al., 2018).

6.1. Real-Time Data Collection and Monitoring

IoT-enabled devices are equipped with various sensors that monitor machinery conditions, such as engine temperature, fuel levels, vibration, and wear. These sensors continuously collect data on the performance and health of the machinery. Additionally, IoT sensors deployed in the field measure soil moisture, temperature, and crop growth conditions. This field data is transmitted to the machinery and central data systems in real-time. IoT devices use wireless communication technologies, such as cellular networks, Wi-Fi, or satellite connections, to transmit data from the machinery and field sensors to cloud-based platforms or central management systems. This continuous data flow allows for real-time monitoring of machinery performance and field conditions, providing up-to-date information to operators and decision-makers.

6.2. Enhanced Machinery Operations

By analysing real-time data from machinery sensors, IoT systems can detect anomalies and predict potential failures before they occur. For example, unusual vibrations or temperature changes can indicate impending issues, allowing for timely maintenance. Predictive analytics help schedule maintenance activities based on actual machinery conditions rather than fixed intervals, reducing downtime and preventing unexpected breakdowns. IoT systems enable machinery to make automatic adjustments based on real-time data. For instance, a tractor equipped with IoT sensors can adjust its speed, engine power, and implement settings according to soil conditions and crop type, optimizing performance and efficiency. Data from IoT devices allows for precision farming practices, such as variable-rate application of seeds, fertilizers, and pesticides, ensuring that inputs are used efficiently and effectively.

6.3. Improved Decision-Making

Data collected from IoT devices is often integrated into centralized management platforms where it can be analysed and visualized. This integrated data provides a comprehensive view of machinery performance and field conditions. Advanced analytics and ML algorithms process the data to generate actionable insights. For example, the system might highlight areas of the field that require additional irrigation or anticipate the optimal time for harvesting based on crop growth data. With real-time data and predictive insights, farmers and operators can make more informed decisions about machinery operations, resource allocation, and field management. This leads to better planning, optimized resource use, and improved crop management. The ability to monitor and adjust machinery operations in real-time enhances overall operational efficiency, reduces waste, and improves productivity.

6.4. Example Use Cases

6.4.1. Smart Irrigation Systems

IoT-enabled irrigation systems use soil moisture sensors and weather data to automatically adjust water application rates. The system can communicate with irrigation machinery to deliver precise amounts of water based on current field conditions. This approach reduces water waste, improves crop health, and ensures that crops receive the right amount of moisture. García et al. (2020), Obaideen et al. (2022), and Vallejo-Gomez (2023) conducted systematic reviews of the literature on smart irrigation systems.

6.4.2. Fleet Management

IoT devices track the location, usage, and condition of agricultural machinery across a fleet. Data on fuel consumption, operational hours, and performance metrics is transmitted to a central platform. Fleet managers can monitor machinery utilization, optimize maintenance schedules, and make data-driven decisions to enhance fleet efficiency and reduce operational costs (Ruiz de la Llata & Kjellberg, 2012).

7. Energy-Efficient and Eco-Friendly Machinery

Innovations in sustainable agricultural machinery focus on harnessing renewable energy, improving energy efficiency, and reducing emissions. Solar-powered equipment offers a renewable alternative to traditional fuel sources, while electric and hybrid machinery, precision agriculture technology, and low-emission engines contribute to lower energy consumption and reduced environmental impact. These advancements support more sustainable farming practices, helping to preserve resources and protect the environment while enhancing productivity and operational efficiency. Gorjian et al. (2021) explored the integration of PV technology with electric farm machinery, highlighting challenges such as high initial costs and limitations in electricity storage technologies. They emphasized the need for further technical improvements, cost reductions, and government incentives to promote the widespread adoption of solar-powered agricultural machines, while also considering the impact of environmental factors on PV module performance.

In the chapter by Hasnain Tariq et al. (2021), the authors explored both direct and indirect applications of solar energy in agriculture. They provided a comprehensive overview of direct uses, such as solar-powered greenhouses, tunnel farming, and solar dryers for crop and product drying. The chapter also covers indirect applications, including solar-powered tubewells, tractors, and lighting systems, highlighting their impact on agricultural practices. Saxena and Kumar (2021) reviewed advancements in solar energy applications in Indian agriculture, highlighting their potential to reduce reliance on costly and environmentally harmful non-renewable energy sources. They emphasized the need for further research to enhance the effectiveness and sustainability of solar energy use in agriculture.

7.1. Solar-Powered Tractors and Machinery

Solar-powered agricultural machinery uses photovoltaic panels to harness solar energy, which is then converted into electricity to power the equipment. This technology can either directly power machinery or charge batteries that store energy for later use. Some tractors and other farm machinery are equipped with solar panels on their roofs or integrated into their design. These panels provide supplementary power, reducing reliance on diesel or other fossil fuels. Solar-powered machinery reduces greenhouse gas emissions and decreases fuel costs (Hasnain Tariq et al., 2021). It also enables operation in remote areas where traditional fuel supply may be challenging. By using renewable energy, solar-powered equipment supports more sustainable farming practices.

7.2. Solar-Powered Irrigation Systems

Solar-powered irrigation systems use solar panels to drive water pumps, enabling efficient water delivery to crops. These systems often include solar-powered controllers that regulate water flow based on real-time data. These systems lower energy costs and reduce dependence on grid electricity or diesel-powered pumps. They also offer a sustainable solution for irrigation in areas with abundant sunlight, promoting water conservation and improving crop yields (Pinto et al., 2021).

7.3. Electric and Hybrid Tractors

Electric and hybrid tractors combine electric motors with traditional internal combustion engines or rely solely on electric power. Electric tractors are powered by batteries that can be recharged using renewable energy sources. Hybrid tractors might use an electric motor to assist with high-torque tasks and a diesel engine for longer operations, while fully electric tractors use only battery power. These machines significantly reduce emissions compared to conventional diesel tractors, leading to lower air pollution and a smaller carbon footprint. Electric tractors also offer quieter operation and reduced energy costs.

7.4. Precision Agriculture Technology

Precision agriculture utilizes GPS, sensors, and ML to optimize machinery operations. This technology enables variable-rate application of inputs such as fertilizers, pesticides, and water, tailored to specific field conditions (Cheema et al., 2023). Precision sprayers and planters adjust their operations based on real-time data, applying resources only where needed. This reduces the amount of chemicals and water used, minimizing environmental impact. By optimizing input use, precision agriculture reduces waste and energy consumption, leading to more sustainable farming practices. It also helps in improving crop yields and reducing operational costs.

7.5. Energy-Efficient Machinery Design

Modern machinery designs focus on improving energy efficiency through advanced engineering and technology. Features like more efficient engines, improved aerodynamics, and enhanced power transmission systems contribute to reduced energy consumption. Newer models of combine harvesters and balers are designed with energy-efficient engines and optimized operational settings to lower fuel usage and emissions. Energy-efficient machinery helps decrease the overall energy requirements of farming operations, reducing both fuel costs and environmental impact (Mantoam et al., 2020; Ragazou et al., 2022).

7.6. Low-Emission Engines

Advances in engine technology have led to the development of low-emission engines that produce fewer pollutants. These engines use cleaner fuels, advanced combustion technologies, and emissions control systems to minimize emissions. New engines comply with stringent emission standards and include features such as selective catalytic reduction and diesel particulate filters to reduce nitrogen oxides and particulate matter. Low-emission engines contribute to better air quality and reduced environmental impact. They also help farmers comply with regulatory requirements and enhance the sustainability of their operations.

8. Data Analytics and Cloud Computing

Cloud-based platforms and data analytics are transforming agriculture by helping farmers optimize machinery performance and streamline operations. Krisnawijaya et al. (2022) conducted a systematic literature review on data analytics platforms in agriculture, analysing 535 papers published between 2010 and 2020 to identify key features and obstacles related to these platforms. Their findings revealed a significant increase in research interest post-2010, highlighting 33 features and 34 obstacles that can guide future studies and developments in agricultural data analytics. Namani and Gonen (2020) discussed how integrating IoT and cloud computing in agriculture could enhance crop production by managing costs, monitoring performance, and facilitating maintenance, benefiting both farmers and the broader community. The paper introduced a smart drone for crop management, where real-time data from the drone, combined with IoT and cloud technologies, contributes to the development of sustainable smart agriculture. Phasinam et al. (2022)

analysed a smart irrigation system utilizing IoT and cloud-based architecture, designed to measure soil moisture and humidity while processing this data in the cloud with various ML techniques. This system provided farmers with accurate water content information, enabling more efficient water use in farming.

8.1. Real-Time Data Access and Monitoring

IoT-enabled sensors on machinery collect data on performance metrics such as fuel usage, engine health, and operating conditions. This data is transmitted to cloud-based platforms, where farmers can monitor their equipment in real-time from any location. Real-time access to data allows farmers to make informed decisions quickly, ensuring machinery operates efficiently, reducing downtime, and preventing potential breakdowns.

8.2. Data Analytics for Performance Optimization

Cloud platforms use advanced data analytics and ML algorithms to process machinery data, identifying trends and patterns. For instance, predictive analytics can forecast when a machine is likely to need maintenance, based on usage patterns and sensor data. By predicting maintenance needs and optimizing performance, farmers can reduce unexpected failures, lower repair costs, and ensure equipment is always running at peak efficiency.

8.3. Operational Efficiency and Precision

Cloud-based platforms aggregate and analyse data from multiple sources, including weather conditions, soil quality, and crop performance. This integrated data helps optimize planting schedules, fuel usage, and field operations. Streamlined operations lead to more efficient use of machinery, lower energy consumption, and improved overall farm productivity.

9. Relation between AI and Agricultural Machinery to the United Nations Sustainable Development Goals

The use of AI in agricultural machinery is closely related to several of the United Nations (UN) Sustainable Development Goals (SDGs), particularly those focusing on environmental sustainability, food security, and economic growth. Various researchers have discussed the relationship between AI-driven agricultural machines, ML, and other high-tech innovations with the SDGs.

Streich et al. (2020) reviewed advancements aimed at addressing technological challenges to achieve multiple UN SDGs and discussed strategies to bridge the gap between research and policy. Mhlanga (2021) investigated how AI influences the attainment of SDGs, focusing on poverty reduction and infrastructure development in emerging economies. The study found that AI significantly contributes to these goals by enhancing data collection, revolutionizing agriculture and financial inclusion, and improving infrastructure reliability, thus emphasizing the need for increased investment in AI and related research to achieve the SDGs.

9.1. SDG 2: Zero Hunger

AI-driven agricultural machinery helps optimize planting, irrigation, and harvesting, improving crop yields and reducing waste. By ensuring efficient use of resources, AI helps increase food production, contributing to global food security. Enhanced efficiency and productivity can help reduce hunger by making more food available, especially in regions facing food shortages.

9.2. SDG 12: Responsible Consumption and Production

AI technologies enable precision agriculture, which involves the precise application of water, fertilizers, and pesticides. This minimizes waste, reduces chemical runoff, and promotes sustainable farming practices. By optimizing resource use, AI helps reduce the environmental impact of farming, contributing to more sustainable production systems.

9.3. SDG 13: Climate Action

AI-powered machinery can help reduce greenhouse gas emissions by optimizing fuel use, adopting electric or hybrid technologies, and enabling sustainable land management practices. AI also supports climate-resilient agriculture by forecasting weather patterns and adjusting operations accordingly. Reducing emissions and promoting sustainable farming practices align with global climate action efforts, helping mitigate the effects of climate change.

9.4. SDG 8: Decent Work and Economic Growth

AI enhances the efficiency of agricultural machinery, reducing labour costs and increasing productivity. Automation through AI-driven machinery also helps address labour shortages in the agricultural sector. By boosting productivity and operational efficiency, AI supports economic growth in agriculture while improving working conditions through automation.

9.5. SDG 9: Industry, Innovation, and Infrastructure

The integration of AI into agricultural machinery fosters innovation in farming practices and contributes to the modernization of agricultural infrastructure. AI-powered tools are part of the broader trend of smart farming and agricultural digitization. This technological advancement promotes sustainable industrial innovation in the agricultural sector, contributing to the development of smart agriculture ecosystems.

9.6. SDG 15: Life on Land

AI enables precision land management, reducing over-exploitation of natural resources such as soil and water. It helps monitor soil health, biodiversity, and environmental impact, supporting sustainable land use. By ensuring the responsible use of land and resources, AI-powered machinery supports biodiversity and ecosystems, protecting terrestrial life.

10. Challenges in Adopting New Agricultural Machinery

10.1. High Costs

Advanced machinery, particularly those integrated with AI and precision technology, often requires a significant initial investment. Small and medium-sized farms may struggle to afford the upfront costs of purchasing or leasing this equipment. Access to affordable financing options can be limited, especially in developing regions, further complicating the adoption of these technologies.

10.2. Training and Skill Development

New machinery equipped with AI, IoT, and precision tools requires specialized knowledge to operate effectively. Many farmers need training in data analysis, machine operation, and digital agriculture. A lack of familiarity with cutting-edge technologies can lead to underutilization of machinery, reducing the potential benefits and productivity gains. There is a growing need for education programs and accessible resources to train farmers and operators.

10.3. Maintenance and Support

AI-powered and automated machinery often requires more sophisticated maintenance, involving specialized knowledge of software, sensors, and mechanical systems. This can increase reliance on external service providers, particularly in remote areas with limited access to skilled technicians. The availability of spare parts and technical support may be limited in certain regions, potentially leading to extended downtime if machinery requires repairs.

11. Future Direction of Agricultural Machinery

11.1. Deeper Integration of AI and Robotics

The future of agricultural machinery lies in further autonomy. AI-driven tractors, harvesters, and drones will increasingly operate with minimal human intervention, using real-time data to make intelligent decisions in the field. For example, autonomous machinery will handle complex tasks like weeding, planting, and precision spraying.

AI will evolve to become more predictive, offering farmers decision-making support by analysing vast amounts of data, such as weather patterns, soil health, and market trends. AI systems could suggest optimal planting schedules, forecast disease outbreaks, and guide resource management more efficiently.

11.2. Biotechnology and Machinery Synergies

Biotechnology is likely to converge with machinery innovation. For instance, genetically engineered seeds (smart seeds) could be designed to communicate with AI-enabled equipment, allowing machines to respond dynamically to the specific needs of crops during their growth cycle.

Biotechnology-driven sensors integrated with machinery will provide real-time feedback on plant health, soil composition, and nutrient needs, enabling precise and customized care for each crop, which can improve yields and sustainability.

11.3. Sustainable and Renewable Energy-Powered Machinery

A shift towards electric and solar-powered machinery is anticipated as part of global efforts to reduce carbon emissions. Machinery will increasingly rely on renewable energy sources, contributing to more sustainable farming practices.

Future machinery will be designed for maximum energy efficiency, with advanced systems to optimize fuel usage, reduce emissions, and minimize environmental impact. Technologies such as regenerative braking and energy recapture systems could be used in field operations.

12. Conclusion

The trajectory of agricultural machinery development underscores a profound shift from manual labour to a sophisticated, technology-driven industry, marked by continuous innovations that enhance productivity and sustainability. The progression from basic hand tools to advanced motorized equipment and precision technologies has revolutionized farming practices, making operations more efficient and productive. Today, tools such as GPS-guided tractors, drones, and AI-powered systems are at the forefront, driving significant improvements in crop management, resource optimization, and operational efficiency. These advancements align closely with the UN SDGs, contributing to objectives such as Zero Hunger, Responsible Consumption and Production, Climate Action, and Decent Work and Economic Growth.

Despite the remarkable progress, challenges remain, including the high costs of new technologies, the complexity of advanced systems, and the need for specialized skills and training. Addressing these issues is crucial for broader adoption and sustained benefits. The future of agricultural machinery lies in further integration of AI and robotics, innovations in biotechnology, and the adoption of sustainable energy solutions. By continuing to advance these technologies and overcoming existing barriers, the agricultural sector can achieve greater efficiency, enhance food security, and support environmental sustainability, ultimately contributing to the realization of global development goals.

References

Abbas, A., Zhang, Z., Zheng, H., Alami, M. M., Alrefaei, A. F., Abbas, Q., Naqvi, S. A. H., Rao, M. J., Mosa, W. F. A., Abbas, Q., et al. (2023). Drones in plant disease assessment, efficient monitoring, and detection: A way forward to smart agriculture. *Agronomy, 13*(7), 1524. https://doi.org/10.3390/agronomy13071524

Ahmad, L., & Nabi, F. (2021). *Agriculture 5.0: artificial intelligence, IoT and machine learning*. CRC Press.

Amer, M., Yahya, A., Daraghmeh, A., Dwaikat, R., & Nouri, B. (2020). Design and development of an automatic controlled planting machine for agriculture in Palestine. *Universal Journal of Control and Automation*, *8*, 32-39.

Cheema, M. J. M., Iqbal, T., Daccache, A., Hussain, S., & Awais, M. (2023). Precision agriculture technologies: Present adoption and future strategies. In Q. Zaman (Ed.), *Precision agriculture* (pp. 231-250). Academic Press. https://doi.org/10.1016/B978-0-443-18953-1.00011-8

del Cerro, J., Cruz Ulloa, C., Barrientos, A., & de León Rivas, J. (2021). Unmanned aerial vehicles in agriculture: A survey. *Agronomy, 11*(2), 203. https://doi.org/10.3390/agronomy11020203

FarmDroid. (n.d.). *FarmDroid FD20*. Retrieved August 24, 2024, from https://farmdroid.com/products/farmdroid-fd20/

Folio3 AgTech. (n.d.). *Drones in agriculture*. Folio3. Retrieved August 24, 2024, from https://agtech.folio3.com/blogs/drones-in-agriculture/

García, L., Parra, L., Jimenez, J. M., Lloret, J., & Lorenz, P. (2020). IoT-based smart irrigation systems: An overview on the recent trends on sensors and IoT systems for irrigation in precision agriculture. *Sensors*, *20*(4), 1042.

Gorjian, S., Ebadi, H., Trommsdorff, M., Sharon, H., Demant, M., & Schindele, S. (2021). The advent of modern solar-powered electric agricultural machinery: A solution for sustainable farm operations. *Journal of Cleaner Production, 292*, 126030. https://doi.org/10.1016/j.jclepro.2021.126030

Hasnain Tariq, G., Ashraf, M., & Sohaib Hasnain, U. (2021). Solar technology in agriculture. In F. Ahmad & M. Sultan (Eds.), *Technology in agriculture*. IntechOpen. https://doi.org/10.5772/intechopen.98266

Javaid, M., Haleem, A., Singh, R. P., & Suman, R. (2022). Enhancing smart farming through the applications of Agriculture 4.0 technologies. *International Journal of Intelligent Networks, 3*, 150-164. https://doi.org/10.1016/j.ijin.2022.09.004

Krisnawijaya, N. N. K., Tekinerdogan, B., Catal, C., & van der Tol, R. (2022). Data analytics platforms for agricultural systems: A systematic literature review. *Computers and Electronics in Agriculture, 195*, 106813.

Liakos, K. G., Busato, P., Moshou, D., Pearson, S., & Bochtis, D. (2018). Machine learning in agriculture: A review. *Sensors*, *18*(8), 2674.

Mantoam, E. J., Angnes, G., Mekonnen, M. M., & Romanelli, T. L. (2020). Energy, carbon and water footprints on agricultural machinery. *Biosystems Engineering, 198*, 304-322. https://doi.org/10.1016/j.biosystemseng.2020.08.019

Maraveas, C., Piromalis, D., Arvanitis, K. G., Bartzanas, T., & Loukatos, D. (2022). Applications of IoT for optimized greenhouse environment and resources management. *Computers and Electronics in Agriculture, 198*, 106993. https://doi.org/10.1016/j.compag.2022.106993

Maslekar, N. V., Kulkarni, K. P., & Chakravarthy, A. K. (2020). Application of unmanned aerial vehicles (UAVs) for pest surveillance, monitoring, and management. In A. Chakravarthy (Ed.), *Innovative pest management approaches for the 21st century*. Springer. https://doi.org/10.1007/978-981-15-0794-6_2

Meshram, V., Patil, K., Meshram, V., Hanchate, D., & Ramkteke, S. D. (2021). Machine learning in agriculture domain: A state-of-art survey. *Artificial Intelligence in the Life Sciences, 1*, 100010. https://doi.org/10.1016/j.ailsci.2021.100010

Mhlanga, D. (2021). Artificial intelligence in Industry 4.0 and its impact on poverty, innovation, infrastructure development, and the sustainable development goals: Lessons from emerging economies. *Sustainability, 13*(11), 5788. https://doi.org/10.3390/su13115788

Mukherjee, D., Nandi, M., Mondal, S., & Nandi, S. (2021). Utilization of IoT: Automated seed plantation based smart agriculture. In *Proceedings of the 2021 5th International Conference on Electronics, Materials Engineering & Nano-Technology (IEMENTech)* (pp. 1-4). IEEE.

Naïo Technologies. (n.d.). *Oz: Autonomous weeding robot*. Retrieved August 24, 2024, from https://www.naio-technologies.com/en/oz/

Namani, S., & Gonen, B. (2020). Smart agriculture based on IoT and cloud computing. In *Proceedings of the 2020 3rd International Conference on Information and Computer Technologies (ICICT)* (pp. 553-556). IEEE. https://doi.org/10.1109/ICICT50521.2020.00094

Obaideen, K., Yousef, B. A., AlMallahi, M. N., Tan, Y. C., Mahmoud, M., Jaber, H., & Ramadan, M. (2022). An overview of smart irrigation systems using IoT. *Energy Nexus*, *7*, 100124.

Octinion. (n.d.). *Strawberry picker*. Retrieved August 24, 2024, from http://octinion.com/strawberry-picker

Phasinam, K., Kassanuk, T., Shinde, P. P., Thakar, C. M., Sharma, D. K., Mohiddin, M. K., & Rahmani, A. W. (2022). Application of IoT and cloud computing in automation of agriculture irrigation. *Journal of Food Quality*, *2022*(1), 8285969.

Pinto, R., Mathias, C., Kokande, N., Thomas, M., & Pushpas, U. S. (2021). Solar powered irrigation system. In V. Nath & J. Mandal (Eds.), *Nanoelectronics, circuits and communication systems* (Vol. 692, pp. 389-400). *Lecture Notes in Electrical Engineering*. Springer. https://doi.org/10.1007/978-981-15-7486-3_34

Ragazou, K., Garefalakis, A., Zafeiriou, E., & Passas, I. (2022). Agriculture 5.0: A new strategic management mode for a cost-cutting and energy-efficient agriculture sector. *Energies, 15*(9), 3113. https://doi.org/10.3390/en15093113

Ruiz de la Llata, A., & Kjellberg, O. (2012). *Improving sustainability of agriculture supplies distribution: A case study of Foria AB* (Master's thesis, Chalmers University of Technology). Department of Technology Management and Economics, Division of Logistics and Transportation. Technical Report No. E2012:065. Gothenburg, Sweden.

Santana-Fernández, J., Gómez-Gil, J., & del-Pozo-San-Cirilo, L. (2010). Design and implementation of a GPS guidance system for agricultural tractors using augmented reality technology. *Sensors*, *10*(11), 10435-10447.

Saxena, N. N., & Kumar, P. (2021). A review on application of solar energy in agriculture sector. *International Journal of Innovative Research in Engineering and Management*, *8*(6), 136-139. https://doi.org/10.55524/ijirem.2021.8.6.23

Shaikh, T. A., Rasool, T., & Lone, F. R. (2022). Towards leveraging the role of machine learning and artificial intelligence in precision agriculture and smart farming. *Computers and Electronics in Agriculture, 198*, 107119. https://doi.org/10.1016/j.compag.2022.107119

Streich, J., Romero, J., Gazolla, J. G. F. M., Kainer, D., Cliff, A., Prates, E. T., … & Harfouche, A. L. (2020). Can exascale computing and explainable artificial intelligence applied to plant biology deliver on the United Nations sustainable development goals? *Current Opinion in Biotechnology, 61*, 217-225.

Ünal, I., & Topakci, M. (2015). Design of a remote-controlled and GPS-guided autonomous robot for precision farming. *International Journal of Advanced Robotic Systems, 12*(12). https://doi.org/10.5772/62059

Vallejo-Gomez, D., Osorio, M., & Hincapie, C. A. (2023). Smart irrigation systems in agriculture: A systematic review. *Agronomy*, *13*(2), 342.

Velusamy, P., Rajendran, S., Mahendran, R. K., Naseer, S., Shafiq, M., & Choi, J.-G. (2022). Unmanned aerial vehicles (UAV) in precision agriculture:

Applications and challenges. *Energies, 15*(1), 217. https://doi.org/10.3390/en15010217

Yépez-Ponce, D. F., Salcedo, J. V., Rosero-Montalvo, P. D., & Sanchis, J. (2023). Mobile robotics in smart farming: Current trends and applications. *Frontiers in Artificial Intelligence, 6,* 1213330. https://doi.org/10.3389/frai.2023.1213330

Zhu, H., Zhang, Y., Mu, D., Bai, L., Zhuang, H., & Li, H. (2022). YOLOX-based blue laser weeding robot in cornfield. *Frontiers in Plant Science, 13*, 1017803. https://doi.org/10.3389/fpls.2022.1017803

ENVIRONMENTALLY FRIENDLY FRICTION MATERIALS

Mustafa ÖNCÜL

Chapter 7

Environmentally Friendly Friction Materials

MUSTAFA ÖNCÜL[1]

1. Introduction

1.1. Friction Materials

Friction materials are engineered to generate controlled friction between surfaces in motion, essential for regulating motion and dissipating energy in braking systems, clutches, and other mechanical components (Yun et al., 2010). These materials must balance effective friction with minimal wear. In the automotive industry, they are crucial for converting kinetic energy into heat during braking, affecting safety, efficiency, and noise reduction (Mulani et al., 2022). In clutches, friction materials ensure smooth power transmission and improve fuel efficiency (Jabbar et al., 2021). In aerospace, advanced composites like carbon materials withstand extreme conditions during landings, providing reliability and reducing weight (Gebrehiwet et al., 2023). In industrial machinery, particularly in heavy-duty sectors like mining and construction, friction materials ensure durability and performance under harsh conditions. They also enable controlled power transfer in machinery, preventing damage and improving operational efficiency, contributing to energy savings across industries (Ilie & Cristescu, 2022; Shah et al., 2021; Wong & Tung, 2016).

Traditional friction materials, such as asbestos, metals, and composites, have been widely used in various industries due to their effective performance in controlling friction and wear. Asbestos, once a common material in brake pads and clutches, is known for its excellent thermal stability and durability. However, the health risks associated with asbestos fibers, which can cause respiratory diseases and cancer, have led to its widespread ban in many countries (Carbone et al., 2024). Metallic friction materials, often made

---

[1] Dr., İzmir Kâtip Çelebi University, Türkiye, mustafa.oncul@ikcu.edu.tr , https://orcid.org/0000-0002-4441-6353

from steel, copper, or other alloys, offer high thermal conductivity and strength, making them suitable for heavy-duty applications like automotive and industrial machinery. Despite their performance advantages, the production and disposal of metallic friction materials contribute to significant environmental pollution, including heavy metal contamination and high energy consumption during manufacturing (Kukutschova et al., 2009). Composite materials, which combine metals, ceramics, and polymers, provide a balance between performance and cost. However, the use of synthetic resins and non-renewable fibers in composites raises concerns about their environmental impact, particularly in terms of resource reduction and waste generation (Raghunathan et al., 2024). As a result, the environmental impact of traditional friction materials has prompted the search for greener alternatives that reduce health risks, lower emissions, and minimize ecological footprints.

1.2. Need for Environmentally Friendly Alternatives

The growing consumer and industry demand for greener solutions in friction materials is driven by increased environmental awareness, regulatory requirements, and the desire for sustainable practices. Consumers are becoming more environmentally conscious, leading to a preference for products that minimize ecological impact, such as those with reduced emissions and lower carbon footprints (Dangelico & Vocalelli, 2017). In response, industries are seeking friction materials that not only meet performance standards but also align with sustainability goals, including the use of recyclable materials, reduced reliance on toxic substances, and energy-efficient manufacturing processes (Wong & Tung, 2016). This shift towards sustainability is adopting innovation in the development of new materials and technologies that prioritize both environmental responsibility and high performance, making green friction materials a key focus for future advancements (Balaji et al., 2023; Saha et al., 2023).

Friction materials play a critical role in reducing the carbon footprint and promoting sustainability, particularly in industries such as automotive, aerospace, and industrial machinery. By improving energy efficiency and extending the lifespan of mechanical components, advanced friction materials contribute to lower fuel consumption and reduced greenhouse gas emissions (Balaji et al., 2023). For example, eco-friendly brake pads and clutch materials that minimize wear not only enhance vehicle performance but also decrease the frequency of replacement, reducing waste and the demand for raw materials. Additionally, the development of friction materials using sustainable, renewable, and recyclable resources further supports the reduction of environmental impact (Tzanakis et al., 2012). As industries face increasing pressure to adopt sustainable practices, the role of friction materials in mitigating environmental impact and enhancing energy efficiency has become more significant, driving innovation in the development of new, eco-friendly solutions (Dangelico & Vocalelli, 2017).

2. Characteristics of Friction Materials

2.1. Key Properties

Tribological properties like the coefficient of friction, wear resistance, and thermal stability are crucial for the performance and durability of friction materials. The coefficient of friction determines the force needed to slide two surfaces against each other, which is vital for effective braking and clutch systems. Stability in this coefficient ensures consistent performance, enhancing safety and reliability. Wear resistance impacts the material's longevity and reduces maintenance, essential for heavy-duty applications where frequent replacements are costly. Thermal stability is vital for maintaining properties under high temperatures, such as in automotive and aerospace braking systems. Advanced friction materials that balance these properties enhance performance, safety, and sustainability across various applications (Ricciardi et al., 2017; Saha et al., 2023; Verma et al., 2016).

Mechanical properties such as strength, toughness, and durability are fundamental to friction materials' reliability in demanding applications. Strength ensures structural integrity under pressure, toughness allows materials to absorb energy without fracturing, and durability minimizes maintenance costs by extending component service life. These properties are critical for maintaining consistent performance, safety, and efficiency in various industrial settings

(Kim et al., 2011; Reeves & Menezes, 2016).

Environmental properties like biodegradability, non-toxicity, and recyclability are increasingly important as industries aim to reduce their ecological footprint and comply with environmental regulations. Biodegradable materials decompose naturally, reducing long-term waste. Non-toxic materials protect human health and the environment, while recyclability conserves resources and supports a circular economy. Integrating these properties into friction material design promotes sustainability and reduces environmental impact (Carbone et al., 2024; Hussain et al., 2022; Prabhu & Devaraju, 2021).

2.2. Comparison with Traditional Materials

Friction materials exhibit a range of advantages and disadvantages in terms of performance, cost, and environmental impact, which are crucial considerations in their selection and application. Performance-wise, advanced friction materials, such as carbon composites and ceramics, offer superior thermal stability, high wear resistance, and consistent friction coefficients, making them ideal for demanding applications like aerospace and high-performance automotive braking systems. However, these high-performance materials often come with a significant cost premium, which can be prohibitive for widespread use in cost-sensitive sectors (Verma et al., 2016). In contrast, traditional materials like asbestos and metallic composites are generally more affordable and offer adequate performance in many applications, but their environmental and health impacts, including toxicity and non-biodegradability, have led to regulatory restrictions and a decline in their use (Carbone et al., 2024; Kukutschova et al., 2009). Environmentally friendly alternatives, such as biodegradable and recyclable friction materials, are gaining traction due to their reduced ecological footprint, but they may still face challenges in achieving the same level of performance as conventional materials, particularly in extreme conditions. Therefore, the choice of friction material often involves balancing these trade-offs, where the optimal solution depends on specific application requirements and regulatory constraints. Table 1 demonstrates the interrelationships between the selection of friction materials based on their performance, cost, and environmental impact.

Table 1. Comparison of the advantages and disadvantages of different types of friction materials

Type of Friction Material	Advantages	Disadvantages
Advanced Friction Materials (e.g., carbon composites, ceramics)	• Superior thermal stability • High wear resistance • Consistent friction coefficients • Ideal for demanding applications like aerospace and high-performance automotive braking systems	• High cost, prohibitive for cost-sensitive sectors
Traditional Materials (e.g., asbestos, metallic composites)	• Generally more affordable • Adequate performance in many applications	• Environmental and health impacts (toxicity, non-biodegradability) • Subject to regulatory restrictions
Environmentally Friendly Materials (e.g., biodegradable and recyclable materials)	• Reduced ecological footprint (biodegradable and recyclable) • Gaining traction due to environmental benefits	• May not achieve the same performance levels as conventional materials in extreme conditions • Challenges in achieving high performance

3. Types of Friction Materials

3.1. Organic and Natural Fiber-Based Materials

Organic and natural fiber-based friction materials have gained significant attention in recent years due to their environmental benefits, renewability, and relatively low cost. Among these materials, fibers derived from agricultural and industrial waste—such as coconut fiber, flax, and palm kernel shell—are emerging as promising candidates for sustainable friction applications. Coconut fibers, known for their high lignin content, offer excellent mechanical properties, making them suitable for use in brake pads and clutch facings (Kholil et al., 2021). Flax fibers, characterized by their high tensile strength and biodegradability, provide a balanced combination of frictional stability and thermal resistance, which is beneficial for applications in both automotive and industrial machinery (Fu et al., 2012). Palm kernel shells, a by-product of the palm oil industry, possess a unique combination of hardness and thermal stability, making them effective in enhancing wear resistance and reducing noise in brake components (Olele et al., 2016). Processing these natural fibers typically involves mechanical, chemical, and thermal treatments to improve their compatibility with polymer matrices and enhance their frictional properties. Mechanical methods like grinding and milling reduce fiber size, while chemical treatments, such as alkalization and resin impregnation, increase surface roughness and improve bonding with the matrix. With their growing applicability in automotive and industrial sectors, these natural fiber-based materials present a promising alternative to conventional asbestos-based friction materials, aligning with global sustainability goals (Koronis & Silva, 2018; Saindane et al., 2020).

3.2. Composite Materials

Green composites represent a class of materials that integrate natural fibers, resins, and other eco-friendly additives to achieve enhanced sustainability and performance. These composites typically employ natural fibers such as flax, hemp, jute, sisal, and kenaf, which are abundant, renewable, and biodegradable, offering an eco-friendly alternative to synthetic fibers like glass and carbon (Pickering et al., 2016). The matrix in green composites is often based on bio-resins derived from renewable resources, such as vegetable oils, starches, and lignin, which not only reduce the carbon footprint but also exhibit lower toxicity and greater biodegradability compared to conventional petroleum-based resins (Ashori, 2008). In addition to natural fibers and resins, these composites can be enhanced with other eco-friendly additives such as nanoclay, cellulose nanocrystals, and natural rubber, which improve mechanical properties, thermal stability, and processability without compromising environmental sustainability. By strategically combining these components, green composites can be engineered to meet specific performance requirements in various applications, ranging from automotive parts and building materials to packaging and consumer goods.

Green composites incorporating natural fibers and eco-friendly resins offer a unique combination of performance characteristics and environmental benefits. Due to their inherent properties, natural fibers such as flax and hemp provide high specific strength and stiffness, which contribute to lightweight yet durable composite structures (Baley, 2002). These materials exhibit excellent vibration damping and acoustic insulation, making them ideal for automotive and aerospace applications where noise reduction and passenger comfort are critical (Mohanty et al., 2005). Furthermore, the use of bio-resins and natural additives enhances the thermal stability, moisture resistance, and impact strength of the composites, allowing them to perform reliably under various environmental conditions. The environmental benefits of green composites are equally compelling; they are derived from renewable resources, require less energy during production, and are more likely to be biodegradable or recyclable at the end of their lifecycle, thereby reducing landfill waste and pollution (Faruk et al., 2012). Moreover, these materials contribute to a reduction in greenhouse gas emissions and lower reliance on non-renewable resources, aligning with global sustainability goals and regulatory demands for greener manufacturing processes (Koronis & Silva, 2018).

3.3. Biodegradable and Recyclable Friction Materials

Emerging materials that reduce waste and support circular economy principles are becoming vital as industries aim to minimize environmental impact and improve resource efficiency. These include biodegradable polymers, recycled composites, and bio-based materials designed for reuse, remanufacture, or safe decomposition. For example, biopolymers like polylactic acid (PLA) and polyhydroxyalkanoates (PHA), derived from renewable resources, provide sustainable alternatives to conventional plastics and are fully compostable (Thakur et al., 2012). Recycled composites, made from post-consumer plastics, reclaimed fibers, or industrial by-products, are increasingly used in construction, automotive, and packaging, reducing waste and extending resource lifespans. These materials embody circular economy principles by closing waste loops, reducing reliance on virgin resources, and promoting sustainable production and consumption.

While emerging materials have great potential to support a circular economy, several challenges must be overcome for widespread adoption. Key obstacles include developing cost-effective production processes that can compete with conventional materials, as many bio-based and recycled materials face higher costs, limited scalability, and quality variability (Peelman et al., 2013). The lack of standardized testing and certification also creates uncertainty about their performance and safety, especially in industries like automotive and aerospace. However, these challenges present opportunities for innovation in material properties, processing methods, and recycling infrastructures. Growing demand for sustainable products, driven by consumer awareness and regulatory pressures, offers a favorable market environment (Geissdoerfer et al., 2017). Collaborations among industry, academia, and government can further advance material science and circular economy practices, promoting broader adoption of these materials. Table 2 gives the properties, applications, and references for different types of sustainable friction materials.

Table 2. The tribological characteristics of various friction materials

Natural Fiber/Component	Key Properties	Applications	References
Coconut Fiber	High lignin content, excellent mechanical properties, suitable for brake pads and clutch facings	Automotive brake pads, clutch facings	Kholil et al., 2021
Flax Fiber	High tensile strength, biodegradable, balanced frictional stability, and thermal resistance	Automotive and industrial machinery	Fu et al., 2012
Palm Kernel Shell	Hardness, thermal stability, enhances wear resistance, reduces noise	Brake components	Olele et al., 2016
Flax, Hemp, Jute, Sisal, Kenaf	High specific strength and stiffness, vibration damping, acoustic insulation, moisture resistance	Automotive parts, building materials, packaging, consumer goods	Pickering et al., 2016; Mohanty et al., 2005
Bio-Resins (e.g., vegetable oils, starches, lignin)	Lower carbon footprint, lower toxicity, biodegradability	Automotive, construction, packaging	Ashori, 2008
Eco-friendly Additives (e.g., nanoclay, cellulose nanocrystals, natural rubber)	Improve mechanical properties, thermal stability, and processability	Various industrial applications	Faruk et al., 2012
Biodegradable Polymers (e.g., PLA, PHA)	Sustainable alternatives to conventional plastics, fully compostable	Automotive, construction, packaging	Thakur et al., 2012
Recycled Composites (e.g., post-consumer plastics, reclaimed fibers)	Reduce waste, extend resource lifespans, promote circular economy	Construction, automotive, packaging	Peelman et al., 2013

4. Case Studies and Applications

4.1. Industrial Applications

Environmentally friendly friction materials, like natural fiber composites and low-toxicity resins, are increasingly used in machinery, manufacturing, and heavy equipment components such as brake linings, clutches, seals, and gaskets, where friction performance and wear resistance are essential (Myshkin & Grigoriev, 2022). Materials made from sustainable sources, such as kenaf, hemp, and flax fibers, help reduce wear, extend component life, and minimize downtime in high-heat and friction applications like conveyor belts and heavy-duty brakes. These materials also provide excellent vibration damping, reducing noise and improving comfort in industries such as mining and construction (Ilie & Cristescu, 2022).

Sustainable friction materials offer benefits like enhanced safety, reduced environmental impact, and cost efficiency by lowering toxicity, minimizing hazardous particulate release, and saving energy due to their lighter weight. However, broader adoption faces challenges due to performance variability, production scalability, quality control, and compatibility with existing manufacturing processes. Ongoing research and development are needed to optimize materials, improve techniques, and establish industry standards (Kamaruddin et al., 2022; Soni et al., 2024).

4.2. Automotive Industry

Environmentally friendly brake pads, clutches, and other automotive components are emerging as viable alternatives to conventional materials, which often contain harmful substances like asbestos and heavy metals. For example, brake pads made from natural fibers such as coconut, flax, and hemp, bonded with organic resins, offer effective frictional properties while being biodegradable and non-toxic (Fu et al., 2012; Kholil etal., 2021). Ceramic-based brake pads with eco-friendly additives like recycled glass and rubber also reduce environmental impact during production and disposal (Mulani et al., 2022). Hybrid composite clutches, combining natural fibers with recycled polymers, provide comparable durability and strength to traditional materials, with lower emissions and greater recyclability. These components contribute to reduced emissions, energy use, and waste, aligning with sustainability goals and regulatory requirements. For instance, natural fiber-based brake pads can reduce noise and vibration, enhancing comfort, while ceramic-based pads produce less dust, improving air quality (Balaji et al., 2023; Mulani et al., 2022; Soni et al., 2024). Overall, the shift to sustainable materials helps manufacturers meet environmental regulations and reduce carbon footprints.

4.3. Aerospace and Other High-Tech Sectors

The aerospace industry, known for its strict performance and safety standards, is increasingly exploring environmentally friendly friction materials. Traditionally, aerospace applications, like aircraft brake systems, have used asbestos, metallic, and carbon-based composites for their excellent thermal and mechanical properties. However, environmental and health concerns, along with regulatory pressures, are driving the search for sustainable alternatives. Advances in material science have produced high-performance, eco-friendly friction materials that maintain essential properties such as thermal stability, wear resistance, and frictional consistency under extreme conditions (Bakshi et al., 2010; Friedrich & Almajid, 2013). The challenge remains in balancing these performance demands with the need for materials that are recyclable, non-toxic, and derived from renewable resources. Promising progress has been made with fiber-reinforced polymers and ceramic-based composites, which offer both low environmental impact and high performance. As these materials evolve, their use in aerospace and other high-tech sectors is expected to grow, supporting a more sustainable future.

5. Environmentally Friendly Friction Materials and United Nations Sustainable Development Goals Relations

Environmentally friendly friction materials are essential in advancing the United Nations Sustainable Development Goals (UN SDGs), particularly those related to health, environmental protection, and sustainable industrial practices (Martin, n.d.). These materials support SDG 3 (Good Health and Well-being) by reducing reliance on toxic substances such as asbestos and heavy metals, which are linked to severe health issues, including respiratory diseases and cancer. By minimizing the release of harmful particulates and chemicals during manufacturing, usage, and disposal, they help protect both workers and the general public from hazardous exposures. Additionally, these materials contribute to SDG 12 (Responsible Consumption and Production) by promoting the use of renewable and biodegradable raw materials, reducing waste, and enhancing recycling efforts. The shift towards sustainable materials in industries such as automotive, aerospace, and manufacturing demonstrates a commitment to more responsible production processes that lower environmental impact while maintaining high performance standards. This approach aligns with the goal of decoupling economic growth from environmental degradation. Furthermore, environmentally friendly friction materials support SDG 13 (Climate Action) by reducing the carbon footprint associated with traditional friction materials. Their adoption, which includes materials with lower energy requirements and the potential for reduced greenhouse gas emissions across their lifecycle, significantly contributes to global efforts to combat climate change (Wegmann et al., 2022). By embedding sustainability into the core of material development, the friction materials industry can play a vital role in achieving a more sustainable and resilient future in accordance with the UN SDGs.

6. Conclusion

Environmentally friendly friction materials have gained significant importance in recent years due to increasing concerns over environmental sustainability and public health. Traditional friction materials, such as those containing asbestos and heavy metals, have been associated with significant environmental and health risks, including toxic emissions during use and disposal, as well as the release of harmful particulates into the atmosphere (Xiao et al., 2016). In contrast, environmentally friendly friction materials are designed to minimize these impacts by utilizing non-toxic, biodegradable, and renewable raw materials. These materials not only reduce the ecological footprint but also enhance worker safety and public health by eliminating hazardous substances from the production process and end-use scenarios. By adopting green alternatives, industries can achieve both environmental and economic benefits, such as reduced waste management costs, improved product marketability, and alignment with global sustainability goals. The transition towards eco-friendly friction materials represents a critical step in the development of safer and more sustainable industrial practices.

The future of friction materials lies in the widespread adoption of eco-friendly, high-performance alternatives that meet strict environmental and safety standards while maintaining efficiency. As the global focus on reducing carbon footprints and minimizing environmental impacts grows, friction materials are expected to evolve to include renewable, recyclable, and biodegradable components, such as natural fibers, bio-based resins, and nano-additives, which offer wear resistance, thermal stability, and durability (Islam et al., 2024). Additionally, smart friction materials capable of self-healing, adapting to changing conditions, or reducing emissions will become more common, particularly in the automotive and aerospace sectors where sustainability and regulatory compliance are crucial. These innovations will be driven by circular economy principles, emphasizing reuse, repair, and recycling to create a sustainable future (Geissdoerfer et al., 2017).

Achieving this vision will require continuous innovation and collaboration across industries, such as automotive, aerospace, and manufacturing. Research and development efforts are needed to overcome current limitations, including performance variability, cost, and scalability (Faruk et al., 2012). Partnerships among academia, industry, and government are crucial for advancing material technologies, establishing new standards, and securing regulatory approvals (Iannuzzi, 2024). Joint initiatives and collaborations can accelerate innovation, reduce costs, and promote the adoption of these materials across various sectors. Through collective efforts, industries can work toward a sustainable future where friction materials play a key role in reducing environmental impact and enhancing efficiency and safety.

References

Ashori, A. (2008). Wood–plastic composites as promising green-composites for automotive industries! *Bioresource Technology*, *99*(11), 4661–4667.

Bakshi, S. R., Lahiri, D., & Agarwal, A. (2010). Carbon nanotube reinforced metal matrix composites—A review. *International Materials Reviews*, *55*(1), 41–64. https://doi.org/10.1179/095066009X12572530170543

Balaji, M. S., Jitendra, K., Arumugam, E., & Sethupathi, B. P. (2023). State of the art on challenges for friction material manufacturers – raw materials, regulations, environmental, and NVH aspects. *Proceedings of the Institution of Mechanical Engineers, Part J: Journal of Engineering Tribology*, *237*(4), 926–942. https://doi.org/10.1177/13506501221135071

Baley, C. (2002). Analysis of the flax fibres tensile behaviour and analysis of the tensile stiffness increase. *Composites Part A: Applied Science and Manufacturing*, *33*(7), 939–948.

Carbone, M., Dodson, R., Pass, H., & Yang, H. (2024). *Asbestos: Risk Assessment, Epidemiology, and Health Effects*. CRC Press.

Dangelico, R. M., & Vocalelli, D. (2017). "Green Marketing": An analysis of definitions, strategy steps, and tools through a systematic review of the literature. *Journal of Cleaner Production*, *165*, 1263–1279.

Faruk, O., Bledzki, A. K., Fink, H.-P., & Sain, M. (2012). Biocomposites reinforced with natural fibers: 2000–2010. *Topical Issue on Polymeric Biomaterials*, *37*(11), 1552–1596. https://doi.org/10.1016/j.progpolymsci.2012.04.003

Friedrich, K., & Almajid, A. A. (2013). Manufacturing Aspects of Advanced Polymer Composites for Automotive Applications. *Applied Composite Materials*, *20*(2), 107–128. https://doi.org/10.1007/s10443-012-9258-7

Fu, Z., Suo, B., Yun, R., Lu, Y., Wang, H., Qi, S., Jiang, S., Lu, Y., & Matejka, V. (2012). Development of eco-friendly brake friction composites containing flax fibers. *Journal of Reinforced Plastics and Composites*, *31*(10), 681–689. https://doi.org/10.1177/0731684412442258

Gebrehiwet, L., Abate, E., Negussie, Y., Teklehaymanot, T., & Abeselom, E. (2023). Application of composite materials in aerospace & automotive industry. *International Journal of Advances in Engineering and Management (IJAEM)*, *5*(3), 697–723.

Geissdoerfer, M., Savaget, P., Bocken, N. M., & Hultink, E. J. (2017). The Circular Economy–A new sustainability paradigm? *Journal of Cleaner Production*, *143*, 757–768.

Hussain, M., Khan, S. M., Al-Khaled, K., Ayadi, M., Abbas, N., & Chammam, W. (2022). Performance analysis of biodegradable materials for orthopedic applications. *Materials Today Communications*, *31*, 103167.

Iannuzzi, A. (2024). *Greener products: The making and marketing of sustainable brands*. CRC press. https://books.google.com/books?hl=tr&lr=&id=RSQREQAAQBAJ&oi=fnd&pg=PA1975&dq=Sustainability+Standards+on+the+Market+Acceptance+of+Green+Products&ots=G6agsugyxR&sig=s_f-mzz0MfbpDe5VZKJ8bV5UGaw

Ilie, F., & Cristescu, A.-C. (2022). Tribological behavior of friction materials of a disk-brake pad braking system affected by structural changes—A review. *Materials*, *15*(14), 4745.

Islam, T., Chaion, M. H., Jalil, M. A., Rafi, A. S., Mushtari, F., Dhar, A. K., & Hossain, S. (2024). Advancements and challenges in natural fiber-reinforced hybrid composites: A comprehensive review. *SPE Polymers*, pls2.10145. https://doi.org/10.1002/pls2.10145

Jabbar, N. A., Hussain, I. Y., & Abdullah, O. I. (2021). Thermal and thermoelastic problems in dry friction clutch: A comprehensive review. *Heat Transfer*, *50*(8), 7855–7878. https://doi.org/10.1002/htj.22257

Kamaruddin, Z. H., Jumaidin, R., Ilyas, R. A., Selamat, M. Z., Alamjuri, R. H., & Yusof, F. A. M. (2022). Biocomposite of Cassava Starch-Cymbopogan Citratus Fibre: Mechanical, Thermal and Biodegradation Properties. *Polymers*, *14*(3), Article 3. https://doi.org/10.3390/polym14030514

Kholil, A., Dwiyati, S. T., Wirawan, R., & Elvin, M. (2021). Brake Pad Characteristics of Natural Fiber Composites from Coconut Fibre and Wood Powder. *Journal of Physics: Conference Series*, *2019*(1), 012068. https://iopscience.iop.org/article/10.1088/1742-6596/2019/1/012068/meta

Kim, S. S., Hwang, H. J., Shin, M. W., & Jang, H. (2011). Friction and vibration of automotive brake pads containing different abrasive particles. *Wear*, *271*(7–8), 1194–1202.

Koronis, G., & Silva, A. (2018). *Green composites for automotive applications*. Woodhead Publishing. https://books.google.com/books?hl=tr&lr=&id=cV55DwAAQBAJ&oi=fnd&pg=PP1&dq=Green+Alternatives+for+Asbestos+in+Automotive+Applications&ots=Sijf6AkDFn&sig=2xLj-XhsM1WohJAvPo2fiTtl_A4

Kukutschova, J., Roubíček, V., Malachová, K., Pavlíčková, Z., Holuša, R., Kubačková, J., Mička, V., MacCrimmon, D., & Filip, P. (2009). Wear mechanism in automotive brake materials, wear debris and its potential environmental impact. *Wear*, *267*(5–8), 807–817.

Martin. (n.d.). The Sustainable Development Agenda. *United Nations Sustainable Development*. Retrieved September 6, 2024, from https://www.un.org/sustainabledevelopment/development-agenda/

Mohanty, A. K., Misra, M., & Drzal, L. T. (2005). *Natural fibers, biopolymers, and biocomposites*. CRC press.

Mulani, S. M., Kumar, A., Shaikh, H. N. E. A., Saurabh, A., Singh, P. K., & Verma, P. C. (2022). A review on recent development and challenges in automotive brake pad-disc system. *Materials Today: Proceedings*, *56*, 447–454.

Myshkin, N. K., & Grigoriev, F. A. (2022). Green Tribology for Sustainable Development Goals. In G. Quaglia, A. Gasparetto, V. Petuya, & G. Carbone (Eds.), *Proceedings of I4SDG Workshop 2021* (Vol. 108, pp. 421–428). Springer International Publishing. https://doi.org/10.1007/978-3-030-87383-7_46

Olele, P. C., Nkwocha, A. C., Ekeke, I. C., Ileagu, M. O., & Okeke, E. O. (2016). Assessment of palm kernel shell as friction material for brake pad production. *International Journal of Engineering and Management Research (IJEMR)*, *6*(1), 281–284.

Peelman, N., Ragaert, P., De Meulenaer, B., Adons, D., Peeters, R., Cardon, L., Van Impe, F., & Devlieghere, F. (2013). Application of bioplastics for food packaging. *Trends in Food Science & Technology*, *32*(2), 128–141.

Pickering, K. L., Efendy, M. G. A., & Le, T. M. (2016). A review of recent developments in natural fibre composites and their mechanical performance. *Special Issue on Biocomposites*, *83*, 98–112. https://doi.org/10.1016/j.compositesa.2015.08.038

Prabhu, R., & Devaraju, A. (2021). Recent review of tribology, rheology of biodegradable and FDM compatible polymers. *Materials Today: Proceedings*, *39*, 781–788.

Raghunathan, V., Sathyamoorthy, G., Ayyappan, V., Srisuk, R., Singaravelu, D. L., Rangappa, S. M., & Siengchin, S. (2024). Advances in brake friction materials: A comprehensive review of ingredients, processing methods, and performance characteristics. *Journal of Vinyl and Additive Technology*, vnl.22149. https://doi.org/10.1002/vnl.22149

Reeves, C. J., & Menezes, P. L. (2016). Advancements in Eco-friendly Lubricants for Tribological Applications: Past, Present, and Future. In J. P. Davim (Ed.), *Ecotribology* (pp. 41–61). Springer International Publishing. https://doi.org/10.1007/978-3-319-24007-7_2

Ricciardi, V., Savitski, D., Augsburg, K., & Ivanov, V. (2017). Estimation of brake friction coefficient for blending function of base braking control. *SAE International Journal of Passenger Cars-Mechanical Systems*, *10*(2017-01–2520), 774–785.

Saha, D., Sharma, D., & Satapathy, B. K. (2023). Challenges pertaining to particulate matter emission of toxic formulations and prospects on using green ingredients for sustainable eco-friendly automotive brake composites. *Sustainable Materials and Technologies*, e00680.

Saindane, U. V., Soni, S., & Menghani, J. V. (2020). Recent research status on synthesis and characterization of natural fibers reinforced polymer composites and modern friction materials–an overview. *Materials Today: Proceedings*, *26*, 1616–1620.

Shah, R., Woydt, M., Huq, N., & Rosenkranz, A. (2021). Tribology meets sustainability. *Industrial Lubrication and Tribology*, *73*(3), 430–435.

Soni, A., Das, P. K., Gupta, S. K., Saha, A., Rajendran, S., Kamyab, H., & Yusuf, M. (2024). An overview of recent trends and future prospects of sustainable natural fiber-reinforced polymeric composites for tribological applications. *Industrial Crops and Products*, *222*, 119501.

Thakur, V. K., Singha, A. S., & Thakur, M. K. (2012). Biopolymers Based Green Composites: Mechanical, Thermal and Physico-chemical Characterization. *Journal of Polymers and the Environment*, *20*(2), 412–421. https://doi.org/10.1007/s10924-011-0389-y

Tzanakis, I., Hadfield, M., Thomas, B., Noya, S. M., Henshaw, I., & Austen, S. (2012). Future perspectives on sustainable tribology. *Renewable and Sustainable Energy Reviews*, *16*(6), 4126–4140.

Verma, P. C., Ciudin, R., Bonfanti, A., Aswath, P., Straffelini, G., & Gialanella, S. (2016). Role of the friction layer in the high-temperature pin-on-disc study of a brake material. *Wear*, *346*, 56–65.

Wegmann, S., Rytka, C., Diaz-Rodenas, M., Werlen, V., Schneeberger, C., Ermanni, P., Caglar, B., Gomez, C., & Michaud, V. (2022). A life cycle analysis of novel lightweight composite processes: Reducing the environmental footprint of automotive structures. *Journal of Cleaner Production*, *330*, 129808.

Wong, V. W., & Tung, S. C. (2016). Overview of automotive engine friction and reduction trends–Effects of surface, material, and lubricant-additive technologies. *Friction*, *4*(1), 1–28. https://doi.org/10.1007/s40544-016-0107-9

Xiao, X., Yin, Y., Bao, J., Lu, L., & Feng, X. (2016). Review on the friction and wear of brake materials. *Advances in Mechanical Engineering*, *8*(5), 168781401664730. https://doi.org/10.1177/1687814016647300

Yun, R., Filip, P., & Lu, Y. (2010). Performance and evaluation of eco-friendly brake friction materials. *Tribology International*, *43*(11). https://www.sciencedirect.com/science/article/pii/S0301679X10001222

THE EFFECT OF INFILL DENSITY ON THE MECHANICAL PROPERTIES OF PLA MATERIALS PRODUCED BY FDM METHOD

Necmettin YIĞITTÜRK

Chapter 8

The Effect of Infill Density on the Mechanical Properties of PLA Materials Produced by FDM Method

NECMETTİN YİĞİTTÜRK[1]

1. 3D Printer Technologies

The concept of Industry 4.0 first emerged in 2011, marking the onset of the Fourth Industrial Revolution (Öztürk, 2019). Humanity has entered a new era of technology, and this revolution is fundamentally a technological one. As a result of this revolution, advancements in fields like autonomous technologies, artificial intelligence, and microchips are progressing rapidly. Today, CNC (computer numerical control) technologies, which are essential in mass production, are also gaining momentum in this direction. The foundations of computer-aided design and manufacturing (CAD/CAM) were laid in the 1970s (Erdem, 2024). Afterward, software development accelerated, enabling the widespread use of CAD/CAM applications across all sectors. Prototype production, initial product manufacturing, quality control, and functionality checks are crucial in the production of a material or product after the design phase. Investments such as molds and machines required for pre-mass production processes in many production methods can lead to unfavorable outcomes in terms of cost and time. For instance, a sample is needed to test the functionality of a part required in machine manufacturing. This sample must be identical in shape and dimensions to the final product. Until recently, sample production was done using CNC machines through subtractive manufacturing methods. However, producing parts with complex geometries using subtractive manufacturing techniques is sometimes not feasible and is also inefficient in terms of cost. After the advent of 3D printers, significant cost efficiency and

---

[1] Lecturer, Dokuz Eylül University, Türkiye, necmettin.yigitturk@deu.edu.tr, https://orcid.org/0000-0001-5554-613X

time savings have been achieved in prototype production. This technology not only facilitates prototype production but also makes small-scale production more accessible. 3D printers were first developed in the 1980s and continue to advance today. The constant development and progress of 3D printing technologies (Alafaghani, Qattawi, Alrawi, and Guzman, 2017; Day and Yodo, 2019) are increasing every day (Marșavina et al., 2022). Due to the availability of easy-to-use and inexpensive desktop printers on the market, 3D printers based on Fused Deposition Modeling (FDM) technology are rapidly becoming widespread. 3D printing technologies have yielded successful results in various sectors (Akkoyun, 2024). These technologies have found their place in both micro and macro fields. Materials can be produced at the micro level, and even structures (in the construction industry) can be manufactured at the macro level.

PLA is a type of filament widely used in 3D printing processes (Lluch-Cerezo, Benavente, Meseguer, and Gutiérrez, 2019; Marșavina et al., 2022). Studies have been conducted on the impact of parameters such as infill density, layer thickness, and printing temperature on the mechanical properties of prints made using the FDM method. Infill density refers to how full the internal structure is during printing. As the infill density increases, the material's mechanical strength typically increases because more material bonding is achieved. With an increase in infill density, mechanical properties such as tensile strength, bending strength, and impact strength generally improve. This is due to the material's more homogeneous structure. Higher infill density allows the layer to be bonded more tightly, making the material more resistant to tensile and bending forces. However, increasing infill density also raises the material's density and can increase its weight. In this case, the material may lose its advantage of being lightweight. Additionally, very high infill densities can sometimes cause cracks or deformations, which can negatively impact mechanical strength. The effect of infill density on mechanical properties can vary depending on factors such as printing parameters, layer thickness, air gaps, and material properties. Therefore, a careful trial and adjustment process may be necessary to optimize the infill density.

1.1 Types of 3D Printers

There are constant innovations and new models emerging in the field of 3D printers. Table 1 lists the most commonly used types of 3D printers and their applications today. As indicated in the table, different types of 3D printers offer solutions in various fields. The correct method must be chosen based on the desired properties of the material to be produced. The printing method (printer type) and raw material type should be selected by considering factors such as the place of use of the material, material properties, geometry, and cost efficiency. For example, if surface roughness is critical for a material, the SLA method should be chosen instead of the FDM method. Although surface roughness can be addressed with post-processing, these processes increase costs and may cause deformations in the material, requiring additional steps. When evaluating materials, many factors need to be considered. If the material to be produced is a fixture or measurement control prototype, polymer raw materials (PLA, ABS, PET-G, etc.) can be selected, but for end-user products, the environment in which it will be used should also be considered. For a product that will be used under sunlight, it is expected to be produced from ASA raw material, which has high UV resistance, while considering the operating temperature of the environment, materials like PLA (60°C), PET-G (85°C), ABS (95°C), and ASA (110°C) should be selected.

Not only polymer materials but also metallic materials can be produced. Metals with the desired properties can be transformed into micron-sized powder particles and used to manufacture metallic materials through the Laser Sintering method. These can be complex geometrical end-use products, as well as spare parts for machines or automobiles.

Table 1. Types of 3D Printers (Source: https://infotron.com.tr/3-boyutlu-yazici-cesitleri/).

FDM (Fused Deposition Modeling)	A method in which plastic filament is melted and objects are produced layer by layer.
SLA (Stereolithography)	A method in which objects are produced by solidifying liquid resin using a light source.
SLS (Selective Laser Sintering)	A method of producing objects by sintering powdered materials using laser technology.
DLP (Digital Light Processing)	Similar to SLA, but uses a faster light source to solidify resin.
MJF (Multi Jet Fusion)	A method developed by HP where objects are produced by spraying binding material onto a powder bed and then heating it.
PolyJet	Realistic surface quality and high resolution. Multi-material printing, where flexible and rigid materials can be produced in a single print.
LOM (Laminated Object Manufacturing)	A method in which objects are produced by cutting and gluing layers of paper, plastic, or metal laminations.
Binder Jetting	A technique that produces objects by binding metal powder particles using a high-powered laser.
CLIP (Continuous Liquid Interface Production)	A resin-based printing method that controls light and oxygen, allowing for fast 3D printing through a continuous production process.
Material Jetting	A technique similar to inkjet printing, where liquid material is deposited in thin layers and solidified.
DOD (Drop on Demand)	Similar to Material Jetting, but material droplets are only deposited at specific points when needed.
Bioprinting	A method in which tissues and organs are 3D printed using live cells, growth factors, and biomaterials.

1.1.1 FDM Printers

Fused Deposition Modeling (FDM) is the most widely used printer type among 3D printer technologies (Jean-Marie, Youssef, Marius and Philippe 2013). After the designed 3D model is adjusted in a slicing program for printing, the final G-Code is extracted and this code is loaded into the FDM type printer. According to the commands it receives from these codes, the extruder, which the 3D printer moves in the x-y-z axes, pushes the filament made of thermoplastic material towards the nozzle. The filament melted by the nozzle is stacked layer by layer on top of each other to produce the model. Figure 1 shows the schematic representation of the working method of printers working with the FDM method.

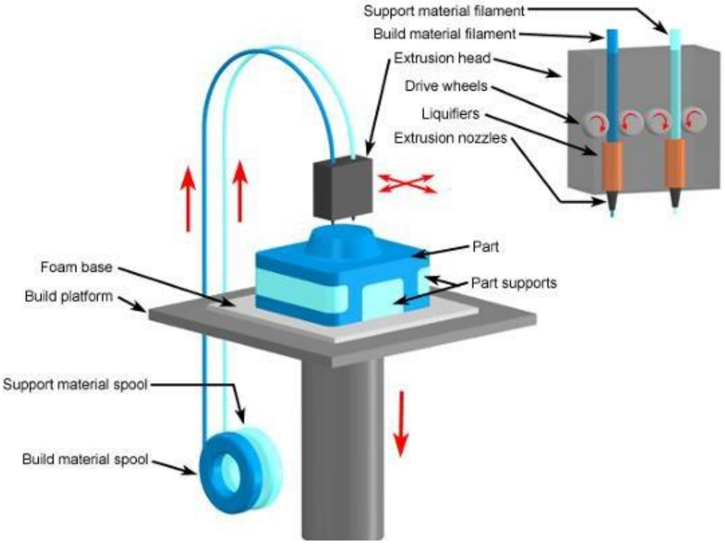

Figure 1. Schematic Representation of FDM Printers (Maden and Kamber 2018)

1.1.2 SLA Method

In the stereolithography (SLA) technique, a resin that is liquid at room temperature is exposed to ultraviolet light at certain points according to the model type, and curing occurs in the areas exposed to ultraviolet light. Afterwards, the model is reduced in the z-axis direction by the layer thickness and the new layer is cured, and model production is carried out (Toprak 2023). Figure 2 shows the schematic representation of the working method of printers working with the SLA method.

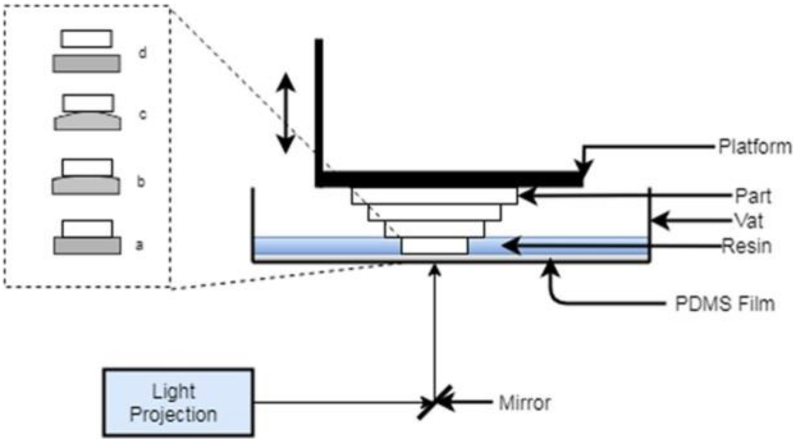

Figure 2. Schematic Representation of the Working Principle of SLA Printers (Khadilkar, Wang and Rai, 2019)

1.1.3 SLS Method

In the Selective Laser Sintering (SLS) technique, powders brought to micron size are used as raw materials. These powders are diversified as metal, plastic or ceramic depending on the type of material to be used. Laser beams are reflected on the powders as points according to the desired geometries and diffusion occurs between the powder particles. In this diffusion, the powder particles form bonds with each other at the atomic level and form the desired geometry. Afterwards, the material moves down in the z direction as much as the layer thickness and new powder is covered on it. The process is repeated cyclically and the material production is carried out. Figure 3 shows the schematic representation of the working method of printers working with the SLS method.

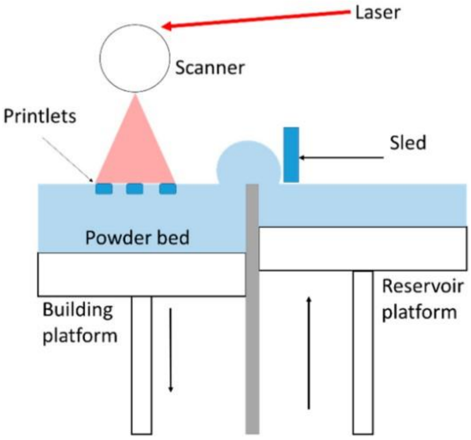

Figure 3. Schematic Representation of the Working Principle of SLS Printers (Gueche, Sanchez-Ballester, Cailleaux, Bataille, Soulairol 2021)

1.1.4 DLP Method

The Digital Light Processing (DLP) method is a method similar to the SLA method. Unlike SLA, the resin to be cured is in a transparent container. With the help of a projector, the beam is reflected from below into the transparent container in the geometry of one layer of the model to be produced. After the first layer solidifies, the model moves up and the liquid resin fills the gap formed at the bottom and the same process continues until the model is completed. The solidified resin is cured in UV ovens and the production is completed (Dokuz 2020). Figure 4 shows the schematic representation of the working method of printers working with the DLP method.

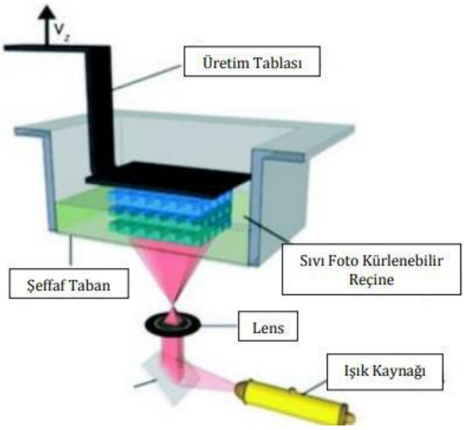

Figure 4. Schematic Representation of the Working Principle of DLP Printers (Dokuz, 2020)

1.1.5 MJF Method

The Multi Jet Fusion (MJF) method generally uses nylon and similar thermoplastic materials. The powdered raw material is sprayed onto a heated plate, then the heating head passes over the powder in accordance with the geometry of the model, melting the material and forming the model. The process is repeated layer by layer to complete the production. Figure 5 shows the schematic representation of the working method of printers working with the MJF method.

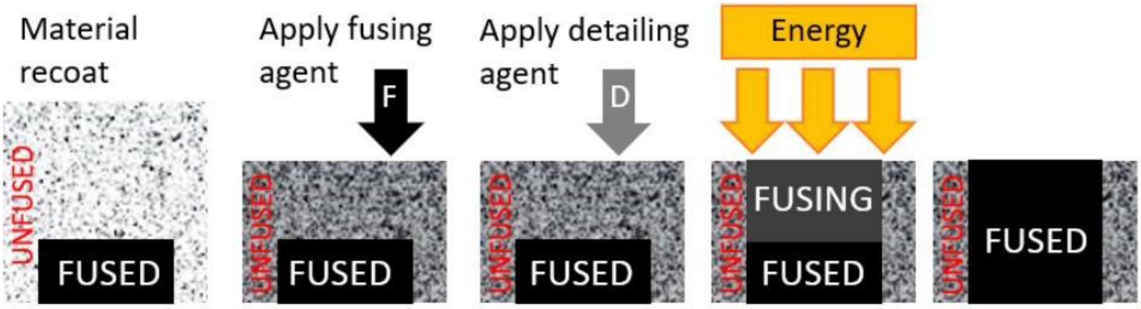

Figure 5. Schematic Representation of the Working Principle of MJF Printers (Ráž, Chval, Thomann 2023)

.1.6 Polyjet Method

In the Polyjet method, the resin, which is liquid at room temperature, is sprayed onto the table from a nozzle. This sprayed resin is cured with ultraviolet rays and solidified. This method is preferred especially for prints where surface quality is required. This printing technology consists of four ink jet heads coming from eight chambers connected to material printing cartridges; two UV light sources cure the photosensitive resin while a cylinder passes over the samples layer by layer (Tee, Peng, Pille, et. al, 2020). Figure 6 shows a schematic representation of the working method of printers working with the Polyjet method.

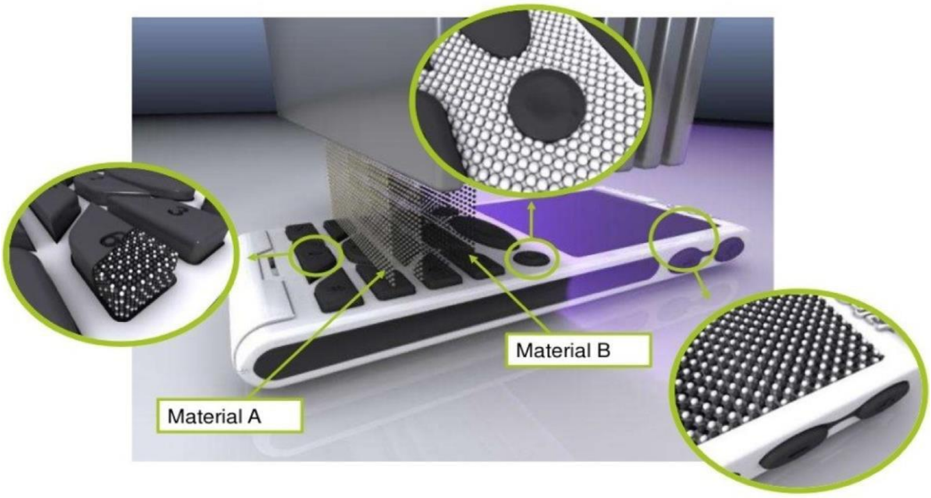

Figure 6. Schematic Representation of Working Principle of Polyjet Printers (Das, Ranganathan and Murugan 2018)

1.1.7 LOM Method

Laminated Object Manufacturing (LOM) method involves the production of sheet-shaped materials from metal, polymer, or cardboard, followed by stacking and cutting these sheets, and then bonding the cut pieces together. Typically, a laminated material such as cardboard, polymer, fabric, or fiber wound onto a roller is pulled across the table by another roller, and the laminated material is cut using a laser head that moves in the x and y axes. The LOM system operates using G-code (Shahriar et al., 2024). After the first layer is cut, the table moves down along the z-axis, the laminated material is pulled again, and the process continues. Figure 7 presents a schematic representation of the working principle of printers using the LOM method

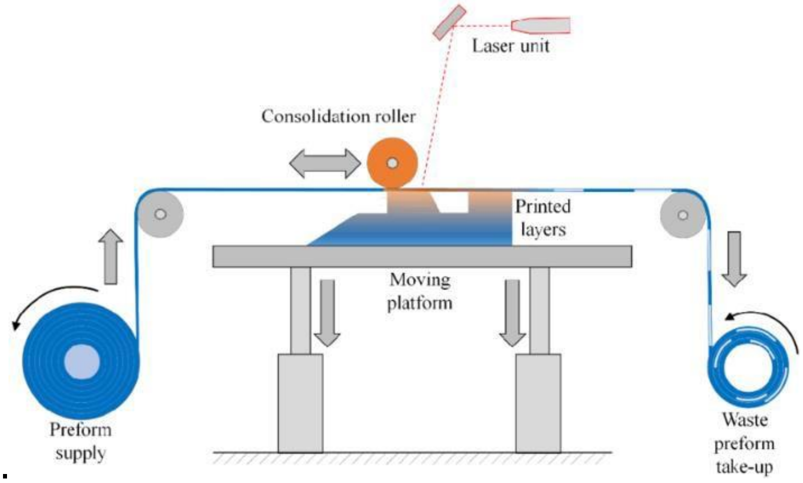

Figure 7. Schematic Representation of the Working Principle of LOM Printers

1.1.8 Binder Jetting Method

In the Binder Jetting method, metal powders are sprayed onto a table. Then, a binder (adhesive) substance is poured onto these powders to ensure that the powders stick to each other and the process continues until the model is completed layer by layer. Figure 8 shows the schematic representation of the working method of printers working with the BJ method.

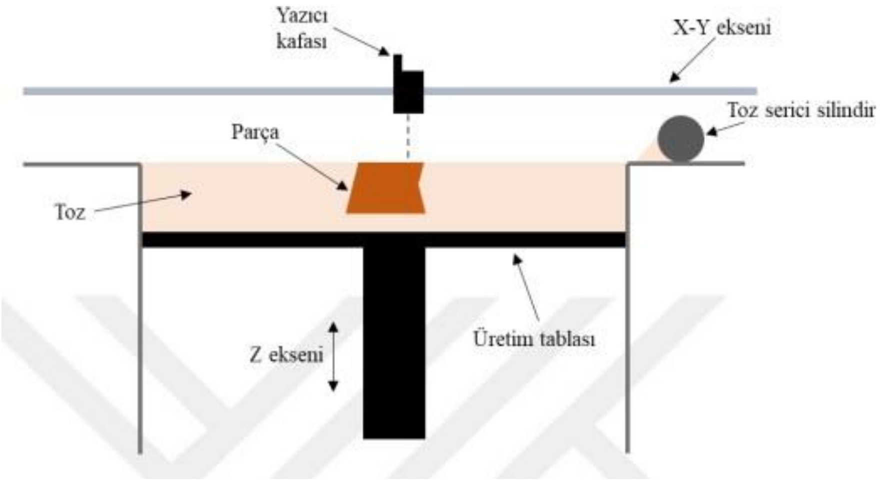

Figure 8. Schematic Representation of the Working Principle of BJ Printers (Baş, 2023)

1.1.9 CLIP Method

Continuous Liquid Interface Production (CLIP) method is a method applied by reflecting UV light to the resin in a transparent container and solidifying it. Unlike SLA, the model moves continuously in the z direction. The resin is pulled into this space by the suction force created in the gap created uring the movement (Jonhson, et. al. 2016). The speed of the printer movement is a speed that will allow enough time for the resin to cure. Figure 9 shows the schematic representation of the working method of printers working with the Clip method.

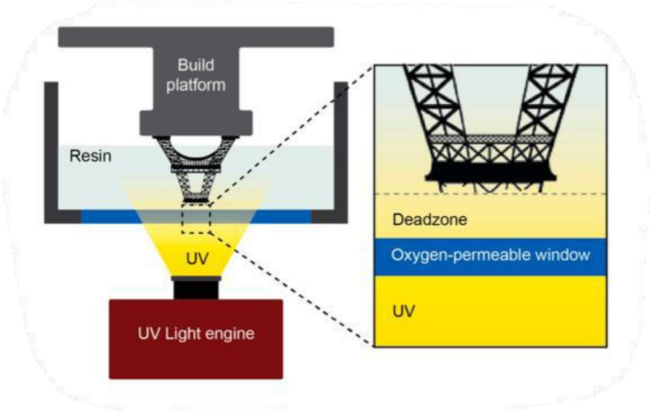

Figure 9. Schematic Representation of the Working Principle of Clip Printers (Brian, et. al., 2022)

1.10 Material Jetting Method

A system similar to inkjet 2D document printing systems is used in the Material Jetting method. It provides easy use in office environments as well as laboratory environments (Yang, et. al., 2016). It is based on the principle of spraying resin from nozzles and solidifying each layer with UV rays. Figure 10 shows the schematic representation of the working method of printers working with the MJ method.

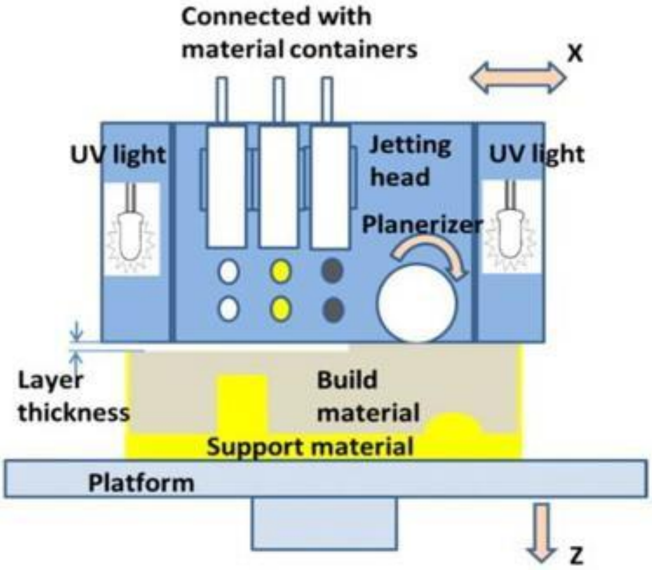

Figure 10. Schematic Representation of the Working Principle of Material Jetting Printers (Yang, et. al., 2016).

1.1.11 Drop On Demand (DOD) Method

The Drop On Demand (DOD) method is similar to the material jetting method; however, in this method, spraying is not done across the entire area. It is a technique where droplets of material are ejected only in the necessary locations according to the model's structure. The diameter of the droplets produced in the print head ranges from 10 to 150 µm (Plog, Jiang, and Pan, 2020). Compared to the material jetting method, it is a technique that results in less material waste. Figure 11 shows a schematic representation of the working principle of printers using the DOD method.

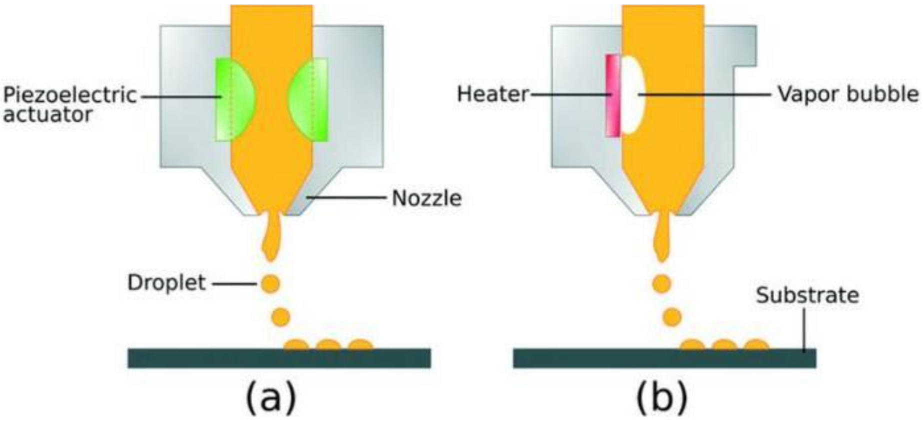

Figure 11. Schematic Representation of the Working Principle of DOD Printers

1.1.12 Bioprinting Method

The bioprinting method is used in Medicine and Tissue Engineering to create tissue-like structures using bio-inks. In this method, similar organ and tissue models can be produced. Bioprinters, unlike other 3D printers, can perform production with gel-based bio-inks. In other words, this method can print organs and tissues using biological inks (bio-inks) or cell-laden inks. Bioprinters reduce the use of animals in experiments. Additionally, they improve the reliability of test results and alleviate the need for organ transplants in areas experiencing organ shortages (Wei et al., 2016). Figure 12 shows an example of a bioprinting printer.

Figure 12. Bioprinting Method (https://malzemebilimi.net/bio-baski-bioprinting-nedir.html)

1.2. Filaments Used in FDM Type Printers

In 3D printing technologies, polymer-based filaments are generally used as raw materials. Approximately 51% of the products produced in additive manufacturing are made from polymer-based materials (Toprak, 2023). The filaments most commonly used in FDM-type printers include PLA (polylactic acid), ABS (acrylonitrile butadiene styrene), PET (Polyethylene Terephthalate), HIPS (High Impact Polystyrene), PVA (Polyvinyl Alcohol), and Nylon (Kristiawan, Imaduddin, Ariawa, Sabino, and Arifin, 2021). Additionally, specially produced Carbon Fiber filaments, composite filaments made of wood/copper/bronze, and TPU filaments used in areas requiring flexibility are also manufactured.

Filament production is a specialized process, and the quality of raw materials and dimensional stability are significant factors. The raw material to be produced into filament is selected; these raw materials are typically in granule form. Pigments that carry the same properties as the raw material are mixed in defined proportions, also in granule form, along with various additives for reinforcement, and then melted in an extrusion machine. The filament is produced in a circular shape with the desired diameter (generally 1.75 ± 0.2 mm) from the die connected to the extrusion machine and wound onto spools in specified quantities.

1.2.1. PLA (Polylactic Acid)

The depletion of fossil fuels and the increasing environmental pollution have directed people towards the exploration of biodegradable materials. In this context, due to its mechanical properties, renewability, biodegradability, and relatively low costs, PLA leads the way among biopolymers (Jean-Marie et al., 2013). PLA stands for Polylactic Acid and is a biologically degradable and bioactive thermoplastic made from renewable sources such as corn starch or sugarcane (Yiğittürk, Ergül, and Ay, 2023). Since it is a type of raw material produced from organic substances, it poses no harm to human health, and there are no adverse effects from the odor and smoke released during printing. However, it is recommended to ventilate the printing area during prolonged prints. PLA raw material is used in many sectors, including baby diapers, women's hygiene products, medical threads, stents, and the pharmaceutical industry. Figure 13 shows the chemical structure of PLA (Bulus et al., 2019).

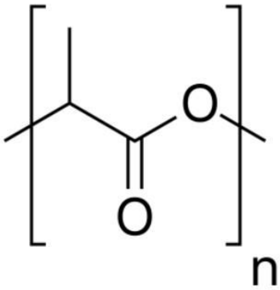

Figure 13. Chemical Structure of PLA (Bulus et al., 2019)

PLA filaments are the most commonly used filaments in FDM-type printers. The reasons for PLA raw material being the most preferred include its eco-friendliness, resistance to water, soap, and detergents, high printing speeds, cost-effectiveness, absence of adhesion problems during printing, and minimal error rates in prints.

Material and Method

PLA is a biodegradable and naturally degradable material. However, these degradation times require appropriate environmental conditions. In this study, filaments provided by Porima® Company were used. These filaments have low thermal shrinkage values, which provide important features such as superior resolution, improved mechanical properties, and improved thermal performance compared to standard PLA filaments. The increased crystalline structure of the filaments allows for higher printing speeds. These features contribute to the production of high-quality printed products in terms of resolution, mechanical strength, and thermal performance. The diameters of the filaments vary from 1.75 mm to 2.85 mm. The processing temperature can be adjusted between 200°C and 230°C to provide optimal conditions for the printing process. The density of the PLA material was measured as 1.23 g/cm³, which indicates a lightweight structure and is advantageous for various applications. In addition, the PLA material exhibits a notch impact strength of 14.2 kJ/m², providing resistance to impact forces. Table 2 shows the filament properties given by the manufacturer, and Table 3 shows the manufacturer's recommended printing values.

Table 2. Properties of PLA according to manufacturer (Source: https://www.porima3d.com/porima-pla-filament).

Parameter	Value
Material density	1,23 g/cm³
Melt flow index	17.3 g/10dk
Tensile strength	56 MPa
Elastic modulus	2850 MPa
Elongation at break	7 %
Notched impact test	14,2 kJ/m^2
Heat deflection temperature	55°C
Glass transition temperature	55-60°C
Surface resistance	>10^{12} Ohm/sq

Table 3. Recommended printing parameters of pla according to manufacturer (Source: https://www.porima3d.com/porima-pla-filament)

Parameter	Value
Printing temperature	200-230°C
Bed temperature	60-75°C
Printing speed	200 mm/s max

The 3D printer seen in Figure 1 was used to print the samples. The samples designed using CAD software on the computer are transferred to another slicing program used by the printers. The necessary settings are made in this slicing program to obtain healthy prints. Parameters such as layer thickness, infill type, infill density, temperature, and cooling are arranged in this slicing program to create a G-Code. These codes are transferred to the printer and the printing process is started. Materials such as PLA are melted in the printer's extruder, poured on the low-temperature printing plate, and brought together in layers. When the print is complete, the object is removed and excess support material is cleaned if necessary.

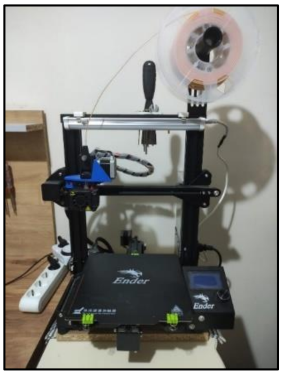

Figure 14. Printer Used in Printing 3D Samples

The inner parts of parts manufactured with 3D printers may differ from other processes. For example, in the injection method, it is a difficult process to manufacture the material in the form of a shell or to support the inner cavities. There are limitations depending on the shape of the design and the type of process. However, when a material is produced with a 3D printer, the inner part can be manufactured completely empty or by leaving a certain amount of space. When leaving space in the inner areas, the shape of these spaces can also be determined. Figure 15 shows the triangle, lattice and honeycomb filler types commonly used in 3D printers. According to Ay (2023), among the triangle, lattice and honeycomb structures, the structure with the highest tensile strength is honeycomb, and the structure with the highest notch impact strength is triangle. Figure 16 shows the lattice structure used in the study.

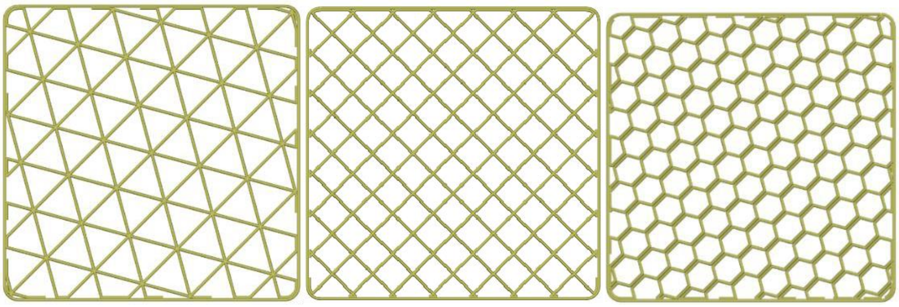

Figure 15. Triangular, Lattice and Honeycomb Structures

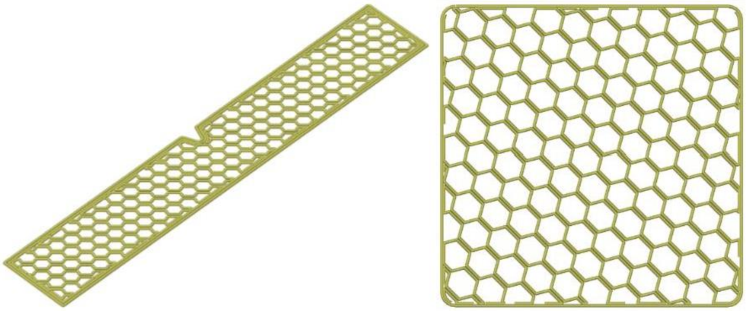

Figure 16. Lattice Structure Used in the Study (Honeycomb)

In addition to lattice structures, layer thickness also appears as an important early. Layer thicknesses affect many features such as surface roughness, strength, and visuality of the material. Figure 17 shows the effect of layer thickness on the number of layers in a 2 mm material thicknes.

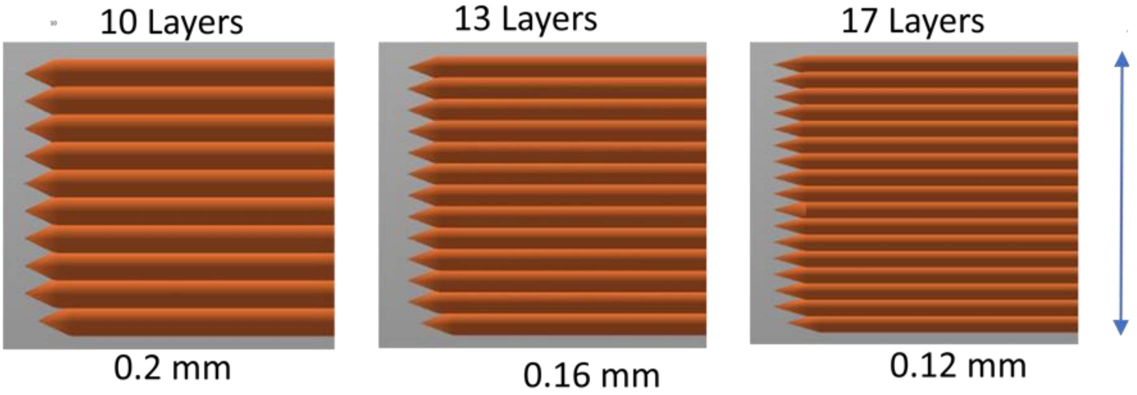

Figure 17. Effect of Layer Thickness on Number of Layers

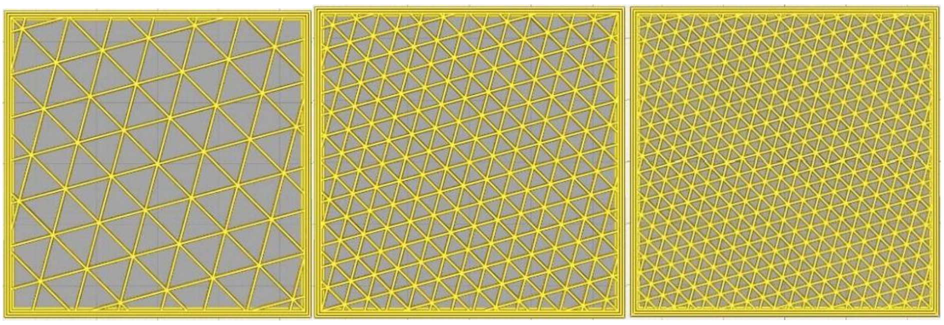

Figure 18. Appearance of 20-40-60% filling ratios in 25 cm2

Tensile testing is a test used to measure the strength or durability of parts produced with 3D printers. Tensile testing is performed to evaluate how the material behaves during tension and how durable it is. Tensile testing is important for understanding the engineering properties of the material, making design decisions and ensuring quality control. It is a common tool for determining the mechanical properties of materials such as PLA. The Tensile Test Specimen shown in Figure 19 was prepared according to DIN EN ISO 3167 standards.

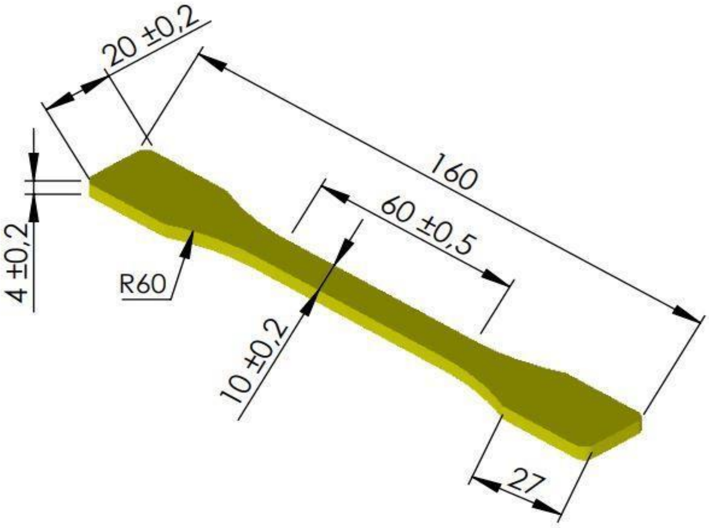

Figure 19. Tensile Test Specimen (DIN EN ISO 3167)

Notch impact testing is a test method used to evaluate material strength and fracture behavior. Notch impact testing of materials such as PLA printed with a 3D printer is an important tool for understanding the mechanical properties of the material and making design decisions. The Notch Impact Test Specimen shown in Figure 20 was prepared according to DIN EN ISO 75 standards.

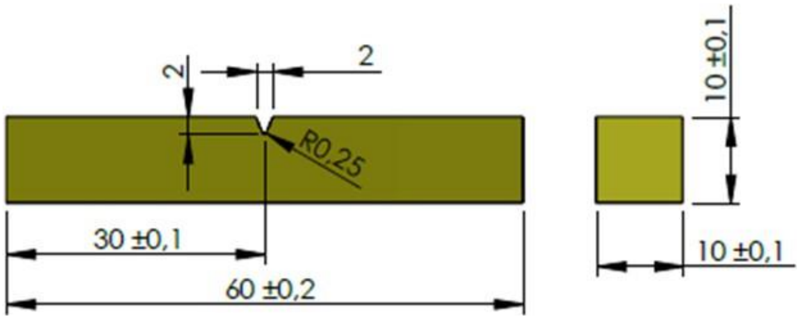

Figure 20. Notched Impact Test Sample (DIN EN ISO 75)

Previous studies have examined the effect of layer thickness on the mechanical properties of samples taken from PLA material produced with a 3D printer. In this study, the tensile strength was calculated to be 33.838 MPa at a layer thickness of 0.12 mm, a fill density of 60%, and a printing speed of 20 mm/s (Yiğittürk et al., 2023). According to Ay (2023), the tensile strength of PLA material in a triangular lattice structure was found to be 34.459

MPa with a layer thickness of 0.16 mm, a fill density of 60%, and a printing speed of 40 mm/s. Zhao et al. (2019) created theoretical models to investigate the tensile strength of PLA material used in additive manufacturing with different printing angles and layer thicknesses. They stated that the printed material with a 90° printing angle and a layer thickness of 0.1 mm had the highest tensile strength at 49.66 MPa.

Experimental Results

3.1. Tensile Test Results

According to the obtained results, the highest tensile strength value can be achieved with the optimal variables determined, such as a honeycomb fill structure, a feed speed of 20 mm/s, a layer thickness of 0.20 mm, and a fill density of 60%. Utilizing these parameters can enhance the tensile strength of PLA materials produced by FDM. Therefore, when aiming to increase the tensile strength of the final product, it is recommended to consider these optimal variables and carry out the printing process with these parameters. The use of a honeycomb fill structure, filaments with low thermal shrinkage values, and other specified parameters can contribute to achieving stronger and more durable printed products by increasing tensile strength. Tensile strength is directly proportional to the fill density. Table 4 presents the results of the tensile test measurements. The maximum tensile strength was determined to be 38.877 MPa. Figure 21 shows the tensile test sample after the experiment. Figure 22 displays the graph of the tensile test results.

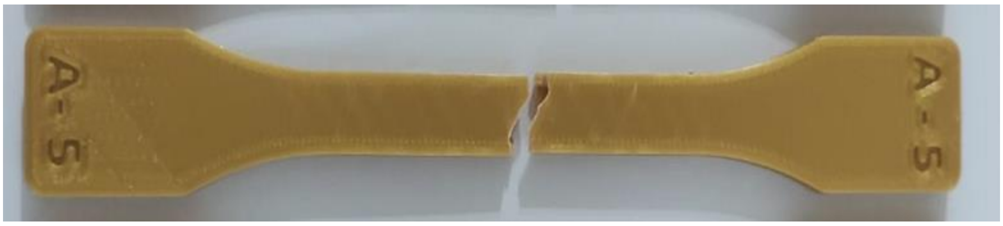

Figure 21. Tensile Test Sample After Testing

Table 4. Tensile test measurement result

Experiment no	Feeding speed (mm/s)	Layer thickness (mm)	Filling structure	Occupancy rate (%)	Max. stress (MPa)	S/N ratio (dB)
1	20	0.20	Honeycomb	20	29,8745	29,5060
2	20	0.20	Honeycomb	40	36,5509	31,2580
3	20	0.20	Honeycomb	60	38.877	31.7938

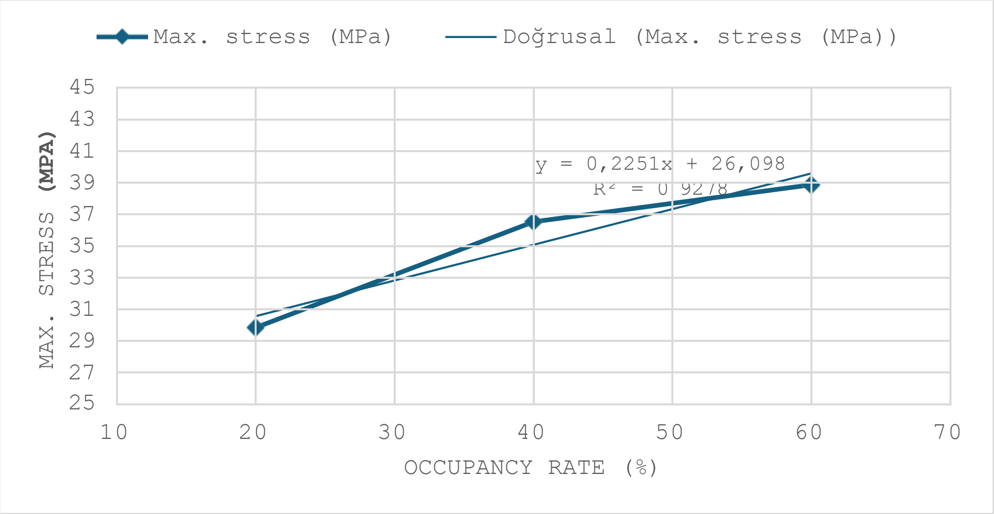

Figure 22. Tensile Test Experiment Results Graph

3.2. Notch Impact Test Results

Notch impact test is a material testing method used to evaluate the durability and fracture behavior of materials. The filler ratio and notch impact strength are directly proportional. According to these results, the maximum notch impact strength was found to be 0.266 J. Figure 23 shows the notch impact test sample after the experiment. Figure 24 shows the notch impact test experimental results graph.

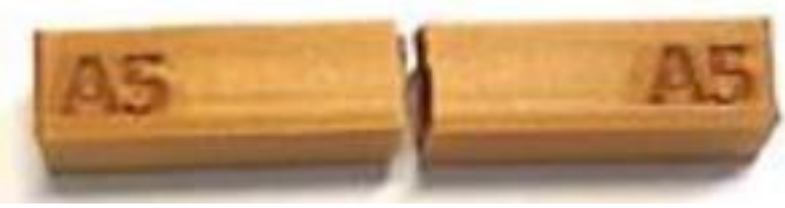

Figure 23. Post-Test Notch Impact Test Specimen

Table 5. Notch impact test measurement results

Experiment no.	Speed (mm/s)	Occupancy rate (%)	Filling structure	Layer thickness (mm)	Max. notch impact strength (J)	S/N (dB)
1	20	20	Honeycomb	0,20	0,207	0,2256
2	20	40	Honeycomb	0,20	0,261	0,2796
3	20	60	Honeycomb	0,20	0,266	0,2846

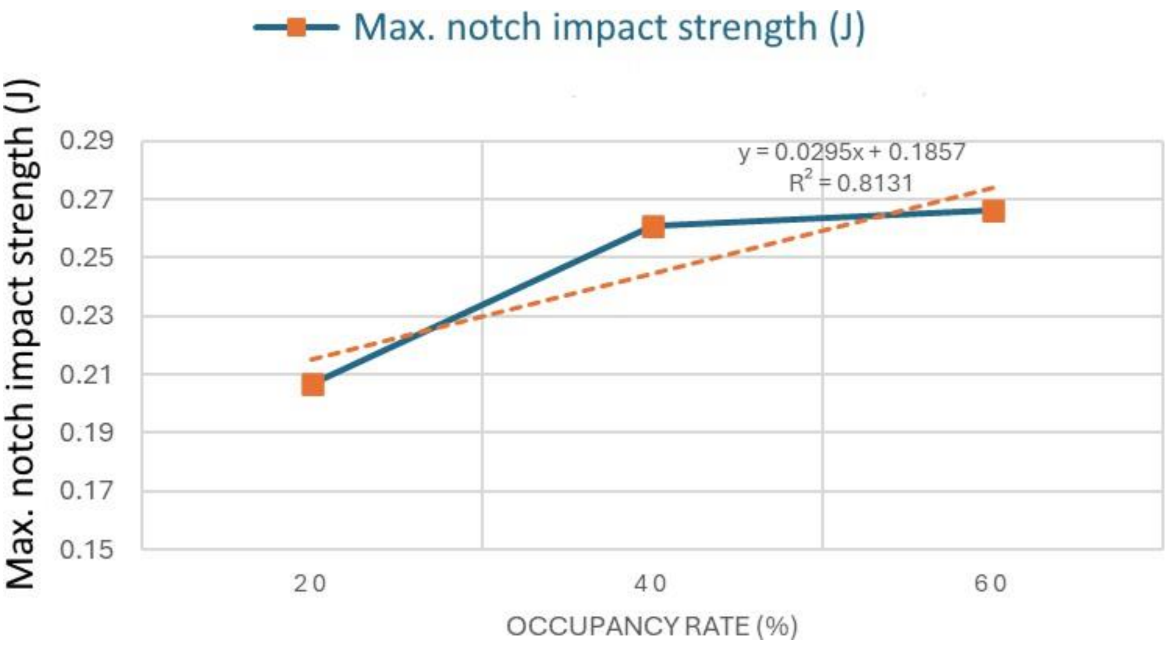

Figure 24. Notch Impact Test Experiment Results Graph

Evaluation of Results

The purpose of this research is to analyze and evaluate the tensile strength of PLA samples produced with an FDM 3D printer. The study aimed to achieve this objective using experimental and statistical analysis methods. Within the scope of the study, experiments were conducted considering combinations of specific parameters such as layer thickness (0.20 mm), printing speed (20 mm/s), and honeycomb fill structure. As a result of these experiments, the optimized settings combination was determined using fill densities of 20%, 40%, and 60%.

The optimum settings combination has a tensile strength of 38.877 MPa at a fill density of 60%. This result represents the highest tensile strength value obtained from the combination of the specified parameters.

In the optimum settings combination, a notched impact strength of 0.266 J was achieved at a fill density of 60%. This result represents the highest notched impact strength among the combinations of the specified parameters.

These findings indicate that using specific parameters effectively improves the mechanical properties of PLA samples produced with an FDM 3D printer. The optimum settings combination, including honeycomb fill structure, a layer thickness of 0.20 mm, a fill density of 60%, and a printing speed of 20 mm/s, has been identified as the recommended combination to achieve the desired tensile strength.

References

3 Boyutlu Yazıcı Çeşitleri. Retrieved from https://infotron.com.tr/3-boyutlu-yazici-cesitleri/

Akkoyun, F.B. (2024). Experimental Investigation Of Hollow Concrete Beam With Several Configurations Prepared By Using 3d Printer Technology, Yüksek Lisans Tezi, Gaziantep Üniversitesi, Fen Bilimleri Esntitüsü, Gaziantep

Alafaghani, A., Qattawi, A., Alrawi, B. & Guzman, A. (2017). Experimental Optimization of Fused Deposition Modelling Processing Parameters: A Design-for-Manufacturing Approach. Procedia Manuf., 10, 791–803. https://doi.org/10.1016/j.promfg.2017.07.079.

Baş, H. (2023). Bağlayici Püskürtme Tekniğinde Adaptif Dilimleme Yöntemi Ve Uygulama Teknolojisi. Doktora Tezi, Ondokuz Mayıs Üniversitesi, Fen Bilimleri Esntitüsü, Samsun.

Bio-Baskı (Bioprinting) Nedir. Retrieved from https://malzemebilimi.net/bio-baski-bioprinting-nedir.html

Brian J.L., Hsiao, K., Lipkowitz, G., Samuelsen, T., Tate, L. & Joseph, M. D. (2022). Characterization of a 30 µm pixel size CLIP-based 3D printer and its enhancement through dynamic printing optimization, Additive Manufacturing, 55, 102800 https://doi.org/10.1016/j.addma.2022.102800.

Bulus, E., İsmik, D., Mansuroğlu, D.S., Fındıkoğlu, M.S., Bozkurt, B., Şahin, Y.M., Doğancı, E., Doğancı, M.D. & Sakarya, G. (2019). Electrohydrodynamic atomization (EHDA) technique for the health sector of polylactic acid (PLA) nanoparticles. *Scientific Meeting on Electrical-Electronics & Biomedical Engineering and Computer Science.* doi: 10.1109/EBBT.2019.8742004

Das, S.C., Ranganathan, R. & Murugan, N. (2018), Yapı yönünün PolyJet 3D yazdırılmış parçaların mukavemeti ve maliyeti üzerindeki etkisi. *Hızlı Prototipleme Dergisi* , *24*(5), 832-839. https://doi.org/10.1108/RPJ-08-2016-0137

Dey, A. & Yodo, N. (2019). A systematic survey of FDM process parameter optimization and their influence on part characteristics. *Journal of Manufacturing and Materials Processing, 3*. https://doi.org/10.3390/JMMP3030064.

Dokuz, M.E. (2020). *3 Boyutlu DLP Yöntemiyle HA Katkılı Kompozit Üretimi ve Karakterizasyonu*. Yüksek Lisans Tezi, Necmettin Erbakan Üniversitesi, Fen Bilimleri Esntitüsü, Konya.

Erdem, C. (2024). *Kişisel Ölçü Kaşiği Rezini Kullanilarak 3 Boyutlu Yaziciyla Üretilen Test Örneklerinin Iç Yapisinin Değiştirilmesinin Malzemenin Mekanik Dayanimina Etkisinin İncelenmesi*. Uzmanlık Tezi. Çukurova Üniversitesi, Fen Bilimleri Esntitüsü, Adana

Gueche, Y.A., Sanchez-Ballester, N.M., Cailleaux, S., Bataille, B. & Soulairol, I. (2021). Selective Laser Sintering (SLS), a New Chapter in the Production of Solid Oral Forms (SOFs) by 3D Printing. *Pharmaceutics, 13*(8), 1212. https://doi.org/10.3390/pharmaceutics13081212

Ay, İ. et. al. (2023). FDM Üretim Yönteminde Kullanılan PLA Malzemesinin Dolgu Şeklinin Mekanik Özellikler Üzerine Etkisi. 4. Uluslararası Türk Dünyası Mühendislik ve Fen Bilimleri Kongresi, Antalya, Turkey

Plog, J., Jiang, Y., Pan, Y. & Yarin, A.L. (2020). Electrostatic charging and deflection of droplets for drop-on-demand 3D printing within confinements. *Additive Manufacturing, 36*, 101400. https://doi.org/10.1016/j.addma.2020.101400.

Raquez, J.M., Habibi, Y. & Murariu, M. (2013) Philippe Dubois, Polylactide (PLA)-based nanocomposites. *Progress in Polymer Science, 38*(10–11), 1504-1542, https://doi.org/10.1016/j.progpolymsci.2013.05.014.

AR, J. vd. (2016) Single-Step Fabrication of Computationally Designed Microneedles by Continuous Liquid Interface. *Production. PLoS ONE 11*(9). doi: 10.1371/journal.pone.0162518

Khadilkar, A., Wang, J. & Rai, R. Deep. (2019). learning–based stress prediction for bottom-up SLA 3D printing process. *Int J Adv Manuf Technol, 102*, 2555–2569. https://doi.org/10.1007/s00170-019-03363-4

Kristiawan, R., Imaduddin, F., Ariawa, D., Sabino, U. & Arifin, Z. (2021) A Review on the Fused Deposition Modeling (FDM) 3D printing: Filament Processing. *Materials and Printing Parameters. Open Engineering, 11*(1), 639-649

Lluch-Cerezo, J., Benavente, R., Meseguer, M.D., & Gutiérrez, S.C. (2019). Study of samples geometry to analyze mechanical properties in Fused Deposition

Modeling process (FDM). *Procedia Manuf, 41*(890), 7. https://doi.org/10.1016/J.PROMFG.2019.10.012.

Maden, H. & Kamber, Ş. (2018). The Faults of Prototype Parts Produced with Fdm Technology And Prevention Of These Faults. *International Journal Of 3d Printing Technologies and Digital Industry, 2*(1), 40-51.

Marșavina, L., Vălean, C., Mărghitaș, M., Linul, E., Razavi, S.M.J., Berto, F. & Brighenti, R. (2022). Effect of the manufacturing parameters on the tensile and fracture properties of FDM 3D-printed PLA specimens. *Eng Fract Mech, 274*:108766. https://doi.org/10.1016/J.ENGFRACMECH.2022.108766.

Öztürk, P. (2019). *3 Boyutlu Yazicilarin Tasarimci-Kullanici İlişkisi Kapsaminda Değerlendirilmesi ve Endüstriyel Ürünlerin Kişiselleştirilmesine Etkisi*. Yüksek Lisans Tezi, Marmara Üniversitesi, Fen Bilimleri Esntitüsü, İstanbul.

PLA Filament, Porima TDS. Retrieved from https://www.porima3d.com/porima-pla-filament

Ráž, K., Chval, Z. & Thomann, S. (2023) Minimizing Deformations during HP MJF 3D Printing. *Materials, 16*(23), 7389. https://doi.org/10.3390/ma16237389

Shahriar, S. R., Jiang, L., Park, J., Islam, M. S., Perez, B., & Peng, X. (2024). Experimental and FEA Simulations Using ANSYS on the Mechanical Properties of Laminated Object Manufacturing (LOM) 3D-Printed Woven Jute Fiber-Reinforced PLA Laminates. *Journal of Manufacturing and Materials Processing, 8*(4), 152.

Tee, Y.L., Peng, C., Pille, P., Leary, M. & Tran, P. (2020). Kompozit Malzemelerin PolyJet 3D Baskısı: Deneysel ve Modelleme Yaklaşımı. *JOM, 72*, 1105–1117. https://doi.org/10.1007/s11837-020-04014-w

Toprak, E. (2023). *Üç Boyutlu Yazicilar İçin Ekstrüder Tasarimi Ve Filament Üretimi: Dinamik Ve Mekanik Özelliklerin İncelenmesi Ve Karşilaştirilmasi.* Yüksek Lisans Tezi, Bülent Ecevit Üniversitesi, Fen Bilimleri Esntitüsü, Zonguldak.

Zhu, W., Ma, X., Gou, M., Mei, D., Zhang, K. & Chen, S. (2016). 3D printing of functional biomaterials for tissue engineering, *Current Opinion in Biotechnology, 40*, 103-112, https://doi.org/10.1016/j.copbio.2016.03.014.

ANALYSIS OF SOLUTION OF THE TWO-DIMENSIONAL HEAT EQUATION IN TERMS OF ELLIPTIC FUNCTIONS

Nurcan BAYKUŞ SAVAŞANERİL

Chapter 9

Analysis of Solution of the Two-Dimensional Heat Equation in Terms of Elliptic Functions

NURCAN BAYKUŞ SAVAŞANERİL[1]

1. Introduction

The two-dimensional heat equation holds critical importance in engineering and applied mathematics, as its solutions in various geometric regions play a vital role in understanding complex physical processes. In this context, the use of elliptic functions for solving the two-dimensional heat equation in different geometric regions has garnered increasing interest in recent years. Specifically, Green's functions and elliptic functions have emerged as significant tools in the analytical solutions of such problems.

The Dirichlet problem for the Laplace equation involves finding a function $U(z)$ that is harmonic within a bounded domain $D \subset \mathbb{R}^2$, continuous up to the boundary ∂D, and assumes given values $U_0(z)$ on the boundary ∂D. Here, $U_0(z)$ is a continuous function on ∂D, and the problem can be expressed as:

$$\nabla^2 U = 0, \quad z \in D; \quad U\big|_{z\in\partial D} = U_0(z). \qquad (1)$$

In this context, for a point (x, y) in the plane $\mathbb{R}^2$, the complex notation $z = x + iy$ is used. $U(z) = U(x, y)$ and $U_0(z) = U_0(x, y)$ are real functions, and, $\nabla^2 = \frac{\partial^2}{\partial x^2} + \frac{\partial^2}{\partial y^2}$ is the Laplace operator.

Similarly, the Dirichlet problem for the Poisson equation can be formulated as:

$$\nabla^2 U = h(z), \quad z \in D; \quad U\big|_{z\in\partial D} = U_0(z). \quad (2)$$

This paper presents a comprehensive analysis of various methods for solving the two-dimensional heat equation in rectangle, square, triangle, and ellipse regions. The proposed solutions for each region are expressed in terms of elliptic functions, and the effectiveness of these methods is compared with traditional solution techniques.

---

[1] Prof. Dr., Dokuz Eylul University, Türkiye, nurcan.savasaneril@deu.edu.tr https://orcid.org/0000-0002-3098-2936

For instance, the study by Brovar et al. (2001) explored the use of Green's functions in solving the Dirichlet and Stokes exterior boundary problems for the Earth's ellipsoid. Similarly, Sezer (1992) presented a solution to the Dirichlet problem using elliptic functions. The works of Kurt and Sezer (2004, 2006) provide significant contributions to solving Dirichlet problems in square and triangular regions using elliptic functions.

This study aims to introduce new methods that enhance the effectiveness of solving the two-dimensional heat equation in different geometric regions, comparing the numerical results of these methods with traditional techniques such as the Method of Separation of Variables and the Finite Element Method. Notably, the analytical solution presented by Baykuş Savaşaneril and Delibaş (2016) for the two-dimensional heat equation in an elliptical region demonstrates the effectiveness of this approach.

In conclusion, this paper offers a comprehensive evaluation of the use of elliptic functions in solving the two-dimensional heat equation in engineering and applied mathematics, making significant contributions to the literature in this field.

As is well known, the solution of the Dirichlet problem using the method of separation of variables can only be obtained for a limited domain D with a sufficiently simple boundary.

Conformal mappings provide a highly universal algorithm for solving the Dirichlet problem for two-dimensional domains. These mappings allow the construction of the Green function for the Laplace equation in a domain D that can be conformally mapped onto the unit circle or the upper half-plane. However, if the domain D is a rectangle, square, triangle, or ellipse, the analytic function that maps D conformally onto the unit circle or the upper half-plane, i.e., the Green function for D, cannot be expressed in terms of elementary functions. Nevertheless, the Green function for a rectangular, square, triangular, or elliptical domain can be expressed in terms of elliptic functions.

The purpose of this study is first to determine the analytic function that maps the rectangular, square, triangular, or elliptical domain D onto the upper half-plane or the unit circle in terms of elliptic functions, using the Schwarz Christoffel transformation and conformal mapping. Then, using the relationship between the obtained analytic function and the Green function, the goal is to find the solution of the Dirichlet problem for the rectangular, square, triangular, or elliptical domain in terms of elliptic functions.

2. Elliptic Integrals and Functions

The integral

$$\int_0^t \frac{d\tau}{\sqrt{\left(1-\tau^2\right)\left(1-k^2\tau^2\right)}} \qquad t=\sin\varphi$$
$$=\int_0^u du_1 = u = sn^{-1}\left(t,k\right) = F\left(\varphi,k\right) \tag{3}$$

is called the normal elliptic integral of the first kind, where k , $\left(0<k<1\right)$ is any number. When $t=1,$ Eq. (3) is said to be complete and becomes

$$\int_0^1 \frac{d\tau}{\sqrt{\left(1-\tau^2\right)\left(1-k^2\tau^2\right)}} = \int_0^K du_1$$
$$=F\left(\frac{\pi}{2},k\right) \equiv K(k) \equiv K. \tag{4}$$

or

$$\int_0^1 \frac{d\tau}{\sqrt{\left(1-\tau^2\right)\left(1-k'^2\tau^2\right)}} = \int_0^{K'} du_1$$
$$=F\left(\frac{\pi}{2},k'\right) \equiv K'(k) \equiv K(k') \equiv K' \tag{5}$$

Here, k is known as the modulus, and k' $\left(0<k'<1\right)$ is the complementary modulus, satisfying $k'^2=1-k^2.$ When $k=0$ in equation (3), we obtain $u=\sin^{-1}t$ or $t=\sin u$. For $k\neq 0$, the integral in equation (3) is represented by $u=\sin^{-1}\left(t,k\right)$, or $u=\sin^{-1}t$, and $t=\sin u$. The function $\mathrm{sn}\,u$ is referred to as the Jacobian elliptic function. Additionally, two other Jacobian elliptic functions are defined as

$$cn\left(u,k\right)=\sqrt{1-sn^2u}, \quad dn\left(u,k\right)=\sqrt{1-k^2sn^2u.}$$

3. The Conform Mapping of Domains

In complex analysis, conformal mappings are powerful tools for transforming one domain into another while preserving angles. These mappings are essential in various fields, such as fluid dynamics, electrostatics, and complex potential theory. The specific types of domains we often deal with include rectangles, squares, triangles, and ellipses. Each domain has its unique conformal mapping properties and applications, and understanding these mappings is crucial for solving complex problems in mathematical physics and engineering.

Below, we explore the conformal mappings associated with different domain shapes:

These sections provide a comprehensive overview of how different geometric shapes can be mapped conformally from one domain to another, preserving the essential properties of the figures while transforming them into more useful or manageable forms.

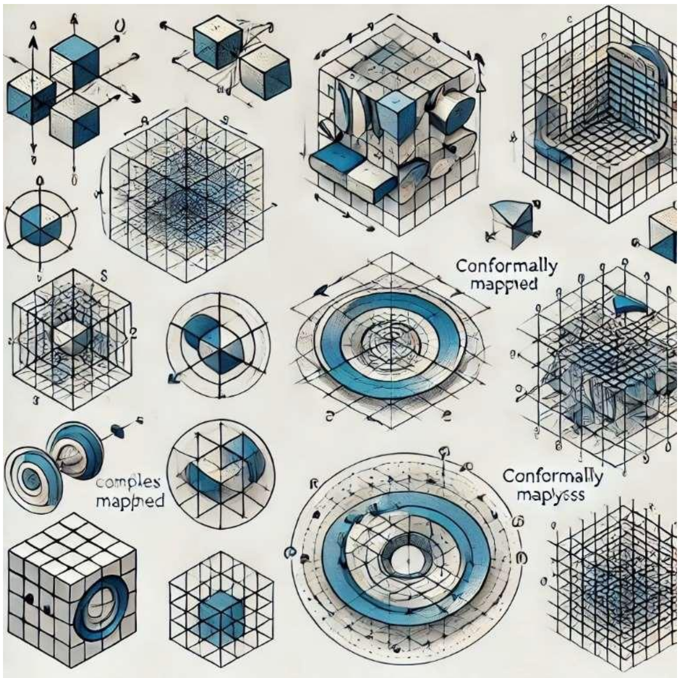

Figure 1. Visualization of conformal mappings in complex analysis

The illustration shows various geometric domains such as rectangles, squares, triangles, and ellipses being transformed into simpler shapes while preserving angles. Conformal mappings are key tools in fields like fluid dynamics, electrostatics, and complex potential theory. The arrows and grids represent the process of transformation, illustrating how these complex shapes can be mapped into more manageable forms like circles or regular shapes.

3.1. The Conform Mapping of a Rectangle Domain

A detailed examination of the conformal mapping that transforms the upper half-plane or another simpler domain into a rectangular domain. This involves techniques like the Schwarz–Christoffel transformation, which allows us to map the upper half-plane onto a rectangle with specified vertices.

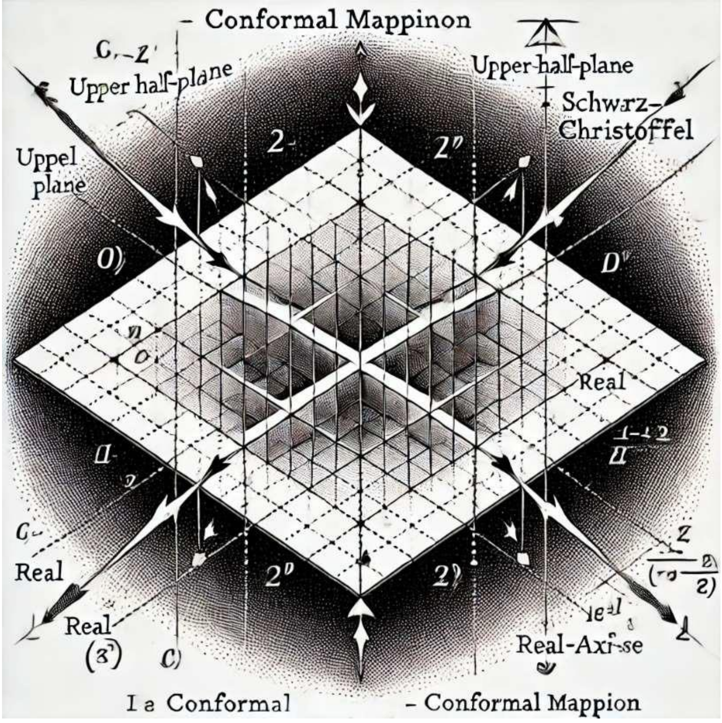

Figure 2. Visualization of the conformal mapping that transforms the upper half-plane into a rectangular domain.

This transformation is performed using the Schwarz–Christoffel transformation. The four symmetric points in the complex plane are mapped from the upper half-plane to the specified vertices of the rectangle. The arrows indicate the transformation process and how the points are mapped. Gridlines and coordinates are included to provide a clearer understanding of the mapping process.

Consider a rectangle in the complex $z-$ plane with vertices located at points $A_1\left(z=a\right)$, $A_2\left(z=a+ib\right)$, $A_3\left(z=-a+ib\right)$,and $A_4\left(z=-a\right)$, where a and b are positive real numbers $(a>0, b>0)$. Additionally, there are four symmetric points on the real axis: $a_1\left(t=1\right)$, $a_4\left(t=-1\right)$, $a_2\left(t=\frac{1}{k}\right)$ and $a_3\left(t=-\frac{1}{k}\right)$, with $0<k<1$. A function $z=f(t)$ exists that maps the upper half of the $t-$

plane (where $\operatorname{Im} t > 0$) conformally onto the rectangle A_1, A_2, A_3, A_4, such that $f(0)=0,\ f(\pm 1)=\pm a$ and $f(\pm \frac{1}{k}) = \pm a + bi$ with the condition that $0 < k < 1$. This function, based on the Schwarz–Christoffel transformation, can be expressed as

$$z = f(t) = c\int_0^t \left[\left(1-\tau^2\right)\left(1-k^2\tau^2\right)\right]^{-1/2} d\tau \qquad (6)$$

The constants c and k can be determined by matching the points a_1 and a_2 on the real $t-$axis with the vertices A_1 and A_1 of the rectangle. The integral in equation (6) cannot be expressed using elementary functions, as it represents a standard elliptic integral of the form given in equation (3), and is expressed as

$$z = f(t) = cF(t,k) \qquad (7)$$

By substituting the conditions

$a_1(t=1) \leftrightarrow A_1(z=a)$ and

$a_4(t=-1) \leftrightarrow A_4(z=-a)$ into equation (6) and applying equation (4), the relationship

$$a = cK(k) \qquad (8)$$

is obtained.

Since $a_2\left(t=\frac{1}{k}\right)$ corresponds to $A_2\left(z=a+ib\right)$, equations (6) and (5) imply that $a+ib = c\left[K(k)+iK'(k)\right]$, which leads to

$$b = cK'(k) \qquad (9)$$

Using equations (8) and (9), for given values of a and b, the equation

$$aK'(k) = bK(k) \qquad (10)$$

can be solved to determine the values of the constants k and c. As a result, the vertices of the rectangle are expressed in terms of elliptic integrals, and the function in equation (6), which conformally maps the upper half of the $t-$plane onto the specified rectangle in the $z-$plane, is fully defined. Moreover, when $c=1$ (since c is arbitrary), the integral in equation (6) becomes the standard elliptic integral, and its inverse is known as the Jacobian elliptic function. Since the mapping is one-to-one, the inverse of equation (6), expressed as

$$t = sn(z,k) \text{ or } t = sn(z) \qquad (11)$$

produces a conformal mapping that transforms the interior of the rectangle with vertices at

$A_1 = K, A_2 = K + iK', A_3 = -K + iK'$, and $A_4 = -K$ onto the upper half-plane where $\operatorname{Im} t > 0$.

On the other hand, given that the conformal mapping of the upper half-plane $(\operatorname{Im} t > 0)$ onto the circle $|w| < 1$ in the $w-$plane is expressed as

$$w = \frac{i - t}{i + t}, \qquad (12)$$

the conformal mapping of the rectangle in the $z-$plane onto the unit circle $|w| < 1$ in the $w-$plane can be written as

$$w = F(z) = \frac{i - snz}{i + snz} \qquad (13)$$

(Moretti, G., 1964)

3.2. The Conformal Mapping of a Square Domain

Here, we discuss the special case of a rectangular domain where all sides are equal, i.e., a square. The conformal mapping process for a square requires similar techniques to those used for a rectangle, but with additional symmetry considerations that can simplify the mapping.

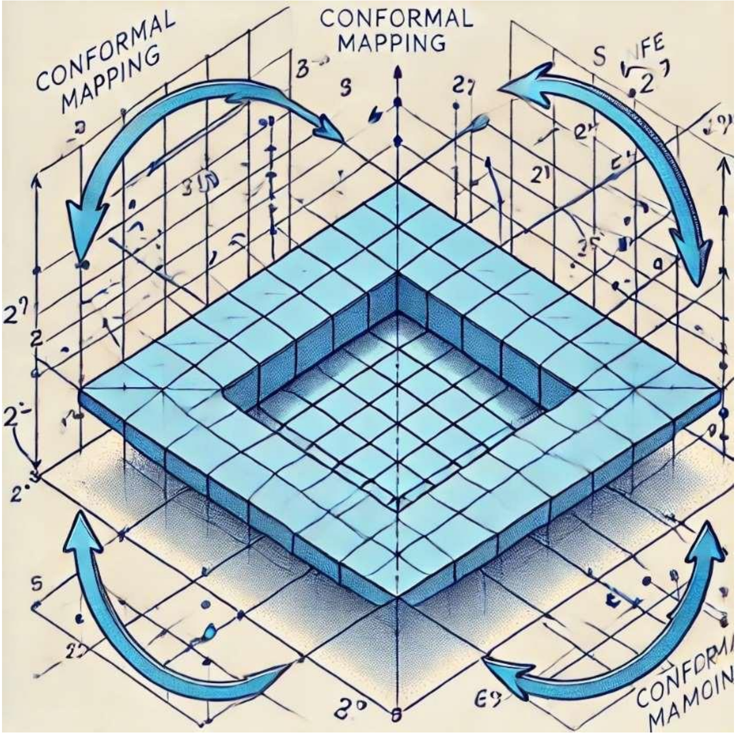

Figure 3. Visualization of the conformal mapping of a square domain.

The square, with all sides equal, is transformed using techniques similar to those used for a rectangle, but with additional symmetry considerations that simplify the transformation. The arrows highlight the transformation process and the symmetry of the square, while the gridlines and symmetry axes illustrate how the transformation occurs.

In the context of the Schwarz–Christoffel formula, if we set $z_0 = 0, z_1 = i, z_2 = -1, z_3 = -i;$

$$a_1 = 0,\ a_2 = \frac{\pi}{2}, a_3 = \pi, a_4 = \frac{3\pi}{2},$$

we obtain $w = w_0 + c\int \frac{dz}{\sqrt{1-z^4}}$

(Moretti, G., 1964).

If the origin is at the center of the square, then $w_0 = 0$ and $c = 1,$ leading to

$$w = \int_0^z \frac{dz}{\sqrt{1-z^4}}. \tag{13}$$

By setting

$$z = \frac{1}{\sqrt{2}} sd\left(\sqrt{2}t \left| \frac{1}{2}\right.\right), \tag{14}$$

we find

$$1 - z^4 = 1 - \frac{1}{4} sd^4\left(\sqrt{2}t\right),$$

$$dz = cd\left(\sqrt{2}t\right) nd\left(\sqrt{2}t\right) dt \tag{15}$$

Hence

$$\begin{aligned} w &= \int_0^t \frac{cd\left(\sqrt{2}t\right) nd\left(\sqrt{2}t\right)}{\sqrt{1-\frac{1}{4} sd^4\left(\sqrt{2}t\right)}} dt \\ &= \int_0^t \frac{cn\left(\sqrt{2}t\right) dt}{\sqrt{\left(dn^2\left(\sqrt{2}t\right) - k^2 sn^2\left(\sqrt{2}t\right)\right)\left(dn^2\left(\sqrt{2}t\right) + k^2 sn^2\left(\sqrt{2}t\right)\right)}} \\ &= \int_0^t \frac{cn\left(\sqrt{2}t\right)}{\sqrt{1-2k^2 sn^2\left(\sqrt{2}t\right)}} dt \\ &= \int_0^t \frac{cn\left(\sqrt{2}t\right)}{\sqrt{cn^2\left(\sqrt{2}t\right)}} dt = t. \end{aligned} \tag{16}$$

As a result, the conformal mapping of the square in the $z-$ plane onto the unit circle $|w| < 1$ in the $w-$plane can be expressed as

$$w = \frac{1}{\sqrt{2}} sd\left(\sqrt{2}z \left| \frac{1}{2}\right.\right) \tag{17}$$

(Kurt, N., 2008)
as shown in Fig.4

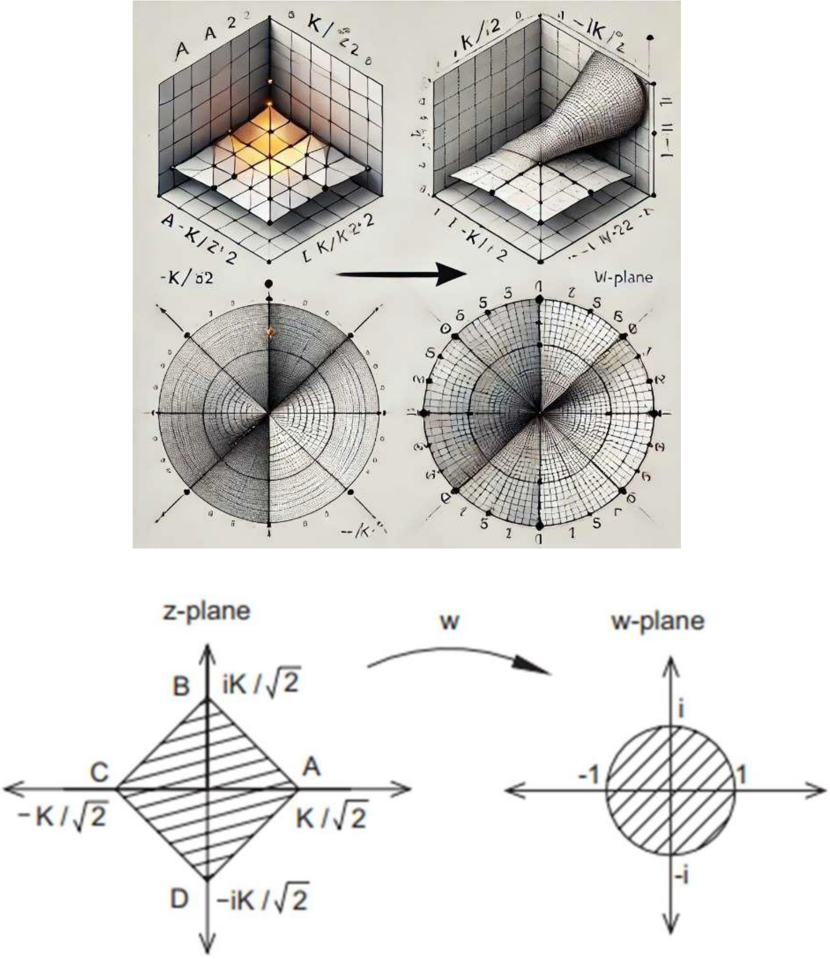

Fig. 4. Conformal mapping of the square in the $z-$plane onto the unit circle in the $w-$plane.

The square region is first rotated by $\alpha = \frac{\pi}{4}$ and then displaced by $z' = z + \frac{K}{2i}$ (Fig. 5) the conformal mapping of the square given in the $z-$plane onto the unit circle $|w|<1$ in the $w-$plane can be written as

$$w = \frac{i\left(1-k^2 sn^4 z\right) - 2snz\,cnz\,dnz}{i\left(1-k^2 sn^4 z\right) + 2snz\,cnz\,dnz},$$

$$k = 3 - 2\sqrt{2} \tag{18}$$

(Kurt, N. 2008)

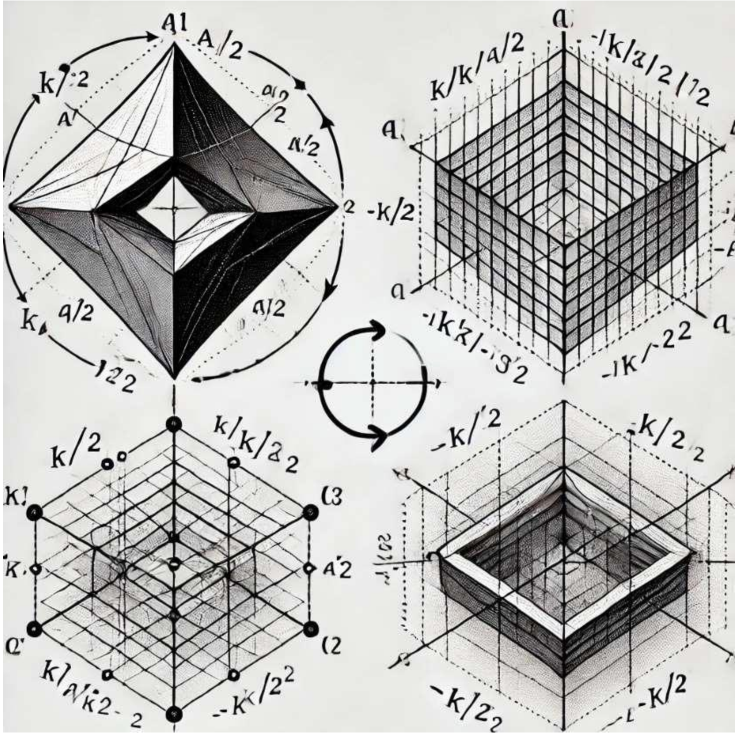

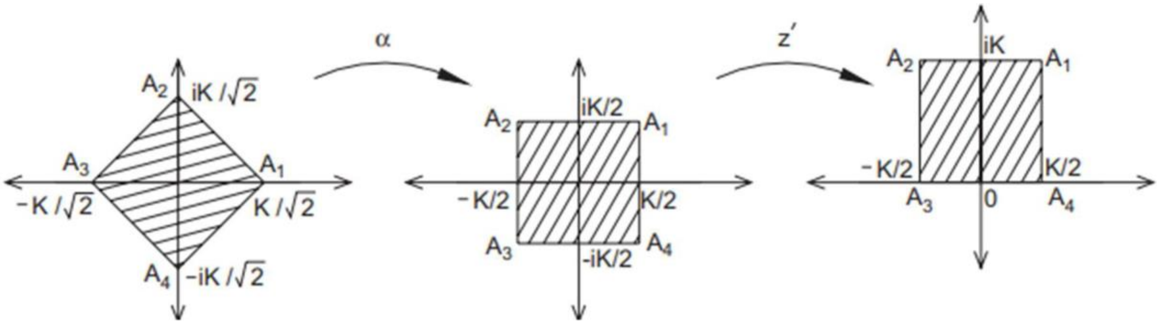

Fig. 5. First rotating by $\alpha = \frac{\pi}{4}$ and displacing by $z' = z + \frac{K}{2i}$ the square.

3.3. The Conform Mapping of a Triangle Domain

This section focuses on the conformal mapping that maps simpler domains onto a triangular domain. The Schwarz Christoffel transformation is again a central tool, as it can be adapted to map a half-plane or unit disk onto a triangle, preserving the angles at the vertices.

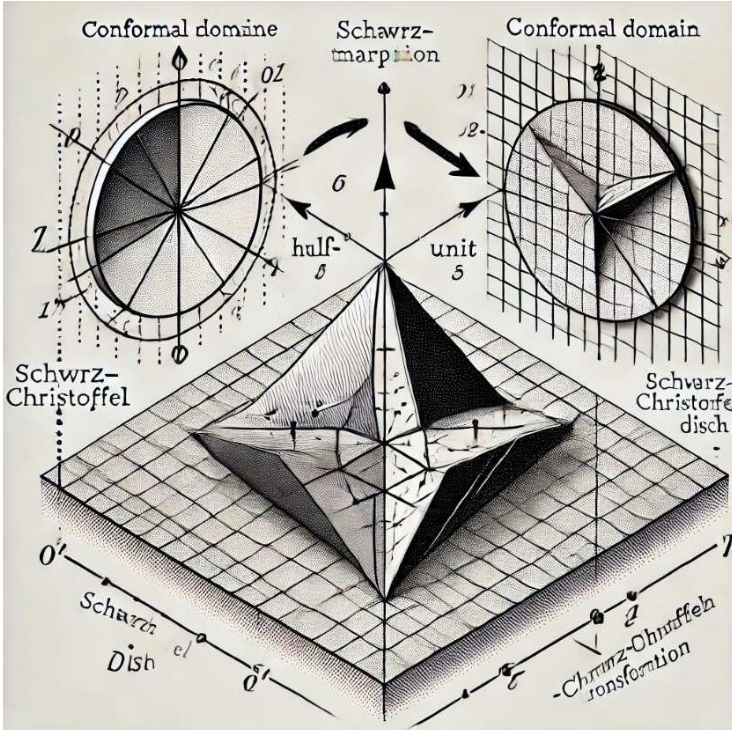

Fig. 6. the conformal mapping that maps simpler domains onto a triangular domain

The conform mapping which transforms the triangle region onto upper half-plane (Moretti, G., 1964) is

$$t = 2sn\left(z\sqrt{2}\right)dn\left(z\sqrt{2}\right). \tag{19}$$

$$K\left(\tfrac{1}{2}\right), \quad k = \tfrac{1}{2}$$

On the other hand, recalling that the conformal mapping of the upper half-plane $\operatorname{Im} t > 0$ onto the circle $|w| < 1$ in the w-plane is given by $w = \frac{i-t}{i+t}$, the conformal mapping of the triangle given in the $z-$plane onto the unit circle, $|w| < 1$ in the w-plane can be written as

$$w = F(z) = \frac{i - \sqrt{2}sn\left(\sqrt{2}z\right)dn\left(\sqrt{2}z\right)}{i + \sqrt{2}sn\left(\sqrt{2}z\right)dn\left(\sqrt{2}z\right)} \tag{20}$$

(Kurt, N., & Sezer, M., 2006)

which is illustrated in Fig. 7.

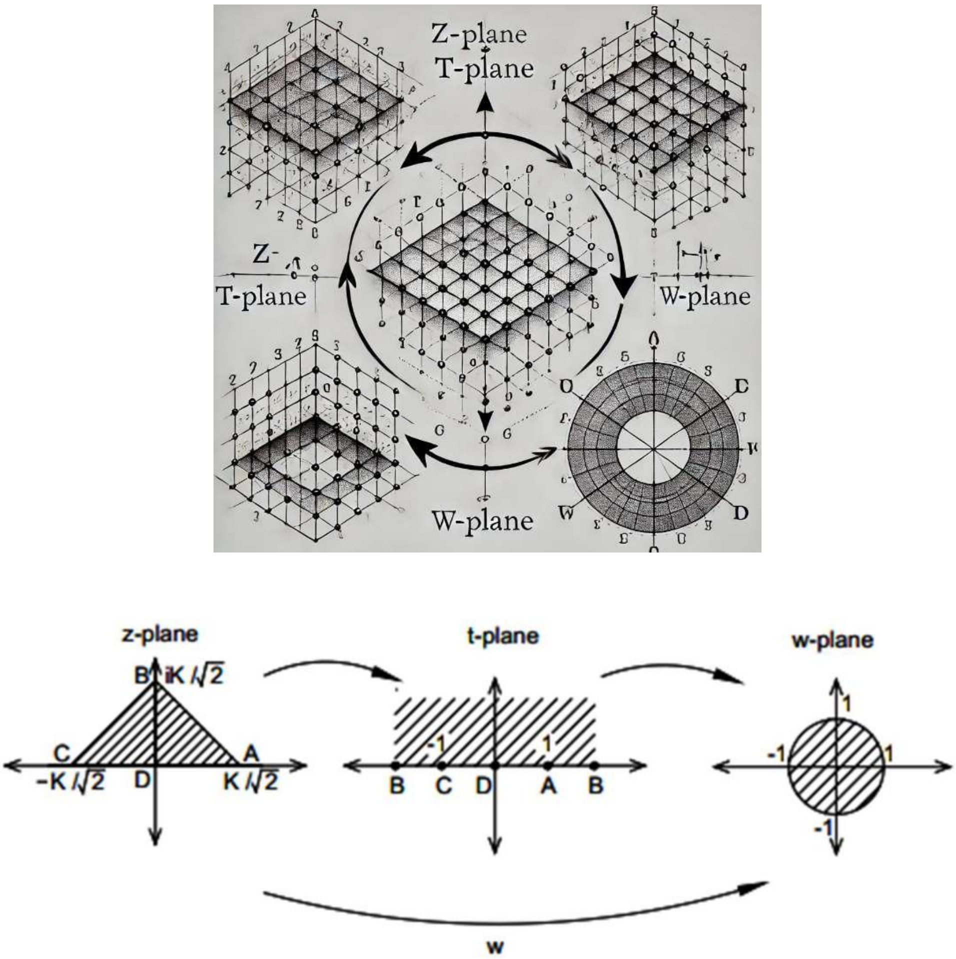

Fig. 7. Conformal mapping of the triangle in the $z-$plane onto the unit circle in the $w-$plane.

3.4. The Conform Mapping of a Ellipse Domain

Finally, we explore the conformal mapping of an ellipse domain. Elliptic domains are more complex due to their curvature, and mappings typically involve elliptic functions or integrals. Understanding these mappings is essential for problems involving elliptic geometries.

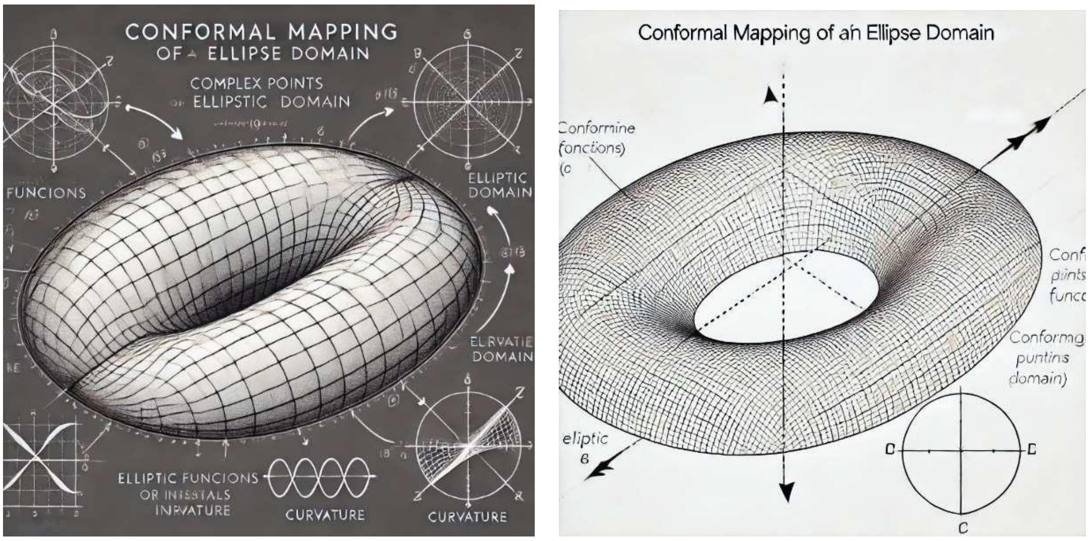

Figure 8. Conformal mapping of the ellipse domain.

Let apply the transformation $\zeta_1 = \frac{z}{c}$ to carry the ellipse onto the unit circle $|w| < 1$. The ellipse with two slits drawn in Fig.3. is mapped onto a rectangle in the ζ_2 – plane by means of

$$\zeta_2 = \arcsin \zeta_1.$$

Let $\frac{\pi}{2} = K$ and $\arcsin h\left(\frac{b}{c}\right) = \frac{K'}{2}$, that is

$$K' = \left(\frac{4K}{\pi}\right)\arcsin h\left(\frac{b}{c}\right).$$

With $\zeta = \left(\frac{2K}{\pi}\right)\zeta_1$, $w_1 = sn\zeta$, the horizontal sides are mapped onto arcs of a circle and the vertical sides onto the edges of two cuts. In this way, each cut in the z –plane corresponds to a cut in the w–plane. Consequently, these cuts can be sealed. In order to obtain m from K and K', note that

$$q = \exp\left(-\frac{K'\pi}{K}\right) = \exp\left(-4\arcsin h\frac{b}{c}\right) = \frac{c^4}{(b+a)^4} = \frac{(a-b)^2}{(a+b)^2} \qquad (21)$$

The conformal mapping of the ellipse given in the z –plane onto the unit circle $|w| < 1$ in the w–plane can be written as (Moretti, G., 1964)

$$w = m^{\frac{1}{4}}\left(\frac{2K}{\pi}\arcsin\frac{z}{c}\right) \qquad (22)$$

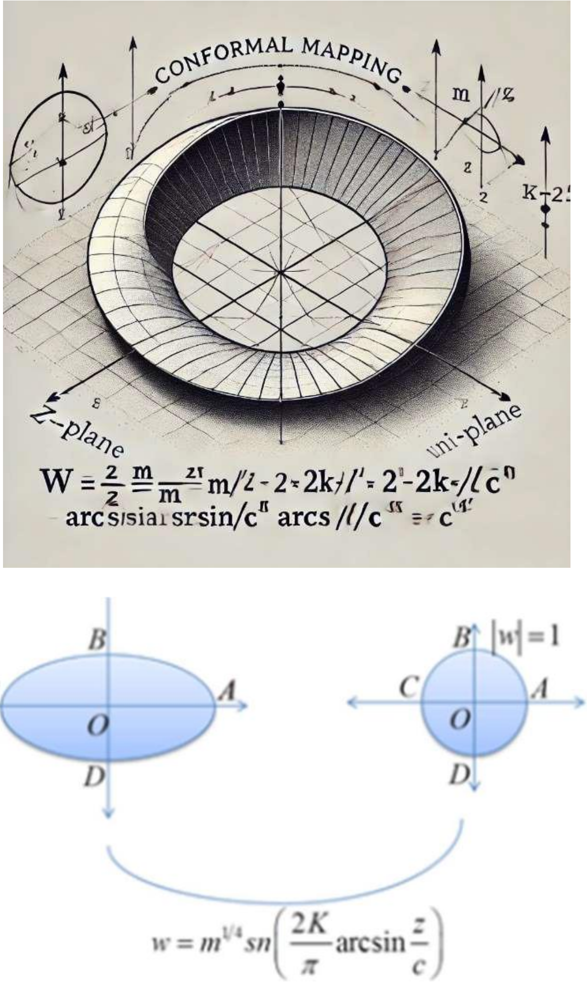
CONFORMAL MAPPING
Z-plane
uni-plane
B
C
A
O
D
|w|=1
$w = m^{1/4} sn\left(\frac{2K}{\pi}\arcsin\frac{z}{c}\right)$

Fig. 9. The ellipse with two slits drawn.

4. The Determination of Green Function for Domains

In this section, we address the process of determining Green's functions for different geometric domains. Green's functions play a crucial role in solving differential equations, and their derivation for various regions takes into account specific boundary conditions and geometric characteristics. The following subsections will explore in detail how Green's functions are determined for rectangular, square, triangular, and elliptical regions.

The Green function $G(z,\zeta)$ for the Dirichlet problem associated with the Laplace equation in the domain D is defined as follows:

$$G(z,\zeta) = \frac{1}{2\pi}\ln|z-\zeta| + g(z,\zeta)$$

where

$$z \in D, \zeta \in D, \tag{23}$$

where g is a harmonic function in D for each $\zeta \in D$, and $g(z,\zeta) = -\frac{1}{2\pi}\ln|z-\zeta|$. Consequently, $G(z,\zeta)=0$ for each z on the boundary ∂D, where $z=x+iy$ and $\zeta = \xi + i\eta$. When the domain D is simply connected, the task of finding this Green function can be transformed into the problem of identifying an analytic function that maps D onto either the upper half-plane $\operatorname{Im}(W)>0$ or the unit disk $|w|<1$. This transformation is possible because $w=F(z)$ is an analytic function that maps the domain D in the $z-$plane onto the upper half-plane in the $w-$ plane, with $F'(z)\neq 0$ within D. Thus, the mapping is one-to-one.

$$G = \frac{1}{2}\left|\frac{F(z)-F(\zeta)}{F(z)-\overline{F(\zeta)}}\right|, \qquad (24)$$
$$z=x+iy, \quad \zeta=\xi+i\eta$$

and, if the analytic function $W=F(z)$ maps D onto the unit circle $|w|<1$, then the Green function of the Dirichlet problem for the Laplace operator in D becomes

$$G(z,\zeta) = \frac{1}{2\pi}\ln|w(z,\zeta)|, \qquad (25)$$
$$w(z,\zeta) = \frac{F(z)-F(\zeta)}{1-F(z)\,\overline{F(\zeta)}}$$

4.1.The Determination of the Green's Function for a Rectangular Region

In this section, we explore the derivation of the Green's function specifically tailored to a rectangular region, a fundamental shape in many physical and mathematical applications. The solution process involves addressing boundary conditions unique to rectangular domains, providing insights into how these conditions influence the resultant Green's function.

If one takes D as the rectangle $A_1(K,0), A_2(K,K'), A_3(-K,K'), A_4(-K,0)$ then from Eqs. (13) and (25), the Green function for the rectangle is found in the form

$$\begin{aligned} G &= \frac{1}{2}\ln\left|\frac{sn\,z - sn\zeta}{sn\,z-\overline{sn\zeta}}\right| \\ &= \frac{1}{2\pi}\operatorname{Re}\ln\left|\frac{sn\,z-sn\zeta}{sn\,z-\overline{sn\zeta}}\right|. \end{aligned} \qquad (26)$$

4.2.The Determination of the Green's Function for a Square Region

Here, we focus on the determination of the Green's function for a square region, a special case of the rectangular domain. Due to its symmetrical properties, the square region allows for unique simplifications in the mathematical formulation, which we will discuss in detail.

If one takes D as the square $A_1\left(\frac{K}{2},K\right), A_2\left(-\frac{K}{2},K\right), A_3\left(-\frac{K}{2},0\right)$, $A_4\left(\frac{K}{2},0\right)$ then from Eqs. (18) and (25), the Green function for the square is derived in the form

$$G=\frac{1}{2\pi}\ln\left|\frac{sn(2z)-sn(2\zeta)}{sn(2z)-\overline{sn(2\zeta)}}\right|$$

$$z=x+iy,\quad \zeta=\xi+i\eta. \qquad (27)$$

4.3.The Determination of the Green's Function for a Triangle Region

This section is dedicated to the development of the Green's function for a triangular region. Given the triangular domain's geometric properties, the derivation presents distinct challenges and requires a different approach compared to rectangular or square regions. If one takes D as the triangle $A_1\left(-\frac{K}{\sqrt{2}},\right)$ $A_2\left(\frac{K}{\sqrt{2}},\right), A_3\left(0\ \frac{K}{\sqrt{2}}\right)$

then from Eqs. (20) and (25), the Green function for the triangle is derived in the form

$$G=\frac{1}{2\pi}\ln\left|\frac{sn\left(z\sqrt{2}\right)dn\left(z\sqrt{2}\right)-sn\left(\zeta\sqrt{2}\right)dn\left(\zeta\sqrt{2}\right)}{sn\left(z\sqrt{2}\right)dn\left(z\sqrt{2}\right)-\overline{sn\left(\zeta\sqrt{2}\right)dn\left(\zeta\sqrt{2}\right)}}\right|$$

$$z=x+iy,\quad \zeta=\xi+i\eta \qquad (28)$$

4.4.The Determination of the Green's Function for a Ellipse Region

In this part, we examine the Green's function within an elliptical region. The elliptical shape introduces a new set of boundary conditions and complexities, necessitating advanced techniques to obtain a precise solution.

If one takes D as the elliptic $A_1(K,0), A_2\,(0,K'), A_3\,(-K,0), A_4\,(0,K')$ the from Eq.(21) and (24), the Green function for the cut-ring is found in the from

$$G=\frac{1}{2\pi}\ln\left|\frac{m^{\frac{1}{4}}sn\left(\frac{2K}{\pi}\arcsin\frac{z}{c}\right)-m^{\frac{1}{4}}sn\left(\frac{2K}{\pi}\arcsin\frac{\zeta}{c}\right)}{1-m^{\frac{1}{4}}sn\left(\frac{2K}{\pi}\arcsin\frac{z}{c}\right)m^{\frac{1}{4}}sn\left(\frac{2K}{\pi}\arcsin\frac{\zeta}{c}\right)}\right|$$

$$z=x+iy,\quad \zeta=\xi+i\eta \qquad (29)$$

5. The Solution of The Dirichlet Problem for Domains

In this section, we focus on solving the Dirichlet problem for various geometric domains. The Dirichlet problem, which involves finding a function that satisfies the Laplace equation within a domain and meets specific boundary conditions, is fundamental in mathematical physics and engineering. We will explore the methods and techniques required to solve this problem in different geometries, including rectangular, square, triangular, and elliptical regions, each presenting unique challenges and considerations.

The solution of the Dirichlet problem for the Poisson equation (2) in D can be obtained as

$$U(z) = \iint_D G(z,\zeta)h(\zeta)d\xi d\eta + \int_{\partial D} \frac{G(z,\zeta)}{\partial n} U_0(\zeta)|d\zeta| \qquad (30)$$

where G is the Green function for the domain D and $\frac{\partial}{\partial n}$ denotes differentiation along an outward normal to the boundary ∂D of D with respect to ζ .

5.1. The Solution of the Dirichlet Problem for a Rectangular Region

In this section, we address the solution of the Dirichlet problem specifically for a rectangular region. By applying appropriate boundary conditions, we aim to find the potential function that satisfies the Laplace equation within this geometry.

Taking the domain D as the rectangle $A_1(K,0), A_2(K,K'), A_3(-K,K'), A_4(-K,0)$, and the boundary $\partial D$of D as the circumference $\partial D = \overline{A_4A_1} \cup \overline{A_1A_2} \cup \overline{A_2A_3} \cup \overline{A_3A_4}$, one may write the conditions

(a) $\eta = 0, d\eta = 0, -K \le \xi \le K$

on $\overline{A_4A_1}$

(b) $\xi = K, d\xi = 0, 0 \le \eta \le K'$

on $\overline{A_1A_2}$ (31)

(c) $\eta = K', d\eta = 0, -K \le \xi \le K'$

on $\overline{A_2A_3}$

(d) $\xi = -K, d\xi = 0, 0 \le \eta \le K'$

on $\overline{A_3A_4}$

Thus, from Eq. (30), the solution of Eq. (2) in the above rectangle becomes

$$\begin{aligned} U(z) = {} & \int_0^{K'} \int_{-K}^{K} G(z,\zeta)h(z)d\xi d\eta \\ & - \int_{-K}^{K} \left[G_\xi^2(z,\zeta) + G_\eta^2(z,\zeta)\right]^{\frac{1}{2}} U_0(\zeta)\Big|_{\eta=0}^{K'} d\xi \\ & + \int_0^{K'} \left[G_\xi^2(z,\zeta) + G_\eta^2(z,\zeta)\right]^{\frac{1}{2}} U_0(\zeta)\Big|_{\xi=-K}^{K} d\eta. \end{aligned}$$

(32)

In the case of $h(z)=0$, the solution of the Dirichlet problem for the Laplace differential equation (1) in the above rectangle is obtained in terms of elliptic functions as:

$$U(z)=\int_0^{K'}\left[G_\xi^2+G_\eta^2\right]^{\frac{1}{2}}U_0(\zeta)\Big|_{\xi=-K}^{K}d\eta-\int_{-K}^{K}\left[G_\xi^2+G_\eta^2\right]^{\frac{1}{2}}U_0(\zeta)\Big|_{\eta=0}^{K'}d\xi$$

(33)

where the Green function G is defined by Eq. (26)

$$G=\frac{1}{2\pi}\operatorname{Re}\ln\left|\frac{sn\,z-sn\zeta}{sn\,z-\overline{sn\zeta}}\right|, \qquad (34)$$

$$z=x+iy,\quad \zeta=\xi+i\eta$$

according to Eq. (16). The boundary values $K(k)$ and $K'(k)$ are the complete elliptic integrals and are tabulated for the range $k\,(0<k<1)$.

5.2. The Solution of the Dirichlet Problem for a Square Region

Here, we explore the Dirichlet problem in the context of a square region. Given the symmetry of the square, the solution process involves unique considerations that simplify the determination of the potential function.

Taking the domain D as the square $A_1\left(\frac{K}{2},K\right), A_2\left(-\frac{K}{2},K\right), A_3\left(-\frac{K}{2},0\right)$, $A_4\left(\frac{K}{2},0\right)$

(Fig.2), and the boundary ∂D of D as the circumference

$\partial D=\overline{A_4A_1}\cup\overline{A_1A_2}\cup\overline{A_2A_3}\cup\overline{A_3A_4}$, one may write the conditions

a) $\eta=0,\quad d\eta=0,\quad -\frac{K}{2}\le\xi\le\frac{K}{2}$

on $\overline{A_3A_4}$,

b) $\xi=\frac{K}{2},\quad d\xi=0,\quad 0\le\eta\le K$

on $\overline{A_4A_1}$,

c) $\eta=K,\quad d\eta=0,\quad -\frac{K}{2}\le\xi\le\frac{K}{2}$

on $\overline{A_1A_2}$,

d) $\xi=-\frac{K}{2},\quad d\xi=0,\quad 0\le\eta\le K$

on $\overline{A_2A_3}$. (35)

In the case of $h(z)=0$, the solution of the Dirichlet problem for the Laplace differential equation (1) in the above square is obtained in terms of elliptic functions as:

$$U(z) = -\int_{-\frac{K}{2}}^{\frac{K}{2}} \frac{\partial G}{\partial n} U_0\left(\xi,\eta\right)\Big|_{\eta=0}^{K} d\xi$$

$$+\int_{0}^{K} \frac{\partial G}{\partial_n} U_0(\xi,\eta)\Bigg|_{\eta=-\frac{K}{2}}^{\frac{K}{2}} d\eta$$

$$= \int_{-\frac{K}{2}}^{\frac{K}{2}} \frac{\partial G}{\partial n} U_0\left(\xi,0\right) d\xi$$

$$+\int_{0}^{K} \frac{\partial G}{\partial n} U_0\left(\frac{K}{2},\eta\right) d\eta$$

$$-\int_{-\frac{K}{2}}^{\frac{K}{2}} \frac{\partial G}{\partial n} U_0\left(\xi,K\right) d\xi$$

$$-\int_{0}^{K} \frac{\partial G}{\partial n} U_0\left(-\frac{K}{2},\eta\right) d\eta$$

(36)

where the Green function G is defined by Eq. (27)

$$G = \frac{1}{2\pi}\ln\left|\frac{sn(2z)-sn(2\zeta)}{sn(2z)-\overline{sn(2\zeta)}}\right|,$$
$$z = x+iy, \quad \zeta = \xi + i\eta.$$

The boundary values $K(k)$ and $K'(k)$ are the complete elliptic integrals and are tabulated for the range $k\ (0<k<1)$

.

5.3.The Solution of the Dirichlet Problem for a Triangle Region

In this section, we solve the Dirichlet problem for a triangular region. The triangular geometry introduces specific challenges that require tailored methods to accurately determine the potential function.

Taking the domain D as the triangle $A_1\left(-\frac{K}{\sqrt{2}},0\right), A_2\left(\frac{K}{\sqrt{2}},0\right), A_3\left(0,\frac{K}{\sqrt{2}}\right),$ (Fig.3), and the boundary $\partial D$of D as the circumference $\partial D = \overline{A_1A_2} \cup \overline{A_2A_3} \cup \overline{A_3A_1}$, one may write the conditions

(a) $\eta = 0, d\eta = 0, |d\zeta| = |d\xi + id\eta|, -\frac{K}{\sqrt{2}} \le \xi \le \frac{K}{\sqrt{2}}$

on $\overline{A_1A_2}$,

(b) $\eta = -\xi + \frac{K}{\sqrt{2}}, d\eta = -d\xi, |d\zeta| = \sqrt{2}d\xi, 0 \le \xi \le \frac{K}{\sqrt{2}}$

on $\overline{A_2A_3}$,

(c) $\eta = \xi + \frac{K}{\sqrt{2}}, d\eta = d\xi, |d\zeta| = \sqrt{2}d\xi, -\frac{K}{\sqrt{2}} \le \xi \le 0$

on $\overline{A_3A_2}$.

(37)

In the case of $h(z)=0$, the solution of the Dirichlet problem for the Laplace differential Eq. (1) in the above triangle is obtained in terms of elliptic functions as

$$U(z) = -\int_{-\frac{K}{\sqrt{2}}}^{\frac{K}{\sqrt{2}}} \frac{\partial G}{\partial n} U_0(\xi,0)\, d\xi + \int_{0}^{\frac{K}{\sqrt{2}}} \frac{\partial G}{\partial n} U_0\left(\xi, -\xi + \frac{K}{\sqrt{2}}\right)\sqrt{2}\, d\xi - \int_{-\frac{K}{\sqrt{2}}}^{0} \frac{\partial G}{\partial n} U_0\left(\xi, \xi + \frac{K}{\sqrt{2}}\right)\sqrt{2}\, d\xi$$

(38)

where the Green function G is defined by Eq. (28)

$$G = \frac{1}{2\pi} \ln \left| \frac{sn\left(z\sqrt{2}\right)dn\left(z\sqrt{2}\right) - sn\left(\zeta\sqrt{2}\right)dn\left(\zeta\sqrt{2}\right)}{sn\left(z\sqrt{2}\right)dn\left(z\sqrt{2}\right) - \overline{sn\left(\zeta\sqrt{2}\right)dn\left(\zeta\sqrt{2}\right)}} \right|,$$

$$z = x + iy, \quad \zeta = \xi + i\eta.$$

The boundary values $K(k)$ and $K'(k)$ are the complete elliptic integrals and are tabulated for the range $k\ (0 < k < 1)$

5.4.The Solution of the Dirichlet Problem for a Ellipse Region

This part of the study focuses on the Dirichlet problem within an elliptical region. The elliptical shape's unique boundary conditions demand a specialized approach to solving the Laplace equation and finding the corresponding potential function

Taking the domain D as the ellipse $A(K,0), B(0,K'), C(-K,0), D(0,-K')$ (Fig.4), and the boundary ∂D of D as the circumference $\partial D = \overline{AB} \cup \overline{BC} \cup \overline{CD} \cup \overline{DA}$, one may write the conditions

(a)

$$\eta = \frac{K'}{K}\sqrt{K^2 - \xi^2}, \quad d\eta = \frac{K'}{K}\frac{-\xi}{\sqrt{K^2-\xi^2}}\, d\xi,$$

$$|d\zeta| = \sqrt{\frac{K^2\left(K^2-\xi^2\right) + (K')^2\xi^2}{K^2\left(K^2-\xi^2\right)}}\, d\xi,$$

$$0 \le \xi \le K$$

on $\overset{\frown}{AB}$

(b)

$$\eta = \frac{K'}{K}\sqrt{K^2 - \xi^2}, \quad d\eta = \frac{K'}{K}\frac{-\xi}{\sqrt{K^2-\xi^2}}\, d\xi,$$

$$|d\zeta| = \sqrt{\frac{K^2\left(K^2-\xi^2\right) + (K')^2\xi^2}{K^2\left(K^2-\xi^2\right)}}\, d\xi,$$

$$-K \le \xi \le 0$$

on $\overset{\frown}{BC}$

(c)

$$\eta = -\frac{K'}{K}\sqrt{K^2 - \xi^2}, \quad d\eta = \frac{K'}{K}\frac{\xi}{\sqrt{K^2-\xi^2}}\, d\xi,$$

$$|d\zeta| = \sqrt{\frac{K^2\left(K^2-\xi^2\right) + (K')^2\xi^2}{K^2\left(K^2-\xi^2\right)}}\, d\xi,$$

$$-K \le \xi \le 0$$

on $\overset{\frown}{CD}$

(d)
$$\eta = -\frac{K'}{K}\sqrt{K^2-\xi^2},$$
$$d\eta = \frac{K'}{K}\frac{\xi}{\sqrt{K^2-\xi^2}}d\xi,$$
$$|d\zeta| = \sqrt{\frac{K^2\left(K^2-\xi^2\right)+(K')^2\,\xi^2}{K^2\left(K^2-\xi^2\right)}}d\xi,$$
$$0 \le \xi \le K$$

on DA

$$U(z) = \int_{-K}^{K}\int_{-K'}^{K'} G\left(z,\zeta\right)h\left(\zeta\right)d\xi d\eta$$
$$+\int_{-K}^{0}\left[G_{\xi}^{2}\left(z,\zeta\right)+G_{\eta}^{2}\left(z,\zeta\right)\right]^{\frac{1}{2}}$$
$$U_0\left(\xi,\frac{K'}{K}\sqrt{K^2-\xi^2}\right)$$
$$\sqrt{\frac{K^2\left(K^2-\xi^2\right)+(K')^2\,\xi^2}{K^2\left(K^2-\xi^2\right)}}d\xi$$
$$-\int_{-K}^{0}\left[G_{\xi}^{2}\left(z,\zeta\right)+G_{\eta}^{2}\left(z,\zeta\right)\right]^{\frac{1}{2}}$$
$$U_0\left(\xi,-\frac{K'}{K}\sqrt{K^2-\xi^2}\right)$$
$$\sqrt{\frac{K^2\left(K^2-\xi^2\right)+(K')^2\,\xi^2}{K^2\left(K^2-\xi^2\right)}}d\xi$$
$$-\int_{0}^{K}\left[G_{\xi}^{2}\left(z,\zeta\right)+G_{\eta}^{2}\left(z,\zeta\right)\right]^{\frac{1}{2}}$$
$$U_0\left(\xi,-\frac{K'}{K}\sqrt{K^2-\xi^2}\right)$$
$$\sqrt{\frac{K^2\left(K^2-\xi^2\right)+(K')^2\,\xi^2}{K^2\left(K^2-\xi^2\right)}}d\xi$$

6. APPLICATION FOR DOMAINS

Now, we will examine practical applications of solving the Dirichlet problem for different geometric regions. For each geometric shape, we will go through the steps of determining the boundary conditions and solving the Laplace equation in accordance with these conditions. By providing concrete examples and solutions for regions such as rectangles, squares, triangles, and ellipses, we will demonstrate how these problems can be applied in practice. These examples are crucial for understanding how theoretical knowledge can be adapted to real-world engineering and physics problems.

6.1. Application for a Rectangular Region

In this section we will explore the practical application of solving the Dirichlet problem specifically for rectangular domain. We will walk through the process of defining the boundary conditions unique to a rectangular region and solving the Laplace equation accordingly.We will illustrate how these mathematical concepts are applied in practice, particularly within the context of engineering and physics problems that involve rectangular geometries.

$$U_{xx}(x,y)+U_{yy}(x,y)=0, \quad 0<x<K, \quad 0<y<2K$$
$$U(x,0)=0, \quad U(x,2K)=1, \quad -K<x<K$$
$$U(-K,y)=U(K,y)=0, \qquad 0<y<2K$$

(39)

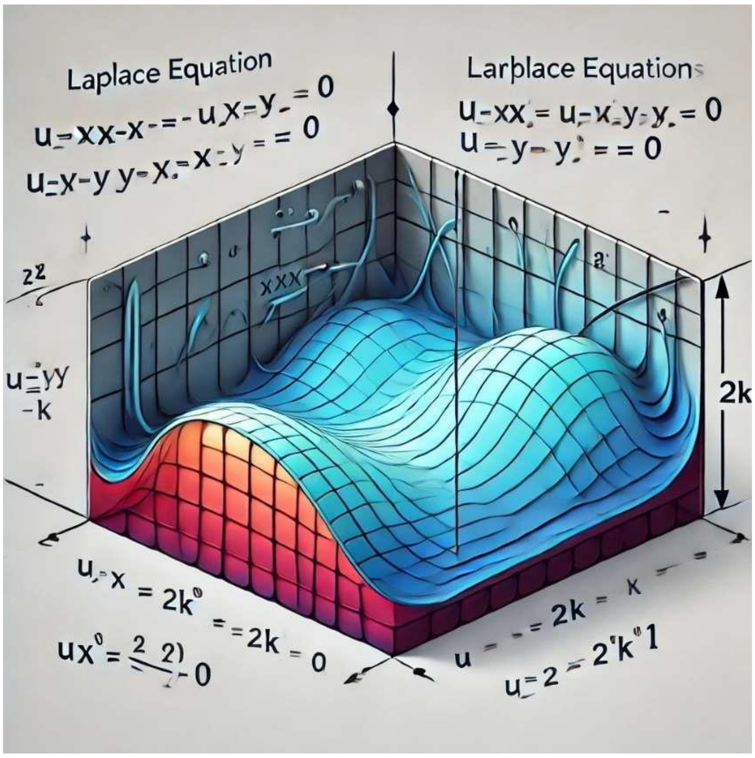

Figure 10. Two-dimensional visualization of the solution to the Dirichlet problem for a rectangular region.

The solution of the function U with two real variables satisfying the above conditions by the method of separation of variables is

$$U_s(x,y)=\frac{4}{\pi}\sum_{k=1}^{\infty}\left(\frac{1}{2k-1}\frac{\sinh((2k-1)\pi x/K)}{\sinh(2(2k-1)\pi)}\sin\frac{(2k-1)\pi y}{K}\right)$$

(40)

where $k=(n+1)/2, \quad n=1,2,\ldots$ On the other hand, the solution of the function U in terms of elliptic functions is

$$U^{E}(z) = -\int_{-K}^{K}\left[G_{\xi}^{2}(z,\zeta)+G_{\eta}^{2}(z,\zeta)\right]^{\frac{1}{2}} U_{0}(\zeta)\Big|_{\eta=0}^{2K} d\xi + \int_{0}^{2K}\left[G_{\xi}^{2}(z,\zeta)+G_{\eta}^{2}(z,\zeta)\right]^{\frac{1}{2}} U_{0}(\zeta)\Big|_{\xi=-K}^{K} d\eta$$

$$= -\int_{-K}^{K}\left[\begin{array}{l}\left[G_{\xi}^{2}(x,y;\xi,2K)+G_{\eta}^{2}(x,y;\xi,2K)\right]^{\frac{1}{2}} U_{0}(\xi,2K)\\ -\left[G_{\xi}^{2}(x,y;\xi,0)+G_{\eta}^{2}(x,y;\xi,0)\right]^{\frac{1}{2}} U_{0}(\xi,0)\end{array}\right] d\xi$$

$$+\int_{0}^{2K}\left[\begin{array}{l}\left[G_{\xi}^{2}(x,y;K,\eta)+G_{\eta}^{2}(x,y;K,\eta)\right]^{\frac{1}{2}} U_{0}(K,\eta)\\ -\left[G_{\xi}^{2}(x,y;-K,\eta)+G_{\eta}^{2}(x,y;-K,\eta)\right]^{\frac{1}{2}} U_{0}(-K,\eta)\end{array}\right] d\eta \quad (41)$$

where

$U_0(\xi,2K)=1, \quad U_0(\xi,0)=0, \quad U_0(K,\eta)=0$

and

$U_0(-K,\eta)=0$ (42)

Subsituting the conditions (42) into Eq.(41) we obtain

$$U_{E}(z) = \begin{cases} \dfrac{1}{\pi}\left[\begin{array}{l} -2\arctan\left(\dfrac{snx\,dny}{cnx\,dnx\,sny\,cny}\right)\\ -\arctan\left(\dfrac{snx\,dny - sn^{2}y\,dn^{2}x+1}{cnx\,dnx\,sny\,cny}\right)\\ +\arctan\left(\dfrac{snx\,dny + sn^{2}y\,dn^{2}x-1}{cnx\,dnx\,sny\,cny}\right)\\ -K<x\le 0. \quad for \quad y=0 \end{array}\right]\\ \dfrac{1}{\pi}\left[\begin{array}{l} 2\arctan\left(\dfrac{snx\,dny}{cnx\,dnx\,snycny}\right)\\ -\arctan\left(\dfrac{snx\,dny - sn^{2}y\,dn^{2}x+1}{cnx\,dnx\,sny\,cny}\right)\\ +\arctan\left(\dfrac{snx\,dny + sn^{2}y\,dn^{2}x-1}{cnx\,dnx\,sny\,cny}\right)\\ K<x\le 0. \quad for \quad y=0 \end{array}\right]\\ \dfrac{1}{\pi}\left[\begin{array}{l} 2\arctan\left(\dfrac{snx\,dny}{cnx\,dnx\,snycny}\right)\\ -\arctan\left(\dfrac{snx\,dny - sn^{2}y\,dn^{2}x+1}{cnx\,dnx\,sny\,cny}\right)\\ +\arctan\left(\dfrac{snx\,dny + sn^{2}y\,dn^{2}x-1}{cnx\,dnx\,sny\,cny}\right)\\ -K<x\le K. \quad for \quad 0<y\le 2K \end{array}\right] \end{cases},$$

(43)

(Kurt, N. et al. 2004).

6.2. Application for a Square Region

In this section, we delve into the Dirichlet problem for a square domain, a special case of the rectangular region where all sides are of equal length. The boundary conditions are defined on each side of the square, and the Laplace equation is solved accordingly. This scenario is particularly relevant in engineering and physics problems where symmetry simplifies the analysis, such as in heat conduction in a square plate or electrostatic potential problems within a square boundary.

The solution process involves setting up the Laplace equation $\nabla^2 u = 0$ with boundary conditions specified on the edges of the square. By employing techniques such as separation of variables or using Fourier series, we derive the solution that satisfies both the differential equation and the boundary conditions.

The results are then interpreted in the context of practical applications, demonstrating how the theoretical solution translates to real-world scenarios.

Now, an illustrative example is given. A boundary of a square sheet of metal is kept at constant temperatures of $100^0 C$ on one of the bottom edges, $50\,^0C$ on the other, bottom edge, and $0\,^0C$ on the upper edge (see Fig. 5). After an enough period of time, the temperature inside the plate reaches an equilibrium distribution. In this section, the steady-state temperature distribution is determined $U(x, y)$. Since no heat sources are present in the plate, the steady-state temperature U must satisfy

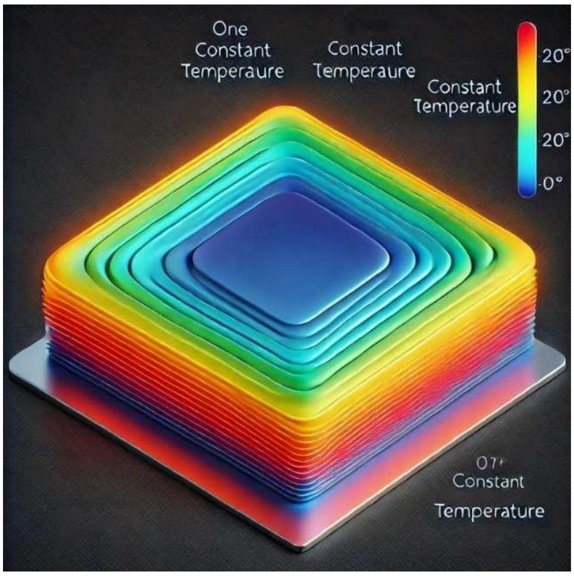

Figure 11. Steady-state temperature distribution in a square metal sheet under constant temperature conditions.

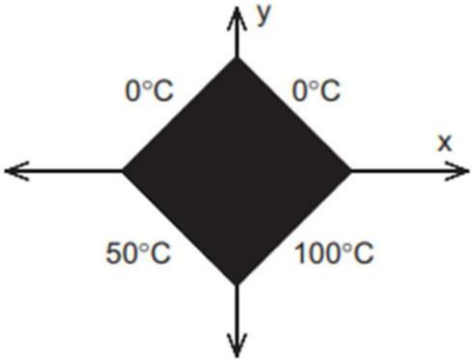

Fig. 12. Illustrative application for a square region.

One side of the bottom edge is kept at a specific temperature, the other side at a different temperature, and the top edge is maintained at a constant temperature. Over time, heat flows within the sheet, and the temperature reaches equilibrium in the interior region. The color gradients represent the temperature gradient, and the arrows indicate the direction of heat flow.

$$U_{xx}\left(x,y\right)+U_{yy}\left(x,y\right)=0$$
$$\left(-\frac{K}{\sqrt{2}}<x<\frac{K}{\sqrt{2}},-\frac{K}{\sqrt{2}}<y<\frac{K}{\sqrt{2}}\right)$$
$$U\left(x,x+\frac{K}{\sqrt{2}}\right)=0^0C,$$

$$U\left(x,-x-\frac{K}{\sqrt{2}}\right)=50^0C,$$
$$-\frac{K}{\sqrt{2}}<x<0,$$
$$U\left(x,-x+\frac{K}{\sqrt{2}}\right)=0^0C,$$
$$U\left(x,x-\frac{K}{\sqrt{2}}\right)=100^0C,$$
$$0<x<\frac{K}{\sqrt{2}}.$$

(44)

The solution of the function U with two real variables satisfying the above conditions by the method of separation of variables is

$$U_s\left(x,y\right)=\frac{200}{\pi}\sum_{k=1}^{\infty}\left(\frac{\sinh\left((2k+1)\pi\left(\frac{K-y}{K}\right)\right)\sin\left(2k+1\right)\pi\frac{x}{K}}{\left(2k+1\right)\sinh((2k+1)\pi)}\right)$$

$$+\frac{400}{\pi}\sum_{k=1}^{\infty}\left(\frac{\sinh\left((2k+1)\pi\frac{x}{K}\right)\sin\left((2k+1)\pi\frac{x}{K}\right)}{(2k+1)\sinh((2k+1)\pi)}\right) \quad (45)$$

where $k=(n+1)/2,\quad n=1,2,\ldots$ On the other hand, the solution of the function U in terms of elliptic functions is

$$\begin{aligned}U_E(z)={}&\int_0^{K/\sqrt{2}}\frac{\partial G}{\partial n}U_0\left(\xi,-\xi+\frac{K}{\sqrt{2}}\right)\sqrt{2}d\xi\\&+\int_{-K/\sqrt{2}}^{0}\frac{\partial G}{\partial n}U_0\left(\xi,\xi+\frac{K}{\sqrt{2}}\right)\sqrt{2}d\xi\\&-\int_{-K/\sqrt{2}}^{0}\frac{\partial G}{\partial n}U_0\left(\xi,-\xi-\frac{K}{\sqrt{2}}\right)\sqrt{2}d\xi\\&-\int_0^{K/\sqrt{2}}\frac{\partial G}{\partial n}U_0\left(\xi,\xi-\frac{K}{\sqrt{2}}\right)\sqrt{2}d\xi\end{aligned}$$

(46)

where

$$U_0\left(\xi,-\xi+\frac{K}{\sqrt{2}}\right)=0,$$

$$U_0\left(\xi,\xi+\frac{K}{\sqrt{2}}\right)=0, \quad ,$$

$$U_0\left(\xi,-\xi-\frac{K}{\sqrt{2}}\right)=50$$

$$U_0\left(\xi,\xi-\frac{K}{\sqrt{2}}\right)=100. \quad (47)$$

Subsituting the conditions (47) into Eq.(46) we obtain

If $-K/\sqrt{2}<x<0$, $y=-x+K/\sqrt{2}$

$$U_E(x,y)=\frac{50}{\pi}\left[\begin{aligned}&2\arctan\left[\frac{sn\left(\sqrt{2}x\right)dn\left(\sqrt{2}\left(-x-y+\frac{K}{\sqrt{2}}\right)+10^{-8}\right)+1}{cn\left(\sqrt{2}x\right)dn\left(\sqrt{2}x\right)sn\left(\sqrt{2}\left(-x-y+\frac{K}{\sqrt{2}}\right)+10^{-8}\right)cn\left(\sqrt{2}\left(-x-y+\frac{K}{\sqrt{2}}\right)+10^{-8}\right)}\right]\\&-\arctan\left[\frac{ksn\left(\sqrt{2}x\right)dn\left(\sqrt{2}\left(-x-y+\frac{K}{\sqrt{2}}\right)+10^{-8}\right)-sn^2\left(\sqrt{2}\left(-x-y+\frac{K}{\sqrt{2}}\right)+10^{-8}\right)dn^2\left(\sqrt{2}x\right)+1}{kcn\left(\sqrt{2}x\right)dn\left(\sqrt{2}x\right)sn\left(\sqrt{2}\left(-x-y+\frac{K}{\sqrt{2}}\right)+10^{-8}\right)cn\left(\sqrt{2}\left(-x-y+\frac{K}{\sqrt{2}}\right)+10^{-8}\right)}\right]\\&+\arctan\left[\frac{ksn\left(\sqrt{2}x\right)dn\left(\sqrt{2}\left(-x-y+\frac{K}{\sqrt{2}}\right)+10^{-8}\right)-sn^2\left(\sqrt{2}\left(-x-y+\frac{K}{\sqrt{2}}\right)+10^{-8}\right)dn^2\left(\sqrt{2}x\right)-1}{kcn\left(\sqrt{2}x\right)dn\left(\sqrt{2}x\right)sn\left(\sqrt{2}\left(-x-y+\frac{K}{\sqrt{2}}\right)+10^{-8}\right)cn\left(\sqrt{2}\left(-x-y+\frac{K}{\sqrt{2}}\right)+10^{-8}\right)}\right]\end{aligned}\right]$$

If $-K/\sqrt{2} < x < 0$, $y = x + K/\sqrt{2}$

$$U_E(x,y) = \frac{50}{\pi}\left[-2\arctan\left[\frac{sn\left(\sqrt{2}x\right) dn\left(\sqrt{2}\left(-x-y+\frac{K}{\sqrt{2}}\right)+10^{-8}\right)+1}{cn\left(\sqrt{2}x\right) dn\left(\sqrt{2}x\right) sn\left(\sqrt{2}\left(-x-y+\frac{K}{\sqrt{2}}\right)+10^{-8}\right) cn\left(\sqrt{2}\left(-x-y+\frac{K}{\sqrt{2}}\right)+10^{-8}\right)} \right] + \arctan\left[\frac{k sn\left(\sqrt{2}x\right) dn\left(\sqrt{2}\left(-x-y+\frac{K}{\sqrt{2}}\right)+10^{-8}\right) - sn^2\left(\sqrt{2}\left(-x-y+\frac{K}{\sqrt{2}}\right)+10^{-8}\right) dn^2\left(\sqrt{2}x\right)+1}{k cn\left(\sqrt{2}x\right) dn\left(\sqrt{2}x\right) sn\left(\sqrt{2}\left(-x-y+\frac{K}{\sqrt{2}}\right)+10^{-8}\right) cn\left(\sqrt{2}\left(-x-y+\frac{K}{\sqrt{2}}\right)+10^{-8}\right)} \right] - \arctan\left[\frac{k sn\left(\sqrt{2}x\right) dn\left(\sqrt{2}\left(-x-y+\frac{K}{\sqrt{2}}\right)+10^{-8}\right) - sn^2\left(\sqrt{2}\left(-x-y+\frac{K}{\sqrt{2}}\right)+10^{-8}\right) dn^2\left(\sqrt{2}x\right)-1}{k cn\left(\sqrt{2}x\right) dn\left(\sqrt{2}x\right) sn\left(\sqrt{2}\left(-x-y+\frac{K}{\sqrt{2}}\right)+10^{-8}\right) cn\left(\sqrt{2}\left(-x-y+\frac{K}{\sqrt{2}}\right)+10^{-8}\right)} \right] \right]$$

If $-K/\sqrt{2} < x < 0$, $y = -x - K/\sqrt{2}$

$$U_E(x,y) = \frac{50}{\pi}\left[2\arctan\left[\frac{sn\left(\sqrt{2}x\right) dn\left(\sqrt{2}\left(-x-y+\frac{K}{\sqrt{2}}\right)+10^{-8}\right)+1}{cn\left(\sqrt{2}x\right) dn\left(\sqrt{2}x\right) sn\left(\sqrt{2}\left(-x-y+\frac{K}{\sqrt{2}}\right)+10^{-8}\right) cn\left(\sqrt{2}\left(-x-y+\frac{K}{\sqrt{2}}\right)+10^{-8}\right)} \right] - \arctan\left[\frac{k sn\left(\sqrt{2}x\right) dn\left(\sqrt{2}\left(-x-y+\frac{K}{\sqrt{2}}\right)+10^{-8}\right) - sn^2\left(\sqrt{2}\left(-x-y+\frac{K}{\sqrt{2}}\right)+10^{-8}\right) dn^2\left(\sqrt{2}x\right)+1}{k cn\left(\sqrt{2}x\right) dn\left(\sqrt{2}x\right) sn\left(\sqrt{2}\left(-x-y+\frac{K}{\sqrt{2}}\right)+10^{-8}\right) cn\left(\sqrt{2}\left(-x-y+\frac{K}{\sqrt{2}}\right)+10^{-8}\right)} \right] - \arctan\left[\frac{k sn\left(\sqrt{2}x\right) dn\left(\sqrt{2}\left(-x-y+\frac{K}{\sqrt{2}}\right)+10^{-8}\right) - sn^2\left(\sqrt{2}\left(-x-y+\frac{K}{\sqrt{2}}\right)+10^{-8}\right) dn^2\left(\sqrt{2}x\right)-1}{k cn\left(\sqrt{2}x\right) dn\left(\sqrt{2}x\right) sn\left(\sqrt{2}\left(-x-y+\frac{K}{\sqrt{2}}\right)+10^{-8}\right) cn\left(\sqrt{2}\left(-x-y+\frac{K}{\sqrt{2}}\right)+10^{-8}\right)} \right] \right]$$

If $0 < x < K/2$, $y = x - K/\sqrt{2}$

$$U_E(x,y)=\frac{50}{\pi}\left[\begin{aligned}&-2\arctan\left[\frac{sn\left(\sqrt{2}x\right)dn\left(\sqrt{2}\left(-x-y+\frac{K}{\sqrt{2}}\right)+10^{-8}\right)+1}{cn\left(\sqrt{2}x\right)dn\left(\sqrt{2}x\right)sn\left(\sqrt{2}\left(-x-y+\frac{K}{\sqrt{2}}\right)+10^{-8}\right)cn\left(\sqrt{2}\left(-x-y+\frac{K}{\sqrt{2}}\right)+10^{-8}\right)}\right]\\&-\arctan\left[\frac{ksn\left(\sqrt{2}x\right)dn\left(\sqrt{2}\left(-x-y+\frac{K}{\sqrt{2}}\right)+10^{-8}\right)-sn^2\left(\sqrt{2}\left(-x-y+\frac{K}{\sqrt{2}}\right)+10^{-8}\right)dn^2\left(\sqrt{2}x\right)+1}{kcn\left(\sqrt{2}x\right)dn\left(\sqrt{2}x\right)sn\left(\sqrt{2}\left(-x-y+\frac{K}{\sqrt{2}}\right)+10^{-8}\right)cn\left(\sqrt{2}\left(-x-y+\frac{K}{\sqrt{2}}\right)+10^{-8}\right)}\right]\\&+\arctan\left[\frac{ksn\left(\sqrt{2}x\right)dn\left(\sqrt{2}\left(-x-y+\frac{K}{\sqrt{2}}\right)+10^{-8}\right)-sn^2\left(\sqrt{2}\left(-x-y+\frac{K}{\sqrt{2}}\right)+10^{-8}\right)dn^2\left(\sqrt{2}x\right)-1}{kcn\left(\sqrt{2}x\right)dn\left(\sqrt{2}x\right)sn\left(\sqrt{2}\left(-x-y+\frac{K}{\sqrt{2}}\right)+10^{-8}\right)cn\left(\sqrt{2}\left(-x-y+\frac{K}{\sqrt{2}}\right)+10^{-8}\right)}\right]\end{aligned}\right]$$

Kurt, N. (2008).6.3.

6.3. Application for a Triangle Region

This section focuses on solving the Dirichlet problem within a triangular domain. Triangular regions frequently arise in engineering, particularly in the finite element method (FEM) for solving partial differential equations. The boundary conditions are applied along the edges of the triangle, and the Laplace equation is solved within this domain.

A thin triangle homogeneous thermally conducting plate lies in the xy-plane and occupies the triangle with corners at $\left(-\frac{K}{\sqrt{2}},0\right),\left(\frac{K}{\sqrt{2}},0\right)$, and $\left(0,\frac{K}{\sqrt{2}}\right)$. The faces of the plate are insulated and no internal sources or sinks are present. The edge $y=0$ is hold at $T\ {}^{0}C$; while remaining edges are hold at $0\ {}^{0}C$ 0. The problem is to find the steady temperature $U(x,y)$ in the plane. Since no heat sources are present in the plate, the steady state temperature

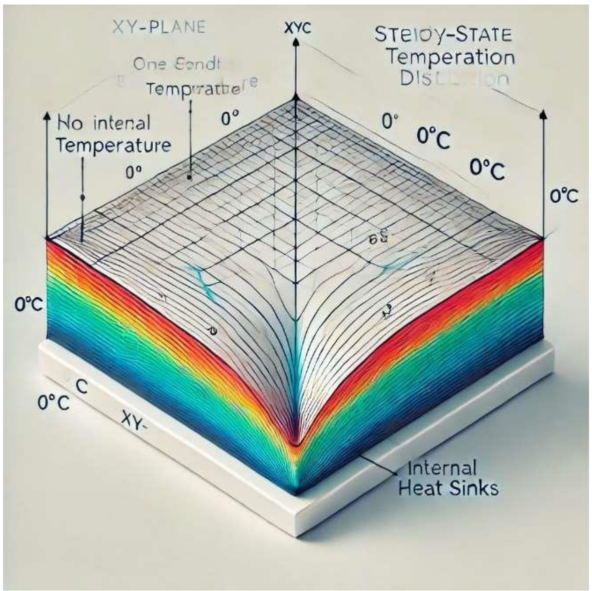

Fig. 13. Steady-state temperature distribution of a thin triangular plate.

One edge is held at a specific temperature, while the other edges are fixed at 0°C. The plate is insulated, with no internal heat sources or sinks. The illustration shows the temperature distribution and heat flow across the plate.

U must satisfy

$$U_{xx}\left(x,y\right)+U_{yy}\left(x,y\right)=0$$
$$\left(-\frac{K}{\sqrt{2}}<x<\frac{K}{\sqrt{2}},0<y<\frac{K}{\sqrt{2}}\right)$$
$$U\left(x,0\right)=T^{0}C,-\frac{K}{\sqrt{2}}<x<0\wedge 0<x<\frac{K}{\sqrt{2}}$$
$$U\left(x,x+\frac{K}{\sqrt{2}}\right)=0^{0}C,-\frac{K}{\sqrt{2}}<x<0,$$
$$U\left(x,-x+\frac{K}{\sqrt{2}}\right)=0^{0}C,0<x<\frac{K}{\sqrt{2}}.$$

(48)

The solution of the function U with two real variables satisfying the above conditions by the method of separation of variables is

$$U_{S}(x,y)=\frac{4T}{\pi}\left\{\begin{array}{l}\displaystyle\sum_{k=1}^{\infty}\left(\left[\frac{-1\,\sinh\left(\frac{\sqrt{2}\left(2k-1\right)\pi\left(-x+\frac{K}{\sqrt{2}}-y\right)}{K}\right)}{2k-1\,\sinh\left(\frac{\sqrt{2}\left(2k-1\right)\pi\left(-x+\frac{K}{\sqrt{2}}\right)}{K}\right)}\right]\sin\left(\frac{\sqrt{2}\left(2k-1\right)\pi x}{K}\right)\right)\\ -\frac{K}{\sqrt{2}}<x<0\end{array}\right.,$$

$$U_S(x,y)=\frac{4T}{\pi}\left\{\sum_{k=1}^{\infty}\left(\left[\frac{1}{2k-1}\frac{\sinh\left(\frac{\sqrt{2}(2k-1)\pi\left(-x+\frac{K}{\sqrt{2}}-y\right)}{K}\right)}{\sinh\left(\frac{\sqrt{2}(2k-1)\pi\left(-x+\frac{K}{\sqrt{2}}\right)}{K}\right)}\right]\sin\left(\frac{\sqrt{2}(2k-1)\pi x}{K}\right)\right),\quad 0<x<\frac{K}{\sqrt{2}}\right.$$

(49)

where $k=(n+1)/2,\quad n=1,2,\ldots$ On the other hand, the solution of the function U in terms of elliptic functions is

$$U_E(z)=\int_{-K/\sqrt{2}}^{K/\sqrt{2}}\frac{\partial G}{\partial n}U_0(\xi,0)\,d\xi+\int_{0}^{K/\sqrt{2}}\frac{\partial G}{\partial n}U_0\left(\xi,-\xi+\frac{K}{\sqrt{2}}\right)\sqrt{2}d\xi-\int_{-K/\sqrt{2}}^{0}\frac{\partial G}{\partial n}U_0\left(\xi,\xi+\frac{K}{\sqrt{2}}\right)\sqrt{2}d\xi$$

(50)

where

$$U_0(\xi,0)=T,$$

$$U_0\left(\xi,\xi+\frac{K}{\sqrt{2}}\right)=0,\qquad (51)$$

$$U_0\left(\xi,-\xi+\frac{K}{\sqrt{2}}\right)=0$$

Subsituting the conditions (47) into Eq.(46) we obtain

for $0<x<\frac{K}{\sqrt{2}}$

$$U_E(x,y)=\frac{T}{\pi}\left(-2\arctan\left(\frac{\alpha\left(x,-x-y+\frac{K}{\sqrt{2}}\right)\delta\left(x,-x-y+\frac{K}{\sqrt{2}}\right)-\beta\left(x,-x-y+\frac{K}{\sqrt{2}}\right)\phi\left(x,-x-y+\frac{K}{\sqrt{2}}\right)}{\alpha\left(x,-x-y+\frac{K}{\sqrt{2}}\right)\phi\left(x,-x-y+\frac{K}{\sqrt{2}}\right)+\delta\left(x,-x-y+\frac{K}{\sqrt{2}}\right)\beta\left(x,-x-y+\frac{K}{\sqrt{2}}\right)}\right)\right)$$

$$U_E(x,y)=\frac{T}{\pi}\left(+\arctan\left(\frac{\alpha\left(x,-x-y+\frac{K}{\sqrt{2}}\right)\delta\left(x,-x-y+\frac{K}{\sqrt{2}}\right)-\beta\left(x,-x-y+\frac{K}{\sqrt{2}}\right)\phi\left(x,-x-y+\frac{K}{\sqrt{2}}\right)+k'}{\alpha\left(x,-x-y+\frac{K}{\sqrt{2}}\right)\phi\left(x,-x-y+\frac{K}{\sqrt{2}}\right)+\delta\left(x,-x-y+\frac{K}{\sqrt{2}}\right)\beta\left(x,-x-y+\frac{K}{\sqrt{2}}\right)}\right)\right)$$

,

$$U_E(x,y)=\frac{T}{\pi}\left(-\arctan\left(\frac{\alpha\left(x,-x-y+\frac{K}{\sqrt{2}}\right)\delta\left(x,-x-y+\frac{K}{\sqrt{2}}\right)-\beta\left(x,-x-y+\frac{K}{\sqrt{2}}\right)\phi\left(x,-x-y+\frac{K}{\sqrt{2}}\right)-k'}{\alpha\left(x,-x-y+\frac{K}{\sqrt{2}}\right)\phi\left(x,-x-y+\frac{K}{\sqrt{2}}\right)+\delta\left(x,-x-y+\frac{K}{\sqrt{2}}\right)\beta\left(x,-x-y+\frac{K}{\sqrt{2}}\right)}\right)\right)$$

$$U_E(x,y)=\frac{T}{\pi}\left(+\arctan\left(\frac{\alpha\left(x,-x-y+\frac{K}{\sqrt{2}}\right)\delta\left(x,-x-y+\frac{K}{\sqrt{2}}\right)-\beta\left(x,-x-y+\frac{K}{\sqrt{2}}\right)\phi\left(x,-x-y+\frac{K}{\sqrt{2}}\right)+k'}{\alpha\left(x,-x-y+\frac{K}{\sqrt{2}}\right)\phi\left(x,-x-y+\frac{K}{\sqrt{2}}\right)+\delta\left(x,-x-y+\frac{K}{\sqrt{2}}\right)\beta\left(x,-x-y+\frac{K}{\sqrt{2}}\right)}\right)\right)$$

for $-\frac{K}{\sqrt{2}}<x<0$

$$U_E(x,y)=\frac{T}{\pi}\left(2\arctan\left(\frac{\alpha\left(x,-x-y+\frac{K}{\sqrt{2}}\right)\delta\left(x,-x-y+\frac{K}{\sqrt{2}}\right)-\beta\left(x,-x-y+\frac{K}{\sqrt{2}}\right)\phi\left(x,-x-y+\frac{K}{\sqrt{2}}\right)}{\alpha\left(x,-x-y+\frac{K}{\sqrt{2}}\right)\phi\left(x,-x-y+\frac{K}{\sqrt{2}}\right)+\delta\left(x,-x-y+\frac{K}{\sqrt{2}}\right)\beta\left(x,-x-y+\frac{K}{\sqrt{2}}\right)}\right)\right)$$

$$U_E(x,y)=\frac{T}{\pi}\left(-\arctan\left(\frac{\alpha\left(x,-x-y+\frac{K}{\sqrt{2}}\right)\delta\left(x,-x-y+\frac{K}{\sqrt{2}}\right)-\beta\left(x,-x-y+\frac{K}{\sqrt{2}}\right)\phi\left(x,-x-y+\frac{K}{\sqrt{2}}\right)-k'}{\alpha\left(x,-x-y+\frac{K}{\sqrt{2}}\right)\phi\left(x,-x-y+\frac{K}{\sqrt{2}}\right)+\delta\left(x,-x-y+\frac{K}{\sqrt{2}}\right)\beta\left(x,-x-y+\frac{K}{\sqrt{2}}\right)}\right)\right)$$

for $0 < x < \frac{K}{\sqrt{2}}$, $y = 0$

$$U_E(x,y) = \frac{T}{\pi}\left(2\arctan\left(\frac{\frac{\alpha(x,y)}{\delta(x,y)} - \frac{\beta(x,y)}{\phi(x,y)}}{\frac{\alpha(x,y)}{\phi(x,y)} + \frac{\delta(x,y)}{\beta(x,y)}} \right) + \arctan\left(\frac{\frac{\alpha(x,y)}{\delta(x,y)} - \frac{\beta(x,y)}{\phi(x,y)+k'}}{\frac{\alpha(x,y)}{\phi(x,y)} + \frac{\delta(x,y)}{\beta(x,y)}} \right) - \arctan\left(\frac{\frac{\alpha(x,y)}{\delta(x,y)} - \frac{\beta(x,y)}{\phi(x,y)-k'}}{\frac{\alpha(x,y)}{\phi(x,y)} + \frac{\delta(x,y)}{\beta(x,y)}} \right) \right)$$

for $-\frac{K}{\sqrt{2}} < x < 0$, $y = 0$

$$U_E(x,y) = \frac{T}{\pi}\left(2\arctan\left(\frac{\frac{\alpha(x,y)}{\delta(x,y)} - \frac{\beta(x,y)}{\phi(x,y)}}{\frac{\alpha(x,y)}{\phi(x,y)} + \frac{\delta(x,y)}{\beta(x,y)}} \right) + \arctan\left(\frac{\frac{\alpha(x,y)}{\delta(x,y)} - \frac{\beta(x,y)}{\phi(x,y)+k'}}{\frac{\alpha(x,y)}{\phi(x,y)} + \frac{\delta(x,y)}{\beta(x,y)}} \right) - \arctan\left(\frac{\frac{\alpha(x,y)}{\delta(x,y)} - \frac{\beta(x,y)}{\phi(x,y)-k'}}{\frac{\alpha(x,y)}{\phi(x,y)} + \frac{\delta(x,y)}{\beta(x,y)}} \right) \right).$$

(Kurt, N., & Sezer, M. 2006)

Where $\alpha, \beta, \delta, \phi, \mu, \lambda, \psi, \tau$ are function of x and y, are given below

$$\alpha(x,y)=\frac{sn\left(\sqrt{2}x\right)dn\left(\sqrt{2}x\right)}{1-sn\left(\sqrt{2}y\right)dn\left(\sqrt{2}x\right)},$$

$$\beta(x,y)=\frac{cn\left(\sqrt{2}x\right)dn\left(\sqrt{2}x\right)sn\left(\sqrt{2}y\right)cn\left(\sqrt{2}y\right)}{1-sn^2\left(\sqrt{2}y\right)dn^2\left(\sqrt{2}x\right)},$$

$$\delta(x,y)=\frac{dn\left(\sqrt{2}x\right)cn\left(\sqrt{2}y\right)dn\left(\sqrt{2}y\right)}{1-sn^2\left(\sqrt{2}y\right)dn^2\left(\sqrt{2}x\right)},$$

$$\phi(x,y)=\frac{-k^2 sn\left(\sqrt{2}x\right)cn\left(\sqrt{2}x\right)sn\left(\sqrt{2}y\right)}{1-sn^2\left(\sqrt{2}y\right)dn^2\left(\sqrt{2}x\right)},$$

$$\mu(x,y)=\frac{sn\left(\sqrt{2}\xi\right)dn\left(\sqrt{2}\eta\right)}{1-sn^2\left(\sqrt{2}\eta\right)dn^2\left(\sqrt{2}\xi\right)},$$

$$\lambda(x,y)=\frac{cn\left(\sqrt{2}\xi\right)dn\left(\sqrt{2}\xi\right)sn\left(\sqrt{2}\eta\right)cn\left(\sqrt{2}\eta\right)}{1-sn^2\left(\sqrt{2}\eta\right)dn^2\left(\sqrt{2}\xi\right)}$$

$$\psi(x,y)=\frac{dn\left(\sqrt{2}\xi\right)cn\left(\sqrt{2}\eta\right)dn\left(\sqrt{2}\eta\right)}{1-sn\left(\sqrt{2}\eta\right)dn\left(\sqrt{2}\xi\right)},$$

$$\tau(x,y)=\frac{-k^2 sn\left(\sqrt{2}\xi\right)cn\left(\sqrt{2}\xi\right)sn\left(\sqrt{2}\eta\right)}{1-sn^2\left(\sqrt{2}\eta\right)dn^2\left(\sqrt{2}\xi\right)}$$

6.4. Application for a Ellipse Region

In this section, we explore the Dirichlet problem within an elliptical domain. The practical applications discussed include scenarios like the distribution of potential around an elliptical conductor or temperature distribution in elliptical domains. These examples illustrate how solving the Dirichlet problem for an elliptical region can provide insights into physical systems with elliptical symmetry.

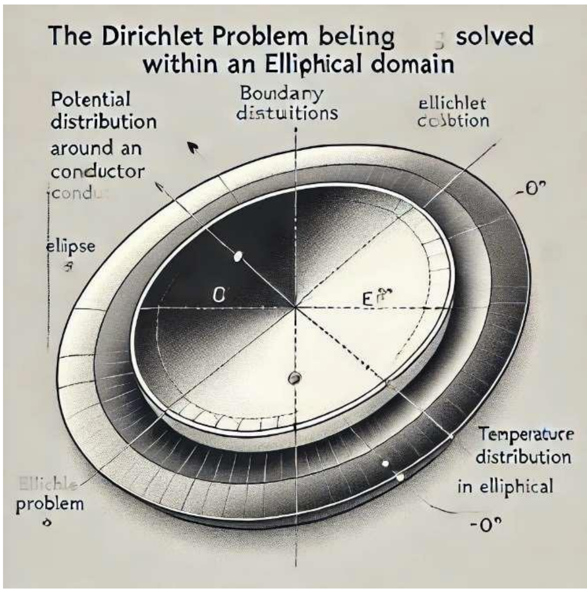
The Dirichlet Problem beling solved within an Elliphical domain
Potential distribution around an conductor
condu
Boundary distuitions
ellichlet cobtion
-0°
ellipse
O
E
Ellichle problem
Temperature distribution in elliphical
-0°

Fig. 14. Illustrative application for a ellipse region.

In the case of $h(z)=0$, the solution of the Dirichlet problem for the Laplace differential equation (1) in the ellipse is obtained in terms of elliptic functions as:

$$U(z)=\int_{0}^{K}\left[\frac{\left[G_{\xi}^{2}(z,\zeta)+G_{\eta}^{2}(z,\zeta)\right]^{\frac{1}{2}}U_0(\xi,\eta)\Big|_{\eta=-\frac{K'}{K}\sqrt{K^2-\xi^2}}^{\frac{K'}{K}\sqrt{K^2-\xi^2}}}{\sqrt{\frac{K^2\left(K^2-\xi^2\right)+(K')^2\xi^2}{K^2\left(K^2-\xi^2\right)}}}\right]d\xi$$

$$+\int_{-K}^{0}\left[\frac{\left[G_{\xi}^{2}(z,\zeta)+G_{\eta}^{2}(z,\zeta)\right]^{\frac{1}{2}}U_0(\xi,\eta)\Big|_{\eta=-\frac{K'}{K}\sqrt{K^2-\xi^2}}^{\frac{K'}{K}\sqrt{K^2-\xi^2}}}{\sqrt{\frac{K^2\left(K^2-\xi^2\right)+(K')^2\xi^2}{K^2\left(K^2-\xi^2\right)}}}\right]d\xi$$

where the Green function G is defined by (29)

$$G=\frac{1}{2\pi}\ln\left|\frac{m^{\frac{1}{4}}sn\left(\frac{2K}{\pi}\arcsin\frac{z}{c}\right)-m^{\frac{1}{4}}sn\left(\frac{2K}{\pi}\arcsin\frac{\zeta}{c}\right)}{1-m^{\frac{1}{4}}sn\left(\frac{2K}{\pi}\arcsin\frac{z}{c}\right)\overline{m^{\frac{1}{4}}sn\left(\frac{2K}{\pi}\arcsin\frac{\zeta}{c}\right)}}\right|$$

7. Conclusion

This study demonstrates a significant advantage in solving complex physics and engineering problems by expressing results in terms of elliptic functions. When applied to the two-dimensional heat equation for a rectangular plate, this method proves superior to traditional approaches, such as the method of separation of variables. Despite the challenges in computing derivatives and integrals of elliptic functions and the associated Green function, this approach holds substantial potential for broader applications. For instance, by utilizing elliptic functions for conformal mapping, the method can be extended to solve similar problems across various geometric domains, such as elliptical, square, and polygonal plates. This extension could considerably enhance the ability to address complex problems across different fields, despite computational challenges. Overall, the versatility of this method and its ability to map complex domains into simpler forms make it a powerful tool for advancing solutions in physics and engineering.

This method's computational load is indeed higher than that of traditional techniques due to the precision required in calculating elliptic functions and integrals. Thus, the suitability of this approach for specific applications depends on computational power, the criticality of accuracy, and application-specific demands. High-precision applications, such as thermal management in electronic systems and structural analysis, significantly benefit from this approach, while simpler cases may still favor traditional methods for efficiency.

Practical Applications in Engineering and Physics: The method presented in this study is especially advantageous in fields such as thermal management, structural mechanics, and electromagnetic field analysis. For example, high-accuracy heat distribution models in electronics, temperature mapping in structural components, and magnetic field studies all benefit from elliptic function-based solutions.

Software and Tools: Practical implementations of elliptic functions and Green function-based methods are greatly supported by specialized software tools. MATLAB, Mathematica, and Python’s SymPy and SciPy libraries are particularly useful, as they offer powerful functionalities for complex calculations in elliptic functions and integrals. These tools enhance accuracy and facilitate the application of this method to complex domains, making it more accessible to researchers and engineers working on precision-based projects.

These additional considerations highlight the computational trade-offs, broad applicability, and practical implementation of the method, establishing it as a versatile and effective tool for advancing complex problem-solving in applied physics and engineering domains.

References

Baykuş Savaşaneril, N., & Delibaş, H. (2016). Analytic solution for two-dimensional heat equation for an ellipse region. *NTMSCI, 4*(1), 65–70. http://dx.doi.org/10.20852/ntmsci.2016115614

Brovar, V. V., Kopeikina, Z. S., & Pavlova, M. V. (2001). Solution of the Dirichlet and Stokes exterior boundary problems for the Earth's ellipsoid. *Journal of Geodesy, 74*, 767–772. https://doi.org/10.1007/s001900000100

Byrd, P. F., & Friedman, M. D. (1954). *Handbook of elliptic integrals for engineers and physicists*. Springer-Verlag. https://doi.org/10.1007/978-3-642-65138-0

Garabedian, P. R. (1964). *Partial differential equations*. John Wiley and Sons Inc.

Hansen, O. (2000). On a boundary integral method for the solution of the heat equation in unbounded domains with nonsmooth boundary. *Journal of Integral Equations and Applications, 12*, 385–420. https://doi.org/10.1216/jiea/1020282236

Hildebrand, F. R. (1976). *Advanced calculus for applications*. Prentice-Hall Inc.

Hsiao, G. C., & Saranen, J. (1993). Boundary integral solution of the two-dimensional heat equation. *Mathematical Methods in the Applied Sciences, 16*(2), 87–114. https://doi.org/10.1002/mma.1670160203

Kurt, N. (2008). Solution of the two-dimensional heat equation for a square in terms of elliptic function. *Journal of the Franklin Institute, 345*, 303–317. https://doi.org/10.1016/j.jfranklin.2007.01.004

Kurt, N., & Sezer, M. (2006). Solution of Dirichlet problem for a triangle region in terms of elliptic functions. *Applied Mathematics and Computation, 182*, 73–78. https://doi.org/10.1016/j.amc.2006.02.036

Kurt, N., Sezer, M., & Çelik, A. (2004). Solution of Dirichlet problem for a rectangular region in terms of elliptic functions. *International Journal of Computer Mathematics, 81*, 1417–1426. https://doi.org/10.1080/00207160410001701202

Lanzara, F. (1998). Numerical approximation of eigenvalues and of Green's operator for an elliptic boundary value problem. *Calcolo, 35*, 63–92. https://doi.org/10.1007/s100920050009

Ledari, S. T., Mirgolbabaee, H., & Ganji, D. D. (2015). Heat transfer analysis of a fin with temperature-dependent thermal conductivity and heat transfer coefficient. *New Trends in Mathematical Sciences*. https://doi.org/10.20852/ntmsci.2016115614

Marshakov, A., Wiegmann, P., & Zabrodin, A. (2002). Integrable structure of the Dirichlet boundary problem in two dimensions. *Communications in Mathematical Physics, 227*, 131–153. https://doi.org/10.1007/s002200200629

Moretti, G. (1964). *Functions of complex variable*. Prentice-Hall.

Saldana, J. G., Bernal, J. A. J., Torres, C. G., & Diez, P. Q. (2006). Numerical solution for the one dimension heat equation by a pseudo-spectral discretization technique. *Cientifica Instituto Politecnico Nacional, 10*, 3–8. https://www.redalyc.org/pdf/614/61410101.pdf

Sezer, M. (1992). Solution of Dirichlet problem in terms of elliptic functions. *Yıldız University Dergisi, 4*, 1–4.

Tao, L. N. (1985). The analyticity of solution of the heat equation with nonlinear boundary conditions. *Quarterly Journal of Mechanics and Applied Mathematics, 38*, 447–459. https://doi.org/10.1093/qjmam/38.3.447

CREEP BEHAVIOURS OF THE ALABASTRINE TYPE GYPSUMS UNDER UNIAXIAL AND TRIAXIAL LOADING CONDITIONS

Ahmet Turan ASLAN

Chapter 10

Creep Behaviours of the Alabastrine Type Gypsums Under Uniaxial and Triaxial Loading Conditions

AHMET TURAN ARSLAN [1]

Introduction

Major structures such as new dwelling sites, industrial complexes, tunnels and dams may be built over the gypsum bearing unit in the Sivas province (Azam, 1998; Yılmaz, 2001; Arslan et al. 2008). Due to these investigations of the time dependent behaviour and strength parameters of evaporitic rocks such as gypsum are of prime importance for the engineering geological assessment and construction of surface and under ground structures.

Underground openings for gas storage should meet the stability requirements conforming with their function along their service life. The design of under ground gypsum caverns for natural gas storage requires the analysis of stability (e.g. permissible stress and strains, time-dependent limitation of cavern closure etc...) over the planned operating time period. The most important to be taken into consideration in the design of a gypsum cavern is short and long-terms mechanical properties such as strength, deformation as well as depth, cavern geometry, fracturing and internal gas pressure of gypsum rock. Time-dependent creep behaviour of gypsum rock must be given special consideration when determining the design and operation parameters of gypsum caverns.

In recent years rock salts have considered as an ideal material for the storage of natural gas into underground openings petroleum and wastes, especially nuclear wastes (Philip, 1981; Jordan et al. 1990). An intensive laboratory-testing programme has been carried out on the alabastrine type gypsums in order

---

[1] Dr, Dokuz Eylül University, Türkiye, ahmet.arslan@deu.edu.tr, ORCID: 0000-0002-8018-1707)

to understand its behaviour in the context of long-term stability of under ground openings related with the storage of natural gass. Due to the cause given above, the exprimental programme on the alabastrine type of gypsums is presented more in details. Time–dependent deformation (creep) is continued deformation without a stress change. Creep strain seldom can be recovered fully when loads are removed, thus it is largely "plastic" deformation. In general, however creep damages rock fabric, and may even lead to failure, particularly if tensile stresses exist, but also under some compressive stress conditions. Rarely, primary creep strain may be recovered without fabric damage when stresses are returned to their original state. In halite (NaCl), gypsum, or rocks under exceptional temperatures (T) and stresses (σ), principal stress orientation "reversal" can result in damage-free reversal of creep strains. In general, however, creep damages rock fabric, and may even lead to failure, particularly if tensile stresses exist, but also under some compressive stress conditions.

Creep is usually reported in terms of strain rate [$\frac{d\varepsilon}{dt}$] (where σ_1- σ_3, T, are constant) Where "ε" is strain, "t" is time, σ_1- σ_3 is principal stress difference and "T" is temperature. Long-term material behaviour under various stress states is explored via creep tests in laboratory. Typical applications are in radioactive disposal and storage of natural gas. Although the mechanical behaviour of rock salts has been studied for many decades by many researchers (Fuenkajorn and Daemen, 1989; Munson, 1991; Hunsche, 1994; Yang et al. 1999) time-dependent properties of gypsums have not been sufficiently investigated by uniaxial and triaxial creep tests so far. Besides, there are a few article based on the time-dependent behaviour of the massive gypsums in the literature until present (De Meer et al. 1997; Hoxha et al. 2005; 2006). Hoxha et al (2005) deals with the modelling of the long-term behaviour of a natural gypsum rock, that manifests a volumetric strain variation during the creep, a significant influence of the relative humidity on the creep strain rate and an inverse creep during unloading. Based upon laboratory results a creep model describing primary and inverse creep was firstly constructed. The paper was organized as follows; firstly, the principles features of the long-term behaviour of the gypsum rock were presented. Then a creep model describing the long-term behaviour of this natural gypsum rock was also presented. As told above, the researcher which deals with the long-term behaviour of gypsum rock, is occupied an important place. Althought time-dependent properties of rock salt have been investigated by uniaxial and triaxial creep tests since Wawersik (1981), these tests on the gypsum samples are not enough.

Scientific creep testing is particularly used to explore deformation mechanisms. Creep tests can be conducted either by multi-step loading or by a single-step loading on samples. Many past experimental results are about the effect of stress levels on primary and steady-state creep deformation and creep strain rates. The results showed creep deformation and creep strain rates depending on applied stress levels (Yang et al. 1999; Yang et al. 2006). Confining pressure was also taken account into the analysis on creep behaviour, which came to the conclusion that creep deformation and steady-state creep rates of rock decreased with increasing confining pressure (Yang & Jiang, 2010; Slizowski & Lankof, 2003; Gasc-Barbier et al. 2004). On the other hand, the tertiary creep of rock, which indicates a time-dependent deformation associated with crack propagation on rock is very important in predicting creep life of rocks (Yang & Jiang, 2010). However, in many previous experimental studies on creep behaviour of rock, instantaneous elastic deformation, primary creep and steady-state creep could often be observed, but tertiary creep is more difficult and less frequently observed in strong rocks.

Main goal of this study is to determine their time-dependent behaviour and strength parameters, under uniaxial and triaxial loading conditions and step-wise uniaxial and triaxial loadings of the alabastrine type gypsums at first. For this, laboratory tests were conducted as given below;

1. Uniaxial compression tests independent time,

2. Triaxial compression tests independent time for the different minor principal stress levels (σ_{31}= 10 MPa, σ_{32}= 20 MPa, σ_{33}= 30 MPa),
3. Step-wise uniaxial loadings to determine time-dependent creep behaviour of gypsums. σ - ε graphs of gypsum behaviour characteristics for the short-time (21 days) and long-term (119 days) periods are obtained.
4. Step-wise triaxial loadings to determine time-dependent creep behaviour of gypsums.

Methods

In order to determine uniaxial and triaxial stresses and time-dependent behavior characteristics of the alabastrine type gypsums, the tests were performed according to the standarts appropriate to DGEG-Empfehlung Nr. 16 - TP BF-STB Teil C 16 (1994). Test specimens were prepared in such a manner that the right circular cylinders (their sides were smoothed and polished) having a length to diameter ratio of between 2.5 and 3.0 and a diameter of NX-core size. These core samples were used in the tests. Specimens were inspected to be free of cracks, fissures, and other flaws, which would act as selective planes of weakness and cause an undesirable change of the real strengths and deformabilities of the rock. In determining deformability of the gypsums in uniaxial compression, MTS 20/M and MTS 815 automatic loading presses were used (Figure 2). In the tests of triaxial compression and triaxial creep deformability, the MTS 815 computer-controlled tests, and automatic loading press has been only used (Figure 3). Uniaxial compression test on the loading rate of 0.05 MPa/min, triaxial compression test in the confining pressure rate of 0.5 MPa/min, the axial loading rate of 0.05 MPa/min by applying, uniaxial and triaxial compressive strengths of the alabastrine type gypsum were determined. Uniaxial and triaxial deformability and creep tests were also performed according to the standards suggested by DGEG-Empfehlung Nr. 16 - TP BF-STB Teil C 16 (1994). The gypsum samples are loaded to 40, 60, 80 % of their maximum uniaxial compressive strength. The tests were conducted in TU Bergakademie Freiberg Germany Institut für Geotechnik Fels und Gebirgsmechanik Laboratory.

In determining deformability of the gypsums in uniaxial compression, two different automatic loading press were used. First one is an old type creep machine (MTS 20/M) and second one is MTS 815. While the strain measurement sensitivity of MTS 815 machine is at the level of $1/10^6$ that of the old one is at the level of $1/10^3$. Uniaxial creep tests were performed on the gypsum samples. After σ - ε graphs of gypsum behaviour characteristics for the short-time (21 days) and long-term (119 days) periods are obtained. This method was applied in this work in order to compare the creep test results from two different test machines with each other and to verify the degree of confidence of the test results.

Compressive creep of rock mass is adopted as the main mechanical process for this study. The deformation of rock mass is assumed to change as a function of time under compression. All short-term and creep tests for gypsum rock samples were carried out under conventional triaxial compression conditions ($\sigma_1 > \sigma_2 = \sigma_3$).

Minerology and Index Properties of Gypsums

Research conducted on alabastrin type (fine-grained) samples were obtained from Miocene formation of Karayun Egribucak in Sivas. In determining the mineralogical properties of alabastrine type of gypsum, X - ray diffraction (XRD) analysis Karacan (1989), Karacan and Yılmaz (2000), Arslan et al. (2004; 2008) analysis executed, results of the characteristic X - ray difraktogram presented in Figure 1. According to the analysis, all samples of minerals were considered to be gypsum and gypsum content 100 %. Again, taken from same member, chemical analysis of the gypsum samples were made by Karacan (1989) and collective results presented in Table 1.

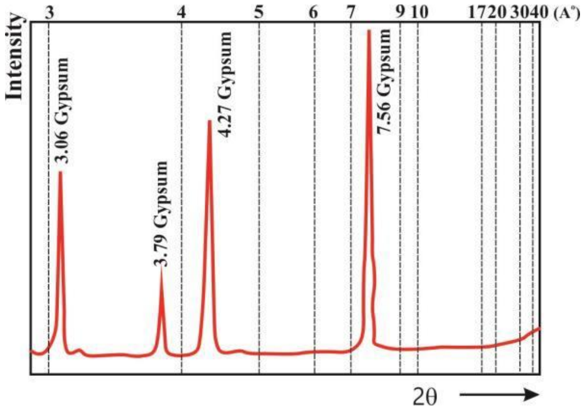

Fig. 1 Typical gypsum alabatrine type, from the area under investigation XRD–TK difractogram

The gypsum samples obtained were from the Miocene age Sivas Basin Karayün Eğribucak members. Alabastrine type of gypsums total porosity, effective porosity, dry unit weight, grain specific weight, thus some index features Karacan (1989), Yılmaz (1997), Karacan and Yılmaz (2000), Yılmaz (2001), Yılmaz and Sendir (2002), Arslan (2003), Yılmaz and Karacan (2005), Karacan and Yılmaz (2007), (Arslan et al. 2008), Yılmaz and Yuksek (2009) Yılmaz and Civelekoglu (2009), Yılmaz and Yüksek (2009), Yılmaz (2010), (Yılmaz et al. 2011), (Yılmaz et al. 2015), identified by and obtained the properties in bulk and presented in Table 2. In this study, specific gravity and dry unit weights of the gypsums were determined in accordance with the methods suggested by ISRM (2007). The specific gravity values of gysums were determined to be at the range of 2.36-2.40. On the other hand, dry unit weights of the samples were determined to be between 20.60 and 21.97 kN/m^3. All of the samples tested were classified as "low unit weights" according to the IAEG classification IAEG (1981). All of the gypsum samples in terms of both effective and total porosity values were classified as “the rock with medium porosity” according to the IAEG classification IAEG (1981).

Table 1. Chemical analysis results of the alabastrine type gypsum samples.

Elements (%)	Minimum	Maximum	Mean
SiO_2	0.02	0.08	0.05
SO_3	44.96	45.18	45.07
Fe_2O_3	0.10	0.14	0.12
SrO	0.10	0.60	0.35
MgO	0.01	0.03	0.02
CaO	31.55	31.63	31.59
Na_2O	0.1	0.5	0.3
Loss of igination at 600 °C	20.54	20.72	20.63
Loss of igination at 1000 °C	21.00	21.26	21.13

Table 2. Some index properties of the gypsums type alabastrine

Physical properties	Alabastrine type gypsum		
	Minimum	Maximum	Mean
Specific gravity	2.36	2.40	2.38
Dry unit weight (kN/m^3)	20.60	21.97	21.39
Effective porosity (%)	1.6	10.9	4.8
Total porosity (%)	5.7	13.0	8.0

Tests Performed Under the Uniaxial and Triaxial Stress Conditions Regardless Time

Stress values are obtained from the compression tests under the uniaxial and triaxial stress conditions regardless time. Graphical analysis including the readings relation with axial and diametrical strains is presented in Fig. 4. Relationships between axial and diametrical strains and stresses under uniaxial and triaxial loading conditions are presented in Fig. 4a and Fig. 4b, respectively. Graphical analysis relation with the elastic parameters such as elasticity modulus and Poisson's ratio are also presented in Fig. 5 and Fig. 6. On the other hand, typical Mohr-Coulomb diagram obtained from the triaxial compression tests and strength envelope of gypsums acquired by using the principal stresses are given in Fig. 7 and Fig. 8, respectively.

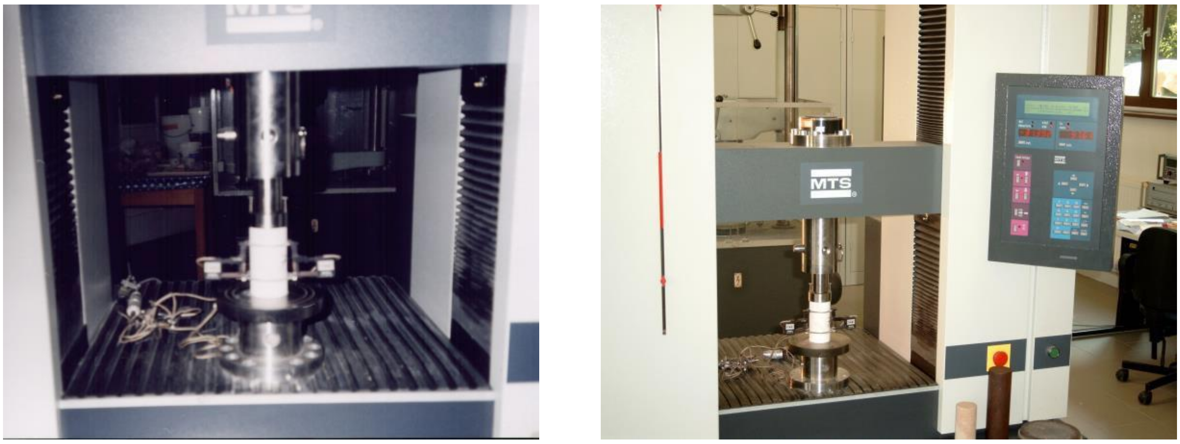

Fig 2. MTS 20 / M press using the uniaxial compression and uniaxial creep tests

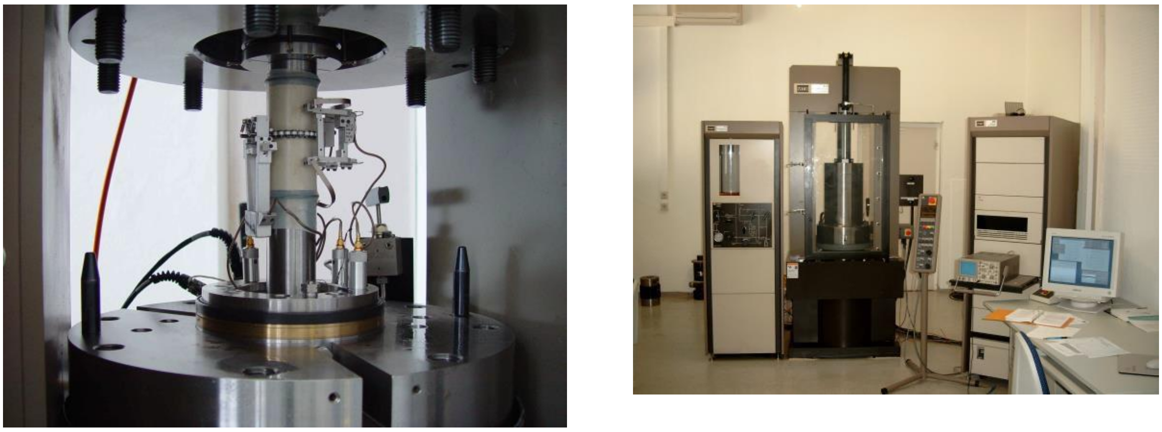

Fig 3. MTS 815 press using the triaxial compression and triaxial creep tests

Time-Dependent Strength Parameters of Gypsums

Creep, in general terms is described as time-dependent deformation of a rigid body without rupture. As known, creep and rupture are issues in cases of high point loads that lead to time-dependent fracture growth. If the processes of unit strain hardening and recovery develop within balance, secondary creep stage (steady-state creep) is dominant. In secondary creep stage, unit strain rate over time is approximately a constant value. Therefore unit strain–time creep curve reaches near linear view. When a strain increase is applied, unit strain hardening becomes influential and increasing creep unit strain rate during the first stage, decrease within time. Thus, the material behavior is described as primary creep. When strain decrease is applied, rapid decreasing unit strain rate at start continues to increase with time until secondary creep stage is reached. Under high stress conditions, creep curve's linear section continues to change again and failure can occur in time by way of dilatation in creep stage, which is expressed as the tertiary creep stage (Hunsche, 1994; Özarslan et al. 2007).

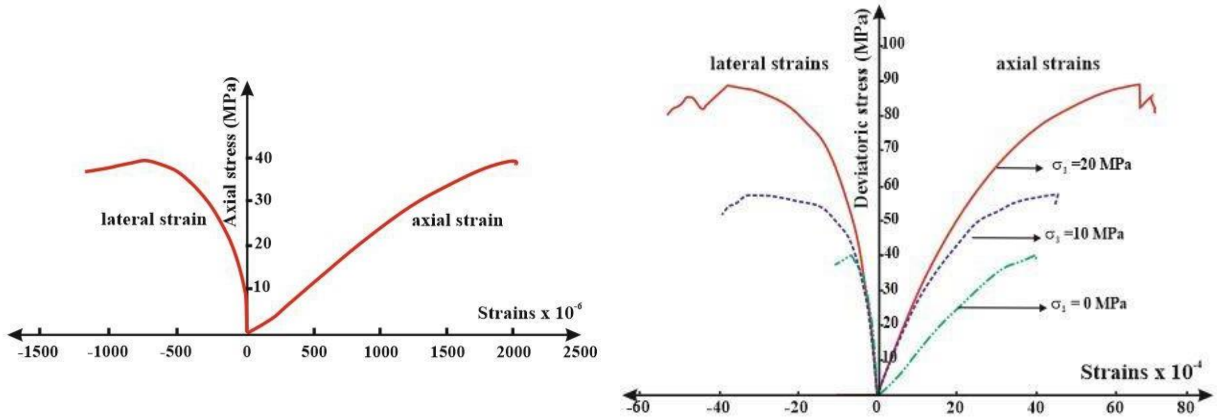

a) *Axial stress conditions* ***b)*** *Triaxial stress conditions*

Figure 4. Stress- strain graph time-independent [σ = f(ε)] of the gypsum samples under the axial and triaxial stress conditions

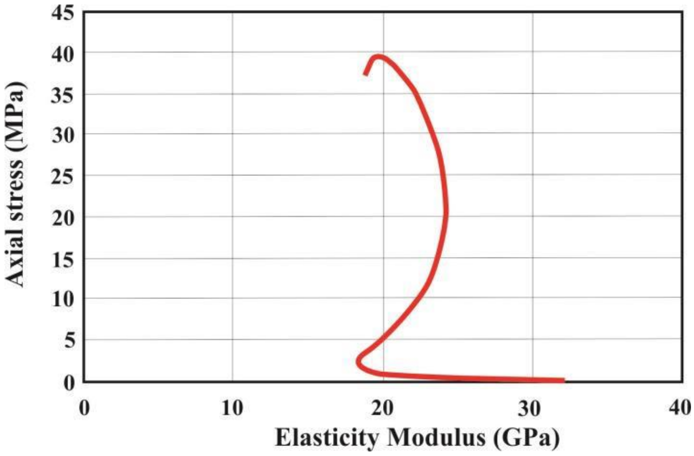

Fig 5. Relationships between uniaxial compressive strength and elasticity modulus

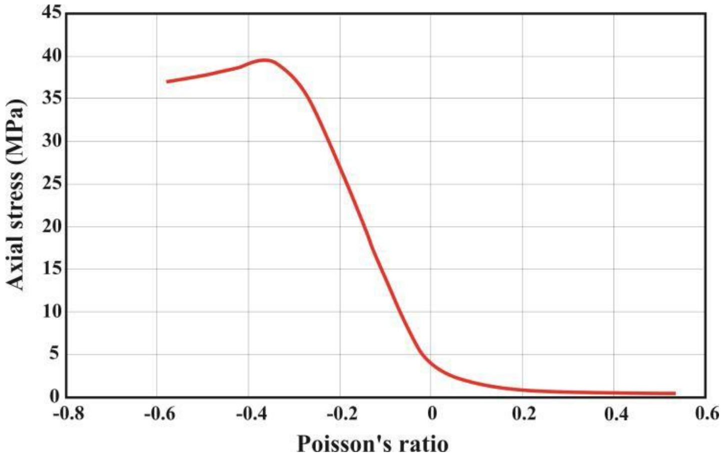

Fig. 6 Relationships between uniaxial compressive strength and Posisson's ratio

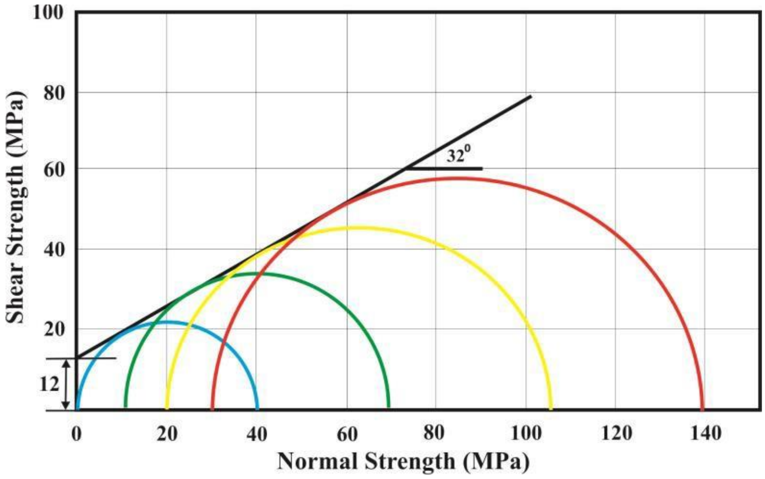

Fig 7. Typical Mohr-Coulomb diagram from the triaxial tests

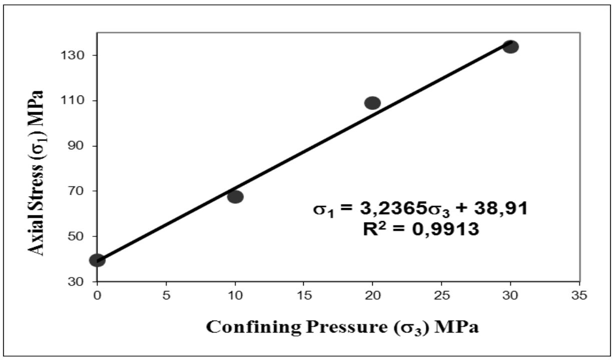

Fig. 8 Relationships between minor and major principle stresses in gypsums

In general, the heterogeneous nature of rocks, is anisotropic, its discontinuities and their properties due to previous tectonic phases thus have the same mineralogical composition of rocks, even the physical and mechanical properties vary from one another. Therefore, the true creep behavior of rocks is very difficult to determine. Laboratory studies and research using the underground rock creep behavior under real environmental conditions have been explained with mathematical equations. In this context, the studies represent an important part of the long-term phase, focusing on the secondary creep stage. The developed mathematical equations with secondary creep rate ($\dot{\varepsilon}_s$) generally the difference between effective principle stresses ($\cdot = \cdot_1 - \cdot_3$), ambient temperature (T) and describes as dependent on material parameters. In order to define the secondary creep stage, the relations have been tried to develop by many researchers. These relations in general describe secondary creep rates ($\dot{\varepsilon}_s$) dilatation ····.····.· and temperature (T) dependent.

$$(\dot{\varepsilon}_s) = f(\cdot, T) \qquad (1)$$

The most commonly used equations below were developed by utilizing the general creep law.

$$\dot{\varepsilon} = A\left(\frac{\sigma_1-\sigma_3}{\sigma^*}\right)^n \exp\left(-\frac{B}{T}\right) \qquad (2)$$

Where;

A= Structural factor

n= Parameter dependent upon stress ratio

Q= Activation energy

R= Universal gas constant (8.314 x 10^3 kJ mol^{-1}K^{-1})

T= Temperature (K)

▪*= 1MN/m^2 (Normalization)

B= (Q/R) Sensitivity to temperature

$$B = \frac{Q}{R} = \frac{\ln\left(\frac{\dot{\varepsilon}_{s,2}}{\dot{\varepsilon}_{s,1}}\right)}{\left(\frac{1}{T_1}-\frac{1}{T_2}\right)} \qquad (3)$$

In order to achieve "n" coefficient given in Equation 4, the same temperature and varying stress conditions obtained under secondary creep rate value used as aid. Reflecting the impact of stress, "n" coefficient is used from the following statement.

$$n = \frac{\log\left(\frac{\varepsilon_{s,1}}{\varepsilon_{s,2}}\right)}{\log\left(\frac{(\sigma_1-\sigma_3)_1}{(\sigma_1-\sigma_3)_2}\right)} \qquad (4)$$

Uniaxial and triaxial creep tests were conducted according to the standarts suggested by DGEG (1994). Thus the results are according to the parameters given and are presented as such. To determine time-dependent behavior and strength characteristics parameters of the alabastrine type gypsum under the uniaxial and triaxial stress conditions, the loadings were applied in varying stages of stress. Under the conditions of uniaxial and triaxial loading, loads were applied in such a manner that corresponded to the maximum uniaxial compressive strength of 40 %, 60 % and 80 %. As a result of the uniaxial and triaxial tests, time-dependent axial and diametrical strain (deformation) changes, time-dependent axial and diametrical creep rate, deformation rate of creep with axial and diametrical relevant parameters were determined.

Creep Behaviour of the Gypsums Under the Uniaxial Stress Conditions

Long-Term (119 days) Creep Tests
To determine the creep behaviour of alabastrine type gypsums under uniaxial stress conditions, cylindrical core samples were used by regarding to the L/D ratio between 2.0-2.5 according to the ISRM (2007). Long-term (119 days) deformability and creep tests of uniaxial loading mechanism known as the old type creep machine was used (Fig. 9).

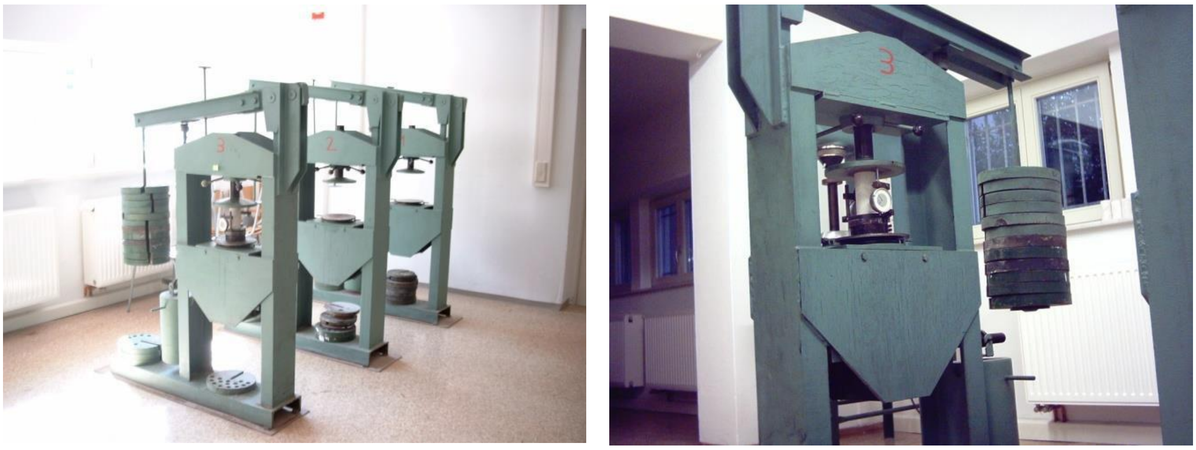

Fig 9. Old type creep machine used 119 days constantly for uniaxial deformability and creep tests

Under the laboratory conditions for duration of 119 days, to determine time-dependent behavior of gypsums under the conditions of uniaxial compression with maximum compressive strength of [30 % - 13 MPa], [50 % - 20 MPa], [70 % – 27 MPa] values response to constant load, three stages creep tests were conducted. During the tests to determine the constant load to be applied, the maximum compressive strength of gypsum was used as the base. Stresses applied in the creep tests changed in the range of uniaxial compressive strength from 30 % to 70 %, due to change in the range given above, gypsum samples tertiary creep phase and before the failure occurrance, secondary creep phase was balanced with nearly constant unit strain rate.

A linear relationship was observed in the tests performed between creep curve and applied stress stage. At 13 MPa, 20 MPa and 27 MPa stress stages at elastic and primary creep stages a sudden increase while in its continuation, during secondary time-dependent creep stage a slow increase in plastic deformations occur (Fig. 10). Creep ··= f (t) and time-independent · = f (·) curves are given in Table 3. As seen in Table 3, total hours 2856 (119 days) and in intervals corresponding to 35, 32, and 52 days for each stage of stress, $\sigma - \varepsilon$ graph was drawn by attaining base values of $\varepsilon_{elastic}$ and ε_{creep}, and presented in Figure 11. According to the graph, the maximum uniaxial compressive strength for gypsums $\cdot_{cmax}$ = 40 MPa, $_{critic}$ = 27 MPa and critic unit strain as $_{creep}$ = 28 x 10^{-4} are determined. However, when duration of the test is longer, the increase value of $\cdot_{critic}$ should be considered critical.

Table 3. Uniaxial creep test results of the gypsum samples

Stress		$\cdot_{elastic}$	$\cdot_{creep}$	($\dot{\varepsilon}_s$) (1/d)		
%	MPa	(x 10^{-4})	(x 10^{-4})	(x 10^{-6})	Time (hour)	Day
30	13	5.52	7.67	4.50	840	35
50	20	8.28	14.08	6.14	1608	67
70	27	11.31	28.52	7.35	2856	119
100	40	20.00	-	-	Time- independent	

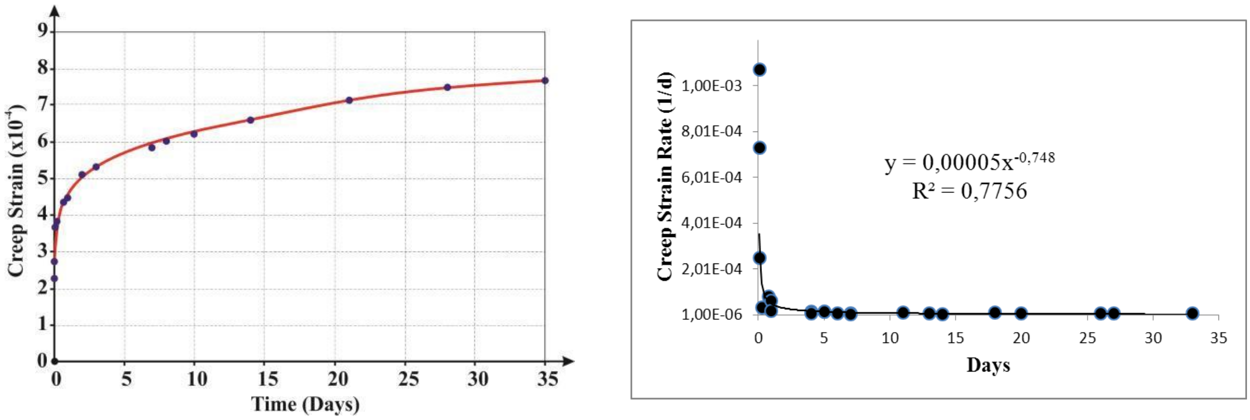

(σ_1=13 MPa, σ_3=0 MPa)

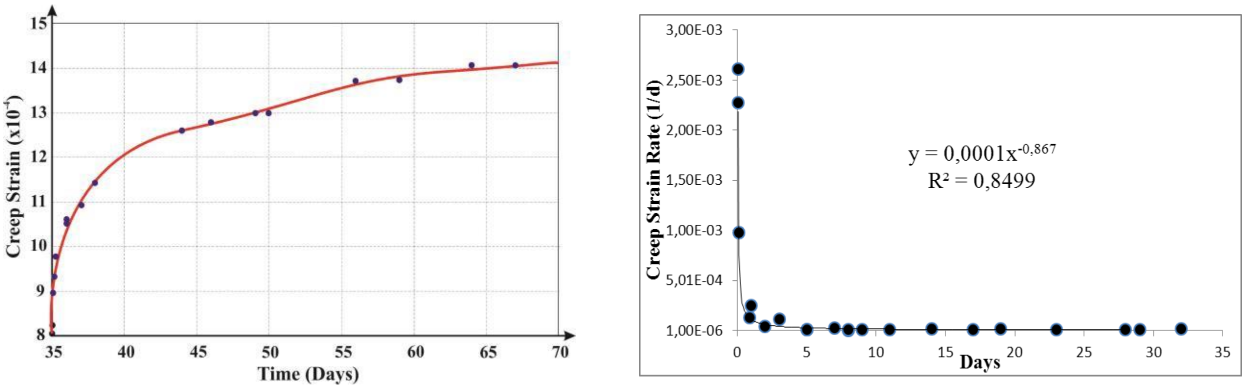

(σ_1=20 MPa, σ_3=0 MPa)

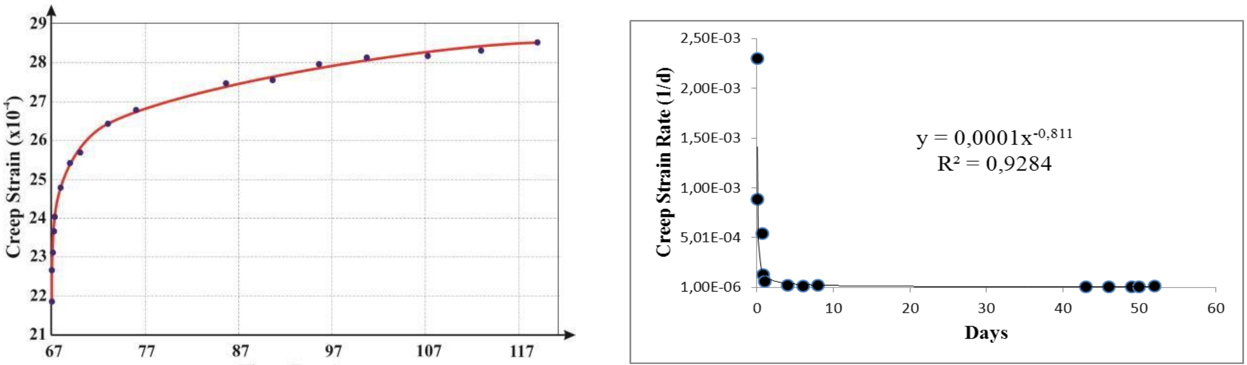

(σ_1=27 MPa, σ_3=0 MPa)

Fig. 10 Varying stress stages for gypsums creep unit strain – time and creep unit strain rate – time relations (Under the uniaxial stress conditions t=119 days)

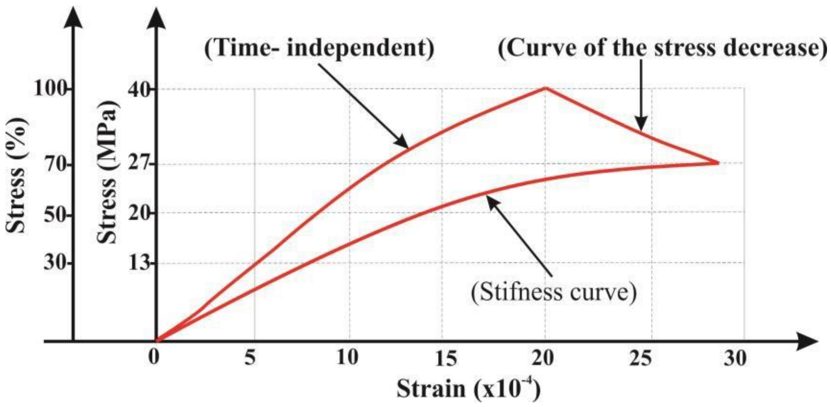

Fig 11. Behaviour characteristic of gypsum (t = 119 days) in the graph of · - ·

(Under the uniaxial stress condition)

Short - Term (21 days) Creep Tests

As seen in Figure 12, a change in the creep curve is observed depending on an increase or decrease of the stress applied on the gypsum sample. Creep curve is responsed with the first creep phase versus the stress changes into a short time (168 hours). However, after a short time creep curve is balanced in the values of secondary creep rate for the different stress stages (16 MPa, 24 MPa, and 32 MPa). In given stress stages, creep curve could not shift to the tertiary creep phase at the end of 21 days (Figure 12). The graphs of creep strain rate – time and creep strain rate – axial strain rate were also obtained from the uniaxial deformability and creep tests at the stress stages of 16 MPa, 24 MPa, and 32 MPa and presented in Figure 13 and 14, respectively.

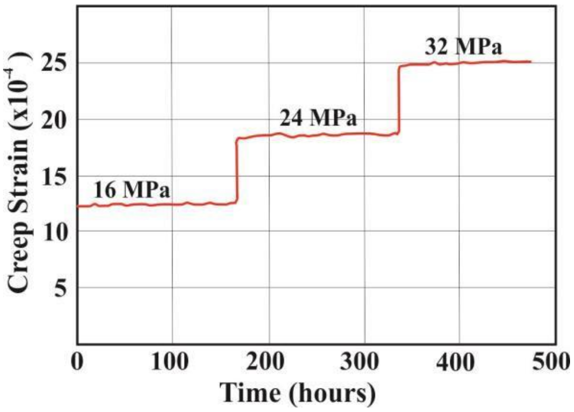

Fig 12. The graph showing relationships between creep strain and time [ε = f(t)] under the uniaxial stress condition of gypsums

When the graph showing the relationship between creep strain rate and time is examined, creep unit strain rate is seen to change in the range from 1x10^{-5} to 1 x10^{-4} 1/day (Figure 13). When the graph showing the relationship between creep strain rate and axial strain rate is also examined, creep strain rate for the three stress stages is determined as a mean value of 1x10^{-2} 1/day (Figure 14).

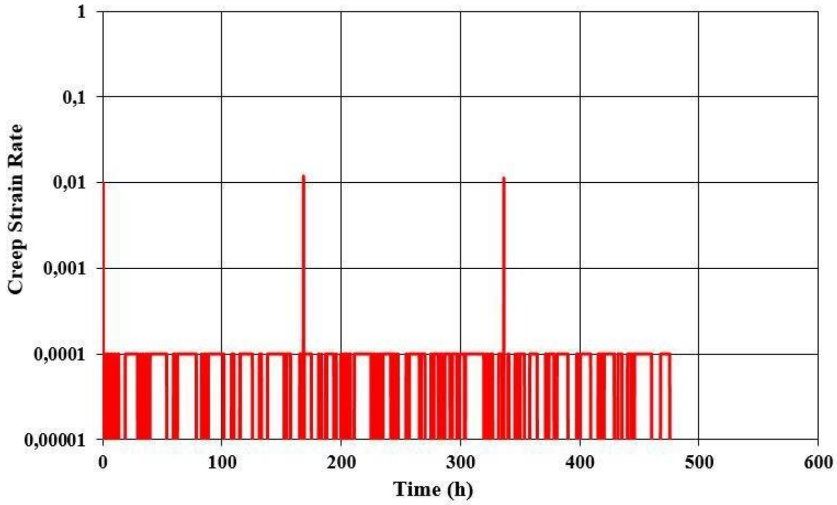

Fig 13. The relationships between creep strain rate and time under the uniaxial stress condition of the gypsums

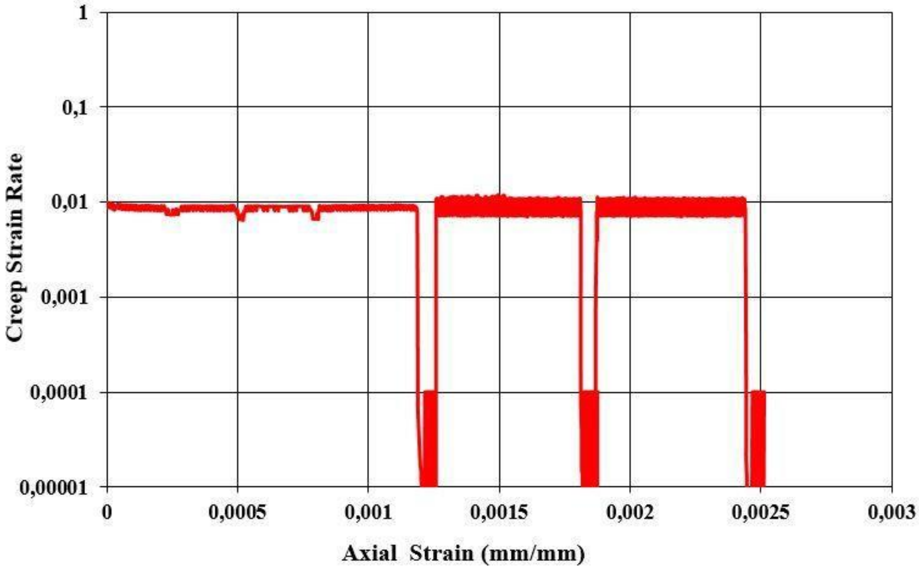

Fig 14. The graph showing the relationships between creep strain rate and the uniaxial strain of the gypsums under the uniaxial stress condition

In 21 days of uniaxial deformability and creep tests a linear relation is observed between applied stress step and creep curve. Under 16 MPa (% 40), 24 MPa (% 60), 32 MPa (% 80) stress stages, elastic and primary creep stages sudden increase and its successor secondary creep stage as time dependent, slow increasing plastic deformations are occurred. From creep · = f(t) and time independent · = f(·) curves results obtained are given in Table 4.

Table 4. The results of the uniaxial creep tests performed on the gypsum samples

Stress		·elastic	·creep		
%	MPa	(x 10^{-4})	(x 10^{-4})	Time (hour)	Day
40	16	6.92	12.36	168	7
60	24	10.32	18.55	336	7
80	32	13.85	24.94	504	7
100	40	20.00	-	Time-independent	

σ - ε graph was drawn by utilizing values shown in Table 4, total of five hundred four hours (504 hrs) - (21 days), and one hundred sixty eight hours (168 hrs) - (one day) of time intervals corresponding to each step of stress $\varepsilon_{elastic}$ and ε_{creep} base values attained from the graph presented in Figure 15. According to the graph the maximum compressive stress value for gypsums is σ_{cmax} = 40 MPa, critical stress being σ_{critic} = 32 MPa and critical unit strain ε_{creep} = 25 x 10^{-4}.

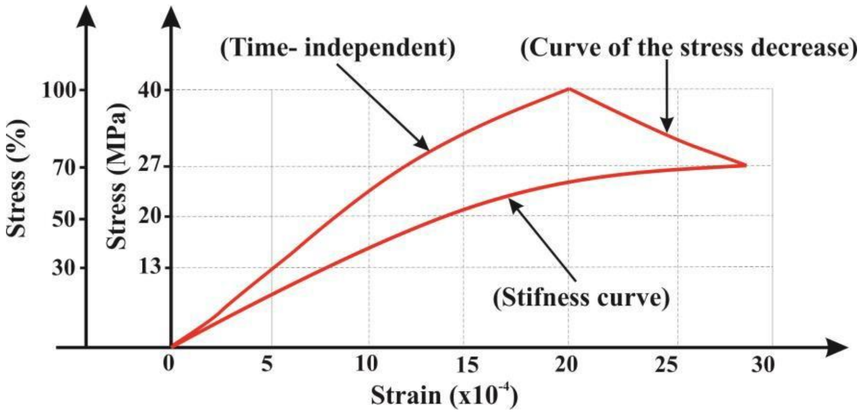

Fig 15. σ - ε graph of gypsum behaviour characteristic (t = 21 days)

Creep Behaviour of the Gypsums Under the Triaxial Stress Conditions

For the first time within the scope of this research, time-dependent creep behaviour of alabastrine type gypsums under the triaxial stress condition is analyzed and discussed. A linear relationship was observed between creep curves slopes and triaxial stress steps performed in creep tests (σ_1-σ_3= 16 MPa, 24 MPa ve 32 MPa). Figure 16 shows the graph of axial strain-time relationship, upon examination of the graph, at 40%, 60%, and 80% stress increase steps an increase of elastic behaviour and in continuation of the steps into primary creep stage, an increase in the curves of a slope is observed, and in secondary creep stage, time-dependent slow increase in plastic deformations occur.

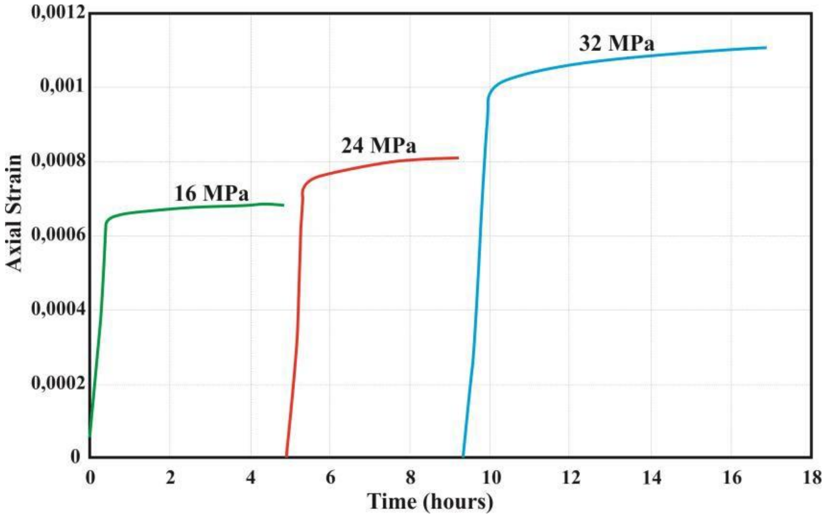

Fig 16. The relationship between axial unit strain and time (σ_1= 26, 34, 42 MPa, σ_3=10 MPa)

If diametrical unit strain-time relationship given in Figure 17 is examined, in applied stress stages of 16, 24, and 32 MPa, a sudden increase in elastic behaviours and in its continium to primary creep stage, slope of the curves decrease being time-dependent, and in secondary creep stage, time-dependent slow decreasing plastic deformation is observed.

Belonging to the triaxial tests the relationships between axial creep unit strain rate and time are shown from the graphs in Figure 18. Secondary creep unit strain rates for the stress conditions of $\sigma_1 - \sigma_3$ = 16 MPa, 24 MPa and 32 MPa were found to be 6.73 x 10^{-5}, 2.23 x 10^{-4}, and 8.60 x 10^{-4} 1/hour from Figure 18, respectively. Calculated secondary creep unit strain rates and n-coefficients which reflect to the stress effect on creep material models were obtained by using Equation- 4 and presented in Table 5.

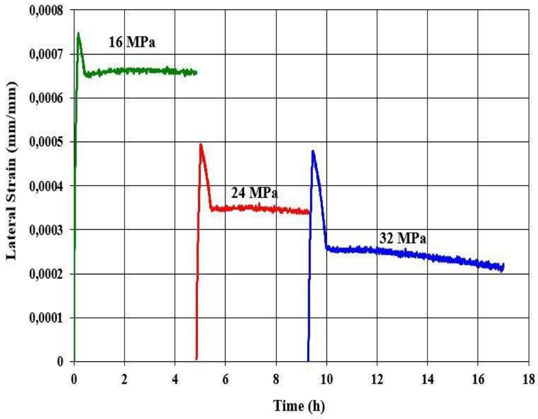

Fig 17. Diametrical unit strain-time relation (σ_1=26, 34, 42 MPa; σ_3=10 MPa)

Diametrical (lateral) creep unit strain rate – time graphics were attained in laboratory creep tests conducted under the triaxial stress conditions and presented in Figure 19. Diametrical creep unit strain rate for the stress steps of $\sigma_1 - \sigma_3$ = 16 MPa, 24 MPa and 32 MPa are found to be 7.32 x 10^{-5}, 7.45 x10^{-5} and 9.28 x 10^{-5} 1/hour, respectively. Triaxial creep test results for axial creep unit strain rate-axial unit strain and diametrical creep unit strain rate-diametrical unit strain graphs were attained and presented in Figure 20 and 21.

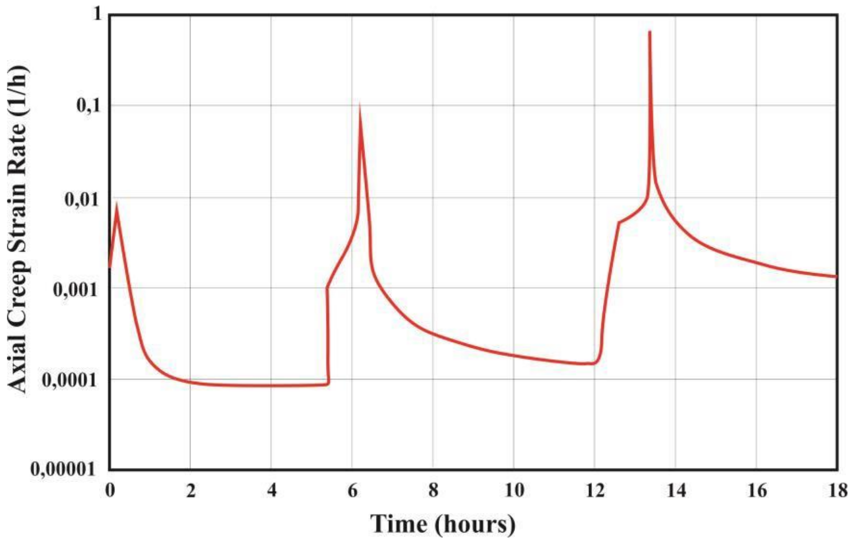

Fig 18. Axial creep unit strain rate-time relation (σ_1=26, 34, 42 MPa; σ_3=10 MPa)

Table 5. Reflecting effect of stress on creep material models n-coefficients

$(\sigma_1 - \sigma_3)$	$(\dot{\varepsilon}_s)$ (1/d)	n
14	6.73×10^{-5}	2.95
16	2.23×10^{-4}	4.70
18	8.60×10^{-4}	

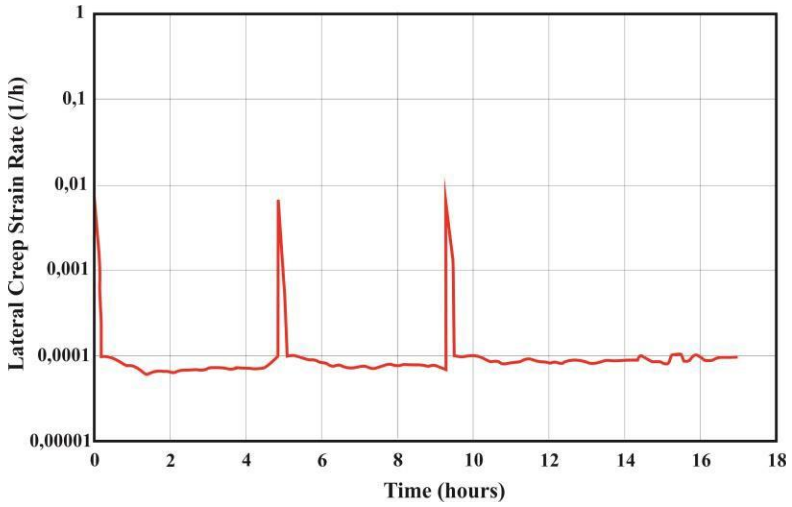

Fig 19. Diametrical creep unit strain rate-time relation (σ_1=26, 34, 42 MPa; σ_3=10 MPa)

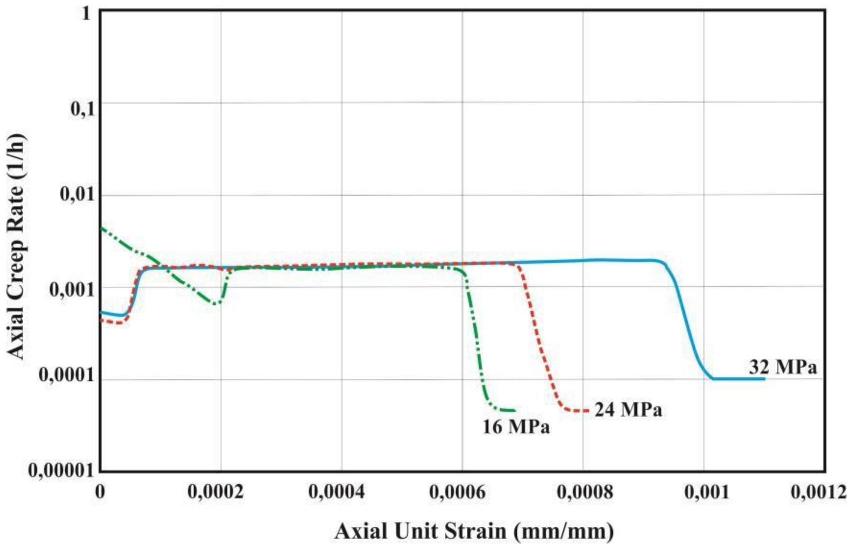

Fig. 20 Relationships between axial unit strain and axial creep rate

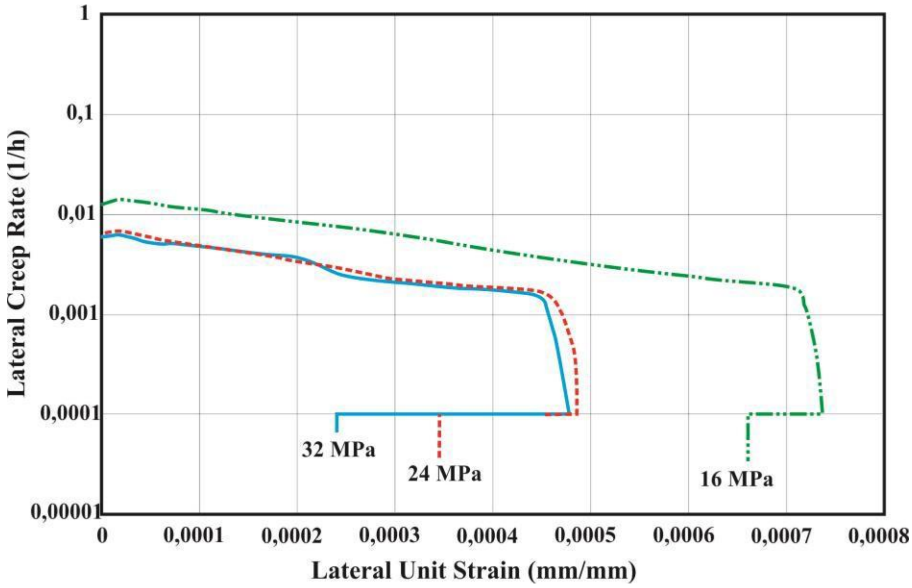

Fig. 21 Relationships between axial unit strain and diametrical creep rate

Conclusion

Due to rheological properties of the rocks, until breakage varying unit strain rate is observed. Prior to breaking, unit strain rate of the gypsums is increased due to the decreasing of rock strength. As a result of this, different flow regions are passed through during the creep. There is no special method to measure time-dependent strain of rocks under constant load. General principle is to provide constant load on the test sample. However, it is not always adequate with constant load to achieve constant stress. Therefore, there is necessary need for electro-hydraulic systems. Thus, gypsums strength and strain characteristics can be allocated to short and long terms. Creep behaviour and long-term strength characteristics of the gypsums gaines vital importance in terms of the long-term mechanical properties. Short term mechanical properties can be analyzed under uniaxial and triaxial strength and strain headings. In addition, rock mechanics of gypsums, stability and safety analysis of failure and dilatation is of crucial in underground and surface engineering applications.

Uniaxial compressive strength value of the alabastrine type gypsums with medium porosity and low unit weight was determined as the mean value of 40 MPa. In addition, elasticity modulus and Poisson’s Ratio values of this type of gypsums were also determined to be at the ranges of 20-25 GPa, 0.30-0.35, respectively. As a result of the triaxial tests, relationship between minor and major principle stresses in gypsums was obtained as the following equation;

$$\sigma_1 = 38.91 + \sigma_3 \text{ x } 3.2365 \qquad R^2 = 0.99$$

Also equation of the Mohr & Coulomb failure envelope from the triaxial tests;

··=12 + σ Tan32 (c = 12 MPa, ········

As a result of the uniaxial and triaxial tests performed on the gypsum core samples, time-dependent axial und diametrical strain changes, time-dependent axial und diametrical creep rate, deformation rate of creep with axial and diametrical relevant parameters were determined in this work. Three stages creep tests (at 13 MPa, 20 MPa and 27 MPa stress stages) were conducted in order to determine time-dependent behavior of gypsums under the condition of uniaxial compression. It was determined that there is a lineer relationship in creep tests performed between creep curve and applied stress stage. In addition, it is observed that at three different stress stages at elastic and primary creep stages a sudden increase occur while in its continuation, during secondary time-dependent creep stage a slow increase in plastic deformation occur. Total days 119 and in intervals corresponding to 35, 32, and 52 days for each stage of stress, σ - ε graph was drawn by attaining base values of $\varepsilon_{elastic}$ and ε_{creep}. σ_{critic} and ε_{creep} (critic unit strain) were determined as 27 MPa, 28 x 10^{-4}, respectively. For three stages creep tests, the equations reflecting the relationships between creep strain rate (V_ε) and time (t) were obtained as following for the condition of σ_1 = 13 MPa and σ_3 = 0 (35 days);

$$V_\varepsilon = 0.0001\ t^{-0.784} \dotfill R^2 = 0.77$$

for the condition of σ_1 = 20 MPa and σ_3 = 0 (32 days);

$$V_\varepsilon = 0.0001\ t^{-0.867} \dotfill R^2 = 0.85$$

for the condition of σ_1 = 20 MPa and σ_3 = 0 (52 days);

$$V_\varepsilon = 0.0001\ t^{-0.811} \dotfill R^2 = 0.93$$

In the stress stages of 16 MPa, 24 MPa and 32 MPa in the short-term creep tests, creep curve could not shift to the tertiary creep phase at the end of 21 days. After a short-time (168 hours: 7 days) creep curve is balanced in the values of secondary creep rate. According to σ - ε graph, σ_{critic} and ε_{creep} were determined as 32 MPa, 25 x 10^{-4}, respectively. It has been understood that ε_{creep} values from either long or short-terms creep tests are almost found in the same level due to being at the same level (27 MPa – 32 MPa) of the critic compression values under the conditions of uniaxial compression. The case given above state that a slow increase in plastic deformation occurs in secondary time-dependent creep stage after the stress level of 27 MPa (σ_{critic}) because an important change in the level of creep deformation was not occurred.

Creep behavior of the gypsum was also investigated under the triaxial stress conditions as well as the uniaxial stress conditions in this work. Applied stress stages in the tests are of the values of 16, 24, and 32 MPa (deviatoric stresses). For these stress conditions (σ_1- σ_3 = 16 MPa, 24 MPa and 32 MPa) secondary axial creep strain rates were found to be 6.73 x 10^{-5}, 2.23 x 10^{-4}, and 8.60 x 10^{-4} 1/hour, respectively. In addition, diametrical creep unit strain rate for the stress steps of σ_1- σ_3 (16, 24 and 32 MPa) were found to be 7.32 x 10^{-5}, 7.45 x 10^{-5}, and 9.28 x 10^{-5} 1/hour, respectively. Under the same deviatoric stress conditions, it was determined that the axial creep unit strain rates are greater than that of the diametrical ones as expected. Accordingly, it was determined that as deviatoric stress values for the gypsums increase n-coefficients also increase for both axial and lateral creep strain rates (Table 6). On the other hand, creep strain rate values of rock salt and gypsum under the uniaxial and triaxial loading conditions and n-coefficient are given as comparatively in Table 6. In this table, if the axial creep strain rates under the some deviatoric stress (σ_1-σ_2: 14, 16, and 18MPa) are examined, it is observed that their values of rock salts are almost accordance with that of the gypsums.

Table 6. As comparatively given creep strain rate values of rock salt and gypsums under the uniaxial and triaxial conditions and n-coefficients

	Time (d) (days)	**Rock Salt (22°C)**				
		(σ_1) (MPa)	**$\dot{\varepsilon}_s$ (1/d) (axial)**	**(σ_1-σ_3) (MPa)**	**$\dot{\varepsilon}_s$ (1/d) (axial)**	**n**
DGEG (1994)	128			14	4.10 x 10^{-5}	5.30
	96			16	8.30 x 10^{-5}	3.10
	140			18	1.20 x 10^{-4}	
Bertram (2000)	32			12	8.49 x 10^{-5}	4.57
	32			18	5.41 x 10^{-4}	4.77
	32			22	1.41 x 10^{-3}	
	30	12.00	9.38 x 10^{-6}			10.40
	35	15.00	9.56 x 10^{-5}			
Özarslan et al. (2007)	90	11.80	5.23 x 10^{-5}			4.94
	105	14.70	1.55 x 10^{-4}			4.75
	105	11.80	6.80 x 10^{-5}			
	105	14.70	1.93 x 10^{-4}			

	Time (t) (hours)	Gypsum (22°C)				
		(σ_1) (MPa)	$\dot{\varepsilon}_s$ (1/t) (axial)	(σ_1-σ_3) (MPa)	$\dot{\varepsilon}_s$ (1/t) (axial)	n
This work	5			14	6.73×10^{-5}	2.95
	6			16	2.23×10^{-4}	4.70
	8			18	8.60×10^{-4}	
					$\dot{\varepsilon}_s$ (1/t) (lateral)	
	5			14	7.32×10^{-5}	0.13
	6			16	7.45×10^{-5}	1.86
	8			18	9.28×10^{-5}	
	168	16.00	12.36×10^{-4}			1.00
	168	24.00	18.55×10^{-4}			1.02
	168	32.00	24.94×10^{-4}			
	840	13.00	7.67×10^{-4}			1.41
	1608	20.00	14.08×10^{-4}			2.35
	2856	27.00	28.52×10^{-4}			

Important property of gypsums, like as rock salt, is not include discontinuities and it is not effected by ground water in homogenous and deep seated geological media. Massif and unweathered rock salt can be admitted as impermeable rock due to its permeability coefficient of 10^{-14}m/s. Olgaard et al (1995) was determined that impermeability value of the alabastrine type gypsums against gasses is 4×10^{-18}m^2. Respectively, when gypsums are not under the effects of failure and dilatency, then they display impermeable rock properties against fluids and gasses; thus fluids and gasses are not the cause of over dissolution. Depending on this property, dimensioning of large underground openings into the alabastrine type gypsums will be met the stability requirements conforming with their function during their service life without need to artificial supports. Time-dependent and independent behaviours of the gypsums as well as the collective some porperties of the gypsums and rock salts given above were determined by long-term and short-term creep tests under uniaxial and triaxial stress conditions. After their results of the creep tests were compared with that of rock salts (Table 6). In the light of these results given above, it is concluded that it is possible to keep the stability of underground openings into gypsums for a long time and to provide the operation safety.

Materials needed in secondary krip modelling A and Q (Equation–2, Equation–3) for such parameters to be at hand, temperature control and varying stress conditions applied in triaxial creep test data is necessary. Since single triaxial test conducted on gypsum comprises long time span (18 hours per one try), data are available however it is limited. In the next stage of the tests, varying temperature controlled triaxial tests on the alabastrine type gypsum samples have been continued.

References

Arslan, A.T. (2003). Experimentelle und theoritische untersuchungen und auswertungen der kriecheigenschaften der gipsfelsen, TU Bergakademie Freiberg, Deutschland.

Arslan, A.T., Koca, Y., Aydoğmuş, T., Akçığ, Z. (2004). Static-elastic and dynamic-elastic properties of Oligocene-Miocene aged gypsum. Earth Sciences GEOSOUND ISSN: 1019-1003, V.44, 1-15.

Arslan, A.T., Koca, M.Y., Aydoğmuş, T., Klapperich, H., and Yılmaz, H.R. (2008). Correlation of unconfined compressive strength with Young's Modulus and Poisson's Ratio in gypsums from Sivas (Turkey), *Rock Mech. and Rock Eng*. 41: 941-950.

Azam, S., Abduljauwad, S.N., Al-Shayea, N., Al-Amoudi, O.S.B. (1998). Expansive characteristics of gypsiferous/anhydritic soil formations, *Eng. Geo.,* 51 (2): 89-107.

Bertram, J. (2000). Untersuchungen zur weiterentwicklung der auslegungskriterien für kavernen im steinsalzgebirge, *Schriftenreihe Professur für Deponietechnik ud Geomechanik Technische Universitaet Clausthal*, Heft Nr. 11, 279 s.

De Meer, S., Spiers, Ch., Peach, C. (1997). Pressure soluation creep in gypsum: evidence for precipitation reaction control, *Physics and Chemistry of the Earth*, 22, (1-2), 33-37.

DGEG (1994). Ein und dreiaxiale kriechversuche an gesteinproben, Ausgabe 1994, Empfehlung Nr. 16, TP BF-StB, Teil C 16, 11 s.

Fuenkajorn, K., Daemen, J.J.K. (1989). Borehole closure in salt, *In: Proceeding of 29th US Symposium on Rock Mechanics*, Rotterdam, Netherlands: Balkema, p. 191-198.

Hoxha, D., Albert, G., Françoise, H. (2005). Modelling long-term behaviour of a natural gypsum rock, *Mechanics of Materials*, 37, 1223-1241.

Hoxha, D., Homand, F., Auvray, C. (2006). Deformation of natural gypsum rock: Mechanism and questions, *Engineering Geology*, 86, 1-17.

Hunsche, U. (1994). Uniaxial and triaxial creep and failure test on rock: experiment technique and interpretation, In: Cristecu N.S., editor. Visco-plastic behaviour of geomaterial, Springer-Verlag.

ISRM (2007). The complete ISRM suggested methods for rock characterization testing and monitoring 1974 – 2006. Compilation arranged by the ISRM Turkish National Group Ankara.

Jordan, P., Noack, T., Widmer, T. (1990). The evaporite shear zone of the Jura boundary thrust-new evidence from Wisen well (Switzerland), *Eclogea Geologicae Helveticae* 83, 525-542.

Karacan, E. (1989). Geo-engineering characteristics Miocene gypsum in the SE of Sivas Turkey, Ph.D. Dissertation, Hacettepe University, Ankara, Turkey.

Karacan, E. and Yilmaz, I. (1997). Collapse dolines in the Miocene gypsum: an example from SW Sivas (Turkey). *Environmental Geology*, 29 (3/4), 263-266.

Karacan, E. and Yilmaz, I. (2000). Geotechnical evaluation of the Miocene gypsum from Sivas (Turkey), *Geotechnical and Geological Engineering*, 18 (2), 79-90.

Munson, D.E. (1991). Constitutive modelling of salt behaviour: state of the technology, *In: Proceeding of 7th International congress on Rock Mechanics*, p. 1979-1810.

Özarslan, A., Geniş, M., Bilir, M.E. (2007). Stability investigation of underground salt caverns for natural gas storage over the planned operating time period. TUBITAK Project Number, 104M132, Ankara, pp. 120.

Philip, B. (1981). In situ experimental and mathematical representation of the behaviour of rock salt used in the storage of gas, *In: First Conference on the Mechanical Behaviour of Salt,* The Pennsylvania State University, Nov. 9-11, p. 453-472.

Yang, C.H., Daemen, J.J.k., Yin, J.H. (1999). Experimental investigation of creep behaviour of salt rock, *International Journal of Rock Mechanics and Minning Sciences*, 36(2): 233-242.

Yang, S.Q., Xu, W.Y., Xie, S.Y., Shao, J.F. (2006). Studies on triaxial rheological deformation and failure mechanism of hard rock in saturated state, *Chinese Journal of Geotechnical Eng.*, 28(8): 962-969, (In Chinese).

Yang, S., and Liang, Y. (2010). Triaxial mechanical creep behaviour of sandstone, *Mining Science and Technology*, 20, 0339-0349.

Yılmaz, I. (2001). Gypsum/anhydrite: some engineering problems, *Bull. Eng. Geol. Env*. 59, 227-230.

Yılmaz I., Sendir H. (2002). Correlation of Schmidt hardness with unconfined compressive strength and elasticity modulus in gypsum from Sivas (Turkey), *Eng Geol,* 66, 211–9.

Yılmaz I., Karacan E. (2005). Slaking durability and its effect on the doline occurrence in the gypsum, *Environ Geol.* 47 (7), 1010-6.

Yılmaz I. (2007). Difference on the geotechnical properties of the two types of gypsum: alabastrine and porphyritic, *Bull Eng Geol Environ*, 66 (2), 187–95.

Yılmaz I., Yuksek AG. (2009). Preduction of the strength and elasticity modulus of gypsum using multiple regression, ANN, ANFIS models and their comparison, *Int J Rock Mech Min Sci.,* 46, 803–10.

Yılmaz, I. and Civelekoglu, B. (2009). Gypsum: An additive for stabilization of swelling clay soils, *Applied Clay Science*, 44 (1-2): 166-172.

Yılmaz, I. and Yüksek, A.G. (2009). Prediction of the strength and elasticity modulus of gypsum using multiple regression, ANN, ANFIS models, *International Journal of Rock Mechanics and Mining Sciences*, 46 (4): 803-810.

Yılmaz I. (2010). Influence of water content on the strength and deformability of gypsum, *Int J Rock Mech Min Sci,* 47, 342-347.

Yılmaz, I. Marschalko, M., Bednarik, M. (2011). Gypsum collapse hazards and importance of hazard mapping, *Carbonates and Evaporites*, 26 (2): 193-209.

Yılmaz, I., Keskin, I., Marschalko, M. (2015). Rock mass parameters based doline susceptibility mapping in gypsum terrain, *Quarterly Journal of Engineering Geology & Hydrogeology*, 48 (2): 124-134.

General Evaluation and Recommendations

This book brings together the latest advancements in engineering, agriculture, and applied sciences, offering an interdisciplinary perspective. Throughout the book, innovative methods are presented and analyzed, covering a wide range of topics, from solving two-dimensional heat equations in complex geometric domains to applying AI and IoT-based systems in modern agriculture.

The methods presented in this book provide more accurate and reliable results compared to classical solution techniques, offering inspiring insights for future research, particularly in the fields of engineering and applied mathematics. Sustainable systems and automation solutions in agricultural technology are also discussed, presenting critical applications for the future of global agriculture.

For future studies, it is recommended that the methods presented in the book be adapted to more complex structural problems and further tested in industrial applications. Automation systems developed using AI and sensor technologies have the potential to enhance the efficiency and sustainability of agriculture. Additionally, exploring solutions for two-dimensional heat equations in more complex geometries offers new avenues for researchers.

Index

- Agricultural Automation – 13, 67, 102
- Artificial Intelligence in Engineering – 25, 78, 150
- Composite Materials in Marine Applications – 40, 95, 170
- Creep Behavior of Alabastrine-Type Gypsum – 48, 116, 135
- Elliptic Function Solutions for Heat Equations – 120, 145, 188
- Green’s Function Method – 30, 55, 102
- IoT in Agriculture – 10, 43, 67
- Numerical Methods in Applied Mathematics – 115, 138, 190
- Sustainable Agriculture Systems – 67, 89, 155
- Two-Dimensional Heat Equation – 110, 115, 138
- Underground Engineering – 40, 60, 98